# Characterization and control of femtosecond electron and X-ray beams at free-electron lasers

**Dissertation**

**zur Erlangung des Doktorgrades**
**des Fachbereichs Physik**
**der Universität Hamburg**

vorgelegt von

Dipl.-Phys. Christopher Behrens
aus Itzehoe

Hamburg
2012

| | |
|---|---|
| Gutachter der Dissertation | Prof. Dr. Jörg Roßbach<br>Prof. Dr. Adrian L. Cavalieri<br>Prof. Dr. Leonid Rivkin |
| Gutachter der Disputation | Prof. Dr. Jörg Roßbach<br>PD Dr. Bernhard Schmidt |
| Datum der Disputation | 6. Juli 2012 |
| Vorsitzender des Prüfungsausschusses | Dr. Georg Steinbrück |
| Vorsitzender des Promotionsausschusses | Prof. Dr. Peter Hauschildt |
| Dekan der Fakultät für Mathematik, Informatik und Naturwissenschaften | Prof. Dr. Heinrich Graener |

## Abstract

X-ray free-electron lasers (FELs) open up new frontiers in photon science, and in order to take full advantage of these unique accelerator-based light sources, the characterization and control of the femtosecond electron and X-ray beams is essential. Within this cumulative thesis, recent results achieved within the active research field of femtosecond electron and X-ray beams at FELs are reported. The basic principles of X-ray FELs are described, and concepts of longitudinal electron beam diagnostics with femtosecond accuracy are covered. Experimental results obtained with a transverse deflecting structure (TDS) and spectroscopy of coherent terahertz radiation are presented, and the suppression of coherent optical radiation effects, required for diagnostics utilizing a TDS, is demonstrated. Control of the longitudinal phase space by using multiple radio frequencies for longitudinal electron beam tailoring is presented, and a new technique of reversible electron beam heating with two TDSs is described. For the characterization of femtosecond X-ray pulses, a novel method based on dedicated longitudinal phase space diagnostics for electron beams is introduced, and recent measurements with a streaking technique using external terahertz fields are presented.



## Kurzbeschreibung

Röntgen-Freie-Elektronen Laser (FELs) eröffnen neue Möglichkeiten in der Forschung mit Photonen, und um diese einzigartigen beschleuniger-basierten Lichtquellen vollständig nutzen zu können, ist die Charakterisierung und Kontrolle der Femtosekunden-Elektronen- und -Röntgenstrahlen wesentlich. Im Rahmen dieser kumulativen Arbeit wird über neueste Ergebnisse aus dem aktiven Forschungsfeld der Femtosekunden-Elektronen- und -Röntgenstrahlen bei FELs berichtet. Die Grundlagen von Röntgen-FELs werden beschrieben, und Konzepte von longitudinalen Elektronenstrahl-Diagnostiken mit Femtosekunden-Genauigkeit werden behandelt. Experimentelle Ergebnisse, erhalten mit einer transversal ablenkenden Struktur (TDS) und Spektroskopie von kohärenter Terahertz-Strahlung, werden präsentiert, und die Unterdrückung von kohärenten optischen Strahlungseffekten, notwendig fuer die Diagnostiken, welche eine TDS nutzen, wird demonstriert. Kontrolle des longitudinalen Phasenraumes durch Verwendung von vielfachen Hochfrequenzen für longitudinale Elektronenstrahl-Schneiderei wird präsentiert, und eine neue Technik des reversiblen Heizens von Elektronenstrahlen mit zwei TDSs wird beschrieben. Für die Charakterisierung von Femtosekunden-Röntgenpulsen wird eine neuartige Methode basierend auf dedizierter longitudinaler Phasenraum-Diagnostik für Elektronenstrahlen eingeführt, und neueste Messungen einer Schmier-Technik mit externen Terahertz-Feldern werden präsentiert.

"Ich hatte von meiner Arbeit niemand etwas gesagt; meiner Frau teilte ich nur mit, daß ich etwas mache, von dem die Leute, wenn sie es erfahren, sagen würden, der Röntgen ist wohl verrückt geworden."

Wilhelm Conrad Röntgen (1845-1923)

# Contents

# List of figures



The figures presented in the journal articles of chapters 3, 4, and 5 are not listed here.

# List of tables



The tables presented in the journal articles of chapters 3, 4, and 5 are not listed here.

# 1 Introduction

Both the discovery of X-rays by Röntgen in 1895 ("On a New Kind of Rays" [1]) and the realization of light amplification by stimulated emission of radiation, i.e., the laser, by Maiman in 1960 ("Stimulated Optical Emission in Ruby" [2]) fundamentally changed our understanding of the physical world. X-rays and lasers have many applications in industry and medicine, and have led to enormous implications for various disciplines of natural sciences.

X-ray beams, capable of penetrating matter, were discovered by experimental studies with cathode rays [1], i.e., particle beams of electrons in vacuum tubes. Their wavelike nature of nanometer ($10^{-9}$ m) wavelength involved the phenomenon of X-ray diffraction by a crystal, described and observed by Friedrich, Knipping, and von Laue in 1912 ("Interferenz-Erscheinungen bei Röntgenstrahlen" [3]). Based on the theoretical work of von Laue, X-ray diffraction could be explained by W.H. Bragg and W.L. Bragg (father and son) in 1913 by describing the observed diffraction patterns geometrically as interferences of the incident X-rays from the crystal lattice planes ("X-rays and Crystals" [4] and "The Diffraction of Short Electromagnetic Waves by a Crystal" [5]). For incident monochromatic X-ray beams of well-known wavelength, the observable diffraction patterns are fundamentally given by the distances of the lattice planes in the crystal. Thus, the structure of crystals can be determined, and X-ray beams provide a unique tool for studying the structure of matter.

The principles of (quantum) lasers evolved from the theory of stimulated emission, described by Einstein in 1916 within the framework of quantum physics ("Strahlungs-Emission und -Absorption nach der Quantentheorie" [6]). Before the first laser was demonstrated [2], amplification by stimulated emission was reported for microwaves by Gordon, Zeiger, and Townes in 1955 ("The Maser—New Type of Microwave Amplifier, Frequency Standard, and Spectrometer" [7]) and proposed for the infrared and optical wavelength range by Schawlow and Townes in 1958 ("Infrared and Optical Masers" [8]). In contrast to conventional radiation sources, lasers provide radiation with outstanding properties, e.g., a high degree of spatial and temporal coherence, a high spectral brightness, and the prospects of pulse durations in the femtosecond ($10^{-15}$ s) range and below, which allow research on extreme states of matter or time-resolved spectroscopy of dynamical systems, to name but a few.

The powerful combination of both X-rays and lasers renders unprecedented research on

matter at atomic length and ultrafast time scales possible, and several methods have been proposed and tested to generate laserlike, coherent X-ray beams. For instance, amplified spontaneous emission (ASE) of soft X-rays by means of population inversion between energy levels in neonlike selenium was reported by Matthews *et al.* in 1985 ("Demonstration of a Soft X-Ray Amplifier" [9]). However, an effective way to realize X-ray lasers are free-electron lasers (FELs) driven by relativistic electron beams from linear accelerators.

The principle of FELs was proposed by Madey in 1971 ("Stimulated Emission of Bremsstrahlung in a Periodic Magnetic Field" [10]) and experimentally demonstrated with an FEL oscillator, i.e., in combination with an optical resonator, at a wavelength of 3.4 $\mu$m by Deacon *et al.* in 1977 ("First Operation of a Free-Electron Laser" [11]). For the X-ray region, an FEL oscillator using a resonator with single-crystal silicon mirrors was proposed by Colella and Luccio in 1984 ("Proposal for a free electron laser in the X-ray region" [12]) but not demonstrated yet. In order to circumvent the restrictive needs for mirrors, principles of FELs operating in a self-amplified spontaneous emission (SASE) mode were developed by Kondratenko and Saldin in 1980 ("Generation of Coherent Radiation by a Relativistic Electron Beam in an Ondulator" [13]) and by Bonifacio, Pellegrini, and Narducci in 1984 ("Collective Instabilities and High-Gain Regime in a Free Electron Laser" [14]), allowing high-gain amplification of X-rays without mirror resonators. The successful operation of SASE FELs was reported for soft X-rays by Ackermann *et al.* in 2007 ("Operation of a free-electron laser from the extreme ultraviolet to the water window" [15]) and for hard X-rays by Emma *et al.* in 2010 ("First lasing and operation of an ångstrom-wavelength free-electron laser" [16]).

Within this cumulative thesis, recent results achieved within the active research field of femtosecond electron and X-ray beams at FELs are reported and discussed. In the remainder of the introduction, accelerator-based light sources for research in photon science are introduced. In chapter 2, the principles of X-ray FELs are described, and emphasis is put on the requirements on the FEL driving electron beams and on the characteristics of FEL radiation. Chapter 3 reports on concepts of diagnostics for femtosecond electron beams, and chapter 4 deals with the control and manipulation of the longitudinal phase space of electron beams. Techniques for the characterization of femtosecond X-ray pulses are presented and discussed in chapter 5, and a summary and conclusions are given in chapter 6.

## 1.1 Accelerator-based light sources

While accelerators were initially built for high-energy particle physics, they have evolved into powerful light and radiation sources for research in various disciplines of natural sciences. The mean energy loss of relativistic electron beams in a betatron (a magnetic-induc-

tion electron accelerator [17, 18]) due to the emission of radiation, predicted by Iwanenko and Pomeranchuk in 1944 ("On the Maximal Energy Attainable in a Betatron" [19]), and the following observation of visible radiation emitted in the bending magnets of a synchrotron (a circular radio-frequency accelerator with the guiding magnetic fields being synchronized to the particle beam energy [20, 21]) by Elder *et al.* in 1947 ("Radiation from Electrons in a Synchrotron" [22]) resulted in the development of accelerator-based light sources, which were classified into four types or generations (e.g., Refs. [23, 24]). The characteristics of the radiation fan emitted in a bending magnet, the so-called synchrotron radiation, were calculated by Schwinger in 1949 ("On the Classical Radiation of Accelerated Electrons" [25]) and utilized for various experiments in the first and second generation of accelerator-based light sources, where the latter were based on storage-ring synchrotrons keeping the electron beams stored at the final energy [26]. The total radiated power of a single electron with the normalized energy $\gamma = W/(m_e c^2)$ in a dipole magnet with the bending radius $R$, where $m_e$ is the electron rest mass and $c$ is the speed of light in vacuum, can be calculated as [25]

$$P_s = \frac{e^2 c}{6\pi\varepsilon_0}\frac{\gamma^4}{R^2}, \tag{1.1}$$

where $\varepsilon_0$ is the permittivity of free space and $e$ is the elementary charge. The total radiation power shows a strong energy dependence, and the main part is emitted in a narrow cone of opening angle $\Theta \approx 1/\gamma$ around the instantaneous direction of the motion of the electron. For highly relativistic electrons with $\gamma \gg 1$, the narrow cone of radiation with $\Theta \ll 1$ is effectively generated within a small part of the trajectory, leading to a short radiation pulse with a corresponding broad spectrum extending frequencies beyond the critical frequency [25]

$$\omega_c = \frac{3c}{2}\frac{\gamma^3}{R}. \tag{1.2}$$

The powerful source of broadband synchrotron radiation emitted in a single bending magnet was improved in terms of brightness (brilliance) by using insertion devices composed of periodic arrays of magnets with alternating polarity, called undulators and described by Motz in 1951 ("Applications of the Radiation from Fast Electron Beams" [27]). The photon beam brightness, defined as the number of photons per unit time per unit area of the radiation source per unit solid angle of the radiation cone per unit spectral bandwidth, is significantly enhanced for undulators due to the concentration of the radiation in narrow cones along the trajectory around the straight undulator axis (see Fig. 1.1) and in narrow

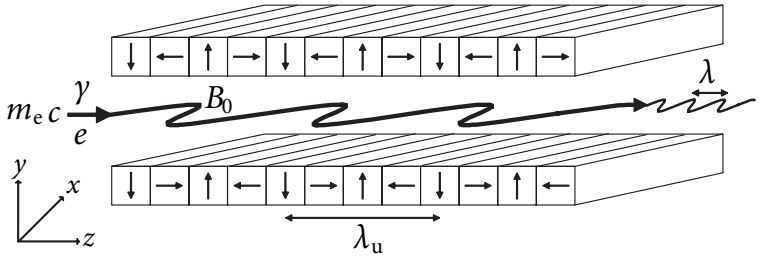


**Figure 1.1:** The sinusoidal trajectory of an electron in a planar undulator, emitting radiation [28].

spectral peaks (a fundamental and harmonics) given by the wavelength (e.g., Refs. [24, 29])

$$\lambda = \frac{1}{h}\frac{\lambda_u}{2\gamma^2}\left(1 + \frac{K^2}{2} + \gamma^2\Theta^2\right) \tag{1.3}$$

with the harmonics $h = 1, 2, 3, \ldots$, the undulator period $\lambda_u$, and the undulator parameter

$$K = \frac{eB_0\lambda_u}{2\pi m_e c}, \tag{1.4}$$

where $B_0$ is the peak field of the sinusoidal magnetic field on the axis of a planar undulator. The fundamental wavelength (first harmonic with $h = 1$) can be calculated by applying a Lorentz transformation of the radiation field emitted by an oscillating dipole. In the moving frame of reference of an electron, the relativistic length contraction reduces the undulator period to $\lambda_u^* = \lambda_u/\gamma$ and the electron is performing dipole oscillations at a corresponding higher frequency. In the laboratory frame of reference of an observer looking towards the moving electron, the frequency of the emitted radiation is further increased (blue-shifted) by the relativistic Doppler effect. Taking into account both the reduced undulator period and the relativistic Doppler effect with the average longitudinal velocity of the sinusoidal trajectory [see Eq. (2.5) in chapter 2] leads to the wavelength described by Eq. (1.3). Higher harmonics can be explained by a maximum bending angle of the sinusoidal trajectory $\sim K/\gamma$ [cf. Eq. (2.3)] exceeding the emission cone angle of $\sim 1/\gamma$. Then the observer only receives radiation generated within a small part of the trajectory, and the periodic radiation pulses of short duration result in a spectrum containing higher harmonics (e.g., Ref. [30]).

Planar undulators generate linearly polarized radiation, and another type, generating circularly polarized radiation, is the helical undulator, which has rotating transverse magnetic fields along the straight undulator axis, forcing the electrons to move on helical trajectories. For undulator parameters with $K \gg 1$, the insertion devices are referred to as wigglers (undulators have $K \lesssim 1$) and generate a quasi-continuous spectrum with higher brightness compared to typical bending magnets. The incorporation of insertion devices into the long

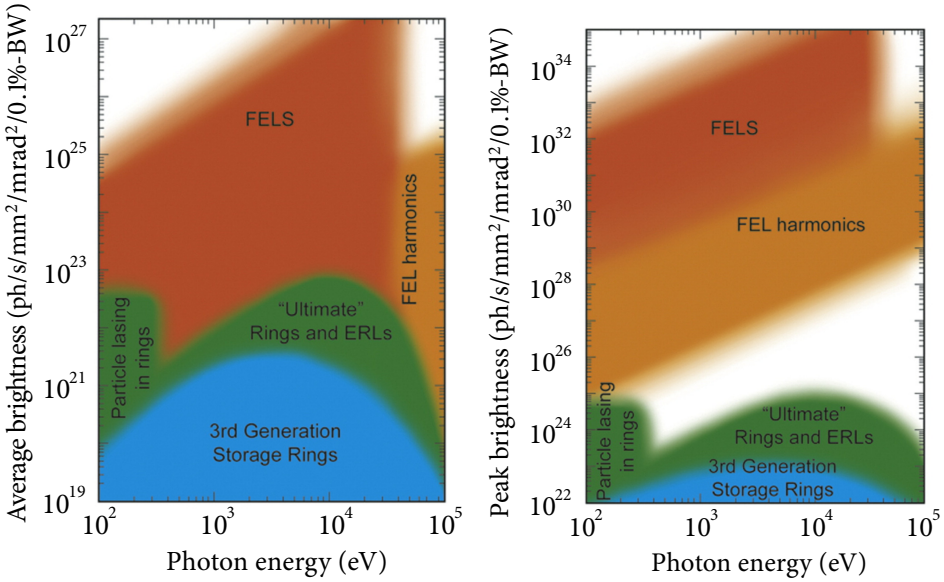


(a) Average brightness. (b) Peak brightness.

**Figure 1.2:** The photon beam brightness (brilliance) provided by several types or generations of accelerator-based light sources with (a) the average brightness and (b) the peak brightness [31].

straight sections of dedicated storage rings, providing electron beams optimized for high brightness, led to the third generation of accelerator-based light sources (e.g., Refs. [23, 24]).

Electron beams in accelerator-based light sources are bunched with a spacing given by the accelerator driving radio-frequency (r.f.) system, and the $N_e$ electrons per bunch generally emit incoherent (spontaneous) radiation with a total intensity being $N_e$ times the intensity of a single electron, i.e., the individual electrons contribute independently and random in phase. The emission of coherent radiation at a particular wavelength $\lambda$, scaling quadratically with the number of electrons, can be achieved either for electron bunches shorter than $\lambda$ or for density modulation in the electron bunch on the scale of $\lambda$ (e.g., Ref. [29]). Only the latter can be satisfied in the X-ray region, based on a process of self-organization of the electrons (so-called microbunching) in a bunch at free-electron lasers (e.g., Refs.[28, 29, 32]), leading to the fourth generation of accelerator-based light sources. X-ray FELs are tunable over a wide photon energy (wavelength) range and exceed the photon beam brightness of third generation light sources by several orders of magnitude, as is presented in Fig. 1.2.

## 1.2 Prospects for photon science

The development of X-ray free-electron lasers opens up new frontiers in photon science, which encompasses the interaction of light with matter, leading to various scientific drivers,

e.g., the understanding and controlling of electronic, atomic, and molecular dynamics on their natural time scales (e.g., Refs. [33, 34]), the study of soft condensed matter (e.g., Refs. [35, 36]), the research in life sciences (see, e.g., Ref. [37]), and many more. An excellent comprehensive overview of scientific drivers for future accelerator-based light sources can be found in the report "Science and Technology of Future Light Sources: A White Paper" [23].

The outstanding capabilities of X-ray FELs, such as providing laserlike, high-brightness radiation tunable over a wide photon energy range, meet many requirements of experiments and techniques in photon science. Further key features are high spatial coherence, needed for diffractive imaging experiments (e.g., Refs. [38, 39]), prospects of polarization control, important for studies in the research field of magnetic materials, or control of the photon beams in terms of pulse shape, duration, and bandwidth (e.g., Ref. [23]). In recent years, several methods to control FEL photon pulse durations have been proposed by manipulating and controlling the FEL driving electron bunches, achieving femtosecond pulse durations (e.g., Refs. [40, 41, 42]). Other methods, with additional prospects of generating FEL photon pulses with durations in the attosecond range, make use of electron bunch manipulation with external quantum lasers (e.g., Refs. [43, 44, 45]). Techniques to achieve Fourier-transform-limited (bandwidth-limited) photon pulses with full temporal coherence complement the versatile capabilities of X-ray FELs (see, e.g., Refs. [23, 31]).

Free-electron lasers providing soft X-rays for photon science are currently the Free-Electron Laser in Hamburg (FLASH) at DESY in Hamburg and Fermi@Elettra at Elettra in Trieste. For hard X-rays, the Linac Coherent Light Source (LCLS) at SLAC in Stanford and the SPring-8 Angstrom Compact Free-Electron Laser (SACLA) at SPring-8 in Hyogo are in operation, and the European X-ray Free-Electron Laser (E-XFEL) at DESY is under construction. Table 1.1 summarizes the wavelength and peak brightness provided by these X-ray FEL facilities. Status information about present FEL projects can be found in Ref. [31].

**Table 1.1:** Minimum wavelength and peak brightness provided by present and future X-ray FELs. The parameters are found in literature or taken from the facility's conceptional design reports.

| | FLASH | Fermi@Elettra | LCLS | SACLA | E-XFEL |
|---|---|---|---|---|---|
| Minimum wavelength (nm) | 4.4 | 10 | 0.15 | 0.1 | 0.05 |
| Peak brightness (ph/s/mm$^2$/mrad$^2$/0.1%-BW) | $< 10^{30}$ | $< 10^{32}$ | $< 10^{33}$ | $< 10^{34}$ | $< 10^{34}$ |

# 2 X-ray free-electron lasers

The basic theory describing free-electron lasers can be derived without methods of quantum physics, as is shown in the following sections of this chapter, and the presented analytical treatment is based on the article "Review of x-ray free-electron laser theory" [28] by Huang and Kim, and on the textbooks "Ultraviolet and Soft X-Ray Free-Electron Lasers: Introduction to Physical Principles, Experimental Results, Technological Challenges" [29] by Schmüser, Dohlus, and Rossbach and "The physics of free electron lasers" [32] by Saldin, Schneidmiller, and Yurkov. The principle of FELs is described particularly with regard to high-gain FELs operating in the X-ray region, and special emphasis is put on the requirements on the FEL driving electron beams and on the characteristics of FEL radiation.

In contrast to quantum lasers, where the electrons in the active laser medium are bound to discrete atomic or molecular energy levels, the principle of FELs is based on free electrons in a relativistic electron beam moving in vacuum and co-propagating with an electromagnetic (EM) wave. As is shown in the following section, net energy transfer from the electrons to the EM wave, i.e., FEL amplification, can only take place when the electrons have a velocity component parallel to the transverse electric field of the EM wave. This can be achieved by means of undulators, forcing the electrons to move on curved periodic trajectories. For a relativistic electron with the longitudinal velocity $v_z = dz/dt$ passing through a planar undulator (see Fig. 1.1), the horizontal component of the Lorentz force can be written as

$$\gamma m_\mathrm{e} \frac{dv_x}{dt} = e v_z B_y = -e v_z B_0 \sin(k_\mathrm{u} z) \tag{2.1}$$

with the magnetic field in the center between the undulator gaps given by

$$\boldsymbol{B} = B_y \boldsymbol{e_y} = -B_0 \sin(k_\mathrm{u} z) \boldsymbol{e_y}\,, \tag{2.2}$$

where $z$ is the longitudinal position along the undulator axis, $k_\mathrm{u} = 2\pi/\lambda_\mathrm{u}$, and $\boldsymbol{e_y}$ is the unit vector in vertical direction. By taking into account $\gamma = \text{const}$ due to the absence of an electric field, the integration yields

$$v_x = \frac{dx}{dt} = \frac{Kc}{\gamma} \cos(k_\mathrm{u} z) \tag{2.3}$$

with the undulator parameter defined in Eq. (1.4). As a result of the sinusoidal trajectory [$x \sim \sin(k_u z)$ and $y = \text{const}$], the longitudinal velocity varies along the undulator axis as

$$\begin{aligned} v_z = \sqrt{v^2 - v_x^2} &= c\sqrt{1 - \frac{1}{\gamma^2} - \frac{v_x^2}{c^2}} \\ &\approx c\left[1 - \frac{1}{2\gamma^2}\left(1 + \frac{K^2}{2}\right)\right] - \frac{cK^2}{4\gamma^2}\cos(2k_u z)\,, \end{aligned} \tag{2.4}$$

and an average longitudinal velocity over an undulator period can accordingly be defined as

$$\overline{v}_z = c\left[1 - \frac{1}{2\gamma^2}\left(1 + \frac{K^2}{2}\right)\right]. \tag{2.5}$$

The transverse velocity component $v_x$ in Eq. (2.3), parallel to the transverse electric field of an EM wave, is required but not sufficient by itself to achieve sustained FEL amplification. The EM wave, traveling with the speed of light, will slip forward with respect to the electrons, moving with $\overline{v}_z \lesssim c$, and a steady energy transfer is only possible for a certain phase slippage, leading to the resonance condition for FELs described and derived in the following.

## 2.1 Principle of free-electron lasers

Free-electron lasers can be classified into two types: amplifiers and oscillators (cf. the terminology of laser physics). The FEL amplifier simply amplifies an input radiation field, whereas the FEL oscillator incorporates an additional feedback between the input and output radiation fields, realized by means of an optical resonator. The main elements of FELs are a beam of relativistic electron bunches with energy $W = \gamma m_e c^2$ and an undulator, which is assumed to be planar in the following. By considering a plane electromagnetic wave, co-propagating with the electron beam, as input radiation with the horizontal electric field component

$$E_x = E_0 \cos(kz - \omega t + \psi_0)\,, \tag{2.6}$$

where $k = \omega/c = 2\pi/\lambda$, and $E_0$ and $\psi_0$ are the initial amplitude and (constant) phase of the electric field, respectively, the rate of energy transfer between electrons and the EM wave is

$$\frac{dW}{dt} = -e\boldsymbol{v}\cdot\boldsymbol{E} = -ev_x E_x\,. \tag{2.7}$$

Using the horizontal velocity given in Eq. (2.3) and electric field given in Eq. (2.6) results in

$$\begin{aligned}\frac{dW}{dt} &= -e\frac{Kc}{\gamma}\cos(k_\mathrm{u}z)E_0\cos(kz-\omega t+\psi_0)\\ &= -\frac{eE_0Kc}{2\gamma}\{\cos[(k+k_\mathrm{u})z-\omega t+\psi_0]+\cos[(k-k_\mathrm{u})z-\omega t+\psi_0]\}\,,\end{aligned} \tag{2.8}$$

where the product of cosine functions has been transformed into a sum in order to describe the rate of energy transfer in an FEL by means of the two phases (arguments of the cosines)

$$\psi_\pm = (k\pm k_\mathrm{u})z-\omega t+\psi_0\,. \tag{2.9}$$

The argument $\psi_+$ is referred to as ponderomotive phase, and a steady energy transfer between the electrons and the EM wave can be achieved for $\psi_+ = \text{const}$ and, accordingly, for

$$\frac{d\psi_+}{dz} = (k+k_\mathrm{u})-\frac{\omega}{\overline{v}_z} = 0 \tag{2.10}$$

along the undulator, where $dz/dt = \overline{v}_z$, neglecting the longitudinal oscillations in the full term of Eq. (2.4) for the sake of simplicity. Taking into account the longitudinal oscillations leads to minor modifications as is described later in this section. The wavelength satisfying the resonance condition in Eq. (2.10) for a sustained energy transfer in an FEL reads [32]

$$\lambda_\mathrm{r} = \frac{\lambda_\mathrm{u}}{\overline{v}_z}(c-\overline{v}_z) = \lambda_\mathrm{u}\frac{(1-\overline{v}_z/c)}{\overline{v}_z/c} \approx \lambda_\mathrm{u}\frac{1}{2\gamma_\mathrm{r}^2}\left(1+\frac{K^2}{2}\right), \tag{2.11}$$

where $\gamma_\mathrm{r}$ is the corresponding (normalized) resonance energy. Thus, sustained energy transfer takes place when the slippage of the EM wave with respect to the electrons is one radiation wavelength per undulator period. The wavelength in Eq. (2.11), satisfying the resonance condition, is the same wavelength as is generated by undulators in forward direction with $\Theta = 0$ [see Eq. (1.3)], hence spontaneous undulator radiation can provide the input radiation field to initiate the FEL amplification process. Equation (2.11) shows that the wavelength of FELs is tunable over a wide range by varying the electron beam energy $\gamma_\mathrm{r} = W_\mathrm{r}/(m_\mathrm{e}c^2)$ or the undulator parameter $K$ by adjusting the gap height between the magnetic poles.

The second cosine function in Eq. (2.8) with the phase $\psi_-$, which can be expressed as

$$\psi_- = \psi_+ - 2k_\mathrm{u}z\,, \tag{2.12}$$

varies rapidly, and for $\psi_+ = \text{const}$, i.e., steady energy transfer, it performs two oscillations per undulator period and cancels out. Thus, the cosine function with the phase $\psi_-$ is not

considered anymore, and the general evolution of the ponderomotive phase, taking into account electron energies that differ from the resonance energy defined via Eq. (2.11), reads

$$\frac{d\psi}{dz} = (k + k_\mathrm{u}) - \frac{\omega}{\overline{v}_z} \approx k_\mathrm{u} - k\frac{1}{2\gamma^2}\left(1 + \frac{K^2}{2}\right), \tag{2.13}$$

where $\psi \equiv \psi_+$ describes the phase of the electrons relative to the EM wave. Even in the approximation of a monoenergetic electron beam of resonance energy $\gamma_\mathrm{r}$, i.e., with the relative energy deviation $\eta = (\gamma - \gamma_\mathrm{r})/\gamma_\mathrm{r} = 0$, differing electron energies must be admitted to take account for the demanded energy transfer in an FEL. In the limit of an electron beam with low energy spread, i.e., with $|\eta| \ll 1$, the evolution of $\psi$ in Eq. (2.13) can be written as [28]

$$\frac{d\psi}{dz} = 2k_\mathrm{u}\eta\,, \tag{2.14}$$

showing a linear dependence on the relative energy deviation. According to Eq. (2.8) and by using $dz/dt = \overline{v}_z \approx c$, the evolution of the phase space $(\psi, \eta)$ is complemented by means of

$$\frac{d\eta}{dz} = -\frac{eE_0K}{2\gamma_\mathrm{r}^2 m_\mathrm{e}c^2}\cos\psi\,, \tag{2.15}$$

and the two coupled first-order differential equations in Eqs. (2.14) and (2.15) can be combined into one second-order differential equation (so-called pendulum equation) given by

$$\frac{d^2\psi}{dz^2} + \frac{eE_0Kk_\mathrm{u}}{\gamma_\mathrm{r}^2 m_\mathrm{e}c^2}\cos\psi = 0\,. \tag{2.16}$$

The low-gain FEL theory, based on Eqs. (2.14) - (2.16), describes the phase space motion of electrons in the presence of an electromagnetic wave, neglecting the growth of the electric field amplitude during FEL amplification, i.e., $E_0$ in Eq. (2.15) is assumed to be roughly constant. This assumption is well justified for FEL oscillators, where the energy gain per passage of the undulator is low and the electric field amplitude grows only slowly. For X-ray FELs operating in the high-gain regime, the electric field amplitude grows significantly in a single pass through a rather long undulator and needs to be taken into account, leading to the high-gain FEL theory described later in this section. However, the low-gain FEL theory already describes the basic principles and underlying physics of any FEL, as is discussed in the following after briefly introducing the modifications due to the neglected longitudinal oscillations of $v_z$ in Eq. (2.10). It can be shown that $\lambda_\mathrm{r}$ in Eq. (2.11) changes to (e.g., Ref. [29])

$$\lambda_\mathrm{r} = \frac{1}{h}\frac{\lambda_\mathrm{u}}{2\gamma_\mathrm{r}^2}\left(1 + \frac{K^2}{2}\right) \tag{2.17}$$

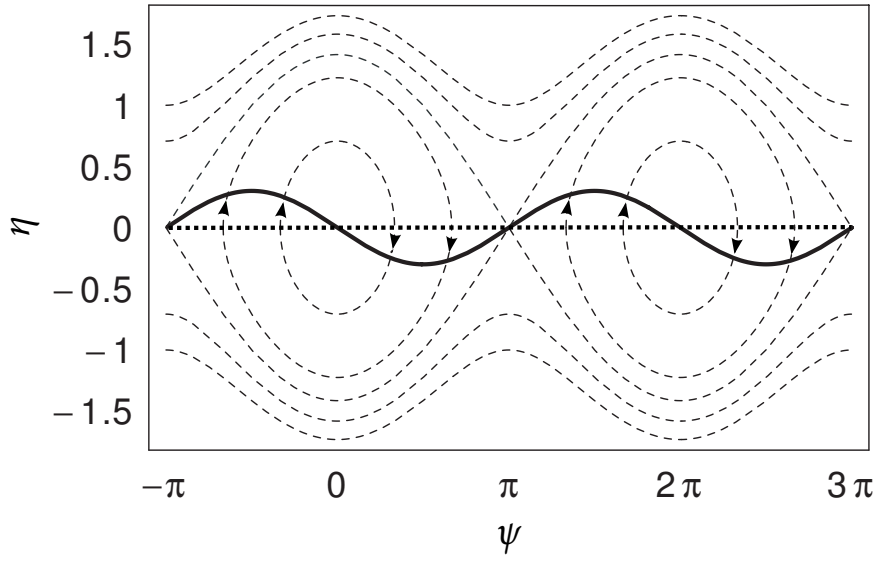


**Figure 2.1:** Phase space trajectories of electrons in the presence of an electromagnetic wave with an initial phase of $\psi_0 = \pi/2$, while the EM wave fulfills the resonance condition for energy transfer [28]. The electrons are initially distributed along $\psi$ with zero relative energy deviation, i.e., $\eta = 0$ for all phases (bold dotted line). When the energy transfer takes place, the electron distribution becomes sinusoidal (bold solid line) in the longitudinal phase space $(\psi, \eta)$, following the trajectories described by the equations of the low-gain FEL theory (thin dashed lines).

with the harmonic number $h = 1, 3, 5, \ldots$, hence odd higher harmonics fulfill the resonance condition and can be amplified in an FEL. In addition to the amplification of harmonics, the coupling of the electrons to the EM wave in a planar undulator is changed, which can be taken into account by replacing the undulator parameter $K$ in Eqs. (2.15) and (2.16) by

$$\mathcal{K} = K \cdot \left[ J_0\left(\frac{K^2}{4+2K^2}\right) - J_1\left(\frac{K^2}{4+2K^2}\right)\right], \tag{2.18}$$

where $J$ denotes the Bessel functions of the first kind. The resonance wavelength for a steady energy transfer in Eq. (2.17) is, however, still calculated by means of $K$ defined in Eq. (1.4).

In the theory of low-gain FELs, the dynamics of electrons in an undulator under the action of electromagnetic fields is fully described by the first order differential equations given in Eqs. (2.14) and (2.15), and Fig. 2.1 presents the phase space trajectories of electrons (curves of a constant Hamiltonian [29]) in the presence of an EM wave that fulfills the resonance condition for energy transfer. When the energy transfer during the FEL process along the undulator takes place, the initially monoenergetic electrons ($\eta = 0$ for all $\psi$) begin to gain or lose energy depending on the phase relative to the EM wave, as is described by Eq. (2.15), and a periodic energy modulation at the resonance wavelength $\lambda_r$ develops. This

energy modulation results in a modulation of the longitudinal velocity [see Eq. (2.5)], which is in turn transformed into a density modulation by means of the phase evolution derived in Eq. (2.14). In this scenario, the net energy transfer is zero since the number of electrons supplying energy to the EM wave is the same number of electrons removing energy. However, there are two favorable conditions leading to a net amplification of the EM wave, which correspond to the FEL operation in the low-gain and high-gain regime, respectively.

### 2.1.1 Low-gain regime

The zero energy exchange on average between monoenergetic electrons ($\eta = 0$) in the presence of a resonant EM wave, as is represented by the phase space trajectories shown in Fig. 2.1, can be counteracted by operating the FEL detuned with electrons of higher energy, i.e., with $\eta > 0$. The growth of the electric field amplitude during FEL amplification is neglected in this operation regime, and the field gain $\Delta E$ per undulator pass is small compared to the actual field $E_0$ of the EM wave, leading to the term low-gain regime. Similar to the conventions in the physics of quantum lasers, the gain $g = 1 + G = (E_0 + \Delta E)^2/E_0^2$ can be described as the ratio of the output and input power ($P_0 \sim E_0^2$), and no amplification corresponds to $g = 1$ and $G = 0$, respectively. For a single pass through a short undulator with $N_\mathrm{u}$ periods, the gain function $G$ can be expressed as (see, e.g., Refs. [29, 32, 46])

$$G(\delta) = -\frac{\Gamma^3 N_\mathrm{u}^3 \lambda_\mathrm{u}^3}{2} \frac{d}{d\delta}\left(\frac{\sin^2\delta}{\delta^2}\right), \tag{2.19}$$

where $\delta = 2\pi N_\mathrm{u}\eta$ is the relative energy detuning and $\Gamma$ is the gain parameter given by [29]

$$\Gamma = \left(\frac{\mu_0 K^2 e^2 k_\mathrm{u} n_\mathrm{e}}{4\gamma_\mathrm{r}^3 m_\mathrm{e}}\right)^{1/3} \tag{2.20}$$

with the electron density $n_\mathrm{e}$ and the permeability of free space $\mu_0$. The argument of the derivative in Eq. (2.19), i.e., the sinc squared function $\sin^2\delta/\delta^2$, describes the intensity distribution $I$ of spontaneous undulator radiation as a function of the frequency deviation $\delta = \pi N_\mathrm{u}\Delta\omega/\omega_1$ relative to the center frequency $\omega_1$ (cf. relative energy detuning). The fact that $G(\delta) \sim -dI/d\delta$ in the low-gain regime is referred to as Madey theorem [47], and both the intensity distribution of spontaneous undulator radiation $I$ (dashed line) and the gain $g = 1 + G$ (solid line) are shown in Fig. 2.2 as a function of the relative energy detuning (frequency deviation) $\delta$. At the resonance energy with $\delta \sim \eta = 0$, the gain is unity, i.e., the net amplification is zero ($G = 0$). By tuning the electron energy to $\delta \sim \eta > 0$, however, FEL amplification takes place and energy is transferred into the EM wave with $g > 1$ ($G > 0$),

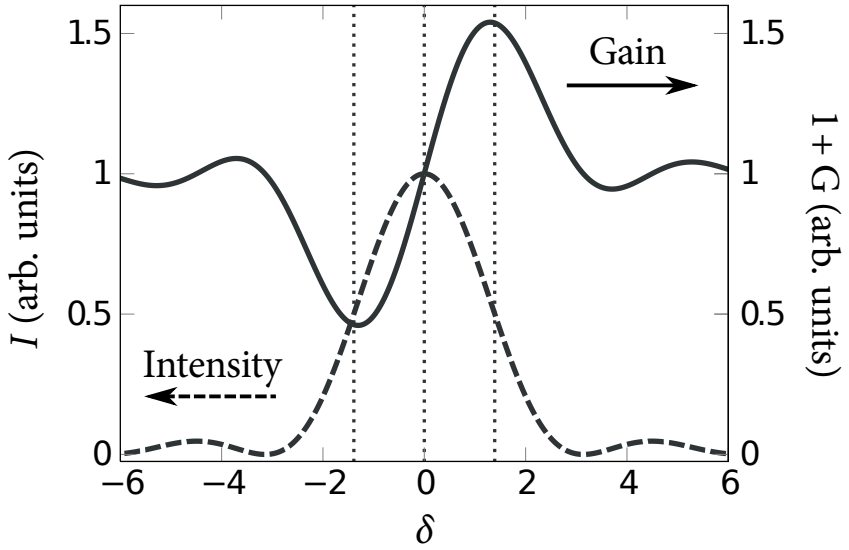


**Figure 2.2:** Intensity distribution $I \sim \sin^2\delta/\delta^2$ of spontaneous undulator radiation (dashed line) and the gain $g = 1 + G$ of an FEL operating in low-gain regime (solid line) as a function of the relative energy detuning (frequency deviation) $\delta$. The presented gain is calculated by using $G(\delta) \equiv -dI/d\delta$, and the vertical dotted lines denote the full width at half maximum $\Delta\delta$ of $I$.

whereas the operation with $\delta \sim \eta < 0$ leads to energy gain of electrons, which is referred to as inverse FEL mechanism. It is worth pointing out that according to Fig. 2.2, the maximum of the gain is within the bandwidth of the spontaneous undulator radiation, and the full width at half maximum of $I$ can be estimated to be $\Delta\delta \approx \pi$, hence the line width of spontaneous undulator radiation is $\Delta\omega \approx \omega_1/N_\mathrm{u}$. This is a result of the EM wave train of $N_\mathrm{u}$ oscillations and duration $\Delta t \approx N_\mathrm{u} 2\pi/\omega_1$ generated in the undulator with $\Delta t \Delta\omega \approx 2\pi$.

### 2.1.2 High-gain regime

In contrast to the low-gain regime, taking into account the growth of the electric field amplitude during the energy transfer in an FEL, i.e., $E_0 = E_0(z)$ in Eq. (2.6), can result in an exponential increase of the gain within a single pass through a long undulator. In the theory of this high-gain regime, a density modulated electron beam as is represented in Fig. 2.1 still results in no net energy transfer by itself but changes the phase of the resonant EM wave according to the Maxwell equations, so that the electrons may end up in the decelerating phase and begin to lose energy on average, i.e. FEL amplification takes place. Thus, the equations of motion in Eqs. (2.14) and (2.15) have to be solved together with the inhomogeneous elec-

tromagnetic wave equation for the electric field vector $\boldsymbol{\mathcal{E}}$ (complex-valued here):

$$\left[\nabla^2 - \frac{1}{c^2}\frac{\partial^2}{\partial t^2}\right]\boldsymbol{\mathcal{E}} = \mu_0\frac{\partial \boldsymbol{j}}{\partial t} + \frac{1}{\varepsilon_0}\nabla(-en_\mathrm{e})\,, \tag{2.21}$$

where $\boldsymbol{j} = -en_\mathrm{e}\boldsymbol{v}$ is the current density of the FEL driving electron bunch. The detailed derivation of the equations describing FELs in the high-gain regime, taking into account the electric field evolution via Eq. (2.21), is somewhat laborious, hence the basic findings of the high-gain FEL theory are given without proof in the following, based on the treatment in Ref. [29] and supported by the comprehensive FEL theory derived in Ref. [32].

A correct and realistic model of high-gain FELs is based on a full three-dimensional theory considering the spatial (transverse) dependencies of the electron beam, of the EM wave and of the magnetic field in the undulator. Unfortunately, the full three-dimensional treatment has no practical analytical solutions and requires sophisticated numerical simulation codes, e.g., FAST [48] or GENESIS [49]. However, by assuming an infinitely long electron beam, co-propagating with a monochromatic plane EM wave with the horizontal electric field $\mathcal{E}_x(z,t) = \mathcal{E}_x(z)\exp[i(kz - \omega t + \psi_0)]$, in a one-dimensional model, i.e., the transverse dimensions ($x$ and $y$) are not considered, analytical solutions exist and already provide a deep insight into the physics of high-gain FELs. The following equations describe the longitudinal phase space motion of the $n$-th electron and the evolution of the current density $\mathcal{J}$ and horizontal electric field $\mathcal{E}_x$ in the one-dimensional model of the high-gain regime [29]:

$$\frac{d\psi_n}{dz} = 2k_\mathrm{u}\eta_n\,, \tag{2.22}$$

$$\frac{d\eta_n}{dz} = -\frac{e}{\gamma_\mathrm{r} m_\mathrm{e} c^2}\,\mathrm{Re}\left[\left(\frac{\mathcal{E}_x \mathcal{K}}{2\gamma_\mathrm{r}} - \frac{i\mu_0 c^2}{\omega}\mathcal{J}\right)\exp(i\psi_n)\right]\,, \tag{2.23}$$

$$\frac{d\mathcal{E}_x}{dz} = -\frac{\mu_0 c \mathcal{K}}{4\gamma_\mathrm{r}}\mathcal{J}\,, \tag{2.24}$$

$$\mathcal{J} = -\frac{2ecn_\mathrm{e}}{N_\mathrm{e}}\sum_{n=1}^{N_\mathrm{e}}\exp(-i\psi_n)\,. \tag{2.25}$$

Here, the evolution of the electric field is taken into account in Eq. (2.23) via Eq. (2.24), which is a function of the modulated current density given in Eq. (2.25) for $N_\mathrm{e}$ electrons per wavelength. The last term differing from Eqs. (2.14) and (2.15) describing the low-gain regime is due to longitudinal space charge forces of a modulated electron beam, which lead to an additional change of the energy of the electrons, described by the second term $\sim \mathcal{J}$ of the real part in Eq. (2.23). The set of $2N_\mathrm{e} + 2$ coupled first-order equations in Eqs. (2.22) - (2.25) describes the main physics of FELs in the high-gain regime, including the effect of

FEL saturation. However, even in the one-dimensional model, the $2N_e+2$ equations have no analytical solution without making further assumptions and need to be solved numerically.

By assuming that the periodic density modulations due to the energy transfer in an FEL remain small, which is not the case in the saturation regime, the evolution of the electric field amplitude can be described by one third-order differential equation (instead of a set of coupled first-order equations), leading to the analytical solution of an exponentially increasing gain curve. A thorough analysis results in the third-order equation (e.g., Refs. [29, 32])

$$\frac{\mathcal{E}_x'''}{\Gamma^3} + 2i\frac{\eta}{\rho}\frac{\mathcal{E}_x''}{\Gamma^2} + \left(\frac{k_p^2}{\Gamma^2} - \frac{\eta^2}{\rho^2}\right)\frac{\mathcal{E}_x'}{\Gamma} - i\mathcal{E}_x = 0\,, \tag{2.26}$$

where $\mathcal{E}_x' \equiv d\mathcal{E}_x/dz$, and a space charge and an efficiency (or FEL) parameter are defined as

$$k_p = \sqrt{\frac{2k_u\mu_0 n_e e^2 c}{\gamma_r m_e \omega}} \quad \text{and} \quad \rho = \frac{\Gamma}{2k_u} = \frac{1}{4\pi\sqrt{3}}\frac{\lambda_u}{L_{g0}}\,, \tag{2.27}$$

respectively. The FEL parameter $\rho$ contains the (ideal) one-dimensional power gain length $L_{g0} = (\sqrt{3}\Gamma)^{-1}$. Equation (2.26) shows an impact of energy deviation for $\eta/\rho > 0$, discussed in following section, whereas for monoenergetic electrons with $\eta = 0$ and in the assumption of negligible space charge forces with $k_p \approx 0$, the linear equation in Eq. (2.26) reduces to $\mathcal{E}_x''' = i\Gamma^3\mathcal{E}_x$ and can be solved by three exponential functions. Two solutions carry out oscillations (one of them is damped) and the third results in the exponential gain curve

$$G(z) = \left|\frac{\mathcal{E}_x(z)}{\mathcal{E}_{in}}\right|^2 - 1 \approx \frac{1}{9}\exp(z/L_{g0})\,, \tag{2.28}$$

which dominates the other two solutions for $z > 2L_{g0}$. The factor 1/9 is determined by the input power shared by the three solutions with $|\mathcal{E}_{in}/3|^2$. The result in Eq. (2.28) is essential and shows the exponential amplification of an input radiation field (seed radiation) in a single pass through a long undulator, demonstrating the feasibility of X-ray FELs without the restrictive needs for mirror resonators. In this exponential gain regime, which can be described by the linear third-order equation in Eq. (2.26), the output radiation fields depend linearly on the input radiation fields. Thus, the exponential gain regime is also referred as linear regime, in contrast to the saturation regime, which is a highly nonlinear regime.

Whereas the generation of a suitable seed radiation, e.g., via high harmonic generation in a gas jet, is a difficult task, the spontaneous undulator radiation emitted by the electron bunches can initiate the FEL start-up process in a high-gain FEL, leading to the operation mode of self-amplified spontaneous emission (SASE). Instead of an input radiation field, a

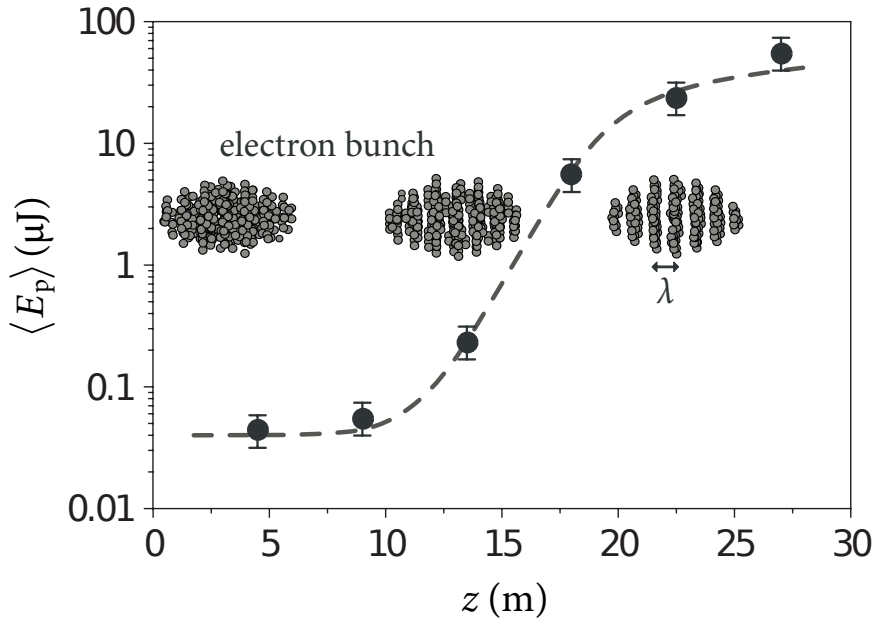


**Figure 2.3:** Evolution of the average FEL radiation pulse energy $\langle E_p \rangle$ along the undulator measured (large black dots with error bars) at FLASH [15], demonstrating the exponential growth and saturation at a wavelength of $\lambda = 13.7$ nm. The FEL driving electron bunch at three different undulator lengths is sketched via bunches of small gray dots, illustrating the process of microbunching.

periodic density modulation can also initiate the FEL start-up process, and spectral components of the randomly distributed electrons (cf. shot noise) within the amplification bandwidth are amplified with a high gain. Both scenarios give a physically equivalent interpretation of SASE, and its start-up process needs to be taken into account in order to define the input radiation field for a calculation of the corresponding gain curve [cf. Eq. (2.28)].

The linear third-order equation in Eq. (2.26) describes the electric field evolution of the EM wave during FEL amplification neglecting the buildup of significant periodic density modulations, hence saturation effects in high-gain FELs are obviously not considered by the gain curve in Eq. (2.28), and numerical solutions of the coupled first-order equations in Eqs. (2.22) - (2.25) are required. The physical reason for saturation in an FEL lies in the fact that after passing the exponential gain regime, the electron beam supplied enough energy to the EM wave to get out of resonance [cf. Eq. (2.17)]. Furthermore, the periodic density modulations (so-called microbunching) reach a maximum at saturation, and the electrons begin to end up in the accelerating phase of the EM wave and to gain energy on average, i.e., energy is taken out of the EM wave. The effect of saturation in a high-gain FEL for soft X-rays after passing the exponential growth regime is demonstrated in Fig. 2.3. The

saturation power $P_{\mathrm{sat}}$ of a high-gain FEL that is driven by an electron beam containing the power $P_{\mathrm{b}} = \mathcal{I}_{\mathrm{e}} W/e$, where $\mathcal{I}_{\mathrm{e}}$ is the bunch peak current, can be expressed as (e.g., Ref. [29])

$$P_{\mathrm{sat}} \approx \rho\, P_{\mathrm{b}}\,, \tag{2.29}$$

and is reached after the saturation length $L_{\mathrm{sat}}$, which reads in the one-dimensional model as

$$L_{\mathrm{sat}} \approx \frac{1}{\rho}\,\lambda_{\mathrm{u}} = 4\pi\sqrt{3}\,L_{\mathrm{g0}} \approx 20\,L_{\mathrm{g0}}\,. \tag{2.30}$$

Typical FEL parameters $\rho$ at X-ray FELs are on the order of $10^{-3}$, and for electron beams with energies $W$ of a few GeV and peak currents of a few kA, the saturation power results in several gigawatts. Equations (2.28) and (2.30) demonstrate gain functions $G > 10^6$ close to saturation, and the maximum amplification (gain) occurs close to the resonance condition with $\eta = 0$ (cf. low-gain regime). The root mean square (r.m.s.) FEL frequency bandwidth in the exponential gain regime between $4L_{\mathrm{g0}} < z < L_{\mathrm{sat}}$ can be given as (e.g., Ref. [29])

$$\frac{\sigma_\omega(z)}{\omega_{\mathrm{r}}} = \rho\sqrt{\frac{18L_{\mathrm{g0}}}{z}}\,, \tag{2.31}$$

which assumes negligible space charge forces and a monoenergetic beam. At the end of the exponential gain regime, the FEL bandwidth becomes $\sigma_\omega/\omega_{\mathrm{r}} \approx \rho$, which shows that high-gain FELs serve as narrow-band amplifiers. It is worth pointing out that the FEL parameter acts like a fundamental scaling parameter for many equations describing high-gain FELs.

The equations and results presented above cover only the basic findings of the comprehensive theory of free-electron lasers, and further information and details can be found in Refs. [28, 29, 32] and in the references cited therein. In the following, the requirements on the FEL driving electron beams and the characteristics of FEL radiation are discussed.

## 2.2 Electron beam requirements

X-ray free-electron lasers operating in the high-gain regime put stringent requirements on the driving electron beams in terms of the longitudinal and transverse brightness, defined as the electron densities in the particular phase spaces (e.g., Ref. [50]). The required high-brightness beams, as is described in the following by taking into account energy spread and transverse beam effects, correspond to a high peak current $\mathcal{I}_{\mathrm{e}}$ and to a small r.m.s. energy spread $\sigma_\eta$ and emittance $\varepsilon_{x,y}$ in the longitudinal and transverse phase space, respectively.

Space charge forces counteract the microbunching process in an FEL, leading to an in-

crease of the gain and saturation length, and have been initially neglected with $k_\mathrm{p}/\Gamma \approx 0$ in Eq. (2.26) in order to derive the gain curve in Eq. (2.28). However, this assumption is justified for the demonstration of exponential amplification, because X-ray FELs typically have $k_\mathrm{p} < \Gamma$ (see, e.g., Refs. [28, 29]) and the impact of beam energy spread is more significant compared to space charge effects. In general, energy spread and transverse (three-dimensional) beam effects lead to an increase of the actual gain length $L_\mathrm{g}$, and their impact can be described by

$$L_\mathrm{g} = L_\mathrm{g0}(1 + \Lambda) \quad \text{with} \quad \Lambda > 0\,. \tag{2.32}$$

The degradation parameter $\Lambda$ has a cumbersome but useful parametrization presented in Ref. [51], which includes the impact of energy spread, angular spread, and diffraction. The degradation due to energy spread can be understood by taking into account that energy spread causes longitudinal velocity spread [via Eq. (2.5)], hence the electrons get out of resonance [see Eq. (2.11)]. A condition for a tolerable r.m.s. energy spread can be defined as [28]

$$\sigma_\eta < \rho\,, \tag{2.33}$$

which demands an energy spread that is smaller than the FEL bandwidth [see Eq. (2.31)]. The one-dimensional gain length in Eq. (2.32) reads $L_\mathrm{g0} = (\sqrt{3}\Gamma)^{-1}$ [cf. Eq. (2.27)], and by using the gain parameter defined in Eq. (2.20), the one-dimensional gain length scales as

$$L_\mathrm{g0} \sim n_\mathrm{e}^{-1/3} \sim \left(\frac{\sigma_x \sigma_y}{\mathcal{I}_\mathrm{e}}\right)^{1/3}\,, \tag{2.34}$$

where $\sigma_{x,y}$ denotes the r.m.s. beam size in the transverse dimensions $x$ and $y$, respectively. Thus, high peak currents and small transverse electron beam sizes are required in order to achieve a short (one-dimensional) gain and saturation length. Taking into account that r.m.s. emittances (area of the phase spaces) can be written as $\varepsilon_{x,y} = \sigma_{x,y}^2/\beta_{x,y}$ (e.g., Ref. [52]), a short one-dimensional gain length corresponds to a small emittance and to a sufficiently focused electron beam in the undulator, described by the beta function $\beta$. According to the Liouville theorem (e.g., Refs. [46, 50]), the phase space area, i.e., the emittance, cannot be reduced by focusing elements, and a small electron beam size due to a small beta function entails a corresponding large beam angular divergence with $\sigma_{x',y'} \sim \sqrt{\varepsilon_{x,y}/\beta_{x,y}}$. A large angular divergence of the electron beam, however, corresponds to an additional longitudinal velocity spread, which in turn is equivalent to an additional energy spread $\sim \gamma_\mathrm{r}^2 \sigma_{x',y'}^2$ (see, e.g., Refs. [29, 53]), leading to an increase of the gain length. By using the condition for a tolerable

energy spread in Eq. (2.33), the tolerable r.m.s. beam angular divergence can be stated as [53]

$$\sigma_{x',y'} < \frac{\sqrt{\rho}}{\gamma_\mathrm{r}} \,. \tag{2.35}$$

A condition for a reasonable electron beam size can be derived by considering diffraction effects of the FEL radiation beam (EM wave). For laserlike radiation, such as provided by FELs, diffraction causes the transverse radiation beam size ($w_t^2 = 4\sigma_t^2$) to increase by a factor of 2 from its minimum over the Rayleigh length $z_\mathrm{R} = 4\pi\sigma_\mathrm{t}^2/\lambda_\mathrm{r}$. By taking into account that most of the FEL radiation power at a given undulator length $z_f$ in the exponential gain regime has been generated a few gain lengths upstream of $z_f$, the transverse radiation beam size at $z_f$ is only affected by the diffraction over of a few gain lengths, which is related to the phenomenon of optical guiding. Thus, in order to achieve a sufficient transverse overlap of the electron beam and the EM wave (FEL radiation beam) with $\sigma_\mathrm{t} = \sigma_{x,y}$ during the FEL amplification, a reasonable condition can be expressed by demanding a Rayleigh length that is about twice the gain length ($z_\mathrm{R} \approx 2L_{\mathrm{g}0}$). Using the gain length by Eq. (2.27) results in

$$\frac{4\pi\sigma_{\mathrm{x,y}}^2}{\lambda_\mathrm{r}} = 2\frac{\lambda_\mathrm{u}}{4\pi\sqrt{3}\rho} \quad \Rightarrow \quad \sigma_{x,y} \approx \sqrt{\frac{\lambda_\mathrm{u}\lambda_\mathrm{r}}{8\pi^2\sqrt{3}\rho}} < \frac{\lambda_\mathrm{r}\gamma_\mathrm{r}}{4\pi\sqrt{\rho}} \,, \tag{2.36}$$

where $\lambda_\mathrm{u} < \lambda_\mathrm{r}\gamma_\mathrm{r}^2\sqrt{3}$ has been used [see Eq. (2.11)] in the latter inequality [53]. By requesting to fulfill the conditions in Eq. (2.35) and Eq. (2.36) simultaneously, their product leads to

$$\varepsilon_{x,y} \sim \sigma_{x,y}\sigma_{x',y'} < \frac{\lambda_\mathrm{r}}{4\pi} \,, \tag{2.37}$$

which is rather approximate but shows the importance of small electron beam emittances. In summary, electron beams with high peak current [see Eq. (2.34)], low energy spread [see Eq. (2.33)], and small emittances [see Eq. (2.37)] are required for driving an X-ray FEL.

## 2.3 FEL radiation characteristics

High-gain X-ray free-electron lasers have outstanding characteristics in terms of the generated FEL radiation. As has been discussed in Sec. 2.1.2, high-gain FELs generate powerful [see Eq. (2.29)] and widely tunable radiation [see Eq. (2.17)], and the high gain is achieved within a single pass through a long undulator [see Eq. (2.28)]. The powerful FEL radiation has a small bandwidth [see Eq. (2.31)], which manifests a high spectral brightness as is presented in Fig. 1.2. For radiation with full spatial (transverse) coherence, the brightness scales

inversely with the square of the wavelength $\sim \lambda_r^{-2}$ [29]. X-ray SASE FELs can achieve almost full spatial coherence close to saturation, even when the condition in Eq. (2.35) is not fulfilled [28]. The reason is that optical guiding effects cause the fundamental ($TEM_{00}$) mode to dominate the higher transverse modes that are present during the FEL start-up process.

In order to discuss the temporal coherence, the total intensity radiated by a bunch of electrons (cf. the last paragraph of Sec. 1.1) in an undulator is introduced by (see, e.g., Ref. [54])

$$I_t = I_s \left| \sum_{n=1}^{N_e} \exp(-i\psi_n) \right|^2 \approx N_e I_s \times \begin{cases} 1 & \text{(incoherent)} \\ N_c & \text{(coherent)} \end{cases} \tag{2.38}$$

with the intensity $I_s$ of a single electron and a number $N_c$ of cooperating electrons given by

$$N_c \approx \frac{\mathcal{I}_e}{e} \tau_c \,, \tag{2.39}$$

where $\tau_c$ is the coherence time. The emission by density modulated electron beams at X-ray FELs adds in phase (coherently) and leads to an intensity enhancement of $N_c$ compared to the incoherent emission [see Eq. (2.38)]. The coherence time describes the temporal extension over which the electrons contribute coherently and with a defined correlation to the radiation field (wave packet). The start-up at SASE FELs is initiated by shot noise, i.e., not by seed radiation with temporal coherence, hence the coherence time is limited by the finite radiation slippage with respect to the electrons and statistical calculations result in [32]

$$\tau_c = \frac{\sqrt{\pi}}{\sigma_\omega(z)} \approx \frac{1}{\rho \omega_r} \tag{2.40}$$

with the FEL bandwidth $\sigma_\omega$ in Eq. (2.31). For $\rho \approx 10^{-3}$ and $\lambda_r = 2\pi c/\omega_r \approx 10\,\text{nm}$, the approximation in Eq. (2.40) gives $\tau_c \approx 5\,\text{fs}$. Then by assuming peak currents of a few kA, the enhancement by means of Eq. (2.39) yields $N_c > 10^7$. The entire SASE FEL pulse duration $T_p$ is typically on the same order as the driving electron bunch ($\sim 100\,\text{fs}$). Due to the finite coherence length, several wave packets (spikes) can exist with the average number of modes:

$$M \approx \frac{T_p}{\tau_c} \,. \tag{2.41}$$

Therefore, in the time-domain, the SASE FEL radiation pulse has a duration of $T_p$ and consists of $\sim M$ spikes with a duration of $\tau_c \sim 1/\sigma_\omega$ each. In the frequency-domain, the radiation spectrum has a bandwidth of $\sigma_\omega$ and consists of $\sim M$ spikes with a width of $\Delta\omega_s \sim 1/T_p$ each. Ultra-short bunches with $T_p < \tau_c$, however, can generate pulses with a single mode $M \approx 1$.

# 3 Femtosecond electron beam diagnostics

X-ray free-electron lasers operating in the high-gain regime are driven by electron beams with high peak current, low energy spread, and small emittance, and their particular requirements have been discussed in Sec. 2.2. The temporal profile of the FEL radiation power, neglecting the statistical properties of SASE FEL radiation (see Sec. 2.3), is generally determined by the electron beam parameters, which can vary along the electron bunch and can exhibit shot-to-shot fluctuations. Thus, in order to understand and optimize the FEL amplification process, time-resolved electron beam diagnostics with high accuracy and single-shot capability are required. For typical electron bunch charges of $Q_e \sim 100\,\mathrm{pC}$ and peak currents of $\mathcal{I}_e > 1\,\mathrm{kA}$, the electron bunch durations result in $T_e \sim Q_e/\mathcal{I}_e \lesssim 100\,\mathrm{fs}$.

Single-shot electron beam diagnostics with temporal resolutions of a few tens of femtoseconds are feasible in the time-domain by using transverse deflecting r.f. structures (e.g., Refs. [55, 56, 57]) and in the frequency-domain by spectroscopy of coherent terahertz (THz) radiation (e.g., Refs. [54, 57, 58]). Diagnostics with electro-optical techniques are currently limited to $\gtrsim 60\,\mathrm{fs}$ r.m.s. (e.g., Refs. [59, 60, 61]). Whereas the frequency-domain diagnostics using a THz spectrometer is based on coherent radiation, the time-domain diagnostics using a transverse deflecting r.f. structure relies on transverse beam profile imaging with incoherent optical radiation. The recent observations of coherent optical emission by electron beams at present X-ray FELs have thus become a severe issue (e.g., Refs. [62, 63, 64]).

In the following, two articles in the research field of femtosecond electron beam diagnostics at X-ray free-electron lasers are introduced and presented. The first article covers electron beam profile imaging in the presence of coherent optical radiation effects and has been published in *Physical Review Special Topics - Accelerators and Beams* (*Phys. Rev. ST Accel. Beams*). The second article reports on a multi-channel THz and infrared spectrometer for femtosecond electron bunch diagnostics by single-shot spectroscopy of coherent radiation and has been published in *Nuclear Instruments and Methods in Physics Research Section A: Accelerators, Spectrometers, Detectors and Associated Equipment*.

## 3.1 Electron beam profile imaging in the presence of coherent optical radiation effects

At X-ray free-electron lasers, transverse electron beam profiles are necessary for measurements of the beam emittance or in order to setup the correct accelerator optics for a proper beam transport and a sufficiently focused beam in the undulator (see Sec. 2.2). By using a transverse deflecting r.f. structure [65], which induces a time-dependent transverse kick within the electron bunches, the longitudinal positions of the passing electrons are translated (streaked) into transverse coordinates, making longitudinal, i.e., time-resolved, electron beam diagnostics possible by measuring transverse beam profiles. One-dimensional beam profiles, projected onto either the horizontal or vertical axis, can be achieved by using wire-scanners (e.g., Ref. [52]) and allow temporal bunch profile measurements in a multi-shot mode. For single-shot measurements or in cases where two dimensions are required, e.g., in time-resolved emittance or longitudinal phase space measurements, transverse beam profile diagnostics based on imaging screens is essential. Imaging of electron beam profiles relies on incoherent radiation, such as incoherent optical transition radiation, whereas coherent optical radiation effects can lead to an incorrect representation of the transverse beam distribution (e.g., Refs. [63, 64]), impeding any beam diagnostics using imaging screens.

Coherent optical radiation effects can be caused by ultrashort charge concentrations [64], such as intrinsically ultrashort electron bunches (e.g., Refs. [41, 66]), or by microbunching instabilities (e.g., Refs. [67, 68]) that may lead to electron density modulations on the scale of optical wavelengths. In either case, the number of cooperating electrons $N_c$ in Eq. (2.38), which can also be applied for optical transition or synchrotron radiation, is significantly larger then unity at optical wavelengths, leading to enhanced radiation intensities. The observation of strong coherent optical transition radiation (COTR) at the LCLS, initially stated as "unexpected physics" [62], has become a frequent observation at present X-ray FELs (e.g., Refs. [62, 69, 70]) and a severe issue for electron beam diagnostics using imaging screens.

Methods to suppress microbunching instabilities exist (e.g., Refs. [71, 72]), and the laser heater at the LCLS demonstrated significant impact on the FEL performance [73]. However, the suppression is not necessarily perfect and a remaining level of COTR still renders beam diagnostics using standard imaging screens impossible [73]. Thus, new techniques to suppress either the emission or the impact of coherent optical radiation are required.

The following article reports on the observation of microbunching and coherent optical radiation, describes a method to suppress coherent optical emission, and finally demonstrates electron beam profile imaging in the presence of coherent optical radiation effects.

# Electron beam profile imaging in the presence of coherent optical radiation effects

Christopher Behrens,[1,*] Christopher Gerth,[1] Gero Kube,[1] Bernhard Schmidt,[1] Stephan Wesch,[1] and Minjie Yan[1,2]

[1]*Deutsches Elektronen-Synchrotron DESY, Notkestraße 85, 22607 Hamburg, Germany*

[2]*Universität Hamburg, Institut für Experimentalphysik, Luruper Chaussee 149, 22761 Hamburg, Germany*

(Received 6 March 2012; published 13 June 2012)

High-brightness electron beams with low energy spread at existing and future x-ray free-electron lasers are affected by various collective beam self-interactions and microbunching instabilities. The corresponding coherent optical radiation effects, e.g., coherent optical transition radiation, impede electron beam profile imaging and become a serious issue for all kinds of electron beam diagnostics using imaging screens. Furthermore, coherent optical radiation effects can also be related to intrinsically ultrashort electron bunches or the existence of ultrashort spikes inside the electron bunches. In this paper, we discuss methods to suppress coherent optical radiation effects both by electron beam profile imaging in dispersive beam lines and by using scintillation imaging screens in combination with separation techniques. The suppression of coherent optical emission in dispersive beam lines is shown by analytical calculations, numerical simulations, and measurements. Transverse and longitudinal electron beam profile measurements in the presence of coherent optical radiation effects in nondispersive beam lines are demonstrated by applying a temporal separation technique.

DOI: 10.1103/PhysRevSTAB.15.062801 PACS numbers: 29.27.−a, 41.60.Cr, 41.60.Dk

## I. INTRODUCTION

X-ray free-electron lasers (FELs) offer a brilliant tool for science at atomic length and ultrafast time scales [1], and they have been realized with the operation of the Free-Electron Laser in Hamburg (FLASH) [2], the Linac Coherent Light Source (LCLS) [3], and the SPring-8 Angstrom Compact Free Electron Laser (SACLA) [4]. The x-ray FEL driving electron bunches are subject to several collective effects, e.g., microbunching instabilities or coherent synchrotron radiation (CSR), which degrade the required high transverse and longitudinal beam brightness [5–8]. These instabilities may not only result in significant deteriorations of the FEL performance [9] but also in coherent radiation effects [10–16] such as coherent optical transition radiation (COTR) or CSR in the optical wavelength range [17] (abbreviated as COSR). Beam profile imaging dominated by coherent optical radiation leads to an incorrect representation of the transverse charge distribution [11] and renders electron beam diagnostics with standard imaging screens, e.g., OTR screens, and all the related diagnostics such as emittance or bunch length diagnostics impossible. However, beam diagnostics with imaging screens are essential for single-shot measurements or in cases where two transverse dimensions are required, e.g., in slice emittance or longitudinal phase space measurements [18–20].

*christopher.behrens@desy.de



Microbunching instabilities associated with longitudinal electron bunch compression can be mitigated by introducing additional uncorrelated energy spread [21–23] as successfully demonstrated by the operation of the laser heater system at the LCLS [9]. However, the microbunching gain suppression is not necessarily perfect, and the corresponding remaining small but existing level of COTR still hampers electron beam profile diagnostics using standard imaging screens (e.g., Ref. [9]). The origin of coherent optical radiation effects is not only restricted to microbunching instabilities but can also be related to ultrashort spikes inside electron bunches or generated by intrinsically ultrashort electron bunches like at laser-plasma accelerators (e.g., Ref. [24]) or at x-ray FELs with ultralow charge operation [25–27].

Transition radiation is emitted when a charged particle beam crosses the boundary between two media with different dielectric properties [28–32], hence transition radiation is emitted using any kind of imaging screen and thus precludes the stand-alone use of scintillation screens in the presence of coherent optical radiation effects (e.g., COTR). However, by using (scintillation) imaging screens in dedicated measurement configurations, COTR can be mitigated (see, e.g., Ref. [15]).

In this paper, we discuss methods to suppress coherent optical radiation effects both by electron beam profile imaging in dispersive beam lines and by utilizing scintillation imaging screens in combination with several separation techniques. The experimental setup and observations of coherent optical radiation effects at FLASH are described in Sec. II. In Sec. III we discuss the suppression of coherent optical emission in dispersive beam lines and present experimental results for COTR generated by a local

ultrashort charge concentration. Section IV covers the suppression of coherent optical radiation effects by using scintillation screens in combination with separation techniques. The experimental results obtained with the temporal separation technique are presented in Sec. V, and a summary and conclusions are given in Sec. VI.

## II. EXPERIMENTAL SETUP AND OBSERVATION OF COHERENT EFFECTS

The measurements presented in this paper have been carried out at FLASH, which is a self-amplified spontaneous emission (SASE) FEL [33] for extreme-ultraviolet (EUV) and soft x-ray radiation, driven by a superconducting radio-frequency (rf) linear accelerator [2]. The schematic layout of FLASH is depicted in Fig. 1, showing the injector, which is based on a laser-driven normal conducting rf gun, the superconducting accelerating structures, two magnetic bunch compressor chicanes, and the undulator magnet system. The positions of the experimental setups used for the measurements presented in this paper are indicated by green dots and arrows.

The third-harmonic rf system (denoted by L3 in Fig. 1) is dedicated to the linearization of the longitudinal phase space upstream of the first bunch compressor [20,34]. In order to properly set up FEL operation with applied third-harmonic rf linearizer, a LOLA-type [35] transverse deflecting rf structure (TDS) has been integrated in a dedicated setup for diagnosis of the longitudinal phase space [36,37] close to the FEL undulators. As depicted in Fig. 1, the TDS can either be operated in combination with imaging screens in the dispersive magnetic energy spectrometer or by using off-axis imaging screens operated with a fast kicker magnet in the nondispersive main beam line during FEL operation. Technical details and performance measurements on the setup for longitudinal beam diagnostics can be found in Refs. [20,36,37].

### A. Time-domain longitudinal beam diagnostics

Transverse deflecting rf structures are widely used for electron bunch length and longitudinal profile measurements at present FELs and provide high-resolution single-shot diagnostics [18–20,38]. Detailed descriptions of time-domain electron bunch diagnostics using a TDS can be found in Refs. [18,38]. Here we describe only the basic principles of longitudinal electron beam diagnostics that are required throughout this paper.

The vertical betatron motion of an electron passing a vertical deflecting TDS around the zero-crossing rf phase, neglecting intrinsic longitudinal-to-vertical correlations [20] which are not relevant for the experiments presented throughout this paper, can be given by [18,20]

$$y(s) = y_0(s) + S_y(s, s_0)c^{-1}z(s_0) \tag{1}$$

with the vertical shear (streak) function

$$S_y(s, s_0) = R_{34}K_y = \sqrt{\beta_y(s)\beta_y(s_0)}\sin(\Delta\phi_y)\frac{e\omega V_y}{pc}, \tag{2}$$

where $R_{34} = \sqrt{\beta_y(s)\beta_y(s_0)}\sin(\Delta\phi_y)$ is the angular-to-spatial element of the vertical beam transfer matrix from the TDS at $s_0$ to any position $s$, $\beta_y$ is the vertical beta function, $\Delta\phi_y$ is the vertical phase advance between $s_0$ and $s$, and $y_0$ describes an intrinsic offset. The expression $K_y = e\omega V_y/(pc)$ is the vertical kick strength with the peak deflection voltage $V_y$ in the TDS, $c$ is the speed of light in vacuum, $e$ is the elementary charge, $p$ is the electron momentum, $z(s_0)$ is the longitudinal position of the electron relative to the zero-crossing rf phase, and $\omega/(2\pi)$ is the operating rf frequency. The expression in Eq. (1) shows a linear mapping from the longitudinal to the vertical coordinate and allows longitudinal electron beam profile measurements by means of transverse beam diagnostics using imaging screens. The shear function $S_y$ determines the slope of this mapping and can be calibrated by measuring the vertical centroid offset of the bunch as a function of the TDS rf phase. The electron bunch current is given by the normalized longitudinal bunch profile multiplied by the electron bunch charge. The bunch length (duration) is given by the root mean square (rms) value $\sigma_{t,\mathrm{e}} = S^{-1}(\sigma_y^2 - \sigma_{y,0}^2)^{1/2}$, where $\sigma_y$ is the vertical rms beam size during TDS operation, and $\sigma_{y,0}$ is the intrinsic vertical rms beam size when the TDS is switched off. Both $\sigma_y$ and $\sigma_{y,0}$ can be determined by measurements, and the latter limits the achievable rms time resolution to $\mathcal{R}_{t,\mathrm{e}} = \sigma_{y,0}/S_y$ [18,20].

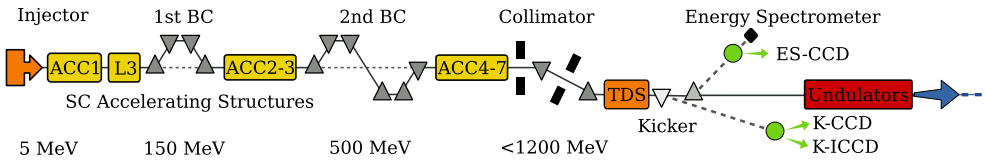


FIG. 1. Schematic layout of the Free-Electron Laser in Hamburg (FLASH) with its superconducting (SC) accelerating structures (ACC), the two magnetic bunch compressor (BC) chicanes, and the third-harmonic rf linearizer system (L3). The positions of the experimental setups and diagnostics used for the measurements presented in this paper are indicated by green dots.

### B. Imaging screen stations and camera systems

The screen stations in both the magnetic energy spectrometer and nondispersive main beam line (see Fig. 1) are each equipped with different imaging screens and a charge-coupled device (CCD) camera [39] (1360 × 1024 pixels with 12 bit dynamic range and 6.45 × 6.45 $\mu$m$^2$ pixel size) with motorized optics (motorized macrolens with teleconverter mounted on a linear translation stage). The translation stage allows variable demagnification $M^{-1}$ in the range between ∼1.5–3 with spatial resolutions of better than 16 $\mu$m. The imaging screen station in the energy spectrometer (ES-CCD in Fig. 1) is equipped with an OTR screen (aluminum coated silicon) and two scintillation screens made of cerium-doped yttrium aluminum garnet (YAG:Ce) and bismuth germanate, respectively. In the nondispersive beam line, the screen station is operated with a fast kicker magnet (K-CCD in Fig. 1), which is able to deflect one bunch out of the bunch train at the bunch train repetition rate of FLASH [40] of 10 Hz, and provides an OTR screen and a cerium-doped lutetium aluminum garnet (LuAG:Ce) scintillation screen. All screens are mounted at a 45° angle (the cameras at a 90° angle) with respect to the incoming electron beam. The scintillation screens have a thickness of 100 $\mu$m. The experimental setup in the nondispersive beam line is additionally equipped with a fast gated intensified CCD camera [41] (K-ICCD in Fig. 1, 1280 × 1024 pixels with 12 bit and 6.7 × 6.7 $\mu$m$^2$ pixel size), which has been used for the temporal separation technique (see Sec. V). Further technical details on the screen stations and camera systems can be found in Refs. [37,42].

### C. Observation of coherent optical transition radiation and microbunching in the time domain

Microbunching instabilities at x-ray FELs can lead to significant generation and amplification of density modulations in the optical wavelength range [5–7] which may result in coherent optical radiation effects such as COTR. This has been observed by spectral measurements and characteristic ring-shaped light patterns at the LCLS [11,12] and FLASH [16], and renders accurate electron beam profile diagnostics using standard imaging screens impossible. First observations of COTR [16] and microbunching in the frequency domain (coherent transition radiation around 10 $\mu$m [43]) at FLASH were made directly upstream of the collimator (see Fig. 1). Electron beam profile imaging performed downstream of the collimator section [37], an achromatic bending system, resulted in considerably more prominent observation of coherent optical radiation effects and microbunching.

The measurements presented in Fig. 2 show single-shot light patterns, generated by moderately compressed electron bunches, at the imaging screens in the nondispersive main beam line at K-CCD directly upstream of the undulators. Ring-shaped structures in the profiles, characteristic for COTR [11], are clearly visible in the images of Figs. 2(a) and 2(b), which have been recorded by using an OTR and LuAG imaging screen, respectively. For both images a long-pass filter, blocking wavelengths below 780 nm, was used. The luminescence emission of the LuAG scintillation screen occurs below 700 nm [44] and is thus well blocked by the 780-nm long-pass filter used during the measurements. Hence, the light pattern in Fig. 2(b) is due to COTR without contribution from scintillation light. Complementary to the observation of COTR, the images in Fig. 3 show single-shot longitudinal phase space measurements in the magnetic energy spectrometer (ES-CCD). The measurements were done for accelerator settings typical for FEL operation with applied third-harmonic rf linearizer system upstream of the bunch compressor chicanes, and they clearly indicate microbunching in the time domain with modulation periods of about 25 and 30 fs, respectively. We note that a maximum modulation wavelength of 10 $\mu$m (33 fs) was predicted theoretically in Ref. [7] and measured by spectroscopy of coherent transition radiation in Ref. [43].

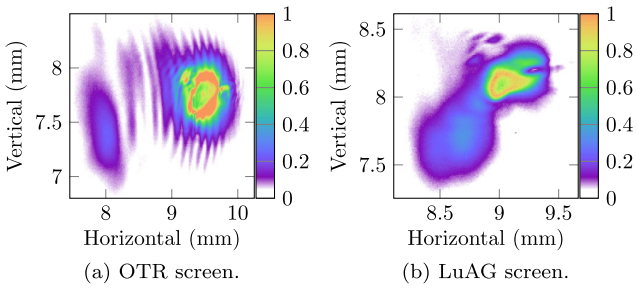


(a) OTR screen. (b) LuAG screen.

FIG. 2. Single-shot images of light patterns at the imaging screens (K-CCD) generated by compressed electron bunches: (a) OTR screen and (b) LuAG screen. For both images a long-pass filter, blocking wavelengths below 780 nm, was used.

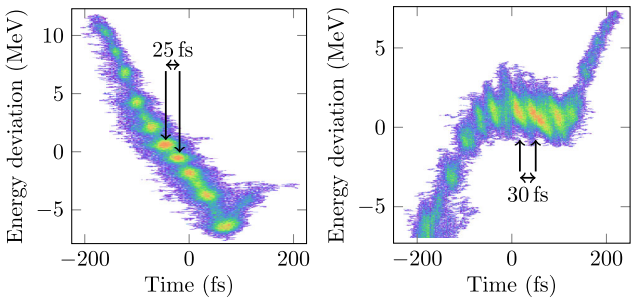


(a) 796 MeV. (b) 661 MeV.

FIG. 3. Longitudinal phase space measurements upstream of the undulators at ES-CCD for two different compression settings and mean energies: (a) 796 MeV and (b) 661 MeV. The density modulations indicate microbunching in the time-domain with periods of ∼25 fs and 30 fs, respectively.

## III. SUPPRESSION OF COHERENT OPTICAL EMISSION IN DISPERSIVE BEAM LINES

The energy-dependent beam trajectories in dispersive beam lines can be utilized as a magnetic energy spectrometer for charged particle beams. By combining such an energy spectrometer with the operation of a TDS and using imaging screens to get two-dimensional transverse beam profiles, longitudinal phase space measurements (see, e.g., Fig. 3) with single-shot capability can be accomplished. The corresponding horizontal betatron motion, which should be perpendicular to the vertical shearing plane of the TDS [18,20], can be written as

$$x(s) = x_0(s) + D_x(s, s_0)\delta(s_0) \tag{3}$$

with the intrinsic offset $x_0$, the horizontal momentum dispersion $D_x(s, s_0)$, and the relative momentum deviation $\delta = \Delta p/p$. For relativistic electron beams with Lorentz factors of $\gamma \gg 1$, the electron beam energy is given by $E \approx pc$, and $\delta$ represents the relative energy deviation.

The dispersion $D_x$ can be determined by measuring the horizontal centroid offset of the bunch as a function of the relative energy deviation. The dispersion in the magnetic energy spectrometer at ES-CCD (see Fig. 1), which is generated by two subsequent dipole magnets with 5° deflection each (equivalent to a single dipole magnet with 10° deflection), amounts to 750 mm (nominal) [20], whereas $D_x$ at K-(I)CCD due to the kicker magnet operation is negligible. In addition to the momentum dispersion introduced in the horizontal betatron motion, the longitudinal particle motion can be described by

$$z(s) = z(s_0) + R_{51}x(s_0) + R_{52}x'(s_0) + R_{56}\delta(s_0) \tag{4}$$

with the initial bunch length coordinate $z$ and the initial horizontal offset $x$ and slope $x' = dx/ds$. The transfer matrix elements $R_{ij}$ describe the mapping from position $s_0$ to $s$, i.e., $R_{ij} \equiv R_{ij}(s, s_0)$ throughout the rest of this paper. The expression in Eq. (4) does not affect the principle of longitudinal phase space diagnostics described by Eqs. (1) and (3), but results in the suppression of coherent optical emission as is shown in the following.

### A. Analytical calculations and numerical particle tracking simulations

The spectral and angular intensity distribution, denoted as $\mathcal{I}(\vec{k}) \equiv dI(\vec{k})/d\Omega$ with the three-dimensional wave vector $\vec{k} = (\vec{k}_r, k_z)$, of transition (synchrotron) radiation emitted by an electron bunch with $N \gg 1$ electrons and charge $Q = Ne$ is given by (e.g., Refs. [45,46])

$$\mathcal{I}(\vec{k}_r, k_z) = N\mathcal{I}_1(\vec{k}_r, k_z) + N^2|F(\vec{k}_r, k_z)|^2\mathcal{I}_1(\vec{k}_r, k_z), \tag{5}$$

where $\mathcal{I}_1(\vec{k}_r, k_z)$ describes the intensity distribution of a single electron as a function of the transverse and longitudinal wave number $\vec{k}_r$ and $k_z$, respectively, and $F(\vec{k}_r, k_z)$ is the three-dimensional form factor of the electron bunch. The latter can be expressed by the Fourier transform of the normalized charge density $\rho(\vec{r}, z)$ as

$$F(\vec{k}_r, k_z) = \int d\vec{r}dz\rho(\vec{r}, z)e^{-i\vec{k}_r\vec{r}}e^{-ik_z z}, \tag{6}$$

where $\rho(\vec{r}, z) \equiv \rho(x, y, z)$. Normalized charge distributions without longitudinal-transverse correlations can be factorized as $\rho(\vec{r}, z) \equiv \rho(\vec{r})\rho(z)$, and by taking into account $\int d\vec{r}\rho(\vec{r}) = \int dz\rho(z) = 1$, which is assumed in the following, we get $F(\vec{k}_r, k_z) = F_t(\vec{k}_r)F_l(k_z)$ with the transverse and longitudinal form factor $F_t$ and $F_l$, respectively. For small observation angles $\theta$ (small covered solid angles $\Omega$) with respect to the central axis ($z$ axis) of the emitted radiation we have $k_z = k\cos\theta \approx k$ with the wave number $k$, and the expression in Eq. (5) reads

$$\mathcal{I}(k, \Omega) \approx N\mathcal{I}_1(k, \Omega) + N^2|F_l(k)|^2|F_t(k, \Omega)|^2\mathcal{I}_1(k, \Omega). \tag{7}$$

The first term on the right-hand side is linear in $N$ and describes the contribution of incoherent radiation, whereas the second term scales with $N^2|F_l(k)|^2|F_t(k, \Omega)|^2$, which describes the coherent radiation part. In order to perform electron beam diagnostics with incoherent radiation, we demand that the total spectral radiation intensity in Eq. (7) is dominated by the incoherent term, i.e., $N \gg N^2|F_l(k)|^2|F_t(k, \Omega)|^2$.

In the following, we derive an analytical expression describing a general strong suppression of the longitudinal form factor at optical wavelengths in a magnetic energy spectrometer. A transverse form factor of $|F_t| = 1$, i.e., full transverse coherence, at the imaging screens is assumed, which is the worst case scenario. The actual transverse form factor in the experiment will be reduced due to the finite beam size and observation angle [45]. However, the suppression of the longitudinal form factor $F_l$ presented below is much stronger in the general case. A cutoff wavelength $\lambda_c = 2\pi/k_c$ can be defined via $|F_l(k_c)| = N^{-1/2}$, and beam diagnostics at wavelengths below $\lambda_c$ becomes dominated by incoherent radiation. The cutoff wavelength initially depends on the charge distribution [via Eq. (6)], and significant values of $|F_l|$ in the optical wavelength range can occur due to the existence of density modulations or charge concentrations at ultrashort length scales. However, following the analytical treatment of microbunching degradation in Ref. [47], we show that the cutoff wavelength in magnetic energy spectrometers is entirely determined by the terms in Eq. (4) with a corresponding strong suppression of coherent emission at optical wavelengths for common magnetic energy spectrometers used at present FELs.

The amount of density modulations in a normalized electron beam distribution $\rho(\vec{X}, s)$ with the phase space vector $\vec{X} = (x, x', z, \delta)$ and $\int d\vec{X}\rho(\vec{X}, s) = 1$ can be quantified by a complex bunching factor $b(k, s)$ as [47]

$$b(k, s) = \int d\vec{X} e^{-ikz} \rho(\vec{X}, s), \tag{8}$$

where $k$ is the wave number of the modulation. According to Refs. [47,48], the evolution of the bunching factor $b[k(s), s]$ along dispersive beam lines can be expressed by

$$b[k(s), s] = b_0[k(s), s] + \int_{s_0}^{s} ds' K(s', s) b[k(s'), s'], \tag{9}$$

where $b_0[k(s), s]$ is the bunching factor in the absence of collective beam interactions due to CSR. The second term on the right-hand side of the integral equation with the kernel $K(s', s)$ [47] (a complicated expression that is not relevant here) describes the induced bunching due to CSR interactions. As discussed in Refs. [47,49] and verified by numerical particle tracking simulations below, the bunching induced in a dipole magnet from the energy modulation generated in the same dipole magnet can be neglected with the kernel $K \approx 0$, and the bunching factor in Eq. (9) becomes $b[k(s), s] \approx b_0[k(s), s]$. This is also the case in a magnetic energy spectrometer consisting of a single dipole magnet, and the resulting evolution of the total bunching factor for a given initial bunching $b_0[k(s_0), s_0]$ can be expressed by [47]

$$\begin{aligned} b[k(s), s] \approx\ & b_0[k(s_0), s_0] \exp\left[ -\frac{k^2(s)\sigma_{\delta 0}^2}{2} R_{56}^2 \right] \\ & \times \exp\left[ -\frac{k^2(s)\varepsilon_0\beta_0}{2} \left( R_{51} - \frac{\alpha_0}{\beta_0} R_{52} \right)^2 \right] \\ & \times \exp\left[ -\frac{k^2(s)\varepsilon_0}{2\beta_0} R_{52}^2 \right], \end{aligned} \tag{10}$$

where the motion in Eq. (4) is taken into account, and an initial beam distribution $\rho[\vec{X}(s_0), s_0]$ that is uniform in $z$ and Gaussian in $x$, $x'$, and $\delta$ is assumed. The initial uncorrelated energy spread and geometrical horizontal emittance are denoted by $\sigma_{\delta 0}$ and $\varepsilon_0$, respectively, and $\alpha_0$ and $\beta_0$ are the initial horizontal lattice functions (Twiss parameters). The compression of the wave number by $k(s) = k(s_0)[1 + hR_{56}(s, s_0)]^{-1}$ with the initial energy chirp $h$ can be neglected, i.e., $k(s) \approx k(s_0)$, since the $R_{56}$ generated by a single dipole magnet is rather small.

In addition to the evolution of an initial bunching, energy modulations generated upstream of a magnetic energy spectrometer can initiate bunching and, according to Ref. [47] and by using Eq. (10), the induced bunching $b_E(k, s)$ due to an initial energy modulation is given by

$$b_E(k, s) \approx -ikR_{56} \Delta E(k, s_0) \frac{b(k, s)}{b_0(k, s_0)}, \tag{11}$$

where $\Delta E(k, s_0)$ is the Fourier amplitude of the initial energy modulation $\Delta E(z, s_0)$. Fortunately, the bunching $b_E$ can be neglected due to the small $R_{56}$ (see above) and the additional suppression discussed in the following.

Equation (10) implies a suppression of initial bunching due to the coupling with the transverse phase space given in Eq. (4), and a suppression factor $\mathcal{S}$ can be defined as

$$\mathcal{S}(k) = \frac{|b(k, s)|^2}{|b_0(k, s_0)|^2} = e^{-k^2\Lambda^2}, \tag{12}$$

where

$$\Lambda = \sqrt{\varepsilon_0\beta_0 \left( R_{51} - \frac{\alpha_0}{\beta_0} R_{52} \right)^2 + \sigma_{\delta 0}^2 R_{56}^2 + \frac{\varepsilon_0}{\beta_0} R_{52}^2}. \tag{13}$$

By comparing Eqs. (6) and (8), and taking into account $\rho[(x, x', z, \delta)] = \rho(z)\rho[(x, x', \delta)]$, the suppression factor can be expressed as $\mathcal{S}(k) = |F_l(k, s)|^2 / |F_l(k, s_0)|^2$ (cf. the analytical treatment in Refs. [17,50]), which describes the general suppression of coherent emission in a common magnetic energy spectrometer. Assuming a maximum initial density modulation or an ultrashort electron bunch, both with $|F_l(k, s_0)| \equiv 1$, the cutoff wavelength [defined via $|F_l(k_c)| = N^{-1/2}$] is given by [cf. Eq. (12)]

$$\lambda_c = \frac{2\pi\Lambda}{\sqrt{\ln N}}. \tag{14}$$

We note that the suppression for ultrashort electron bunches is simply given by the lengthening due to the transverse phase space parameters and longitudinal motion given in Eq. (4), which act like a low-pass filter.

The analytical treatment has been verified by numerical simulations using the tracking code ELEGANT [51] with Gaussian and uniform beam distributions ($10^6$ particles) including CSR effects, and by using the parameters of the magnetic energy spectrometer at FLASH, summarized in Table I. Figure 4 shows the suppression factor for both numerical simulations with initial density modulations (10% peak amplitude) and analytical calculations using Eqs. (12) and (13) for the parameters of FLASH. The analytical calculations are in perfect agreement with the numerical simulations. The shown approximation is calculated by using $\Lambda \approx \sqrt{\varepsilon_0\beta_0} R_{51}$, which is a good practical estimate ($R_{51} = \sin\Theta$ for a single dipole magnet with

TABLE I. Parameters given in the magnetic energy spectrometer at FLASH and used for the particle tracking simulations.

| Parameter | Symbol | Value | Unit |
|---|---|---|---|
| Beam energy | $E$ | 1000 | MeV |
| Lorentz factor | $\gamma$ | 1957 | |
| Electron bunch charge | $Q$ | 150 | pC |
| Horizontal emittance (normalized) | $\gamma\varepsilon_0$ | 1.0 | $\mu$m |
| Relative slice energy spread | $\sigma_{\delta 0}$ | $10^{-4}$ | |
| Horizontal beta function | $\beta_0$ | 13.55 | m |
| Horizontal alpha function | $\alpha_0$ | 5.33 | |
| Spatial-to-longitudinal coupling | $R_{51}$ | $-0.174$ | |
| Angular-to-longitudinal coupling | $R_{52}$ | $-0.089$ | |
| Momentum compaction factor | $R_{56}$ | 0.006 | m |

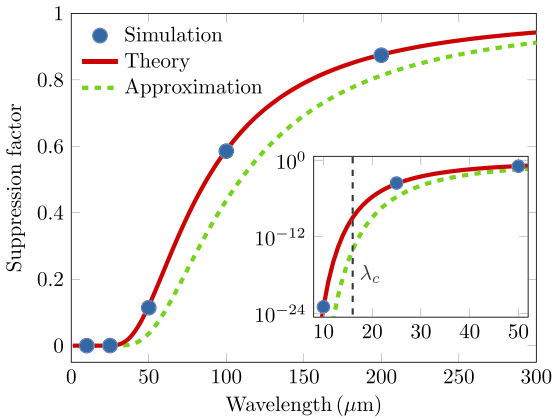


FIG. 4. Analytical calculations and numerical simulations (blue dots) of the suppression $\mathcal{S}$ for initial density modulations. The theory curve (solid red line) is calculated for the full term in Eq. (13), and the approximation (dashed green line) is calculated for $\Lambda \approx \sqrt{\varepsilon_0 \beta_0} R_{51}$. The inset shows the wavelength range below 52 $\mu$m on a logarithmic scale including the cutoff wavelength $\lambda_c$ calculated for $N \approx 10^9$ electrons.

bending angle $\Theta$). According to the full term in Eq. (13), the cutoff wavelength in the magnetic energy spectrometer at FLASH amounts to $\lambda_c \approx 16$ $\mu$m, which manifests a strong suppression of coherent optical emission.

### B. Suppression of COTR generated by a local ultrashort charge concentration

Coherent emission does not only lead to intense radiation, which is described by means of the form factor $|F_l|$ in the intensity distribution given in Eq. (7), but also to an incorrect representation of the transverse charge distribution in beam profile imaging [11]. The imaging of transverse beam distributions with optical systems, e.g., by using an imaging screen, a lens, and a camera, is generally described by means of the intensity distribution of a point source in the image plane (e.g., Ref. [32]), which is the so-called point spread function. According to Ref. [11], the image formation with optical transition radiation of a normalized three-dimensional charge distribution $\rho(\vec{r}, z)$ with $N$ electrons can be expressed by

$$|\vec{\mathcal{E}}(\vec{r}, k)|^2 = N \int d\vec{r}' dz \rho(\vec{r}', z) |\vec{\mathcal{E}}_1(\vec{r} - \vec{r}', k)|^2 + N^2 \left| \int d\vec{r}' dz e^{-ikz} \rho(\vec{r}', z) \vec{\mathcal{E}}_1(\vec{r} - \vec{r}', k) \right|^2, \tag{15}$$

where $|\vec{\mathcal{E}}(\vec{r}, k)|^2$ describes the measured intensity distribution proportional to the absolute square of the total electric field $\vec{\mathcal{E}}$ evolved from the charge distribution, and $\vec{\mathcal{E}}_1$ corresponds to the imaged electric field of a single electron, which can be expressed by means of the Fresnel-Kirchhoff diffraction integral (e.g., Ref. [32]). The second integral in Eq. (15) describes the coherent radiation part ( $\sim N^2$), and by taking into account $\rho(\vec{r}, z) \equiv \rho(\vec{r})\rho(z)$ with $\int d\vec{r} \rho(\vec{r}) = \int dz \rho(z) = 1$, the expression for image formation in Eq. (15) can be rewritten as [cf. Eq. (7)]

$$|\vec{\mathcal{E}}(\vec{r}, k)|^2 = N \int d\vec{r}' \rho(\vec{r}') |\vec{\mathcal{E}}_1(\vec{r} - \vec{r}', k)|^2 + N^2 |F_l(k)|^2 \left| \int d\vec{r}' \rho(\vec{r}') \vec{\mathcal{E}}_1(\vec{r} - \vec{r}', k) \right|^2. \tag{16}$$

The first integral in Eq. (16) simply describes the incoherent imaging as a convolution of the transverse charge distribution $\rho(\vec{r}')$ with the point spread function related term $|\vec{\mathcal{E}}_1|^2$. In the case of a nonvanishing longitudinal form factor $|F_l(k)| \neq 0$, the second integral in Eq. (16) contributes to the image formation and describes no longer a simple convolution with a point spread function, but rather takes into account the actual field distribution. Thus, significant deviations in the measured transverse charge distribution can occur even with a small longitudinal form factor due to the second term $\sim N^2 |F_l(k)|^2$ in Eq. (16), where $N \sim 10^9$. An example with initially inconspicuous COTR, impeding the electron beam diagnostics finally, is demonstrated in the following.

Figures 5(a) and 5(b) show single-shot images of longitudinal bunch profile measurements using the TDS that were recorded in the nondispersive main beam line at K-CCD and in the energy spectrometer at ES-CCD, respectively. The images were measured under the same electron beam conditions with a bunch charge of 0.45 nC and do not display any conspicuous features of COTR. However, as can be seen in Fig. 5(e), the corresponding longitudinal bunch profile taken at K-CCD comprises a much narrower spike with higher peak current. When increasing the bunch charge to 0.55 nC, COTR emission became apparent at K-CCD [Fig. 5(c)], whereas the image in the energy spectrometer at ES-CCD [see Fig. 5(d)] did not show any coherent radiation effects. The COTR emission in Fig. 5(c) (we chose a single-shot image with low saturation of the CCD) is clearly localized in the longitudinal electron bunch profile at a time coordinate of about 0.5 ps. At the same time coordinate, the longitudinal phase space in Fig. 5(d) exhibits a huge but narrow increase in energy spread (the width in the time is limited by the TDS resolution). From this we conclude that the single-shot image in Fig. 5(a) already partially contains COTR as a consequence of a small but nonvanishing form factor $|F_l|$ [cf. Eqs. (7) and (16)] and that the COTR emission in Fig. 5(c) seems most probably to be generated by a local ultrashort charge concentration such as a sharp spike inside the electron bunch. We note that the measurements presented in Fig. 5(e) should give the same longitudinal electron bunch profiles, and the existing deviations cannot be explained due to a worse resolution as is the case in Sec. V C. In order to demonstrate the local energy spread

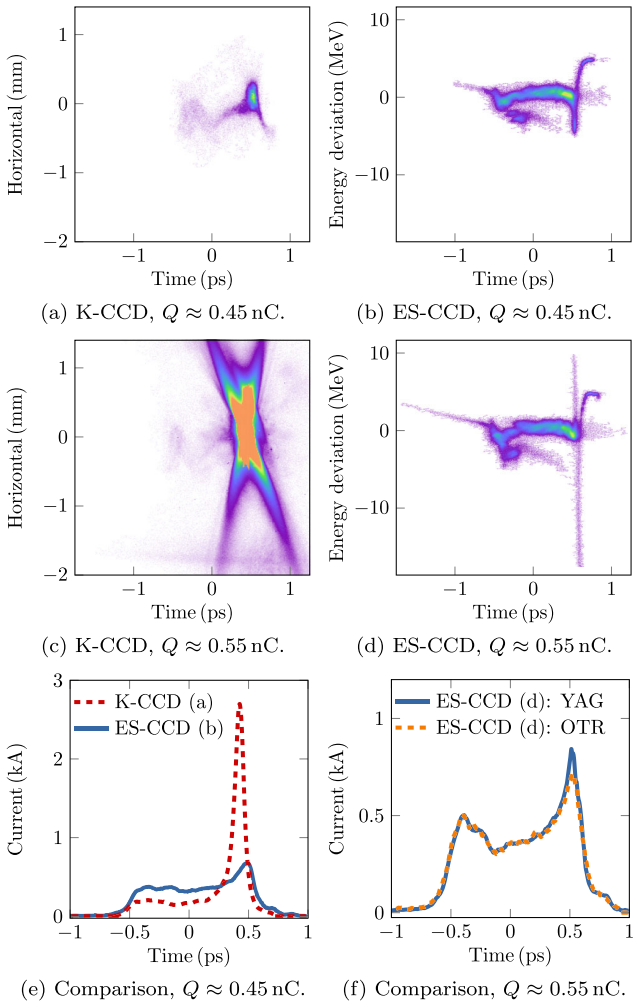


(a) K-CCD, $Q \approx 0.45$ nC. (b) ES-CCD, $Q \approx 0.45$ nC.

(c) K-CCD, $Q \approx 0.55$ nC. (d) ES-CCD, $Q \approx 0.55$ nC.

(e) Comparison, $Q \approx 0.45$ nC. (f) Comparison, $Q \approx 0.55$ nC.

FIG. 5. Single-shot measurements of the $t$-$x$ plane in (a) and (c) using a LuAG screen at K-CCD with time $t = -z/c$ (bunch head at $t < 0$), and of the longitudinal phase space $(t,\Delta E)$ in (b) and (d) using a YAG screen at ES-CCD with $\Delta E = \delta E_0$ and $E_0 \approx 1165$ MeV for bunch charges of $Q \approx 0.45$ nC and 0.55 nC, respectively. The comparison of the electron bunch currents between K-CCD and ES-CCD for $Q \approx 0.45$ nC is shown in (e), and for $Q \approx 0.55$ nC at ES-CCD with different imaging screens it is presented in (f).

increase in Figs. 5(b) and 5(d) with a reasonable signal-to-noise ratio (SNR), the longitudinal phase space measurements are presented with the YAG imaging screen. The measurement performed with the OTR imaging screen, presented in Fig. 5(f), shows the same strong COTR suppression (but worse SNR).

## IV. TECHNIQUES FOR SEPARATION OF COHERENT OPTICAL RADIATION

As demonstrated in Sec. III, electron beam profile measurements can be accomplished in dispersive beam lines, such as magnetic energy spectrometers, with standard optical imaging systems as the emission of coherent optical radiation is strongly suppressed. However, linear accelerators consist mainly of beam lines which are in general designed to be dispersion free, and imaging in energy spectrometers precludes measuring pure transverse beam profiles due to the dispersion. In this section, we discuss methods that suppress the impact of coherent radiation by separation from an incoherent radiation part.

### A. Spectral separation

The spectral intensity of transition (synchrotron) radiation emitted by an electron bunch consists of two terms that describe the incoherent ($\sim N$) and coherent ($\sim N^2|F_l|^2|F_t|^2$) radiation part [cf. Eq. (7) or Eq. (16)]. A spectral separation of these terms in electron beam profile imaging can be accomplished by restricting the imaging with wavelengths below the cutoff wavelength $\lambda_c$, i.e., where the emission is dominated by incoherent radiation. Spectral separation has been considered in Ref. [15] by using a scintillation screen in combination with a bandpass filter. However, this method requires a good knowledge and control of the expected spectra, and a vanishing form factor ($|F_l||F_t| \ll N^{-1/2}$) in the detectable wavelength range, which is not the general case as the spectra can vary strongly with the operation modes of a linear accelerator. This is demonstrated in Fig. 6, in which spectral measurements of transition radiation in the visible and near-infrared wavelength range are presented for different compression settings at FLASH. The dashed black line represents the incoherent radiation part convoluted with the transmission of the optical setup. In contrast to the measurements presented in Sec. II C, the measurements shown in Fig. 6 were performed upstream of the collimator section. We note that similar, reproducible measurements

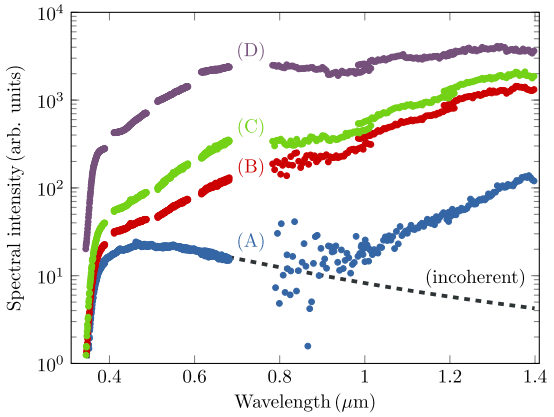


FIG. 6. Spectral intensity measurements of transition radiation in the visible and near-infrared wavelength range for four different compression settings: (A) FEL operation and (B)–(D) marginal compression, i.e., on-crest rf operation with decreasing $R_{56}$ in the bunch compressors (see Ref. [16] for experimental details). The spectral intensity of the incoherent part of transition radiation is indicated as dashed black line.

for uncompressed electron bunches, showing coherent radiation prominently at the micrometer scale, have been presented in Ref. [43], and COTR for uncompressed bunches has been reported in Ref. [11].

In general, the probability of coherent emission decreases at shorter wavelengths, which is often not sufficiently reduced for optical wavelengths, and imaging with transition radiation in the EUV region might be an option [52–54]. In addition to the knowledge and control of the spectra, the imaging with EUV radiation also requires dedicated detectors and optics, and a complete setup in vacuum to prevent strong absorption in air.

### B. Spatial separation

The luminescence of scintillation screens [55], which is a stochastic process, is inherently linear in the number of interacting electrons (neglecting quenching and saturation effects), hence coherent radiation effects are not expected in pure scintillation light. However, transition radiation is also emitted at the boundary of vacuum and scintillator, and coherent optical radiation can still appear [see, e.g., Fig. 3(b)]. Then, the total spectral and angular intensity distribution can be written as [omitting the arguments $(k, \Omega)$ in the intensity distributions $\mathcal{I}$]

$$\mathcal{I}_t = N\mathcal{I}_s + [N + N^2|F_l(k)|^2|F_t(k,\Omega)|^2]\mathcal{I}_o, \qquad (17)$$

where $\mathcal{I}_s$ and $\mathcal{I}_o$ are related to scintillation light and transition radiation, respectively. As discussed in Sec. IV A for OTR imaging screens and with the same requirements and restrictions, spectral separation can also be applied when using scintillation screens ($\mathcal{I}_t \approx N\mathcal{I}_s + N\mathcal{I}_o$). Another method, particularly suited for scintillation screens, which have nearly isotropic emission, is to make use of the strong angular dependence of optical transition radiation (e.g., Refs. [31,32]) and to perform electron beam profile imaging with radiation that is dominated by scintillation light, i.e., $\mathcal{I}_o(k,\Omega) \ll \mathcal{I}_s(k,\Omega)/[1 + N|F_l(k)|^2|F_t(k,\Omega)|^2]$ in Eq. (17). Spatial separation can be achieved with imaging geometries having large angular or spatial offsets, e.g., by using tilted imaging screens [42] or central masks [56], where $\mathcal{I}_o(\Omega)|F_t(\Omega)|^2$ is suppressed sufficiently. However, just as for spectral separation, this method also requires good knowledge and control of the form factor, and dedicated imaging geometries. In addition, the resolution depends on the observation angle of the scintillation screen (e.g., Ref. [42]), which has to be taken into account in the layout of the imaging system. We note that an experiment on the spatial separation technique is currently being commissioned at FLASH.

### C. Temporal separation

The fundamentally different light generation processes of scintillators and optical transition radiators result in clearly distinct temporal responses. The emission of transition radiation from relativistic electrons is instantaneous ($\sim$ fs) and prompt [57,58] compared to the decay times ($\sim$ ns) of common scintillators (e.g., Ref. [55]). Accordingly, the temporal profiles of the OTR pulses resemble the longitudinal electron beam profiles, whereas the temporal scintillation light pulses are fully dominated by the decay of the excited states in the scintillator. Temporal separation makes use of the distinct temporal responses and allows to entirely eliminate OTR, i.e., the term $\mathcal{I}_o$ in Eq. (17) which is time dependent with $\mathcal{I}_o \equiv \mathcal{I}_o(k,\Omega,t)$, and, therewith, coherent optical radiation effects in electron beam profile imaging with scintillation screens when reading out a gated camera with a certain time delay after the prompt emission of OTR. Image recording with delayed readout (e.g., Ref. [58]) can be accomplished with intensified CCD (ICCD) cameras, where a control voltage in the intensifier between photocathode and microchannel plate allows fast gating and exposure times of a few nanoseconds (e.g., Refs. [57–59]). The experiments on the temporal separation technique at FLASH have been performed by using the ICCD camera "PCO: Dicam Pro (S20)" [41] in combination with the off-axis LuAG scintillation imaging screen in the nondispersive main beam line at K-ICCD, which has a decay time of $\sim$50 ns [44]. The cameras used for the presented measurements are able to readout images at the bunch train repetition rate of FLASH of 10 Hz, hence one bunch per bunch train can be measured with single-shot capability. Further technical details on the equipment used for the measurements presented in the following can be found in Sec. II B and in Refs. [42,60].

The series of single-shot images in Fig. 7 present first proof-of-principle measurements on the temporal separation technique. The image shown in Fig. 7(a) was recorded at K-ICCD with an OTR screen, whereas for Figs. 7(b) and 7(c) a LuAG scintillation screen was used. The image shown in Fig. 7(c) has been recorded with a time delay of 100 ns, which is rather long compared to the emission time of OTR but takes into account the large camera trigger jitter that existed during the measurements. The image recorded with the OTR screen and time delay simply showed background noise and is not presented here. The intensity distributions in Fig. 7 have been generated by moderately compressed electron bunches with a charge of 0.5 nC and a beam energy of 700 MeV. Figures 7(a) and 7(b) show a composite of COTR and COSR with a contribution of scintillation light in Fig. 7(b). The round-shaped light pattern on the right-hand side of Figs. 7(a) and 7(b) is most probably due to synchrotron radiation generated upstream of the off-axis screens (a polarizer was not available during the measurements), where the appearance in Fig. 7(b) is reduced by the transparency of the LuAG screen. The image in Fig. 7(c), recorded with a time delay of 100 ns, can be attributed purely to scintillation light allowing for a quantitative analysis of the transverse beam profiles.

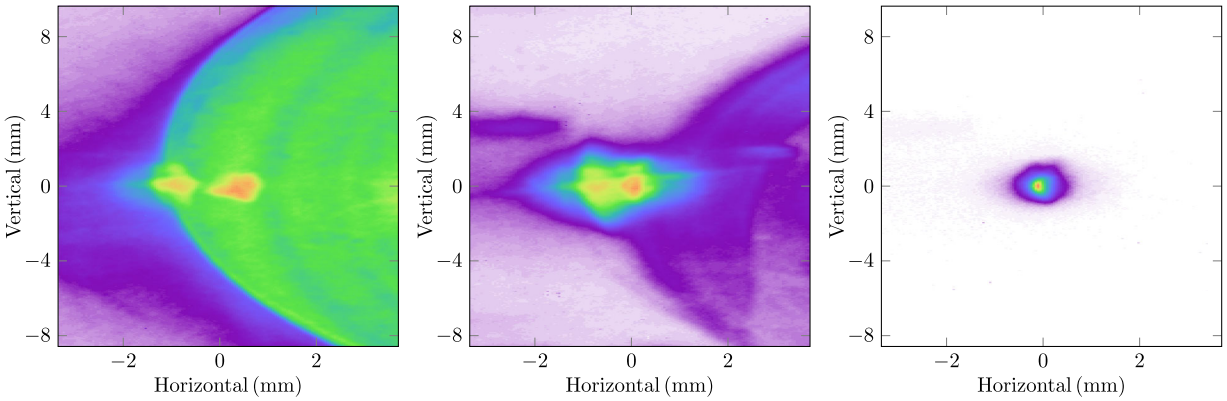


(a) OTR screen, no time delay. (b) LuAG screen, no time delay. (c) LuAG screen, time delay.

FIG. 7. Proof of principle for the temporal separation technique in transverse beam profile imaging, demonstrated for compressed electron bunches at K-ICCD with the three screen/readout configurations: (a) OTR screen, (b) LuAG screen, and (c) LuAG screen with delayed readout. The images in (a) and (b) show a composite of optical transition and synchrotron radiation with a contribution of scintillation light in (b). The image in (c) is expected to show delayed but pure scintillation light.

In contrast to spectral and spatial separation, the temporal separation technique provides a definite method to suppress coherent optical transition radiation without further relying on the wavelength-dependent longitudinal form factor. In addition, this technique inherently includes the suppression of secondary incoherent radiation sources such as synchrotron radiation generated from magnets directly upstream of the imaging screen or backward OTR emitted from the second imaging screen boundary, whereas spectral components in the UV region or at shorter wavelengths may excite the scintillator, affecting the temporal separation. As is shown in Ref. [17], however, potential synchrotron radiation sources can be identified and thus separated by adjusting the upstream magnets. Furthermore, the coherent emission of OTR at the second scintillator screen boundary is mitigated due to multiple scattering in the scintillator material as is described and demonstrated in Refs. [11,61]. We note that the current implementation of the temporal separation technique presented throughout this paper utilizes fast ICCD cameras, which are currently an order of magnitude more expensive than conventional CCD cameras.

## V. EXPERIMENTAL RESULTS WITH TEMPORAL SEPARATION

The proof-of-principle measurements on the temporal separation technique presented in Fig. 7 were carried out at K-ICCD. However, a reference measurement to quantitatively prove this technique in terms of transverse beam profiles, as would be provided by a wire scanner, which is insensitive to coherent effects, is not available at this position. In this section, we verify the method of temporal separation by investigations on the charge-dependent image intensities and comparisons with longitudinal bunch profiles recorded in the energy spectrometer at ES-CCD.

### A. Charge dependence of integrated intensity

Incoherent radiation is linear in the number of electrons contributing to the emission process (cf. Sec. III A), i.e., linear in the electron bunch charge ( $\sim Q$), and deviations caused by the nonlinear charge dependence of coherent radiation ($\sim |F_l|^2 Q^2$) are ideally suited to verify the temporal separation technique. The integrated image intensities presented in Fig. 8 were measured for bunch charges between 0.13 and 0.87 nC at K-ICCD for different imaging screen and readout configurations. Each data point represents the average intensity of 20 background-corrected single-shot images and the error bars indicate the statistical rms image intensity fluctuations. Up to an electron bunch charge of $Q \sim 0.5$ nC, the integrated intensity is linear (solid black line) in $Q$ for all presented

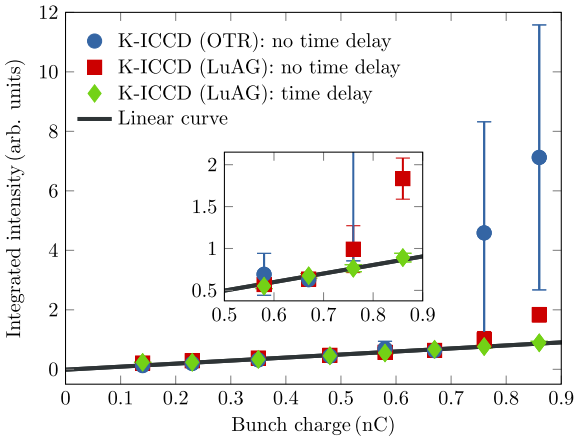


FIG. 8. Measurements on the bunch charge dependence of the integrated intensity at K-ICCD generated by compressed electron bunches using different screen/readout configurations, where the inset shows the range from 0.55 to 0.9 nC. The linear curve shows the dependence of incoherent radiation.

configurations. For higher bunch charges, deviations from the linear dependence appear in the configurations without delayed readout, i.e., the form factor $|F_l|$ becomes significant in the visible wavelength range, which are caused by contributions from coherent optical radiation. The inset in Fig. 8 shows the bunch charge range from 0.55 to 0.9 nC more detailed. We note that the integrated intensity of the OTR (blue dots) has actually been higher than presented for $Q > 0.7$ nC, because of camera saturation due to the strong optical emission and the corresponding underestimated integrated intensity. The large error bars, representing the rms jitter, indicate strong fluctuations due to the COTR. In the case of the LuAG imaging screen recorded with a time delay (green diamonds), the dependence of the integrated intensity is entirely linear in the bunch charge, which verifies the power of the temporal separation technique.

### B. Longitudinal electron bunch compression

As the emission of COTR is strongly suppressed in the magnetic energy spectrometer at FLASH (see Sec. III), electron bunch profiles measured at the screen station ES-CCD can serve as a reference for comparison with the temporal separation technique applied in the nondispersive beam line at K-ICCD. While the transverse bunch profiles can differ at both locations due to different Twiss parameters and dispersion at ES-CCD, longitudinal bunch compression does not take place in between, and longitudinal bunch profile measurements using the TDS can be used for a direct comparison. The measurements presented in Fig. 9 show the mean rms electron bunch length of 20 single-shot images, including the statistical rms jitter indicated via error bars, for various ACC1 rf phases measured at ES-CCD and K-ICCD by using the TDS. The electron bunches were set up with an energy of 700 MeV and a bunch charge of 0.5 nC. The rf phase of ACC1 affects the energy chirp of the electron bunches upstream of the first bunch compressor and, accordingly, the final electron bunch lengths. The rms electron bunch lengths measured in the magnetic energy spectrometer at ES-CCD (black dots) decrease almost linearly and do not possess large fluctuations.

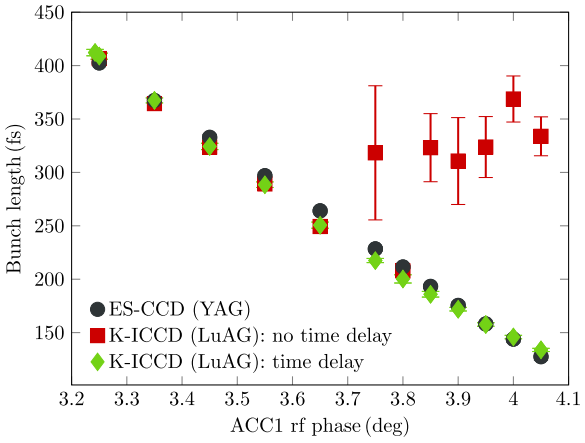


FIG. 9. Electron bunch length measurements for varying ACC1 rf phase at ES-CCD and K-ICCD using different readout configurations. According to Sec. III, the measurements in the magnetic energy spectrometer ("ES-CCD (YAG)") are intended to provide an absolute reference measurement.

In contrast to the magnetic energy spectrometer at ES-CCD, coherent optical emission is not suppressed in the nondispersive beam line at K-ICCD, leading to a sudden increase of the rms electron bunch lengths in combination with large fluctuations, represented by the large error bars (statistical rms jitter), for ACC1 rf phases $\gtrsim 3.75$ deg measured with a LuAG screen without a certain time delay (red squares), i.e., without applied temporal separation. The electron bunch length measurements using an OTR screen are omitted in Fig. 9 due to even larger deviations and fluctuations compared to the reference at ES-CCD for ACC1 rf phases $\gtrsim 3.75$ deg. Instead, the OTR images (single shots) for ACC1 rf phases of 3.25 and 3.75 deg are presented in Figs. 10(a) and 10(b), respectively, with obvious coherent optical radiation effects in Fig. 10(b). Because of the fact that the electron beam

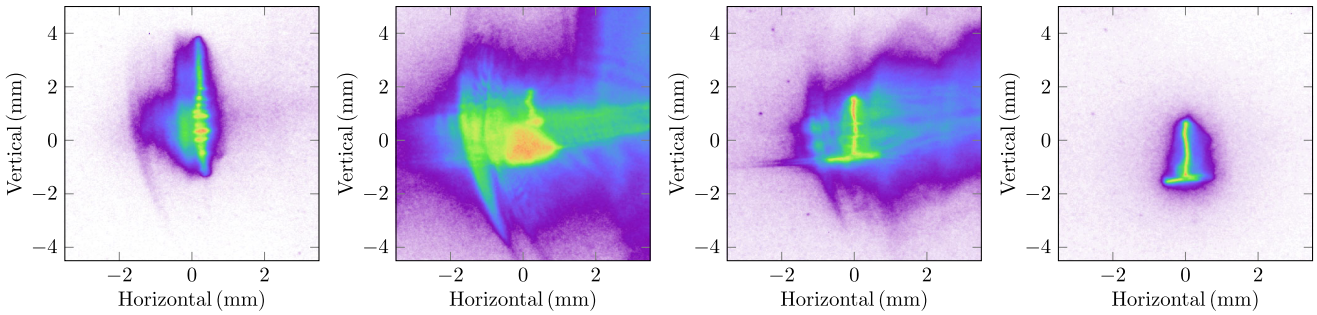


(a) 3.25 deg, OTR. (b) 3.75 deg, OTR. (c) 3.75 deg, LuAG. (d) 3.75 deg, LuAG, time delay.

FIG. 10. Single-shot electron beam profile images at K-ICCD for two ACC1 rf phases used in the measurements shown in Fig. 9 with different screen/readout configurations: (a) OTR screen for 3.25 deg, (b) OTR screen for 3.75 deg, and (c) LuAG screen for 3.75 deg without and (d) with delayed readout. The presented single-shot beam profile images are background-corrected.

images shown in Fig. 10 are sheared vertically by means of the TDS, the vertical coordinate implies time information [see Eq. (1)] and the faint bunching visible in Fig. 10(a) may be assigned to microbunching.

Figure 10(c) shows a single-shot image taken at K-ICCD using a LuAG screen without time delay for an ACC1 rf phase of 3.75 deg. The image clearly shows contributions of coherent optical radiation similar to the image in Fig. 10(b). By imaging the LuAG screen with a time delay of 100 ns, the obtained distribution shown in Fig. 10(d) is acceptable without obvious contributions from coherent optical radiation. In addition, the corresponding electron bunch length measurements with applied temporal separation (green diamonds) in Fig. 9 are in perfect agreement with the reference measurements in the energy spectrometer at ES-CCD (black dots). The electron bunch durations for FEL operation at FLASH are typically shorter than 150 fs (e.g., Ref. [20]), and typical electron beam parameters are given in Table I.

### C. Longitudinal electron beam profiles

The temporal separation technique, which has demonstrated accurate rms electron bunch length measurements in the presence of coherent optical radiation effects, gives confidence that single-shot measurements of longitudinal bunch profiles and, accordingly, electron bunch currents using temporal separation result in reliable results. The single-shot measurements presented in Fig. 11 (cf. measurements shown in Figs. 9 and 10 for the same ACC1 rf phase settings) have been recorded for an ACC1 rf phases of 3.75 deg in Fig. 11(a) and for 4.05 deg in Fig. 11(b), i.e., in the presence of coherent optical radiation effects. The longitudinal electron bunch profiles taken in the nondispersive beam line at K-ICCD (blue line) with temporal separation show good agreement with the reference measurements at ES-CCD (red line), and the observed deviations are most probably due to slightly nonlinear amplification in the intensifier (photocathode and microchannel plate) of the ICCD camera. The reduced peak current with broadening in time in the case of "K-ICCD: time delay," which is apparent on the right-hand side (time $> 0$) of Fig. 11(b), can be explained by the different time resolutions of $\mathcal{R}_{t,\mathrm{e}} = 13$ fs and 43 fs achieved with the TDS during the measurements for ES-CCD and K-ICCD, respectively. In order to compare the longitudinal bunch profiles with comparable resolution, a convolution has been applied for the measurement at ES-CCD in Fig. 11(b) by taking into account the actual time resolution. The longitudinal bunch profile after carrying out the convolution (green dashed line) is in good agreement with the bunch profile taken at K-ICCD with applied temporal separation (blue line).

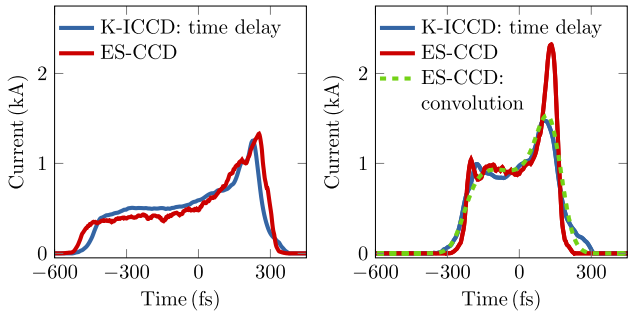


(a) ACC1 rf phase of 3.75 deg. (b) ACC1 rf phase of 4.05 deg.

FIG. 11. Single-shot longitudinal electron bunch profiles measured in the nondispersive beam line at K-ICCD by using the LuAG screen recorded with a certain time delay (blue line) and in the magnetic energy spectrometer at ES-CCD by using the YAG screen (red line) for ACC1 rf phases of (a) 3.75 deg and (b) 4.05 deg, respectively. A convolution has been applied in (b) for the measurement at ES-CCD (green dashed line) to compare the longitudinal profiles with similar resolution.

## VI. SUMMARY AND CONCLUSIONS

Electron beam profile imaging is crucial for many applications in electron beam diagnostics at FELs, and particularly required to perform single-shot diagnostics. However, the frequent appearance of coherent optical radiation effects, e.g., COTR, in high-brightness electron beams impedes incoherent beam profile imaging with standard techniques. The theoretical considerations, numerical simulations, and experimental data presented in this paper show that coherent optical emission can be strongly suppressed by performing beam profile imaging in a magnetic energy spectrometer due to sufficient spatial-to-longitudinal coupling. However, energy spectrometers preclude measuring pure transverse beam profiles due to dispersion in the bending plane. For incoherent beam profile imaging in nondispersive beam lines, we discussed methods to separate the incoherent radiation from scintillation screens and to simultaneously exclude coherent optical radiation from detection. In contrast to spectral and spatial separation, the temporal separation technique, utilizing an ICCD camera, provides a definite method to suppress coherent optical transition radiation without knowledge of the longitudinal form factor. In terms of readout times and rates, ICCD cameras have the same applicability as standard CCD cameras. By applying the temporal separation technique in the presence of coherent optical radiation, we demonstrated reliable measurements of longitudinal electron beam profiles, and measurements of rms electron bunch lengths in excellent agreement with reference measurements in a magnetic energy spectrometer. Limitations may appear due to scintillator excitation by secondary coherent radiation sources. However, the presented experimental results prove the temporal separation technique as a promising method for future applications in beam profile diagnostics for high-brightness electron beams.

## ACKNOWLEDGMENTS

We would like to thank the whole FLASH team, and the engineers and technicians of the DESY groups F. L. A., M. C. S., and M. V. S. for their great support. We also thank B. Faatz, K. Honkavaara, and S. Schreiber for providing beam time, and Y. Ding and H. Loos for fruitful discussions. In particular, we are deeply grateful to E. A. Schneidmiller for careful reading of the manuscript and to Z. Huang for providing many helpful explanations.

[1] S. Jamison, Nature Photon. **4**, 589 (2010).
[2] W. Ackermann *et al.*, Nature Photon. **1**, 336 (2007).
[3] P. Emma *et al.*, Nature Photon. **4**, 641 (2010).
[4] D. Pile, Nature Photon. **5**, 456 (2011).
[5] E. L. Saldin, E. A. Schneidmiller, and M. V. Yurkov, Nucl. Instrum. Methods Phys. Res., Sect. A **398**, 373 (1997).
[6] M. Borland, Y. C. Chae, P. Emma, J. W. Lewellen, V. Bharadwaj, W. M. Fawley, P. Krejcik, C. Limborg, S. V. Milton, H.-D. Nuhn, R. Soliday, and M. Woodley, Nucl. Instrum. Methods Phys. Res., Sect. A **483**, 268 (2002).
[7] E. L. Saldin, E. A. Schneidmiller, and M. V. Yurkov, Nucl. Instrum. Methods Phys. Res., Sect. A **528**, 355 (2004).
[8] M. Venturini and A. Zholents, Nucl. Instrum. Methods Phys. Res., Sect. A **593**, 53 (2008).
[9] Z. Huang, A. Brachmann, F.-J. Decker, Y. Ding, D. Dowell, P. Emma, J. Frisch, S. Gilevich, G. Hays, Ph. Hering, R. Iverson, H. Loos, A. Miahnahri, H.-D. Nuhn, D. Ratner, G. Stupakov, J. Turner, J. Welch, W. White, J. Wu, and D. Xiang, Phys. Rev. ST Accel. Beams **13**, 020703 (2010).
[10] Y. Glinec, J. Faure, A. Norlin, A. Pukhov, and V. Malka, Phys. Rev. Lett. **98**, 194801 (2007).
[11] H. Loos, R. Akre, A. Brachmann, F.-J. Decker, Y. Ding, D. Dowell, P. Emma, J. Frisch, S. Gilevich, G. Hays, Ph. Hering, Z. Huang, R. Iverson, C. Limborg-Deprey, A. Miahnahri, S. Molloy, H.-D. Nuhn, D. Ratner, J. Turner, J. Welch, W. White, and J. Wu, in Proceedings of the 30th International Free Electron Laser Conference, Gyeongju, Korea, 2008, THBAU01.
[12] R. Akre, D. Dowell, P. Emma, J. Frisch, S. Gilevich, G. Hays, Ph. Hering, R. Iverson, C. Limborg-Deprey, H. Loos, A. Miahnahri, J. Schmerge, J. Turner, J. Welch, W. White, and J. Wu, Phys. Rev. ST Accel. Beams **11**, 030703 (2008).
[13] C. M. S. Sears, E. Colby, R. Ischebeck, C. McGuinness, J. Nelson, R. Noble, R. H. Siemann, J. Spencer, D. Walz, T. Plettner, and R. L. Byer, Phys. Rev. ST Accel. Beams **11**, 061301 (2008).
[14] A. H. Lumpkin, R. J. Dejus, and N. S. Sereno, Phys. Rev. ST Accel. Beams **12**, 040704 (2009).
[15] A. H. Lumpkin, N. S. Sereno, W. J. Berg, M. Borland, Y. Li, and S. J. Pasky, Phys. Rev. ST Accel. Beams **12**, 080702 (2009).
[16] S. Wesch, C. Behrens, B. Schmidt, and P. Schmüser, in *Proceedings of the 31st International Free Electron Laser Conference, Liverpool, United Kingdom, 2009* (STFC Daresbury Laboratory, Warrington, 2009), WEPC50.
[17] K. L. F. Bane, F.-J. Decker, Y. Ding, D. Dowell, P. Emma, J. Frisch, Z. Huang, R. Iverson, C. Limborg-Deprey, H. Loos, H.-D. Nuhn, D. Ratner, G. Stupakov, J. Turner, J. Welch, and J. Wu, Phys. Rev. ST Accel. Beams **12**, 030704 (2009).
[18] M. Röhrs, Ch. Gerth, H. Schlarb, B. Schmidt, and P. Schmüser, Phys. Rev. ST Accel. Beams **12**, 050704 (2009).
[19] D. Filippetto *et al.*, Phys. Rev. ST Accel. Beams **14**, 092804 (2011).
[20] C. Behrens, N. Gerasimova, Ch. Gerth, B. Schmidt, E. A. Schneidmiller, S. Serkez, S. Wesch, and M. V. Yurkov, Phys. Rev. ST Accel. Beams **15**, 030707 (2012).
[21] M. Cornacchia and P. Emma, Phys. Rev. ST Accel. Beams **5**, 084001 (2002).
[22] Z. Huang, M. Borland, P. Emma, J. Wu, C. Limborg, G. Stupakov, and J. Welch, Phys. Rev. ST Accel. Beams **7**, 074401 (2004).
[23] C. Behrens, Z. Huang, and D. Xiang, Phys. Rev. ST Accel. Beams **15**, 022802 (2012).
[24] O. Lundh, J. Lim, C. Rechatin, L. Ammoura, A. Ben-Ismaïl, X. Davoine, G. Gallot, J.-P. Goddet, E. Lefebvre, V. Malka, and J. Faure, Nature Phys. **7**, 219 (2011).
[25] Y. Ding, A. Brachmann, F.-J. Decker, D. Dowell, P. Emma, J. Frisch, S. Gilevich, G. Hays, Ph. Hering, Z. Huang, R. Iverson, H. Loos, A. Miahnahri, H.-D. Nuhn, D. Ratner, J. Turner, J. Welch, W. White, and J. Wu, Phys. Rev. Lett. **102**, 254801 (2009).
[26] Z. Huang, A. Baker, C. Behrens, M. Boyes, J. Craft, F.-J. Decker, Y. Ding, P. Emma, J. Frisch, R. Iverson, J. Lipari, H. Loos, and D. Walz, in *Proceedings of the 24th Particle Accelerator Conference, New York, USA, 2011* (IEEE, New York, 2011), THP183.
[27] I. Zagorodnov, Proceedings of the 32nd International Free Electron Laser Conference, Malmö, Sweden, 2010, WEOBI2.
[28] L. Wartski, J. Marcou, and S. Roland, IEEE Trans. Nucl. Sci. **20**, 544 (1973).
[29] D. W. Rule, Nucl. Instrum. Methods Phys. Res., Sect. B **24/25**, 901 (1987).
[30] D. W. Rule and R. B. Fiorito, AIP Conf. Proc. **229**, 315 (1991).
[31] X. Artru, R. Chehab, K. Honkavaara, and A. Variola, Nucl. Instrum. Methods Phys. Res., Sect. B **145**, 160 (1998).
[32] D. Xiang, W.-H. Huang, and Y.-Z. Lin, Phys. Rev. ST Accel. Beams **10**, 062801 (2007).
[33] A. M. Kondratenko and E. L. Saldin, Part. Accel. **10**, 207 (1980).
[34] H. Edwards, C. Behrens, and E. Harms, in *Proceedings of the 25th International Linear Accelerator Conference, Tsukuba, Japan, 2010* (ICR, Kyoto, 2010), MO304.
[35] O. Altenmueller, R. Larsen, and G. Loew, Rev. Sci. Instrum. **35**, 438 (1964).
[36] C. Behrens, Ch. Gerth, and I. Zagorodnov, in Proceedings of the 31st International Free Electron Laser Conference, Liverpool, United Kingdom, 2009 (Ref. [16]), WEPC45.
[37] C. Behrens and Ch. Gerth, in Proceedings of the 32nd International Free Electron Laser Conference, Malmö, Sweden, 2010, MOPC08.
[38] P. Emma, J. Frisch, and P. Krejcik, Technical Report No. LCLS-TN-00-12, 2000.

## 3.2 A multi-channel THz and infrared spectrometer for femtosecond electron bunch diagnostics by single-shot spectroscopy of coherent radiation

Single-shot electron beam diagnostics using transverse deflecting r.f. structures demonstrated temporal resolutions of sub-10 fs r.m.s. [57] and are expected to achieve unprecedented ~ 1 fs r.m.s. by using X-band r.f. technology [74]. Transverse deflecting r.f. structures are routinely used at present X-ray FELs, even though recent observations of coherent optical radiation effects may hamper these time-domain diagnostics that rely on transverse beam profile measurements. Apart from that, techniques to accomplish electron beam profile imaging in the presence of coherent optical radiation effects are available (see Sec. 3.1).

A different approach, making use of the coherent emission of femtosecond electron beams and complementing the time-domain diagnostics, is based on frequency-domain spectroscopy of coherent THz and infrared radiation. According to Eq. (2.38), which can also be expressed as a Fourier transform of the longitudinal electron bunch charge distribution (e.g., Refs. [54, 57, 58]), the coherent emission depends on the temporal distribution of the electrons. Coherent emission of transition or synchrotron radiation emerges for wavelengths comparable or longer than the electron bunches, hence the relevant wavelengths for diagnosis of femtosecond electron beams are in the THz and infrared range. By utilizing phase retrieval techniques (Kramer-Kronig relations), inverse Fourier transform of the measured wavelength spectra allows to reconstruct the temporal bunch profiles (e.g., Refs. [54, 75, 76]). However, accurate temporal bunch profile reconstruction requires a sufficiently large wavelength coverage, i.e., a broadband THz and infrared spectrometer.

A unique design of a broadband THz spectrometer with single-shot capability has been discussed and demonstrated in Ref. [77]. In order to cover a large wavelength range sufficiently for typical electron bunch durations at present X-ray FELs, the presented spectrometer is based on a multi-stage setup of reflective blazed gratings. A fully developed version of this THz spectrometer with excellent performance is reported in Refs. [58, 78]. For ultrashort bunches with durations of $\lesssim$ 20 fs, such as demonstrated by the low-charge operation at the LCLS [40, 41] or planned for the E-XFEL [79], a design for a broadband spectrometer using a single prism for the near- and mid-infrared has been considered in Ref. [80].

The following article reports on the design and development of a multi-channel THz spectrometer for single-shot diagnosis of femtosecond electron bunches. The commissioning of this unique device is described and comparative measurements are presented. Temporal bunch profile reconstruction from spectroscopic data is demonstrated in Sec. 5.1.

Nuclear Instruments and Methods in Physics Research A 665 (2011) 40–47

Contents lists available at SciVerse ScienceDirect

Nuclear Instruments and Methods in Physics Research A

journal homepage: www.elsevier.com/locate/nima

# A multi-channel THz and infrared spectrometer for femtosecond electron bunch diagnostics by single-shot spectroscopy of coherent radiation

Stephan Wesch*, Bernhard Schmidt, Christopher Behrens, Hossein Delsim-Hashemi, Peter Schmüser

*Deutsches Elektronen-Synchrotron DESY, Notkestraße 85, 22607 Hamburg, Germany*

ARTICLE INFO

*Article history:*
Received 5 September 2011
Received in revised form
11 November 2011
Accepted 12 November 2011
Available online 20 November 2011

*Keywords:*
Coherent radiation
Form factor
Electron bunch length
THz and infrared spectroscopy

ABSTRACT

The required high peak current in free-electron lasers (FELs) is realized by longitudinal compression of the electron bunches to sub-picosecond length. In this paper, a frequency-domain diagnostic method is described that is capable of resolving structures in the femtosecond regime. A novel in-vacuum spectrometer has been developed for spectroscopy of coherent radiation in the THz and infrared range. The spectrometer is equipped with five consecutive dispersion gratings and 120 parallel readout channels; it can be operated either in short (5–44 μm) or in long wavelength mode (45–430 μm). Fast parallel readout permits the spectroscopy of coherent radiation from single electron bunches. Test measurements at the soft X-ray free-electron laser FLASH, using coherent transition radiation, demonstrate excellent performance of the spectrometer. The device is planned for use as an online bunch profile monitor during regular FEL operation.



## 1. Introduction

The electron bunches in high-gain free-electron lasers are longitudinally compressed to achieve peak currents in the kA range which are necessary to drive the FEL gain process in the undulator magnets. Bunch compression is accomplished by a two-stage process: first an *energy chirp* (energy–position relationship) is imprinted onto the typically 10 ps long bunches emerging from the electron gun, and then the chirped bunches are passed through magnetic chicanes.

Magnetic compression of intense electron bunches is strongly affected by collective effects in the chicanes and cannot be adequately described by linear beam transfer theory. Space charge forces and coherent synchrotron radiation have a profound influence on the time profile and internal energy distribution of the compressed bunches. The collective effects have been studied by various numerical simulations (see [1] and the references quoted therein) but the parameter uncertainties are considerable and experimental data are thus indispensable for determining the longitudinal bunch structure. Using a transverse deflecting microwave structure (TDS) [2,3] our group has carried out a time-resolved phase space tomography [4] of the compressed bunches in the free-electron laser FLASH. The TDS converts the temporal profile of the electron bunch charge density into a transverse streak on a view screen by a rapidly varying electromagnetic field, analogous to the sawtooth voltage in a conventional oscilloscope tube. The time resolution depends on the microwave voltage and the beam optics in the diagnostic section. In the present beam optics configuration at FLASH, a resolution of down to 25 fs rms has been achieved.

The electro-optical (EO) technique is an alternative method of measuring the longitudinal bunch charge distribution. Several variants of single-shot EO bunch diagnostics have been applied [5–7], all sharing the underlying principle of utilizing the field-induced birefringence in an electro-optic crystal to convert the time profile of a bunch into a temporal, spectral or spatial intensity modulation of a probe laser pulse. The EO techniques have the advantage of being non-destructive, thereby permitting correlation studies of EO measurements on selected bunches with the FEL radiation pulses produced by the same bunches. In Ref. [8] an absolute calibration of the EO technique was performed utilizing simultaneous TDS measurements. A record resolution of 50 fs (rms) in the detection of single electron bunches was achieved.

Frequency-domain techniques provide a complementary access to the femtosecond time regime. The spectral intensity of the coherent radiation emitted by a bunch with $N$ electrons is

$$\frac{dU}{d\lambda} = \frac{dU_1}{d\lambda} N^2 \left|F_\ell(\lambda)\right|^2 \tag{1}$$

where $dU_1/d\lambda$ is the intensity per unit wavelength emitted by a single electron, and $F_\ell(\lambda)$ is the longitudinal form factor of the bunch, the Fourier transform of the normalized line charge density $S(z)$

$$F_\ell(\lambda) = \int S(z)\exp(-2\pi i z/\lambda)\,dz \tag{2}$$

In Eq. (1) we have made use of the fact that radiation from relativistic particles is confined to small angles whereby the influence of the

* Corresponding author.
*E-mail address:* stephan.wesch@desy.de (S. Wesch).

0168-9002/$ - see front matter © 2011 Elsevier B.V. All rights reserved.
doi:10.1016/j.nima.2011.11.037

transverse form factor is strongly suppressed. For an rms beam radius of 100−200 μm, as in our case, the determination of the longitudinal charge profile from the measured coherent radiation spectrum depends only weakly on the precise knowledge of the transverse charge distribution.

A measurement of the coherent radiation spectrum yields the absolute magnitude of the form factor as a function of wavelength but the phase remains unknown. Hence the determination of the longitudinal charge distribution by inverse Fourier transformation is not directly possible. Phase information can be obtained with the help of the Kramers–Kronig relation [9] if a sufficient wavelength range is covered.

The typical lengths of compressed electron bunches of a few hundred micrometer leads to coherent emission in the far infrared (FIR) and millimeter wavelength range. The commonly used technique of spectroscopy for this regime is to measure the autocorrelation function with a Michelson type interferometer and to deduce the power spectrum by Fourier transformation (Fourier-spectroscopy). This technique has been applied for bunch length measurements at various electron linacs [10–15]. Since the interferometer is a step-scan device, it cannot be used for online monitoring. For this, polychromators measuring different wavelengths simultaneously have been proposed [16] but were of limited use due to their small number of read-out channels and thus restricted wavelength range.

We have developed a novel broadband spectroscopic instrument with single-shot capability [17]. With two sets of five consecutive gratings, which can be interchanged by remote control, the most recent version of the spectrometer covers the far-infrared wavelength range from 45 to 435 μm or the mid-infrared range from 5 to 44 μm. The spectral intensity is recorded simultaneously in 120 wavelength bins.

In this paper, we describe the design of the spectrometer, the detectors, amplifiers and readout electronics. Test measurements with coherent transition radiation (CTR) are presented which were carried out on bunches whose time profile was determined simultaneously using the transverse deflecting microwave structure TDS.

## 2. Design and realization of the spectrometer

### 2.1. Reflection gratings

Coherent radiation from short electron bunches extends over a wide range in wavelength, from a few micrometers up to about 1 mm. Gratings are useful to disperse the polychromatic radiation into its spectral components. For a monochromatic plane wave that is incident normally on a transmission grating with slit spacing $d$, the transmitted wave has interference maxima at angles $\beta_m$ given by the equation $d\sin\beta_m = m\lambda$. Here $m$ is the order of diffraction. The free spectral range of a grating is defined by the requirement that different diffraction orders do not overlap. Since light of wavelength $\lambda$, diffracted in the order $m=1$, will coincide with light of wavelength $\lambda/2$, diffracted in the order $m=2$, the ratio of the longest and the shortest wavelength in the free spectral range is close to two. Hence a single grating can only cover a small part of the entire coherent radiation spectrum, and many gratings of different spectral ranges have to be used simultaneously. Ambiguities due to overlap of different orders are avoided if the radiation impinging on a grating is filtered to limit the bandwidth appropriately. It will be shown below that this filtering is accomplished by a preceding grating.

A transmission grating with a large number of slits, whose width is small compared to the slit separation, distributes the diffracted radiation power almost equally among many orders. A great improvement in efficiency for a specific order is obtained using a blazed reflection grating [18] with triangular grooves as shown in Fig. 1. For an incoming wave that is incident at an angle $\alpha$ with respect to the normal of the grating, the grating equation becomes

$$d(\sin\alpha+\sin\beta_m)=m\lambda \tag{3}$$

To enhance the intensity in a given order $m$, the blaze angle $\theta_B$ and the incidence angle $\alpha$ are chosen such that the direction of the diffracted light coincides with the direction of specular reflection at the inclined surfaces [18]. For the first order $m=1$ this implies $\theta_B-\alpha=\beta_1-\theta_B$, hence $\theta_B=(\alpha+\beta_1)/2$. In this case most of the diffracted power goes into the order $m=1$.

It is a general feature of gratings that the diffraction effects vanish if the wavelength becomes too large. The incidence angle is $\alpha=19^\circ$ in our spectrometer setup, hence the largest possible value of $\sin\alpha+\sin\beta_m$ is 1.33. This implies that for wavelengths $\lambda\geq 1.33d$, the grating Eq. (3) can only be satisfied with $m=0$ which means that no diffracted wave exists and the reflection grating behaves as a plane mirror. This specular reflection of long wavelengths is utilized in the multistage spectrometer described below.

The efficiency of a grating in the diffraction order $m$ is defined as the ratio of diffracted light energy to incident energy. It was computed with two commercial codes (*PCGrate-S6.1* by I.I.G. Inc. and *GSolver V4.20c* by Grating Development Company) which are in reasonable agreement. In Fig. 2, the efficiencies as a function of wavelength are shown for the diffraction orders $m=0,1,2$. In the range $0.78<\lambda/d<1.31$ first-order diffraction ($m=1$) dominates and has an high efficiency for linearly polarized radiation whose electric field is perpendicular to the grooves of the grating. This is essentially the useful free spectral range of the grating. All radiation with $\lambda>\lambda_0=1.33d$ is directed into the zeroth order, which means that the grating acts as a mirror. The short-wavelength range below $0.78d$ may cause problems because different diffraction orders overlap. Radiation in this range must be removed by a preceding grating stage to avoid confusion caused by overlapping orders.

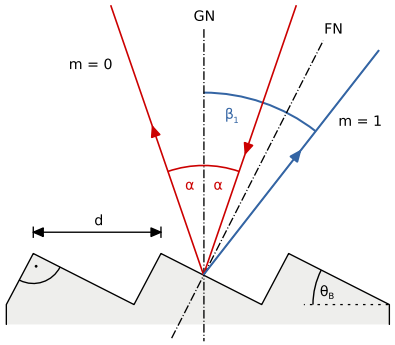


**Fig. 1.** Principle of a blazed reflection grating. For optimum efficiency of first-order diffraction, the incoming ray and the first-order diffracted ray have to enclose equal angles with respect to the facet normal *FN*. The blaze angle chosen is $\theta_B=27^\circ$, the incidence angle is $\alpha=19^\circ$ as measured with respect to the grating normal GN.

### 2.2. Multiple grating configuration

Our spectrometer is equipped with five consecutive reflection gratings, G0–G4 (see Fig. 3). A photo of the spectrometer is shown in Fig. 4. Each grating exists in two variants, for the mid-infrared (MIR) and the far-infrared (FIR) regime. The parameters are summarized in Table 1. The MIR and FIR gratings are mounted on top of each other in vertical translation stages (Fig. 5). Between each grating pair is either a mirror (for G1, G2 and G3) or a

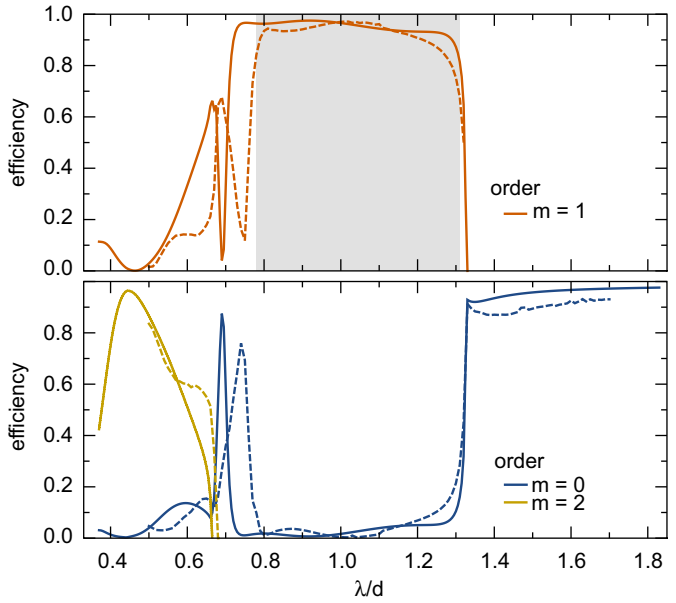


**Fig. 2.** Efficiency curves of a gold-plated reflection grating for radiation polarized perpendicular to the grooves, computed with the codes *PCGrate* (solid curves) and *GSolver* (dashed curves). Top graph: first-order diffraction $m=1$. The wavelength range $0.78<\lambda/d<1.31$ marked by the shaded area is used as a basis for the spectrometer layout providing an almost flat efficiency. Bottom graph: diffraction orders $m=0$ and $m=2$. Above $\lambda_0/d=1.33$ all radiation is directed into the zeroth order which simply means that the grating acts as a plane mirror. For small wavelengths ($\lambda/d<0.78$) all three orders $m=0,1,2$ contribute to the diffraction pattern. In order to avoid ambiguities this wavelength range must be removed by filtering the incident radiation.

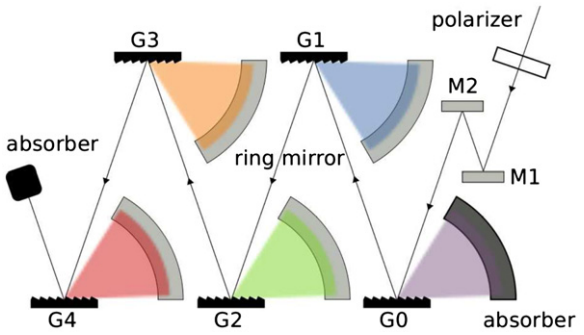


**Fig. 3.** Principle of the staged spectrometer equipped with five reflection gratings. Explanations are given in the text. To avoid FIR absorption in humid air, the spectrometer is mounted in a vacuum vessel (not shown). The detector arrays mounted above the focusing mirrors are not displayed.

pyroelectric detector (for G0 and G4) which are needed for alignment.

In the following we describe the far-infrared (THz) configuration, the mid-infrared configuration works correspondingly. The incident radiation is passed through a polarization filter (HDPE thin film THz polarizer by TYDEX) to select the polarization component perpendicular to the grooves of the gratings, and is then directed towards grating G0 which acts as a low-pass filter: the high-frequency part of the radiation (wavelength $\lambda<\lambda_0=44\ \mu m$) is dispersed and guided to an absorber, while the low-frequency part ($\lambda>\lambda_0$) is specularly reflected by G0 and sent to grating G1. This is the first grating stage of the spectrometer. Radiation in the range $\lambda_{min}=45.3\ \mu m<\lambda<\lambda_{max}=77.4\ \mu m$ is dispersed in first-order and focused by the use of a ring mirror onto a multi-channel detector array, while radiation with $\lambda>\lambda_0=77.6\ \mu m$ is specularly reflected and sent to G2. The subsequent gratings work similarly

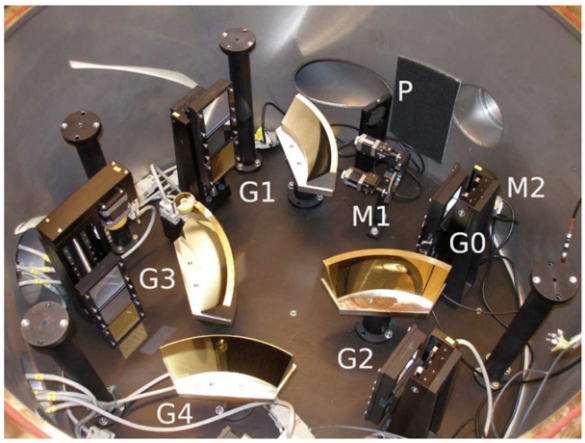


**Fig. 4.** Photo of the multi-grating spectrometer as mounted in a vacuum vessel attached to the CTR beam line. The detector arrays are not yet installed, hence four reflection gratings, G0–G3, are visible. G4 is just outside the photo but its mirror can be seen. P is the polarizer, and M1, M2 are the input alignment mirrors.

**Table 1**
Parameters of the gratings. The distance between two grooves is called *d*. For light with $\lambda\geq\lambda_0$ the grating acts as a plane mirror. The minimum and maximum wavelengths of the free spectral range for first-order diffraction are called $\lambda_{min}$ and $\lambda_{max}$. All dimensions are quoted in μm. The coarse gratings with $d\geq 58.82\ \mu m$ are gold-plated and were custom-made by Kugler GmbH, the fine gratings with $d\leq 33.33\ \mu m$ are aluminium-plated and were purchased from Newport Corporation.

| Grating | $d$ | $\lambda_{min}$ | $\lambda_{max}$ | $\lambda_0$ |
|---|---|---|---|---|
| Mid-infrared configuration 5.1–43.5 μm | | | | |
| G0 | 4.17 | – | – | 5.5 |
| G1 | 6.67 | 5.13 | 8.77 | 8.8 |
| G2 | 11.11 | 8.56 | 14.6 | 14.7 |
| G3 | 20.0 | 15.4 | 26.3 | 26.4 |
| G4 | 33.33 | 27.5 | 43.5 | – |
| Far-infrared configuration 45.3–434.5 μm | | | | |
| G0 | 33.33 | – | – | 44 |
| G1 | 58.82 | 45.3 | 77.4 | 77.6 |
| G2 | 100.0 | 77.0 | 131.5 | 132 |
| G3 | 181.8 | 140.0 | 239.1 | 240 |
| G4 | 333.3 | 256.7 | 434.5 | – |

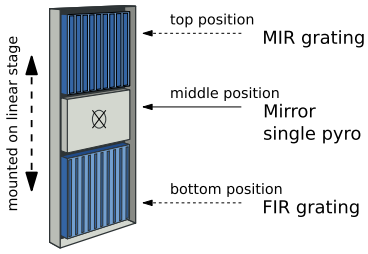


**Fig. 5.** The corresponding pairs of gratings are mounted on vertical translation stages with the aluminium-plated mid-infrared gratings in the upper position and the gold-plated far-infrared gratings in the lower position. Between each grating pair is either a plane mirror (for G1, G2, G3) or a pyro-electric detector (for G0 and G4) which are used for alignment purposes.

and disperse the wavelength intervals [77.0,131.5] μm (G2), [140.0,239.1] μm (G3), and [256.7,434.5] μm (G4).

### 2.3. Imaging system

For each grating, the first-order diffracted radiation is focused by a ring mirror of parabolic shape [17] onto an array of 30 pyroelectric detectors which are arranged on a circular arc (Fig. 6).

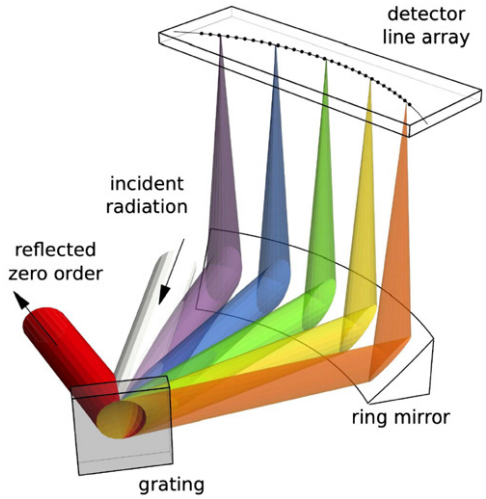


**Fig. 6.** Arrangement of the grating, the ring mirror and the array of 30 pyroelectric detectors. The light dispersion and focusing have been computed with a ray tracing code. For clarity only 5 of the 30 wavelength channels are shown.

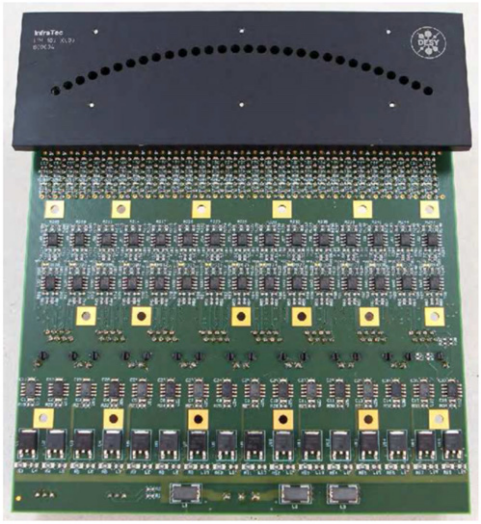

**Fig. 8.** Photo of the 30-channel pyroelectric detector array with integrated preamplifiers and twisted-pair line drivers.

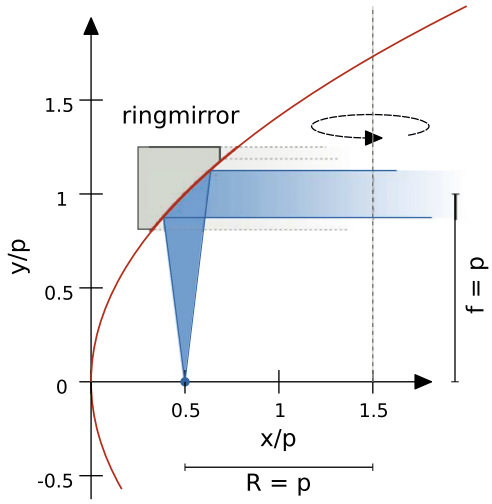


**Fig. 7.** The ring mirror is obtained by rotating a section of the parabola $y=\sqrt{2px}$ about a vertical axis at $x=3p/2$. The gold plated mirrors are visible in Fig. 4.

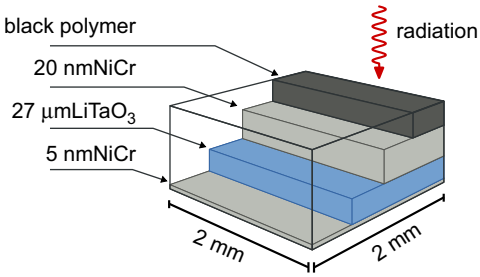


**Fig. 9.** Layout of the pyroelectric detector LIM-107-X005.

The grating spreads the first-order dispersed radiation over an angular range from 27° to 80°. To focus the light onto a circular arc passing through the 30-channel detector array, a ring-shaped parabolic mirror has been designed with an angular acceptance of 60°. The ring mirror design is shown in Fig. 7. The indicated 35 mm wide section of the parabola $y=\sqrt{2px}$ is rotated about a vertical axis at $x=3p/2$. The radius of curvature is $R=p=150$ mm. The grating is located in the center of the ring mirror which deflects the radiation by 90° and has a focal length of $f=p=150$ mm.

### 2.4. Detector array

The first-order diffracted radiation is recorded in a specially designed detector array equipped with 30 pyroelectric detectors (Fig. 8) which are arranged on a circular arc covering 57° and thus matching the acceptance of the focusing ring mirrors.

A critical component of the broadband single-shot spectrometer is a detector featuring high sensitivity over the entire THz and infrared regime. Only bolometric devices, responding to the deposited radiation energy through a temperature rise, can cover such a wide wavelength range. The simplest and widely used bolometric detectors are pyroelectric crystals. Although inferior to cryogenic detectors in sensitivity, they have many advantages: they are very compact, comparatively inexpensive, and do not require an entrance window.

A special pyroelectric detector has been developed by a industrial company (InfraTec) according to our specification. This sensor possesses sufficient sensitivity for the application in a coherent radiation spectrometer and has a fast thermal and electrical response. The layout of the detector is shown in Fig. 9. It consists of a 27 µm thick lithium tantalate ($LiTaO_3$) crystal with an active area of $2\times2$ mm$^2$. The front surface is covered with a fairly thick NiCr electrode (20 nm instead of 5 nm). The backside electrode is a NiCr layer of only 5 nm thickness instead of the conventional thick gold electrode. To enhance the radiation absorption below 100 µm the front electrode is optionally covered with a black polymer layer.

The combination of a thick front electrode and a thin backside metallization greatly reduces internal reflections which are the origin of the strong wavelength-dependent efficiency oscillations observed in conventional pyroelectric detectors. The beneficial effect of the novel layer structure is illustrated in Fig. 10. Efficiency variations for the new pyroelectric detector (solid curve) are strongly suppressed compared to a conventional detector (dashed curve) leading to superior performance characteristics in case of spectroscopic applications. A drawback is the lower overall efficiency, but this is of minor importance in our case as there is ample coherent radiation intensity at FLASH.

The pyroelectric detector is connected to a charge-sensitive preamplifier (Cremat CR110) followed by a Gaussian filter amplifier (CR220) with 4 µs time constant. This combination has been

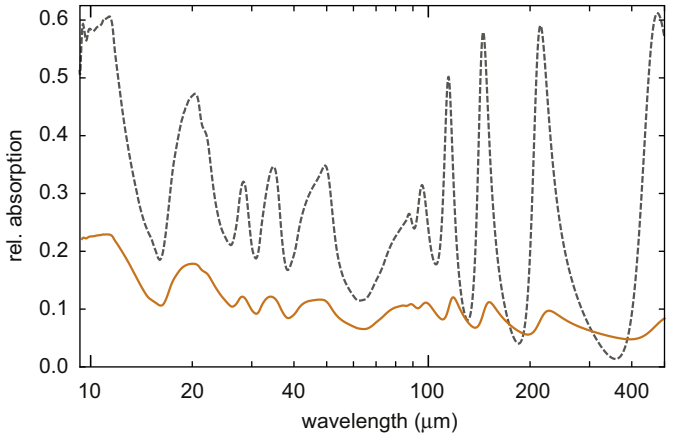


**Fig. 10.** Computed infrared absorption as a function of wavelength. Dashed curve: 27 μm $LiTaO_3$ detector with standard coatings: a 5 nm NiCr layer at the front surface and a thick gold layer at the back surface. Solid curve: 27 μm $LiTaO_3$ detector with optimized coatings for minimizing internal reflections (20 nm NiCr at front surface and 5 nm NiCr at back surface).

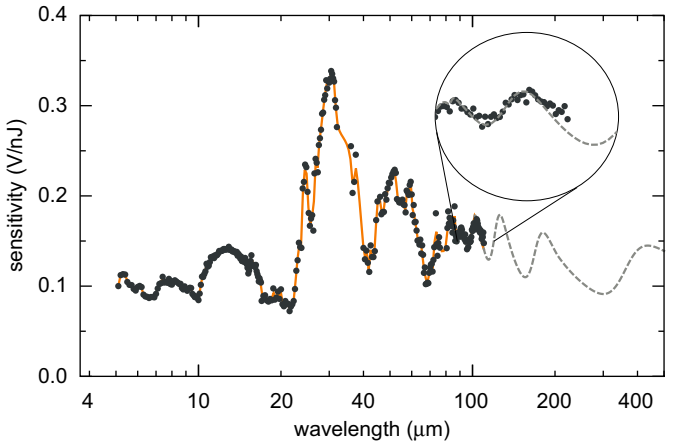


**Fig. 11.** Calibration of the pyroelectric detector equipped with a charge-sensitive preamplifier and subsequent Gaussian filter amplifier (Fig. 13). The sensitivity is plotted as function of wavelength. Below 110 μm, the experimental data from FELIX (dots) are shown together with an interpolating curve. For longer wavelengths, a calculated curve for the novel coating arrangement (see Fig. 10) is shown as dashed line. It is normalized to the measured data in the range 90–110 μm. Below 90 μm the properties of the black coating are poorly known hence a meaningful comparison with the model calculation is not possible.

calibrated [19] with infrared pulses of selectable wavelength at the infrared FEL user facility FELIX [20] in the wavelength range from 5 to 110 μm. The measured sensitivity as a function of wavelength is shown in Fig. 11. While the wavelength dependence of the sensitivity has been determined rather accurately, the absolute calibration is uncertain by at least 50%. Two different power meters were available to measure the total power in the FELIX test beam. They agreed in the wavelength dependence but the absolute power readings differed by a factor of two.

The black polymer coating introduces a thermal time constant of the detector response of typically 30 μs. Its contribution to the overall sensitivity can be studied by recording the electric pulse shape directly after the preamplifier. It turned out that the coating is basically transparent for wavelengths above 90 μm. This allows to extrapolate the sensitivity curve to longer wavelengths where no data exists by using the computed absorption for the bare sensor shown in Fig. 10.

For a given spectrometer configuration, mid-infrared (MIR) or far-infrared (FIR), the dispersed radiation is recorded in 120

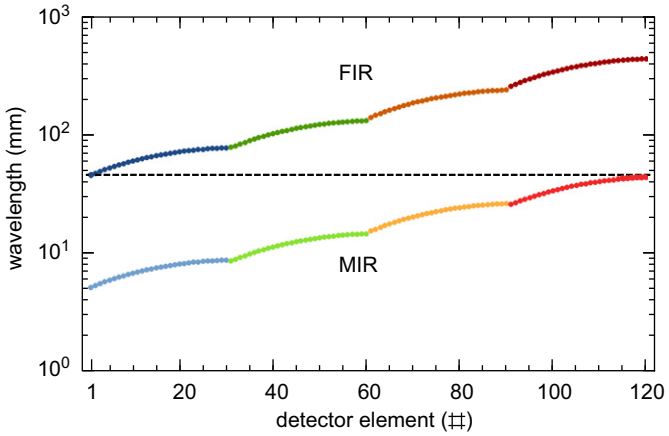


**Fig. 12.** Wavelength vs. detector number for the mid-infrared (MIR) and the far-infrared (FIR) configuration of the multi-channel spectrometer.

parallel detectors. The wavelength as a function of detector number is plotted in Fig. 12. The MIR spectrometer covers the wavelength range from 5.1 μm to 43.5 μm, the FIR spectrometer covers the range from 45.5 μm to 434.5 μm.

All 30 pyroelectric sensors have the same angular acceptance $\Delta\beta_1 = w/f$ where $w = 2$ mm is the width of the sensor and $f = 150$ mm the focal length of the ring mirror. However, the wavelength interval $\Delta\lambda$ subtended by a sensor depends strongly on its angular position. From Eq. (3) it follows with $m = 1$

$$\Delta\lambda = d \cos\beta_1 \cdot \Delta\beta_1 \tag{4}$$

hence $\Delta\lambda$ drops rapidly with increasing detector number since the angle $\beta_1$ grows from $\beta_1 = 27^\circ$ at detector 1 to $\beta_1 = 80^\circ$ at detector 30.

The complete electronics diagram is depicted in Fig. 13 where also the pulse shape at various stages can be seen. The commercial charge-sensitive preamplifier CR110 generates pulses with a rise time of 35 ns and a decay time of 140 μs. A Gaussian shaping amplifier (Cremat CR200 with 4 μs shaping time) is used to optimize the signal-to-noise ratio. This is adequate for the application at the CTR beamline [21] where the repetition rate is only 10 Hz. The shaped signals are digitized with 120 parallel ADCs with 9 MHz clock rate, 14-bit resolution and 50 MHz analog bandwidth. A fast version of the electronics with 250 ns shaping time, allowing 1 MHz repetition rate, is used for an identical spectrometer inside the FLASH tunnel. This system is presently being commissioned.

### 2.5. Spectrometer alignment and computed response function

Within each spectrometer stage the alignment of the grating, the ring mirror and the detector line array was done with a laser beam. The overall alignment of the spectrometer was carried out in situ with coherent transition radiation emerging from the CTR beamline [21] which will be described in the next section. For this purpose the vertical translation stages were moved to their mid-position (see Fig. 5). The two input alignment mirrors M1 and M2 (see Fig. 3) can be remotely adjusted in two orthogonal angles. Varying these four independent angles the radiation was centered on the pyroelectric sensors mounted on the G0-stage and the G4-stage.

The computed overall response function of the multi-channel spectrometer as installed at the CTR beamline is shown in Fig. 14. The power transmission of the beamline depends on the wavelength but in addition on the emission characteristics of the radiation source. A dedicated Mathematica code, *THzTransport*, was developed to model the generation of coherent transition radiation by an infinitely short electron bunch (longitudinal form

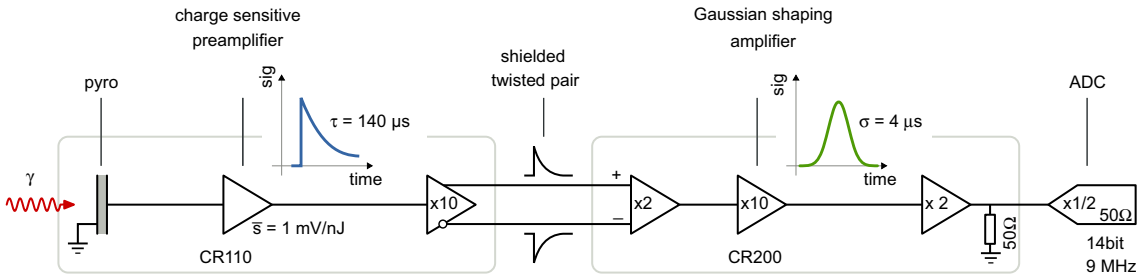


**Fig. 13.** Electronics diagram. The preamplifier and the twisted-pair line driver amplifier are mounted on the electronics board inside the vacuum vessel (see Fig. 8). Line receiver, Gaussian shaping amplifier and ADC are located outside the vacuum vessel.

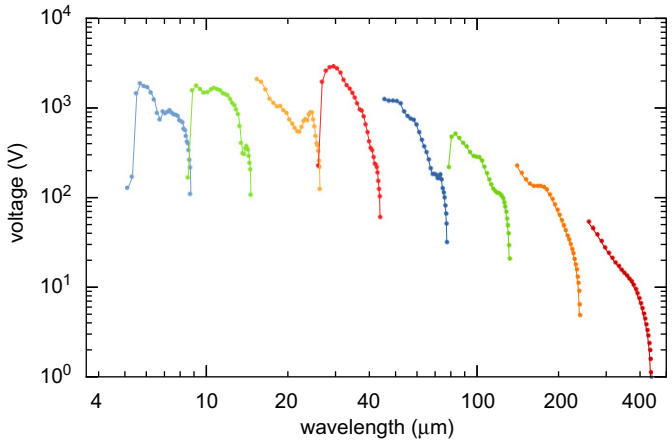


**Fig. 14.** Computed overall response function of the multi-channel spectrometer as installed at the CTR beamline at FLASH and the beam parameters given in the text. The expected voltage at the 14-bit ADCs is plotted as a function of wavelength. The sawtooth-like structure is caused by the variation of wavelength acceptance within each detector array, described by Eq. (4).

factor $F_\ell \equiv 1$) with an rms radius of $\sigma_r = 200$ µm and a charge of 1 nC. The same code was applied to simulated the transport of the radiation through the CTR beamline, taking near-field diffraction effects into account. A detailed description of the numerical procedures can be found in [21]. Additionally, the following wavelength-dependent effects were taken into consideration: transmission of the polarization filter, grating efficiencies (Fig. 2), pyroelectric detector sensitivity (Fig. 11), and wavelength acceptance $\Delta\lambda$ of the sensors as a function of grating constant $d$ and sensor number according to Eq. (4).

The Fourier transformation of an infinitely short electron bunch yields a flat frequency spectrum, and because of $\omega = 2\pi c/\lambda, d\omega = -2\pi c/\lambda^2\, d\lambda$, a wavelength spectrum proportional to $1/\lambda^2$. The angular distribution of transition radiation from a screen of finite size together with diffraction losses in the beam line and in the focusing of the radiation onto the small pyroelectric detectors contribute also to the drop of the spectral intensity towards large wavelengths. In the small-wavelength regime the response function levels off. This is due to the finite transverse electron beam size.

## 3. Commissioning of the spectrometer and benchmarking results

### 3.1. The FLASH facility

The soft X-ray FEL facility FLASH is schematically shown in Fig. 15. A detailed description of the design criteria and the layout can be found in [22,23], here we give only a short overview. The electron source is a laser-driven photocathode mounted in a 1.3 GHz copper cavity. The main components of the linear accelerator are seven 1.3 GHz superconducting acceleration modules (ACC1–ACC7) and two magnetic bunch compressors BC. The electron gun generates trains of electron bunches at a repetition rate of 10 Hz, each train comprising up to 800 bunches with a time spacing of 1 µs. The electron bunches leaving the gun have an energy of 4.5 MeV and an adjustable charge of 0.02–1.5 nC. The energy is boosted to about 150 MeV in module ACC1. The module is operated at an off-crest phase in order to induce an energy gradient along the bunch axis that is needed for longitudinal bunch compression in the magnetic chicanes. The recently installed third-harmonic cavity module M3 [24] linearizes the energy chirp and is essential for producing bunches of variable length. Modules ACC2 and ACC3 accelerate the electron bunches to about 450 MeV, and the final compression takes place in the second BC. The acceleration modules ACC4–ACC7 boost the energy up to a maximum of 1.2 GeV. The undulator magnet consists of six 4.5 m long segments. Two collimators in combination with a magnetic deflection protect the permanent magnets of the undulator against radiation damage by beam halo.

### 3.2. CTR beam line

To facilitate frequency domain experiments at FLASH, an ultra-broadband optical beamline for transition radiation (TR) was built which transports electromagnetic radiation ranging from 0.2 THz up to optical frequencies and permits spectroscopic measurements in a laboratory outside the accelerator tunnel [21]. The radiation is produced on an off-axis screen by single electron bunches that are picked out of the bunch train by a fast kicker magnet. The TR screen is a 350 µm thick polished silicon wafer with a 150 nm thick aluminium coating on the front surface. The screen is tilted by 45° with respect to the electron beam direction, hence the radiation is emitted perpendicular to the beam. It leaves the electron beam vacuum chamber through a 0.5 mm thick diamond window with diameter of 20 mm. The transmission is 71% (caused by reflection losses at the two surfaces) for wavelength between 400 nm and 3 mm, except for a narrow absorption band of diamond between 4 and 7 µm where the transmission drops down to 40%. The radiation is guided through a 20 m long evacuated beam line equipped with six focusing mirrors to a vacuum vessel outside the accelerator tunnel which houses the spectrometer or other diagnostic devices.

### 3.3. Test measurements with bunches of known shape

To verify the performance of the spectrometer, test measurements were carried out with bunches of different length and structure. The longitudinal profiles of the electron bunches were determined with high accuracy using the transverse deflecting microwave structure TDS mounted in front of the undulator (see

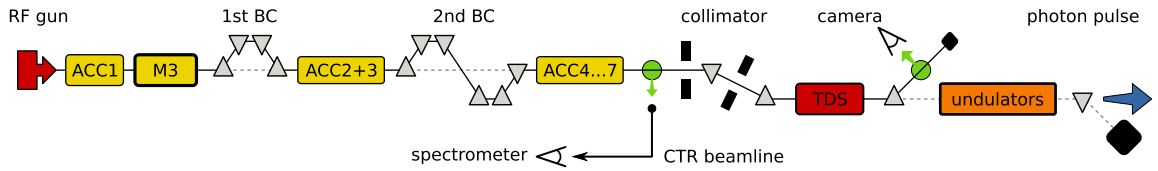


**Fig. 15.** Schematic layout of the free-electron laser FLASH. Shown are the components which are important for the present experiment: radio-frequency (RF) gun, the seven acceleration modules ACC1–ACC7, the third-harmonic cavity module M3, and the two magnetic bunch compressors BC. The transition radiation screen and the diamond window of the coherent transition radiation (CTR) beamline are installed behind ACC7. The radiation is guided to a spectrometer outside the accelerator tunnel. The transverse deflecting microwave structure TDS is mounted in front of the undulator magnets.

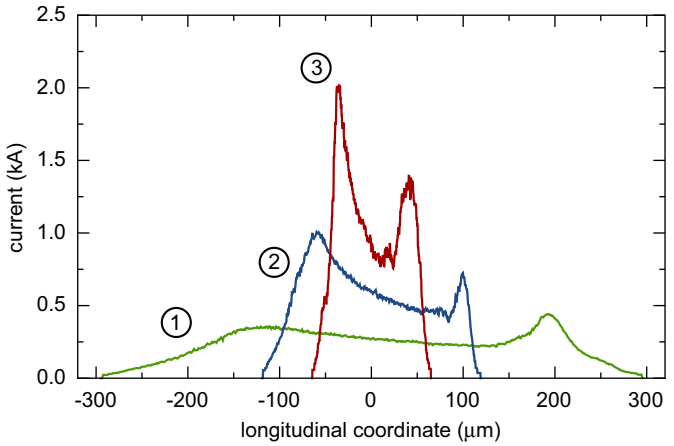


**Fig. 16.** Longitudinal profiles of three different electron bunch shapes in the FLASH linac as measured with the transverse deflecting microwave structure.

Fig. 15). Three different bunch shapes with total lengths between 100 and 400 μm were realized by a proper choice of the RF phases in the acceleration modules ACC2 and ACC3. To reduce statistical fluctuations, 40 bunches were recorded with the TDS setup for each shape. Two different sweep directions of the TDS were applied to minimize systematic errors in the determination of the longitudinal charge distribution.

The averaged longitudinal profiles are shown in Fig. 16. The form factors were computed by Fourier transformation of the averaged longitudinal profiles, Eq. (2). They are shown as solid curves in Fig. 17.

The rms time resolution of the TDS system depended on the total bunch length to be covered and varied between $\sigma_t = 27$ fs for the shortest bunches and $\sigma_t = 43$ fs for the longest ones. This finite time resolution of the TDS system leads to a suppression of the form factor towards small wavelengths. The suppression factor is $\exp(-\lambda_{\mathrm{cut}}^2/\lambda^2)$ with the "cutoff wavelength" $\lambda_{\mathrm{cut}} = \sqrt{2}\pi c\sigma_t$; here $c$ is the speed of light. For the three bunch shapes shown in Fig. 16, the cutoff wavelengths are 58, 40 and 36 μm, respectively.

For all three bunch shapes spectroscopic measurements were carried out on 200 bunches each. The form factors derived from the measured spectra are depicted as dotted curves in Fig. 17. For all three bunch shapes, there is an impressive overall agreement between the form factors derived by the two complementary methods. In the short-wavelength region below 20 μm the spectroscopically determined form factors are generally higher than the form factors derived from the TDS measurements. This is evidence for the presence of a fine structure which cannot be resolved by the TDS system in its present configuration. This is a convincing demonstration of the capabilities of the multi-channel spectrometer.

The importance of the single-shot capability of the spectrometer is demonstrated in Fig. 18. The spectroscopically determined form factors of two successive bunches, having nominally the same shape, exhibit both significant structures which however are shifted

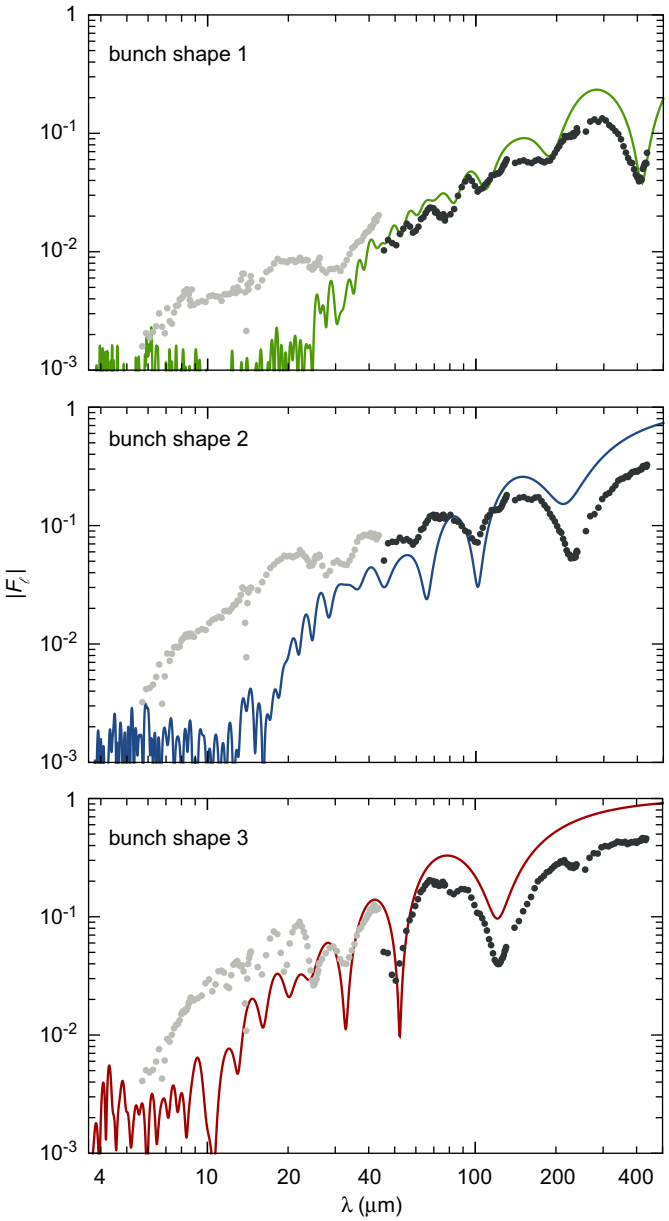


**Fig. 17.** The magnitude $|F_\ell(\lambda)|$ of the longitudinal form factors of the bunch shapes shown in Fig. 16. Solid curves: form factors computed by Fourier transformation from the TDS longitudinal bunch profiles. Dotted curves: form factors derived from the spectroscopic measurements (black dots: FIR configuration, gray dots: MIR configuration).

against each other. This shows that there exist substantial shot-to-shot fluctuations even if the accelerator parameters are kept as constant as technically feasible. Averaging over several bunches in either system will wash out many of the structural details. Hence a

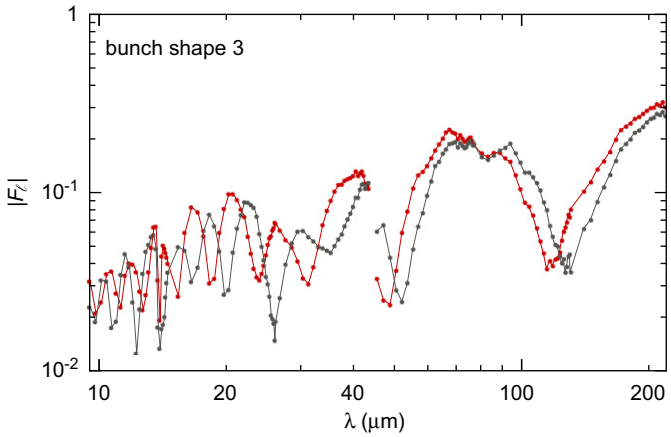


**Fig. 18.** The form factor $|F_\ell(\lambda)|$ of two successive bunches, derived from two single-shot spectroscopic measurements.

perfect agreement between TDS and spectrometer data cannot be expected. With our present setup at the FLASH linac it is not possible to measure exactly the same bunch with both instruments.

## 4. Summary

A multi-channel single-shot spectrometer for the THz and infrared range has been developed and successfully commissioned with coherent transition radiation from electron bunches of known shape. The spectrometer covers a factor of 10 in wavelength with parallel readout. With two sets of remotely interchangeable gratings the wavelength ranges from 5.1 to 43.5 μm and 45.3 to 434.5 μm can be analyzed. Very good agreement is found between the spectroscopic longitudinal bunch form factors and the form factors derived from time-domain measurements using a transverse deflecting microwave structure. This is a proof of the high performance of the broadband spectrometer.

The unique single-shot capability of the multi-channel spectrometer will allow to study and monitor electron bunch profiles in great detail and will help to control the bunch compression process in view of an optimized FEL performance of the facility.

## Acknowledgments

We thank our engineers Kai Ludwig (mechanical design) and Petr Smirnov (readout electronics) for their important contributions of the spectrometer. An essential accelerator component for the benchmarking to the spectrometer was the third-harmonic cavity module M3 which was constructed at Fermilab and commissioned at DESY under the leadership of Helen Edwards. We want to thank Helen Edwards for this important contribution to the present experiment and moreover for her careful reading of the manuscript and valuable comments.

## References

[1] I. Zagorodnov, M. Dohlus, Physical Review Special Topics—Accelerators and Beams 14 (2011) 014403.
[2] O.H. Altenmueller, R. Larsen, G.A. Loew, Review of Scientific Instruments 35 (1964) 438.
[3] M. Hüning, et al., Proceedings of the Free Electron Laser Conference 2005, Stanford, USA, 2005, pp. 538–540.
[4] M. Röhrs, et al., Physical Review Special Topics—Accelerators and Beams 12 (2009) 050704.
[5] I. Wilke, et al., Physical Review Letters 88 (2002) 124801.
[6] G. Berden, et al., Physical Review Letters 93 (2004) 114802.
[7] A.L. Cavalieri, et al., Physical Review Letters 94 (2005) 114801.
[8] G. Berden, et al., Physical Review Letters 99 (2007) 164801.
[9] R. Lai, A.J. Sievers, Nuclear Instruments and Methods in Physics Research Section A 397 (1997) 221.
[10] R. Lai, U. Happek, A.J. Sievers, Physical Review E 50 (1994) 4294.
[11] A. Murokh, et al., Nuclear Instruments and Methods in Physics Research Section A 410 (1998) 452.
[12] M. Geitz, et al., Proceedings of the Particle Accelerators Conference 1999, New York, USA, 1999, pp. 2172–2174.
[13] L. Fröhlich, O. Grimm, Proceedings of the Free Electron Laser Conference 2005, Standford, USA, 2005, pp. 114–117.
[14] P. Evtushenko, et al., Proceedings of the Beam Instrumentation Workshop 2006, Batavia, AIP Conference Proceedings, vol. 868, 2006, pp. 193–201.
[15] R. Thurman-Keup, et al., Proceedings of the Beam Instrumentation Workshop 2008, Tahoe City, USA, 2008, pp. 153–157.
[16] T. Watanabe, et al., Nuclear Instruments and Methods in Physics Research Section A 480 (2002) 315.
[17] H. Delsim-Hashemi, Infrared Single-Shot Diagnostics for the Longitudinal Profile of the Electron Bunches at FLASH, Ph.D. Thesis, University of Hamburg, Report DESY-THESIS-2008-024, 2008.
[18] C. Palmer, E. Loewen, Diffraction Grating Handbook, sixth ed., Newport Corporation, 2005.
[19] C. Behrens, Detection and Spectral Measurements of Coherent Synchrotron Radiation at FLASH, Diploma Thesis, University of Hamburg, Report DESY-THESIS-2010-02, 2008.
[20] D. Oepts, A.F.G. van der Meer, P.W. van Amersfoort, Infrared Physics and Technology 36 (1995) 297.
[21] S. Casalbuoni, et al., Physical Review Special Topics—Accelerators and Beams 12 (2009) 030705.
[22] P. Schmüser, M. Dohlus, J. Rossbach, Ultraviolet and soft X-ray free-electron lasers. in: Springer Tracts in Modern Physics, vol. 229, Springer, 2008.
[23] S. Schreiber, et al., Proceedings of the Free Electron Laser Conference 2010, Malmö, Sweden, 2010, pp. 198–201.
[24] H. Edwards, C. Behrens, E. Harms, Proceedings of the Linear Accelerators Conference 2010, Tsukuba, Japan, 2010, pp. 41–45.

# 4 Longitudinal phase space control for electron beams

High-gain X-ray free-electron lasers are driven by electron beams with high peak currents and low energy spreads (see Sec. 2.2), i.e., with a high longitudinal brightness $\sim \mathcal{I}_e/\sigma_\eta$ (see, e.g., Ref. [50]), which describes the electron density in the longitudinal phase space. In the following, the longitudinal phase space is expressed via $(z, \delta)$, where $z$ is the internal electron bunch length coordinate and $\delta$ is the relative momentum (energy) deviation. This representation is independent of any resonant electromagnetic wave, hence the notation $(\psi, \eta)$ is only used for describing FEL dynamics as is discussed in Sec. 2.1. In the relativistic limit with $\gamma \gg 1$, the longitudinal brightness is invariant under compression [50], and the latter can only be achieved by making use of the energy-dependent path lengths of chirped electron bunches ($d\delta/dz \neq 0$) in a magnetic chicane. Thus, higher peak currents and corresponding shorter bunches result in larger energy spreads and chirps. Optimization of these parameters requires accurate diagnosis and precise control of the longitudinal phase space.

The longitudinal compression of high-brightness electron beams in magnetic chicanes is accompanied by several collective beam effects, e.g., coherent synchrotron radiation or microbunching instabilities (e.g., Refs. [67, 68, 81]), which do not only lead to coherent optical radiation effects, impeding electron beam diagnostics (see Sec. 3.1), but furthermore to degradation of the electron beam brightness and finally to significant deterioration of the FEL performance [73]. Longitudinal phase space control in terms of optimized bunch compression schemes (e.g., Refs. [82, 83]) or by introducing additional beam energy spread, i.e., "heating" the electron beam [71, 72], can effectively suppress microbunching instabilities.

In the following, two articles in the research field of longitudinal phase space control for electron beams are introduced and presented. The first article deals with the generation and characterization of electron bunches with ramped current profiles in a dual-frequency superconducting linear accelerator and has been published in *Physical Review Letters*. The second article describes reversible electron beam heating for suppression of microbunching instabilities at free-electron lasers and has been published in *Phys. Rev. ST Accel. Beams*.

## 4.1 Generation and characterization of electron bunches with ramped current profiles in a dual-frequency superconducting linear accelerator

The characteristics of the radiation pules generated by X-ray free-electron lasers, e.g., temporal profile, wavelength spectrum, or frequency chirp, are generally affected by the characteristics of the longitudinal phase space $(z, \delta)$ of the FEL driving electron beams. The corresponding temporal profile and energy spectrum of the electron beams are given by the one-dimensional projections of the longitudinal phase space onto the time ($t = -z/c$) and energy axis ($\sim \delta$), respectively, while the energy chirp is given by the correlation between them. The longitudinal phase space at X-ray FELs is determined by the r.f. fields of the driving linear accelerator, hence the simultaneous operation with higher harmonic r.f. frequencies is supposed to enable tailoring of the longitudinal phase space [84]. As reported in Refs. [62, 85, 86], uniform bunch compression at X-ray FELs can be achieved by linearization of the longitudinal phase space using higher harmonic r.f. frequencies. However, in order to take full advantage of multi-frequency linear accelerators, dedicated longitudinal phase space diagnostics with high time and energy resolution are required (e.g., Refs. [87, 88]).

In addition to the practical importance for the operation of X-ray FELs, the longitudinal phase space control for electron beams has applications in advanced acceleration techniques such as beam-driven wakefield acceleration (e.g., Refs. [89, 90, 91]) in a plasma or in high-impedance structures, e.g., dielectric-lined waveguides. It is worth pointing out that advanced acceleration techniques have prospects for affordable, more compact X-ray FELs for photon science and next-generation lepton colliders for particle physics. In beam-driven wakefield acceleration experiments, the control of the longitudinal phase space of electron beams can be utilized to enhance the efficiency of the energy transfer between a drive bunch, exciting a wakefield, and a trailing witness bunch, being accelerated in the wakefield. The efficiency of this energy transfer can be expressed by means of the so-called transformer ratio (e.g., Refs. [92, 93]). Tailoring of the longitudinal phase space by using higher harmonic r.f. frequencies in dual-frequency linear accelerators allows the generation of electron bunches with ramped current profiles, demonstrating the potential of high accelerating wakefields and unprecedentedly large transformer ratios (e.g., Refs. [94, 95]).

The following article reports on the generation of electron bunches with ramped current profiles relevant for wakefield acceleration experiments. The ramped current profiles have been generated by means of longitudinal phase space tailoring, and the same methods can be applied for X-ray FELs in order to control temporal bunch profiles and energy chirps.

# Generation and Characterization of Electron Bunches with Ramped Current Profiles in a Dual-Frequency Superconducting Linear Accelerator

P. Piot,[1,2] C. Behrens,[3] C. Gerth,[3] M. Dohlus,[3] F. Lemery,[1] D. Mihalcea,[1] P. Stoltz,[4] and M. Vogt[3]

[1]*Northern Illinois Center for Accelerator & Detector Development and Department of Physics, Northern Illinois University, DeKalb, Illinois 60115, USA*

[2]*Accelerator Physics Center, Fermi National Accelerator Laboratory, Batavia, Illinois 60510, USA*

[3]*Deutsches Elektronen-Synchrotron DESY, Notkestraße 85 D-22607 Hamburg, Germany*

[4]*Tech-X Corporation, Boulder, Colorado 80303, USA*

(Received 7 September 2011; published 18 January 2012)

We report on the successful experimental generation of electron bunches with ramped current profiles. The technique relies on impressing nonlinear correlations in the longitudinal phase space using a superconducing radio frequency linear accelerator operating at two frequencies and a current-enhancing dispersive section. The produced ~700-MeV bunches have peak currents of the order of a kilo-Ampère. Data taken for various accelerator settings demonstrate the versatility of the method and, in particular, its ability to produce current profiles that have a quasilinear dependency on the longitudinal (temporal) coordinate. The measured bunch parameters are shown, via numerical simulations, to produce gigavolt-per-meter peak accelerating electric fields with transformer ratios larger than 2 in dielectric-lined waveguides.

DOI: 10.1103/PhysRevLett.108.034801 PACS numbers: 29.27.−a, 41.75.Fr, 41.85.−p

Electron acceleration is a rapidly advancing field of scientific research with widespread applications in industry and medicine. Producing and accelerating high-quality electron bunches within very compact footprints is a challenging task that will most probably use advanced acceleration methods. These techniques can be categorized into laser-driven [1–3] and charged-particle-beam-driven methods [4–7]. In the latter scheme, a popular configuration consists of a ''drive'' electron bunch with suitable parameters propagating through a high-impedance structure or plasma medium thereby inducing an electromagnetic wake. A following ''witness'' electron bunch, properly delayed, can be accelerated by these wakefields.

Collinear beam-driven acceleration techniques have demonstrated accelerating fields in excess of GV/m [8,9]. The fundamental wakefield theorem [10] limits the transformer ratio—the maximum accelerating wakefield over the decelerating field experienced by the driving bunch—to 2 for bunches with symmetric current profiles. Tailored bunches with asymmetric, e.g., a linearly ramped, current profiles can lead to transformer ratio $>2$ [11]. To date, there has been a small number of techniques capable of producing linearly ramped electron bunches. A successful experiment demonstrated the production of 50-A ramped electron bunches using sextupole magnets located in a dispersive section [12] to impart nonlinear correlation in the longitudinal phase space (LPS) [13]. Unfortunately, the method introduces coupling between the longitudinal and transverse degrees of freedom which ultimately affects the transverse brightness of the drive and witness bunches.

In this Letter we present an alternative technique that uses a radio frequency (rf) linear accelerator (linac) operating at two frequencies. It has long been recognized that linacs operating at multiple frequencies [14,15] or nonrelativistic compression schemes [16] could be used to correct for LPS distortions and improve the final peak current. We show analytically and demonstrate experimentally how a two-frequency linac could be operated to tailor the nonlinear correlations in the LPS thereby providing control over the current profile.

We first elaborate the proposed method using a 1D-1V single-particle model of the LPS dynamics and take an electron with coordinates $(z, \delta)$ where $z$ refers to the longitudinal position of the electron with respect to the bunch barycenter (in our convention $z > 0$ corresponds to the head of the bunch) and $\delta \equiv p/\langle p\rangle - 1$ is the fractional momentum error ($p$ is the electron's momentum and $\langle p\rangle$ the average momentum of the bunch). Considering a photoemission electron source, the LPS coordinates downstream are $(z_0, \delta_0 = a_0 z_0 + b_0 z_0^2 + \mathcal{O}(z_0^3))$ where $a_0$, and $b_0$ are constants that depend on the bunch charge and operating parameters of the electron source. For sake of simplicity we limit our model to second order in $z_0$ and $\delta_0$. Next, we examine the acceleration through a linac operating at the frequencies $f_1$ and $f_n \equiv nf_1$ with total accelerating voltage $V(z) = V_1 \cos(k_1 z + \varphi_1) + V_n \cos(k_n z + \varphi_n)$ where $V_{1,n}$ and $\varphi_{1,n}$ are, respectively, the accelerating voltages and operating phases of the two linac sections, and $k_{1,n} \equiv 2\pi f_{1,n}/c$. In our convention, when the phases between the linac sections and the electron bunch are $\varphi_{1,n} = 0$ the bunch energy gain is maximum (this is refer to as on-crest operation). Under the assumption $k_{1,n} z_0 \ll 1$ and neglecting nonrelativistic effects, the electron's LPS coordinate downstream of the linac are $(z_l = z_0,$

 

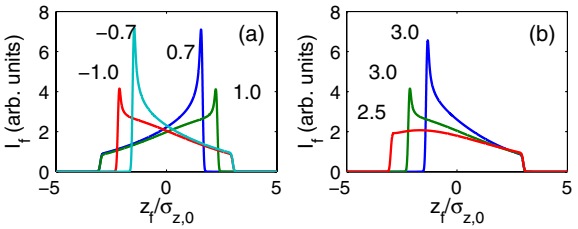


FIG. 1 (color online). Analytically computed current profiles for several values of $b_f$ for fixed $a_f = 2.5$ (a) and for several values of $a_f$ with $b_f = 0.7$ (b) The numbers in (a) [(b)] are the values of $b_f$ [$a_f$]; for all the cases $\sigma_u = 0.05$.

$\delta_l = a_l z_0 + b_l z_0^2$) where $a_l \equiv a_0 - e(k_1 V_1 \sin\varphi_1 + k_n V_n \times \sin\varphi_n)/\bar{E}_l$, $b_l \equiv b_0 - e(k_1^2 V_1 \cos\varphi_1 + k_n^2 V_n \cos\varphi_n)/(2\bar{E}_l)$ with $e$ being the electronic charge and $\bar{E}_l$ the beam's average energy downstream of the linac. Finally, we study the passage of the bunch through an achromatic current-enhancing dispersive section [henceforth referred to as "bunch compressor" (BC)]. The LPS dynamics through a BC is approximated by the transformation $z_f = R_{56}\delta_l + T_{566}\delta_l^2$ where $R_{56}$ (also referred to as longitudinal dispersion), and $T_{566}$ are the coefficients of the Taylor expansion of the transfer map $\langle z_f|\delta_l\rangle$ of the BC. Therefore, the final position is given as function of the initial coordinates following $z_f = a_f z_0 + b_f z_0^2$ with $a_f \equiv 1 + a_l R_{56}$ and $b_f \equiv b_l R_{56} + a_l^2 T_{566}$. Taking the initial current to follow the Gaussian distribution $I_0(z_0) = \hat{I}_0 \exp[-z_0^2/(2\sigma_{z,0}^2)]$ (where $\hat{I}_0$ is the initial peak current), and invoking the charge conservation $I_f(z_f)dz_f = I_0(z_0)dz_0$ gives the final current distribution $I_f^u(z_f) = \hat{I}_0/\Delta^{1/2}(z_f)\exp[-(a_f + \Delta^{1/2}(z_f))^2/(8b_f^2\sigma_{z,0}^2)]\Theta[\Delta(z_f)]$ where $\Delta(z_f) \equiv a_f^2 + 4b_f z_f$ and $\Theta()$ is the Heaviside function. The latter current distribution does not include the effect of the initial uncorrelated fractional momentum spread $\sigma_{\delta,0}^u$. The final current, taking into account $\sigma_{\delta,0}^u$, is given by the convolution $I_f(z_f) = \int d\tilde{z}_f I_f^u(\tilde{z}_f)\exp[-(z_f - \tilde{z}_f)^2/(2\sigma_u^2)]$ where $\sigma_u \equiv R_{56}\sigma_{\delta,0}^u$. The final current shape is controlled via $a_f$ and $b_f$ and can be tailored to follow a linear ramp as demonstrated in Fig. 1.

The experiment described in this Letter was performed at the Free-electron LASer in Hamburg (FLASH) facility [17]. In the FLASH accelerator, diagrammed in Fig. 2, the electron bunches are generated via photoemission from a cesium telluride photocathode located on the back plate of a $1 + 1/2$ cell normal-conducting rf cavity operating at 1.3 GHz on the $TM_{010}$ $\pi$ mode (rf gun). The bunch is then accelerated in a 1.3-and 3.9-GHz superconducting accelerating modules (respectively ACC1 and ACC39) before passing through a bunch compressor (BC1). The ACC39 3rd-harmonic module was installed to nominally correct for nonlinear distortions in the LPS and enhance the final peak current of the electron bunch [18]. Downstream of BC1, the bunch is accelerated and can be


FIG. 2 (color online). Diagram of the FLASH facility. Only components affecting the longitudinal phase space beam (LPS) dynamics of the bunches are shown. The acronyms ACC, BC, and DBL stand, respectively, for accelerating modules, bunch compressors, and dogleg beam line (the blue rectangles represent dipole magnets). The transverse deflecting structure (TDS), spectrometer and Ce:YAG screen compose the LPS diagnostics.

further compressed in BC2. A last acceleration stage (ACC4/5/6/7) brings the beam to its final energy (maximum of ~1.2 GeV). The beam's direction is then horizontally translated using a dispersionless section referred to as dog-leg beam line (DLB). Nominally, the beam is sent to a string of undulators to produce ultraviolet light via the self-amplified stimulated emission free-electron laser (FEL) process. For our experiment, the bunches were instead vertically sheared by a 2.856-GHz transverse deflecting structure (TDS) operating on the $TM_{110}$-like mode and horizontally bent by a downstream spectrometer [19]. Consequently, the transverse density measured on the downstream cerium-doped yttrium aluminum garnet (Ce:YAG) scintillating screen is representative of the LPS density distribution. The horizontal and vertical coordinates at the Ce:YAG screen are respectively $x_s \simeq \eta\delta_F$, where $\eta \simeq 0.75$ m is the horizontal dispersion function, and $y_s \simeq \kappa z_F$ where $\kappa \simeq 20$ is the vertical shearing factor and $(z_F, \delta_F)$ refers to the LPS coordinate upstream of the TDS. The exact values of $\eta$ and $\kappa$ are experimentally determined via a beam-based calibration procedure.

The accelerator parameters settings are gathered in Table I. The nominal settings of BC2 were altered to reduce its longitudinal dispersion $R_{56}^{(2)}$ and the ACC2/3 and ACC4/5/6/7 accelerating modules were operated on crest. Such settings insure that the BC2 and the DBL

TABLE I. Settings of accelerator subsystems relevant to the LPS dynamics used in the experiment and simulations.

| parameter | symbol | value | unit |
|---|---|---|---|
| ACC1 voltage | $V_1$ | [140–157] | MV |
| ACC1 phase | $\varphi_1$ | [ − 10, 10] | deg |
| ACC39 voltage | $V_3$ | [13, 21] | MV |
| ACC39 phase | $\varphi_3$ | [160–180] | deg |
| ACC2/3 voltage | $V_{1,2-3}$ | 311 | MV |
| ACC2/3 phase | $\varphi_{1,2-3}$ | 0 | deg |
| ACC4/5/6/7 voltage | $V_{1,4-7}$ | 233.9 | MV |
| ACC4/5/6/7 phase | $\varphi_{1,4-7}$ | 0 | deg |
| BC1 longitudinal dispersion | $R_{56}^{(1)}$ | ~170 | mm |
| BC2 longitudinal dispersion | $R_{56}^{(2)}$ | ~15 | mm |
| Single-bunch charge | $Q$ | 0.5 | nC |
| Bunch energy | $E$ | ~690 | MeV |

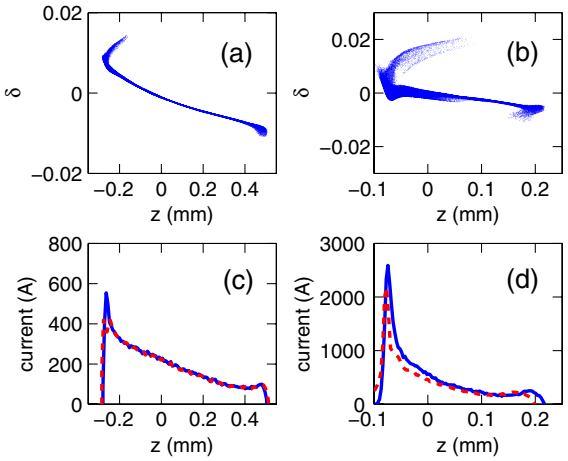


FIG. 3 (color online). Simulated LPS distribution [(a) and (b)] with associated current profile downstream of BC1 (solid blue trace) and DBL (dash red trace) [(c) and (d)]. The set of plots [(a),(c)] and [(b),(d)] correspond to different ($V_{1,3}$, $\varphi_{1,3}$) settings.

sections do not significantly affect the LPS beam dynamics. Therefore the measured current profile is representative of the profile downstream of BC1.

In order to validate the simple analytical model described above, numerical simulations of the LPS beam dynamics were carried using a multiparticle model. The simulations also enable the investigation of possible detrimental effects resulting from collective effects such as longitudinal space charge (LSC) and beam self interaction via coherent synchrotron radiation (CSR) [20]. In these simulations, the beam dynamics in the rf gun was modeled with the particle-in-cell program ASTRA [21] and the obtained distribution was subsequently tracked in the accelerating modules using a 1D-1V program that incorporates a one-dimensional model of the LSC. The program CSRTRACK [22], which self-consistently simulates CSR effects, was used to model the beam dynamics in the BC1, and BC2 sections. An example of simulated LPS distributions and associated current profiles computed for different settings of ACC1 and ACC39 parameters appear in Fig. 3. The results indicate that the production of ramped bunches is possible despite the intricate LPS structures developing due to the collective effects and higher-order nonlinear effects not included in our analytical model. The simulations also confirm that the current profile upstream of the TDS (as measured by the LPS diagnostics) is representative of the one downstream of BC1.

Figure 4 displays examples of measured LPS distributions with associated current profiles obtained for different settings of ACC1 and ACC39. As predicted, the observed current profiles are asymmetric and can be tailored to be ramped with the head of the bunch ($z > 0$) having less charge than the tail; see Figs. 4(b)–4(d). The latter feature is in contrast with the nominal compression case

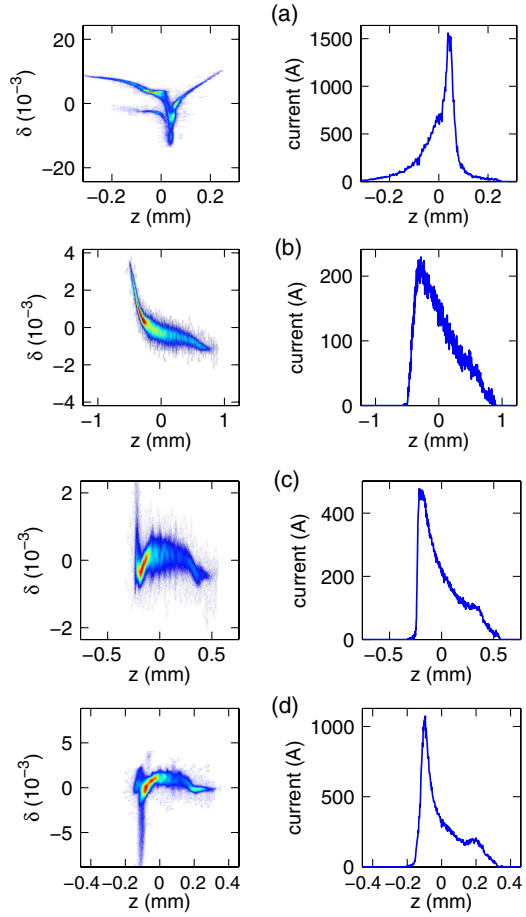


FIG. 4 (color online). Snapshots of the measured longitudinal phase spaces (left column) and associated current profiles (right column) for different settings of the ACC1 and ACC39 accelerating modules. The values ($V_1$, $\varphi_1$, $V_3$, $\varphi_3$) [in (MV,°; MV,°)] are: (150.5, 6.1; 20.7, 3.8), (156.7, 3.8; 20.8, 168.2), (155.6, 3.6; 20.6, 166.7), and (156.8, 4.3; 20.7, 167.7) for, respectively, case (a),(b),(c), and (d).

at FLASH where the LPS distortion usually results in a low-charge trailing population as seen in Fig. 4(a).

We now quantify the performance of the produced current profiles to enhance beam-driven acceleration techniques by considering a drive bunch injected in a cylindrical-symmetric dielectric-lined waveguide (DLW)

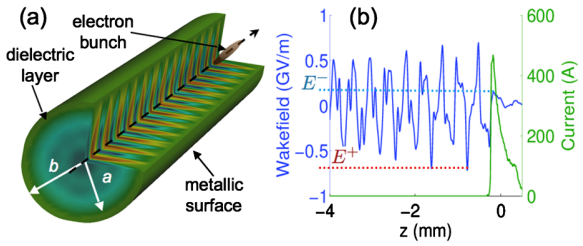


FIG. 5 (color online). Cylindrical-symmetric dielectric-loaded waveguide considered (a) and axial wakefield produced by the current profile shown in Fig. 4(c) for $(a, b) = (20, 60)$ $\mu$m.

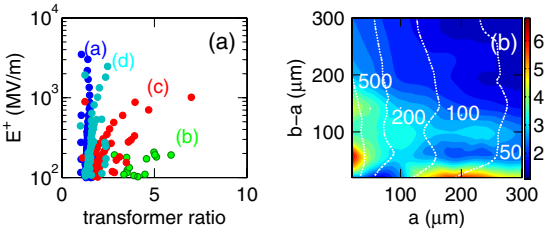


FIG. 6 (color online). Simulated transformer ratio versus peak accelerating field (a) for the four measured current profiles (displayed as different colors with label corresponding to cases shown in Fig. 4). Transformer ratio (false color map) as a function of the DLW inner radius $a$ and dielectric layer thickness $b - a$ with corresponding $|E^+|$ shown as isoclines with values quoted in MV/m for case (c) of Fig. 4.

[6]. The DLW consists of a hollow dielectric cylinder with inner and outer radii $a$ and $b$. The cylinder is taken to be diamond (relative electric permittivity $\epsilon_r = 5.7$); and its outer surface is contacted with a perfect conductor; see Fig. 5(a). The measured current profiles are numerically convolved with the Green's function associated to the monopole mode to yield the axial electric field [23]. These semianalytical calculations were benchmarked against finite-difference time-domain electromagnetic simulations executed with VORPAL [24]. The transformer ratio is numerically inferred as $\mathcal{R} \equiv |E_+/E_-|$ where $E_-$ ($E_+$) is the decelerating (accelerating) axial electric field within (behind) the electron bunch; see Fig. 5(b). The achieved $\mathcal{R}$ and $E_+$ values as the structure geometry is varied are shown in Fig. 6. As $a \in [20, 300]$ $\mu$m and $b \in a + [20, 300]$ $\mu$m are varied the wavelengths of the excited wakefield modes change. The simulations show that profiles (b) and (c) of Fig. 4 can yield values of $\mathcal{R} > 2$. A possible configuration with $(a, b) = (20, 60)$ $\mu$m, results in $\mathcal{R} \simeq 5.8$ with $E^+ \simeq 0.75$ GV/m; see corresponding wake in Fig. 5(b). Such a high field with transformer ratio significantly higher than 2 and driven by bunches produced in a superconducting linac could pave the way toward compact high-repetition-rate short-wavelength FELs [25].

Finally, the proposed technique could be adapted to non-ultra-relativistic energies using a two- (or multi-) frequency version of the velocity-bunching scheme [26]. Such an implementation would circumvent the use of a BC and would therefore be immune to CSR effects.

In summary, we proposed and experimentally demonstrated a simple method for shaping the current profile of relativistic electron bunches. The technique could be further refined by, e.g., including several harmonic frequencies.

We are thankful to the FLASH team for the excellent technical support. We thank K. Flöttmann, T. Limberg, I. Zagorodnov, E. Vogel, S. Wesch, H. Edwards, B. Faatz, K. Honkavaara, and S. Schreiber for discussions and support. This work was sponsored by the DTRA Grant HDTRA1-10-1-0051 to Northern Illinois University, the German's Bundesministerium für Bildung und Forschung and by the DOE contract DE-AC02-07CH11359 to the Fermi research alliance LLC.

[1] T. Tajima and J.M. Dawson, Phys. Rev. Lett. **43**, 267 (1979).
[2] W. Leemann *et al.*, Nature Phys. **2**, 696 (2006).
[3] C. Varin, M. Piche, and M. A. Porras, Phys. Rev. E **71**, 026603 (2005).
[4] P. Chen, J. M. Dawson, Robert W. Huff, and T. Katsouleas, Phys. Rev. Lett. **54**, 693 (1985).
[5] G. A. Voss and T. Weiland, DESY Hamburg, Report No. DESY-M-82-10 1982.
[6] W. Gai, P. Schoessow, B. Cole, R. Konecny, J. Norem, J. Rosenzweig, and J. Simpson, Phys. Rev. Lett. **61**, 2756 (1988).
[7] A. Caldwell, K. Lotov, A. Pukhov, and F. Simon, Nature Phys. **5**, 363 (2009).
[8] I. Blumenfeld *et al.*, Nature (London) **445**, 741 (2007).
[9] M. C. Thompson *et al.*, Phys. Rev. Lett. **100**, 214801 (2008).
[10] R. D. Ruth, A. Chao, P. L. Morton, and P. B. Wilson, Part. Accel. **17**, 171 (1985).
[11] K. L. F. Bane, P. Chen, and P. B. Wilson, Report No. SLAC-PUB-3662, 1985.
[12] R. J. England, J. B. Rosenzweig, and G. Travish, Phys. Rev. Lett. **100**, 214802 (2008).
[13] P. Piot, D. R. Douglas, and G. A. Krafft, Phys. Rev. ST Accel. Beams **6**, 030702 (2003).
[14] T. Smith, in *Proceedings of the 1984 Linear Accelerator Conference(LINAC'84), SLAC Report* (1986), Vol. 303, p. 421.
[15] D. H. Dowell, J. L. Adamski, T. D. Hayward, C. G. Parazzoli, and A. M. Vetter, Nucl. Instrum. Methods Phys. Res., Sect. A **375**, 108 (1996).
[16] G. A. Krafft, *Proc. Microbunches Workshop, AIP Conf. Proc.* (1996), Vol. 367, p. 46.
[17] W. Ackermann *et al.*, Nature Photon. **1**, 336 (2007).
[18] K. Flöttmann, T. L. Limberg, and P. Piot, DESY Report No. TESLA-FEL 2001-06, 2001.
[19] C. Behrens and C. Gerth, in *Proceedings of the 2010 Free-Electron Laser Conference (FEL10) Malmö* (Sweden, 2010), p. 133.
[20] E. Saldin, E. Schneidmiller, and M. Yurkov, Nucl. Instrum. Methods Phys. Res., Sect. A **398**, 373 (1997).
[21] K. Flöttmann, ASTRA: A Space Charge Algorithm, User's Manual (unpublished).
[22] M. Dohlus, T. L. Limberg, in *Proceedings of the 2004 Free-electron Laser Conference (FEL04) Triestre* (Italy, 2004), p. 18
[23] M. Rosing and W. Gai, Phys. Rev. D **42**, 1829 (1990).
[24] C. Nieter and J. R. Carry, J. Comput. Phys. **196**, 448 (2004).
[25] C. Jing, J. G. Power, and S. Zholents, "Dielectric wakefield accelerator to drive the future FEL light source", Argonne APS note ANL/APS/LS-326 (2011).
[26] M. Ferrario and L. Serafini, AIP Conf. Proc. **581**, 87 (2001).

## 4.2 Reversible electron beam heating for suppression of microbunching instabilities at free-electron lasers

The required high transverse and longitudinal brightness of the electron beams at X-ray free-electron lasers (see Sec. 2.2) are subject to various degradation effects, e.g., coherent synchrotron radiation or space charge forces, and need to be preserved during the beam transport up to the undulators. Repulsive, transverse space charge forces inside the electron bunches, scaling with $\sim \mathcal{I}_e/\gamma^2$ (see, e.g., Refs. [29, 52]), may lead to a transverse beam blow-up with a corresponding increase of the transverse emittances. Thus, in order to maintain the small transverse beam emittances provided by so-called r.f. injectors (e.g., Refs. [62, 96, 97]), the high electron bunch peak currents $\mathcal{I}_e$ required to drive an X-ray FEL are achieved by bunch compression in magnetic chicanes at relativistic energies with $\gamma \gg 1$ (e.g., Ref. [83]). However, the compression of high-brightness electron beams in magnetic chicanes comes along with microbunching instabilities (e.g., Refs. [67, 68]), which can also degrade the beam brightness significantly and may lead to coherent optical radiation effects (see Sec. 3.1).

Microbunching instabilities associated with the bunch compression in magnetic chicanes can be suppressed by introducing additional uncorrelated energy spread within the electron bunches (so-called slice energy spread) prior to the compression [68, 71]. The slice energy spread of electron bunches can be effectively increased, i.e., "heated", by making use of the resonant interaction of electrons with an optical quantum laser in a small undulator (cf. Sec. 2.1), as has been demonstrated by the laser heater system at the LCLS [71, 73]. However, the laser heater irreversibly increases the energy spread and needs to be limited in order to keep the FEL performance [see Eq. (2.33)]. The amount of tolerable electron beam heating is particularly critical for future FELs seeded with external radiation fields (e.g., Ref. [98]).

A different approach to increase the slice energy spread utilizes the characteristics of transverse deflecting r.f. structures (TDSs), which are based on the Panofsky-Wenzel theorem [99]. According to this theorem, the time-dependent transverse kicks of a TDS (cf. Sec. 3.1) are fundamentally related to an additional energy spread induced by the TDS operation [100, 101, 102]. The energy spread induced by a TDS is correlated with the transverse offsets inside the TDS during the passage, hence the effect of an induced energy spread is reversible and can be eliminated by a second TDS [103, 104]. A scheme of two TDSs upstream and downstream of a magnetic chicane thus allows electron beam heating for suppression of microbunching instabilities and simultaneous preservation of the slice energy spread.

The following article reports on the reversible electron beam heating for suppression of microbunching instabilities at FELs. This advanced TDS heater concept includes the preservation of the initial electron beam brightness and is thus particularly suited for seeded FELs.

# Reversible electron beam heating for suppression of microbunching instabilities at free-electron lasers

Christopher Behrens,[1,*] Zhirong Huang,[2] and Dao Xiang[2]
[1]*Deutsches Elektronen-Synchrotron DESY, Notkestraße 85, 22607 Hamburg, Germany*
[2]*SLAC National Accelerator Laboratory, Menlo Park, California 94025, USA*
(Received 18 November 2011; published 6 February 2012; corrected 15 June 2012)

The presence of microbunching instabilities due to the compression of high-brightness electron beams at existing and future x-ray free-electron lasers (FELs) results in restrictions on the attainable lasing performance and renders beam imaging with optical transition radiation impossible. The instability can be suppressed by introducing additional energy spread, i.e., heating the electron beam, as demonstrated by the successful operation of the laser heater system at the Linac Coherent Light Source. The increased energy spread is typically tolerable for self-amplified spontaneous emission FELs but limits the effectiveness of advanced FEL schemes such as seeding. In this paper, we present a reversible electron beam heating system based on two transverse deflecting radio-frequency structures (TDSs) upstream and downstream of a magnetic bunch compressor chicane. The additional energy spread is introduced in the first TDS, which suppresses the microbunching instability, and then is eliminated in the second TDS. We show the feasibility of the microbunching gain suppression based on calculations and simulations including the effects of coherent synchrotron radiation. Acceptable electron beam and radio-frequency jitter are identified, and inherent options for diagnostics and on-line monitoring of the electron beam's longitudinal phase space are discussed.

DOI: 10.1103/PhysRevSTAB.15.022802 PACS numbers: 29.27.−a, 41.60.Cr, 41.85.Ct

## I. INTRODUCTION

X-ray free-electron lasers (FELs) provide an outstanding tool for studying matter at ultrafast time and atomic length scales [1], and have become a reality with the operation of the Free-Electron Laser in Hamburg (FLASH) [2], the Linac Coherent Light Source (LCLS) [3], and the SPring-8 Angstrom Compact Free Electron Laser (SACLA) [4]. The required high transverse and longitudinal brightness of the x-ray FEL driving electron bunches may encounter various degradation effects due to collective effects like coherent synchrotron radiation (CSR) or microbunching instabilities (e.g., Refs. [5–7]), and need to be preserved and controlled. In order to suppress a microbunching instability associated with longitudinal bunch compression that deteriorates the FEL performance, the LCLS uses a laser heater system to irreversibly increase the uncorrelated energy spread within the electron bunches, i.e., the slice energy spread, to a level tolerable for operation of a self-amplified spontaneous emission FEL [8,9]. For future x-ray FELs that plan to use external quantum lasers (seed lasers) to seed the FEL process in order to achieve better temporal coherence and synchronization for pump-probe experiments, a smaller slice energy spread is required to leave room for the additional energy modulation imprinted by the seed laser. Thus, the amount of tolerable beam heating is more restrictive and the longitudinal phase space control becomes more critical (e.g., Refs. [10,11]). The same strict requirement on small slice energy spreads is valid for optical klystron enhanced self-amplified spontaneous emission free-electron lasers [12].

Originally designed for high-energy particle separation by radio-frequency (rf) fields [13], transverse deflecting rf structures (TDSs) are routinely used for high-resolution temporal electron beam diagnostics at present x-ray FELs (e.g., Refs. [14–17]) and are proposed to use for novel beam manipulation methods (e.g., Refs. [18–23]). Recently, a TDS was used to increase the slice energy spread in an echo-enabled harmonic generation FEL experiment [24,25]. In this paper, we present a reversible electron beam heating system that uses two TDSs located upstream and downstream of a magnetic bunch compressor chicane. The additional slice energy spread is introduced in the first TDS, which suppresses the microbunching instability, and then is eliminated in the second TDS.

The method of reversible beam heating is shown in Sec. II by means of linear beam optics and a corresponding matrix formalism. In Sec. III, we show the feasibility of this scheme to preserve both the transverse and longitudinal brightness of the electron beam, and discuss the impact of coherent synchrotron radiation. Section IV covers the gain suppression of microbunching instabilities by analytical calculations and numerical simulations, and in Sec. V we discuss the impact of beam and rf jitter, and show

*christopher.behrens@desy.de

inherent options for diagnosis and on-line monitoring of the electron beam's longitudinal phase space. The results and conclusions are summarized in Sec. VI.

## II. METHOD

In this and the following sections, we consider a linear accelerator (linac) employing a single bunch compressor for a soft x-ray FEL, such as the proposed linac configuration for the Next Generation Light Source (NGLS) at LBNL [26]. The choice of a single magnetic bunch compressor simplifies our consideration and analysis, although the concept is also applicable for typical bunch compressor arrangements with multiple stages. We note that a single bunch compressor arrangement has also been considered for the FERMI@Elettra FEL in order to minimize the impact of microbunching instabilities [27].

The generic layout of the reversible electron beam heater system is depicted in Fig. 1. It consists of linac sections providing and accelerating high-brightness electron beams, a magnetic bunch compressor chicane in order to achieve sufficient peak currents to drive the FEL process, and two transverse deflecting rf structures located upstream and downstream of the bunch compressor. An additional higher-harmonic rf linearizer system (Linearizer), like at the LCLS or FLASH [28], can be used to achieve uniform bunch compression by means of longitudinal phase space linearization upstream of the bunch compressor. The whole system can be supplemented by dedicated longitudinal phase space diagnostics (see Sec. V), and except for the two TDSs, the layout is commonly used for bunch compression at present and future x-ray FELs.

The principle of the reversible electron beam heater relies on the physics of TDSs arising from the Panofsky-Wenzel theorem [29,30], which states that the transverse momentum gain $\Delta\vec{p}_\perp$ of a relativistic electron imprinted by a TDS is related to the transverse gradient of the longitudinal electric field $\nabla_\perp \mathcal{E}_z$ inside the TDS, and yields

$$\Delta\vec{p}_\perp = -i\frac{e}{\omega}\int_0^L \nabla_\perp \mathcal{E}_z d\tilde{z}, \tag{1}$$

where $\omega/(2\pi)$ is the operating rf frequency, $e$ is the elementary charge, $L$ is the structure length, and $\tilde{z}$ is the longitudinal position inside the structure (not to be confused with the beam line coordinate, which is given by $s$ in the following). Operating a TDS with vertical deflection, i.e., in the $y$ direction, near the zero-crossing rf phase $\psi = \omega/cz$, electrons experience transverse kicks [14]

$$\Delta y' = \frac{e\omega V_y}{cE} z = K_y z \tag{2}$$

and relative energy deviations ($\delta = \Delta E/E$) [31,32]

$$\Delta\delta = K_y \frac{1}{L}\int_0^L y(s)ds = K_y \bar{y}, \tag{3}$$

where $K_y = e\omega V_y/(cE)$ is the vertical kick strength, $V_y$ is the peak deflection voltage in the TDS, $c$ is the speed of light in vacuum, $E$ is the electron energy, and $\bar{y}$ is the mean vertical position over the structure length $L$ along the beam line relative to the central axis inside the finite TDS. Here, $z$ is the internal bunch length coordinate of the electron relative to the zero-crossing rf phase. Both the additional transverse kicks and relative energy deviations are induced by the TDS operation itself and generate correlations within an electron bunch. In fact, near the zero-crossing rf phase [see Eq. (2)], the induced transverse kick correlates linearly with the internal bunch length coordinate ($z = ct$) and enables high-resolution temporal diagnostics (e.g., Refs. [14–16]), whereas the induced relative energy deviation correlates with the vertical offset inside the TDS and results in an induced relative energy spread $\Delta\sigma_\delta = K_y\sigma_y$. Here, the symbol $\sigma$ denotes the root mean square (rms) value, and $\sigma_y$ is the vertical rms beam size. This additional energy spread (cf. laser heater [8,9]), in combination with the momentum compaction $R_{56}$ of a bunch compressor chicane, is able to smear microbunch structures, and correspondingly suppresses the associated instability as is shown in Sec. IV. The effect of induced energy spread ("beam heating") is generated by off-axis longitudinal electric fields, related to the principle of a TDS by the Panofsky-Wenzel theorem, and has been observed experimentally at FLASH [33] and the LCLS [34]. The induced energy spread is uncorrelated in the longitudinal phase space ($z$, $\delta$), but shows correlations in the phase space ($y$, $\delta$), which is the reason that it can be eliminated ("beam cooling") with a second TDS in a reversible mode as is shown in the following by two different approaches.

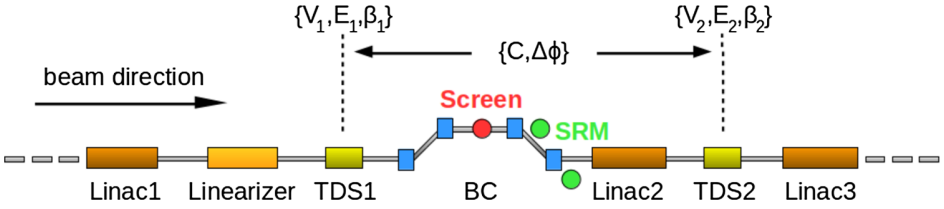


FIG. 1. Layout of a reversible electron beam heater system including two transverse deflecting rf structures located upstream and downstream of a magnetic bunch compressor (BC) chicane, and longitudinal phase space diagnostics using screens and synchrotron radiation monitors. Parameters related to the reversible beam heater system are denoted in curly brackets.

### A. Linear beam optics

The transverse betatron motion of an electron passing through a TDS with vertical deflection (in $y$) is given by

$$y(s) = y_0(s) + S_y(s, s_0)z \tag{4}$$

with the vertical shear function (e.g., Refs. [14,15,32])

$$S_y(s, s_0) = R_{34}K_y = \sqrt{\beta_y(s)\beta_y(s_0)}\sin[\Delta\phi_y(s, s_0)]\frac{e\omega V_y}{cE}, \tag{5}$$

where $R_{34}$ is the angular-to-spatial element of the vertical beam transfer matrix from the TDS at $s_0$ to any position $s$, $\beta_y$ is the vertical beta function, $\Delta\phi_y$ is the vertical phase advance between $s_0$ and $s$, and $y_0$ describes the vertical beam offset independent of any TDS shearing effect. Referring to the layout depicted in Fig. 1 and taking bunch compression into account, the induced vertical beam offset ($\Delta y = y - y_0$) downstream of the second TDS becomes (omitting the subscript $y$ in $S_y$)

$$\begin{aligned}\Delta y(s) &= S_1(s, s_1)z_1 + S_2(s, s_2)z_2 \\ &= [CS_1(s, s_1) + S_2(s, s_2)]z_2\end{aligned} \tag{6}$$

with the bunch compression factor $C = z_1/z_2$ and the shear functions $S_{1,2}(s, s_{1,2})$ of the corresponding TDSs. Here, $S_1(s, s_1)z_1$ describes the vertical beam offset induced by the first TDS located at $s_1$ that is independent of the second TDS. In order to cancel the spatial chirp induced by the combined TDS operation, the beam offset $\Delta y$ in Eq. (6) must vanish for any $z_2$. Hence, using Eq. (5) for $S_{1,2}$ in Eq. (6) and taking acceleration from $E_1$ to $E_2$ in Linac2 into account by making the replacement $\beta_y(s)\beta_y(s_1) \rightarrow \beta_y(s)\beta_y(s_1)E_1/E_2$ [14], we get

$$\begin{aligned}&C\sqrt{\beta_y(s_1)}\sin[\Delta\phi_y(s, s_1)]\sqrt{E_1}K_1 \\ &+\sqrt{\beta_y(s_2)}\sin[\Delta\phi_y(s, s_2)]\sqrt{E_2}K_2 = 0,\end{aligned} \tag{7}$$

where $K_{1,2}$ are the vertical kick strengths of the corresponding TDSs, and $\Delta\phi_y(s, s_{1,2})$ describes the vertical phase advances between $s_{1,2}$ and $s$, respectively. As a consequence, the phase advance between both TDSs is $\Delta\phi_y(s_2, s_1) = \Delta\phi_y(s, s_1) - \Delta\phi_y(s, s_2)$. A general solution, valid for any position $s$ downstream of the second TDS, is only possible for a phase advance difference of

$$\Delta\phi_y(s_2, s_1) = n \cdot \pi \tag{8}$$

with $n$ being integer, and the kick strength

$$K_2 = \pm C\sqrt{\frac{\beta_y(s_1)}{\beta_y(s_2)}}\sqrt{\frac{E_1}{E_2}}K_1, \tag{9}$$

where the sign depends on the actual phase advance, i.e., $\Delta\phi_y(s_2, s_1) = \pi + n \cdot 2\pi$ for $(+)$ and $\Delta\phi_y(s_2, s_1) = n \cdot 2\pi$ for $(-)$. The different sign of $K$ can technically be achieved by changing the rf phase in the TDS by 180° which results in a zero-crossing rf phase with opposite slope and deflection. Besides cancellation of the induced spatial chirps, the induced energy spread of the first TDS needs to be eliminated in the second structure in order to have a fully reversible electron beam heater. Applying Eq. (3) similar to Eq. (6), the relative energy deviation downstream of the second TDS for finite structure lengths become [omitting the argument in $y(s)$ and $S(s)$]

$$\Delta\delta = K_1\bar{y}_1C\frac{E_1}{E_2} + K_2\overline{(y_2 + S_1z_1)} \tag{10}$$

with the mean vertical offsets $\bar{y}_1$ and $\overline{(y_2 + S_1z_1)}$ inside the TDSs. For constant vertical offsets inside the TDSs or short structure lengths, the mean vertical offsets can be replaced by the actual offsets, i.e., $\bar{y}_1 \rightarrow y_1$ and $\overline{(y_2 + S_1z_1)} \rightarrow (y_2 + S_1z_1)$. The latter describes the offset in the second TDS and involves the spatial chirp induced by the first TDS with $S_1 \sim \sin[\Delta\phi_y(s_2, s_1)]$, which vanishes in the case of spatial chirp cancellation given by Eq. (8). In order to cancel the relative energy spread induced by the combined TDS operation, it follows

$$K_1\bar{y}_1C\frac{E_1}{E_2} + K_2\bar{y}_2 = 0. \tag{11}$$

The general transverse beam transport optics with the vertical phase advance condition in Eq. (8) gives $\bar{y}_2 = \pm\bar{y}_1\sqrt{\beta_y(s_2)/\beta_y(s_1)}$, and taking $\beta_y(s_2) \rightarrow \beta_y(s_2)E_1/E_2$ [see prior Eq. (7)] into account yields exactly the same condition as in Eq. (9). Simultaneous spatial chirp and energy spread cancellation in the second TDS is the basic principle for reversible electron beam heating and enables local increase of slice energy spread. The additional energy spread in the bunch compressor, which is added in quadrature by the first TDS, can be controlled by the kick strength $K_1$ and the vertical beam size $\sigma_y(s_1)$.

In the following, a complementary approach to discuss the reversible beam heating system is shown. It uses the matrix formalism for beam transport and provides an analytical way to show microbunching gain suppression and to discuss the impact of beam and rf jitter.

### B. Matrix formalism

We adopt the beam transport matrix notation of a $6 \times 6$ matrix for $(x, x', y, y', z, \delta)$ but leaves $(x, x')$ out for simplicity, i.e., $(y, y', z, \delta)$ is used in the following. The $4 \times 4$ beam transport matrix for a vertical deflecting TDS in thin-lens approximation reads (e.g., Refs. [19,31,33])

$$\mathbf{R}_T^{\text{thin}} = \begin{pmatrix} 1 & 0 & 0 & 0 \\ 0 & 1 & K & 0 \\ 0 & 0 & 1 & 0 \\ K & 0 & 0 & 1 \end{pmatrix}. \tag{12}$$

As discussed above, the main components of the given reversible heater system shown in Fig. 1 consist of TDS1

with the kick strength $K_1$, a bunch compressor with the momentum compaction factor $R_{56}$, and TDS2 with the kick strength $K_2$. Including the momentum compaction factor $R_{56}$ and acceleration in Linac2 ($E_1 \rightarrow E_2$), the $4 \times 4$ beam matrix between the two TDSs is given by

$$\mathbf{R}_C = \begin{pmatrix} R_{33} & R_{34} & 0 & 0 \\ R_{43} & R_{44} & 0 & 0 \\ 0 & 0 & 1 & R_{56} \\ 0 & 0 & 0 & \frac{E_1}{E_2} \end{pmatrix}. \tag{13}$$

In order to allow the energy change in the first TDS to be compensated for in the second TDS, we require the point-to-point imaging from TDS1 to TDS2 (i.e., $R_{34} = 0$), which corresponds to an equivalent vertical phase advance of $\Delta\phi_y(s_2, s_1) = n \cdot \pi$ with $n$ being integer [see Eq. (8)]. Then we get the magnification factor $R_{33} = \pm\sqrt{\beta_y(s_2)/\beta_y(s_1)}$ and $R_{44} = 1/R_{33}$.

The linear accelerator section with higher-harmonic rf linearizer (Linac1 and Linearizer) upstream of the first TDS introduces an appropriate energy chirp $h$ for uniform bunch compression. Without loss of generality, we neglect acceleration between the two TDSs, i.e., we do not consider Linac2 anymore. Including Linac2 would simply result in a correction term $\sqrt{E_1/E_2}$ [cf. Eqs. (9) and (15) below] but would leave the physics unchanged. Then the entire $4 \times 4$ beam transport matrix from the beginning of TDS1 to the end of TDS2 becomes

$$\begin{pmatrix} R_{33} & 0 & 0 & 0 \\ R_{43} + K_1 K_2 R_{56} & \frac{1}{R_{33}} & \frac{K_1}{R_{33}} + K_2(1 + hR_{56}) & K_2 R_{56} \\ K_1 R_{56} & 0 & 1 + hR_{56} & R_{56} \\ K_1 + R_{33} K_2 & 0 & 0 & \frac{1}{1+hR_{56}} \end{pmatrix}. \tag{14}$$

Cancellation of the induced spatial chirp [$\Delta y' \sim z_0$ cf. Eq. (2)] requires $R_{45} = 0$ ($6 \times 6$-matrix notation), i.e.,

$$K_1/R_{33} + K_2(1 + hR_{56}) = 0, \tag{15}$$

where $R_{45}$ describes the coupling between $y'$ and $z_0$. We note that the coupling between $\delta$ and $y_0$ (i.e., $R_{63}$ element) is nonzero in Eq. (14) because the bunch is energy chirped after compression ($\delta \sim z \sim y_0$), which can be removed by Linac3 downstream of TDS2. For uniform bunch compression with $C^{-1} = (1 + hR_{56})$, no acceleration in Linac2, i.e., $E_2 = E_1$, and taking into account that $R_{33} = \pm\sqrt{\beta_y(s_2)/\beta_y(s_1)}$, Eq. (15) is identical to Eq. (9). Thus, both formalisms yield the same result.

Since the kick strength of the first TDS is very weak, it can be implemented by means of a short rf structure and the thin-lens approximation is still valid. However, the kick strength of the second TDS is usually stronger, and the effect of the finite structure length should be taken into account. The symplectic beam transport matrix of a finite TDS with the length $L_2$ is given in Ref. [19] by

$$\mathbf{R}_T^{\text{thick}} = \begin{pmatrix} 1 & L_2 & K_2 L_2/2 & 0 \\ 0 & 1 & K_2 & 0 \\ 0 & 0 & 1 & 0 \\ K_2 & K_2 L_2/2 & K_2^2 L_2/6 & 1 \end{pmatrix}. \tag{16}$$

In this case, we require the point-to-point imaging is from the first TDS to the middle of the second TDS in order to have a complete cancellation. The overall matrix from TDS1 to the end of TDS2, when Eq. (15) is fulfilled, becomes more complicated. A few correction terms containing the length $L_2$ of TDS2 appear, which however does not change the working principle of the reversible beam heater system. It should be pointed out that, downstream of the reversible heater system, the beam is slightly coupled in $y' - \delta_0$ and $y - z_0$, which results in a small growth of the projected emittance given by

$$\epsilon_{y,z}^2 = \epsilon_{y0,z0}^2 + \epsilon_{y0}\epsilon_{z0}\frac{\beta_{y0}\gamma_{z0}K_1^2 R_{56}^2}{(1 + hR_{56})^2}, \tag{17}$$

where $\epsilon_{y0,z0}$ is the initial vertical (longitudinal) emittance, and $\beta_{y0}$ and $\gamma_{z0}$ are the initial Twiss parameters. As is shown in the following section, this projected emittance growth is typically negligible.

## III. REVERSIBLE HEATING AND EMITTANCE PRESERVATION

We demonstrate the feasibility of the reversible beam heater system by numerical simulations using the particle tracking code ELEGANT [35], and the simulations in the following include $5 \times 10^5$ particles. Table I summarizes the main parameters used in the simulations, and the adopted accelerator optics model, including the positions of the TDSs, is shown in Fig. 2. The magnetic bunch compressor chicane is assumed to bend in the horizontal plane, and the TDSs are oriented perpendicularly with vertical deflection. In the previous section, we included

TABLE I. Parameters of the electron beam, of the bunch compressor system, and of the transverse deflecting rf structures.

| Parameter | Symbol | Value | Unit |
|---|---|---|---|
| Beam energy at TDS1/2 | $E$ | 350 | MeV |
| Lorentz factor at TDS1/2 | $\gamma$ | 685 | |
| Initial transverse emittance | $\gamma\epsilon_{x,y}$ | 0.6 | $\mu$m |
| Initial slice energy spread | $\sigma_E$ | ~1 | keV |
| Momentum compaction factor | $R_{56}$ | −138 | mm |
| Compression factor | $C$ | ~13 | |
| Final bunch current | $I_f$ | ~520 | A |
| TDS1/2 rf frequency | $\omega/2\pi$ | 3.9 | GHz |
| Voltage of TDS1 | $V_1$ | 0.415 | MV |
| Voltage of TDS2 (without CSR) | $V_2$ | 5.440 | MV |
| Length of TDS1 | $L_1$ | 0.1 | m |
| Length of TDS2 | $L_2$ | 0.5 | m |

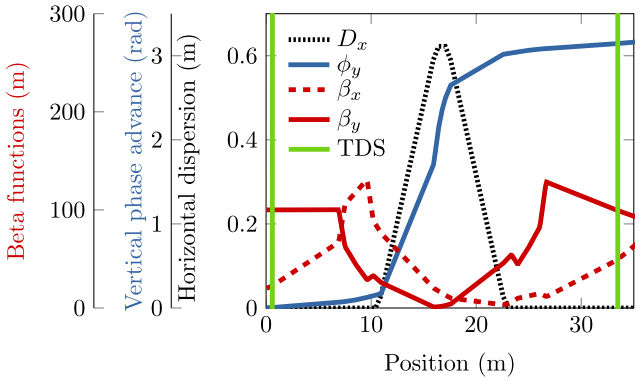


FIG. 2. Relevant accelerator optics (Twiss parameters) and positions of the transverse deflecting rf structures used to numerically demonstrate the reversible beam heater system.

Linac2 for a general derivation of the method, but in practice, due to wakefield concerns, we recommend putting TDS2 right after the bunch compressor. In order to show numerical examples based on this approach, Linac2 is not considered anymore throughout the rest of this paper. Except for the TDSs, the parameters are similar to the magnetic bunch compressor system discussed for the Next Generation Light Source at LBNL [26,36].

The initial longitudinal electron bunch profile is assumed to be flattop with a peak current of ~40 A and a slice energy spread of ~1 keV (rms). The initial linear and quadratic chirp is set for a uniform compression factor $C$ of about 13 across the entire bunch length. This is possible even with bunch compressor nonlinearities by using a higher-harmonic rf linearizer upstream of the bunch compressor [28] and needed to achieve uniform cancellation of the induced energy spread downstream of TDS2.

Figure 3 shows the principle of the reversible beam heater system by means of simulation of the longitudinal phase space at different positions along the beam line. The impact of CSR is not taken into account (cf. next subsection for CSR effects). The initial slice energy spread is heated up to ~10 keV (rms) in the first TDS, increased by the compression factor in the bunch compressor to ~130 keV (rms), and finally cooled down to ~13 keV (rms) by the second TDS [see Figs. 3(a)–3(d)]. The plot in Fig. 4(b) shows that the heating induced by the first TDS is perfectly reversible, and the final slice energy spread is simply the initial slice energy spread scaled with the compression factor, which would be exactly the same like in the case without using the reversible beam heater system. Figure 4(a) shows the heater system impact on both the projected emittance (horizontal and vertical) and the core energy spread, i.e., the slice energy spread in the center of the bunch, for different voltages in the second

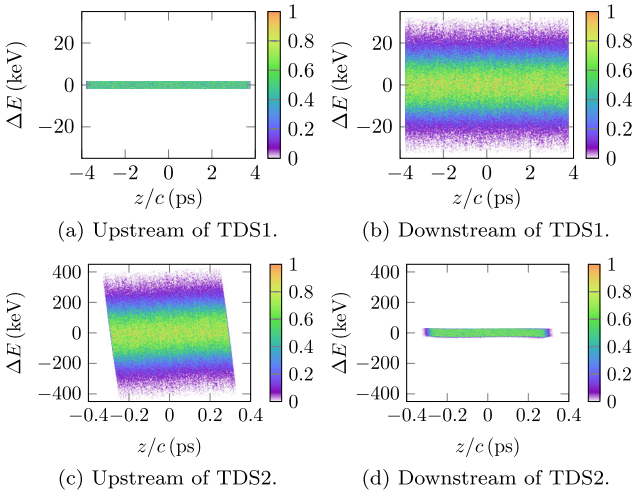


(a) Upstream of TDS1. (b) Downstream of TDS1.

(c) Upstream of TDS2. (d) Downstream of TDS2.

FIG. 3. Simulation of the longitudinal phase space after removing the correlated energy chirp: (a) Upstream of the first TDS, (b) directly downstream of the first TDS, (c) directly downstream of the bunch compressor and upstream of the second TDS, and (d) downstream of the second TDS. The axes scales change from (b) to (c) when bunch compression takes place. The bunch head is on the left, i.e., where $z/c < 0$.

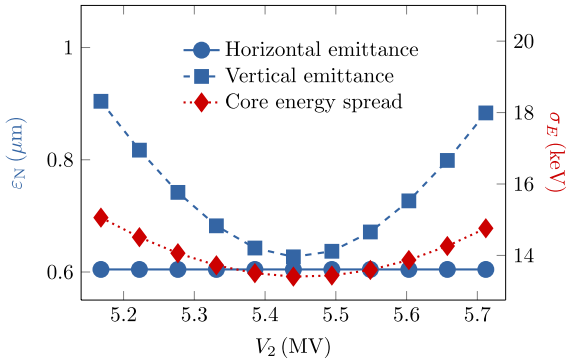


(a) Projected emittances and core energy spread.

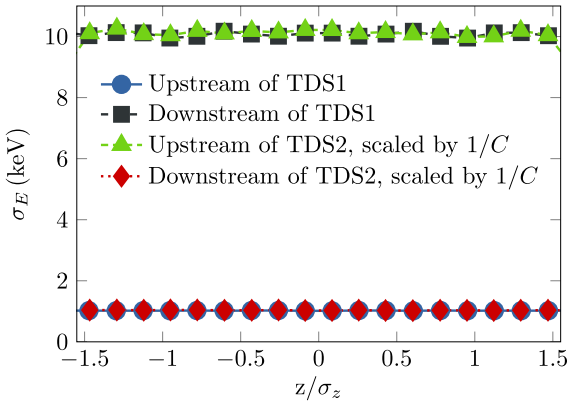


(b) Slice energy spread.

FIG. 4. Simulations without CSR effects on the impact of the reversible heater system on projected emittances, core energy spread, and slice energy spread: (a) Projected emittances (normalized) and core energy spread, and (b) slice energy spread for $V_2$ at minimum emittance [see Fig. 4(a)]. The longitudinal coordinate is normalized to the bunch length.

TDS. The minimum of the vertical emittance is related to the cancellation of the spatial chirp and energy spread induced by the first TDS. The horizontal emittance is not affected at all, and the small projected emittance growth (6%) in the vertical plane at the minimum is due to residual coupling generated by the system that is described by Eq. (17). Nevertheless, as shown in Sec. , even in the case with CSR effects, the horizontal slice emittance stays unaffected at all and the vertical slice emittance exhibits only deviations in the bunch head ($z/c < 0$) and tail ($z/c > 0$).

### Impact of coherent synchrotron radiation

The previous results undergo small modifications when including CSR effects, which is shown in Fig. 5. The voltage of the second TDS for minimum projected emittance in the vertical is shifted by about 0.2 MV to lower values which is due the additional energy chirp induced by CSR. In comparison to the case without any CSR effects (cf. Fig. 4), the projected emittance in the vertical plane is slightly increased and the slice energy spread is not perfectly canceled in the head and tail. The slice energy spread in the core part of the bunch is also slightly increased to 17.5 keV (rms) [instead of 13.5 keV (rms) in the absence of CSR]. The projected emittance in the horizontal is about 1.7 larger which is independent of the reversible beam heater operation. This horizontal emittance growth can further be reduced by minimizing the horizontal beta function in the last dipole of the chicane where the bunch length becomes the shortest. This optimization is independent of the relevant motion in the vertical and does not affect the results of the reversible heater system. Albeit the fact that the projected emittances are increased, the horizontal slice emittance stays unaffected and the vertical slice emittance exhibits only deviations in the head and tail due to CSR effects as is shown in Fig. 6. Thus, the core emittances are well preserved. We note that vertically streaked bunches in the bunch compressor chicane may change the impact of CSR effects but require a 3-dimensional "point-to-point" tracking which is not available neither in ELEGANT nor in CSRTRACK [37], and is beyond the scope of this paper.

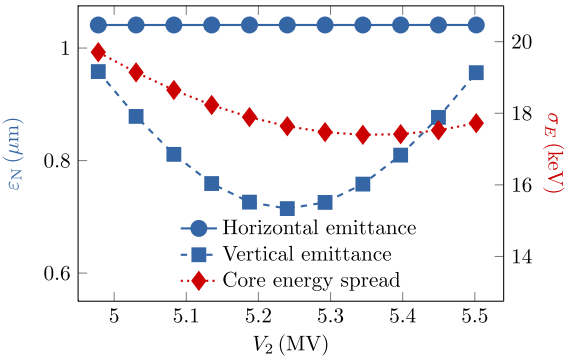


(a) Projected emittances and core energy spread.

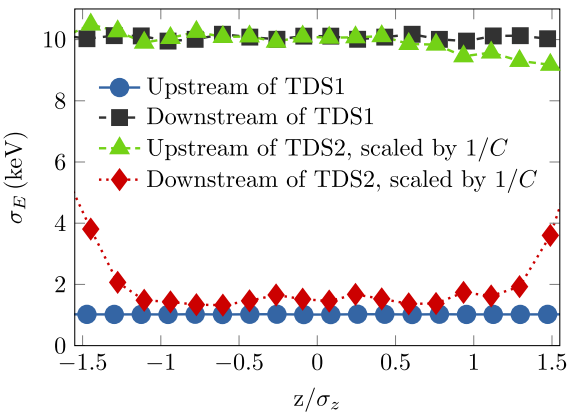


(b) Slice energy spread.

FIG. 5. Simulation on the impact of the reversible beam heater system on projected emittances, core energy spread, and slice energy spread: (a) Projected emittances (normalized) and core energy spread, and (b) slice energy spread for $V_2$ at minimum emittance [see Fig. 5(a)]. CSR effects are included by means of the 1-dimensional model in ELEGANT [35].

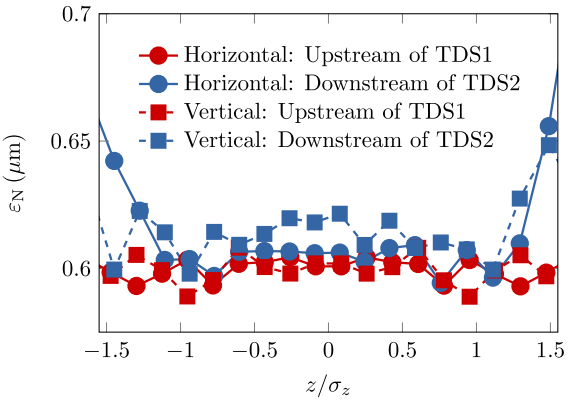


FIG. 6. Simulation of the normalized slice emittance for both the vertical and horizontal upstream of the first and downstream of the second TDS. CSR effects are included.

## IV. MICROBUNCHING GAIN SUPPRESSION

The principle of the microbunching gain suppression with the reversible beam heater system is shown by an analytical treatment following Ref. [9] and by using the beam transport matrix in Eq. (14). Then we show the feasibility of the reversible heater system to suppress microbunching instabilities by means of particle tracking simulations with initial density and energy modulations.

### A. Analytical calculations

Using the vector notation $(y_0, y_0', z_0, \delta_0)$ for particles in the first linac upstream of the first TDS, the longitudinal position downstream of the second TDS is given by

$$z = K_1 R_{56} y_0 + (1 + h R_{56}) z_0 + R_{56} \delta_0. \qquad (18)$$

Suppose that $\delta_0 = \delta_u + \delta_m$, where $\delta_u$ is the uncorrelated relative energy deviation, and $\delta_m(z_0)$ is the relative energy modulation accumulated before and in the first linac (Linac1). Following Ref. [9], the initial energy modulation at the wave number $k_0$ is converted into additional density modulation at a compressed wave number $k$. For a 4-dimensional (4D) distribution function $F(y, y', z, \delta)$, the bunching factor $b(k)$ is given by

$$\begin{aligned} b(k) &= \int dy dy' dz d\delta e^{-ikz} F(y, y', z, \delta) \\ &= \int dy_0 dy_0' dz_0 d\delta_u e^{-ikK_1 R_{56} y_0 - ik(1+hR_{56})z_0} \\ &\quad \times e^{-ikR_{56}[\delta_u + \delta_m(z_0)]} F_0(y_0, y_0', z_0, \delta_u), \end{aligned} \tag{19}$$

where $F_0(y_0, y_0', z_0, \delta_u)$ is the initial 4D distribution. If the induced energy modulation is small such that $|kR_{56}\delta_m| \ll 1$, we can expand the exponent of Eq. (19) up to the first order in $\delta_m$ to obtain

$$\begin{aligned} b(k) &\approx b_0(k_0) - ikR_{56} \int dz_0 \delta_m(z_0) e^{-ik_0 z_0} \\ &\quad \times \int dy_0 d\delta_u e^{-ikK_1 R_{56} y_0 - ikR_{56}\delta_u} U(y_0) V(\delta_u), \end{aligned} \tag{20}$$

where $k = Ck_0$, $C = 1/(1 + hR_{56})$, $U(y_0)$ describes the transverse profile, and $V(\delta_u)$ is the initial energy distribution. For both Gaussian profiles ($U$ and $V$), we have

$$\begin{aligned} b(k) &= b_0(k_0) - ikR_{56}\delta_m(k_0) \exp[-(k^2 R_{56}^2 K_1^2 \sigma_{y1}^2/2)] \\ &\quad \times \exp[-(k^2 R_{56}^2 \sigma_{\delta u}^2/2)]. \end{aligned} \tag{21}$$

Here, we denote the Fourier transform of $\delta_m(z_0)$ as $\delta_m(k_0)$, which is the accumulated energy modulation at the wave number $k_0$ in the first linac due to longitudinal space charge and other collective effects. The initial energy spread is given by $\sigma_{\delta u}$, and $\sigma_{y1}$ is the vertical beam size in the first TDS. We see that $K_1\sigma_{y1}$ acts like effective energy spread for microbunching gain suppression.

### B. Numerical simulations

Suppression of microbunching instabilities is demonstrated by using both a pure initial density modulation with 5% peak amplitude and 100 $\mu$m modulation wavelength ($\lambda_m$), and a pure initial energy modulation with 3 keV peak amplitude and $\lambda_m = 50$ $\mu$m. Whereas the case with initial energy modulation is immediately consistent with the previous analytical treatment and describes the longitudinal space charge driven microbunching instability [7], the initial density modulations need to be converted into energy modulations by longitudinal CSR impedance which expresses the consistency and describes the CSR-driven microbunching instability [6]. The simulations were performed using the code ELEGANT with $1 \times 10^6$ particles. Figure 7 shows the longitudinal phase space downstream of the second TDS, after removing the correlated energy chirp (linear and quadratic chirp), for both the reversible beam heater system switched off [Fig. 7(a)] and on [Fig. 7(b)]. In the case without reversible beam heater, energy and density modulations at the compressed modulation wavelength $\lambda_m/C$ appear, i.e., CSR-driven microbunching becomes visible. When switching the reversible beam heater on, the microbunching instability disappears and the resulting longitudinal phase space remains smooth. The reason is that the microbunches at the compressed wavelength are smeared due to $R_{56}K_1\sigma_{y1}$ [cf. Eq. (21)], and accordingly, the modulations appear as correlations in the phase spaces $(y, z)$ and $(y', \delta)$. The same effect of microbunching suppression is given for initial energy modulations as shown in Fig. 8. The effect of the microbunching instability appears even stronger compared to the simulations case with initial density modulations, but the performance of the reversible heater system is the same with a smooth residual longitudinal phase space when the reversible beam heater is switched on [see Fig. 8(b)].

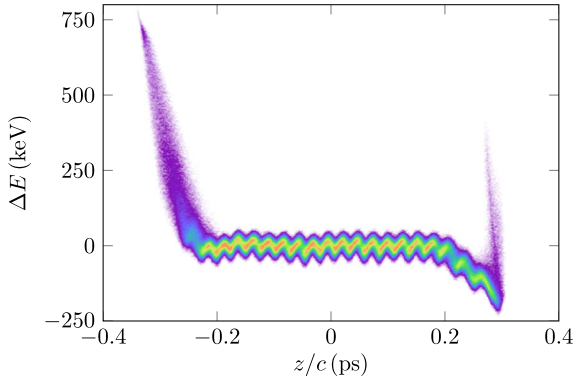


(a) Downstream of TDS2: Heater system off.

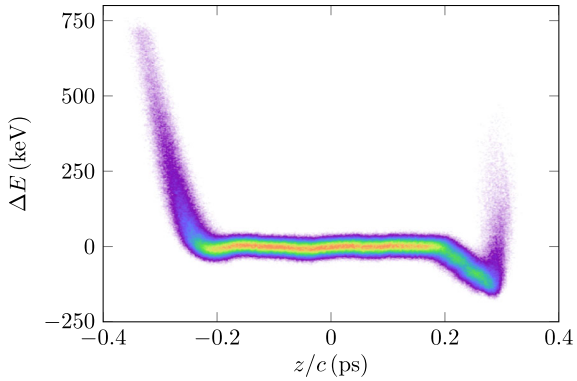


(b) Downstream of TDS2: Heater system on.

FIG. 7. Simulation on suppression of microbunching instabilities due to an initial density modulation, i.e., simulating CSR-driven microbunching. The entire longitudinal phase space, after removing the correlated energy chirp, is shown.

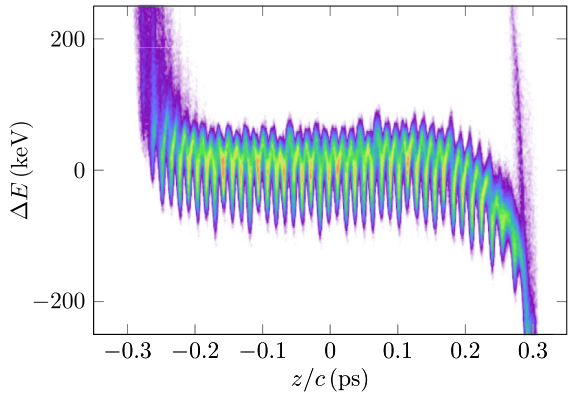


(a) Downstream of TDS2: Heater system off.

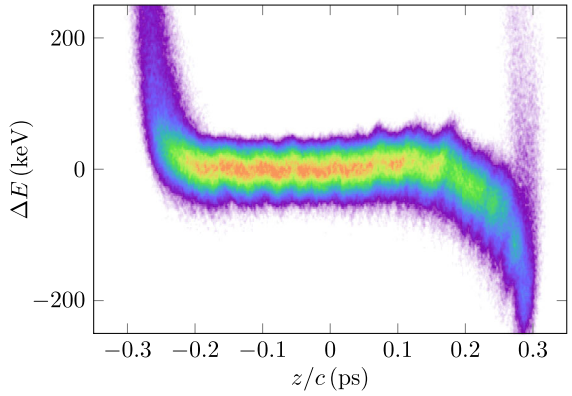


(b) Downstream of TDS2: Heater system on.

FIG. 8. Simulation on suppression of microbunching instabilities due to an initial energy modulation, i.e., simulating longitudinal space charge driven microbunching. For the sake of clarity, only the core of the longitudinal phase space, after removing the correlated energy chirp, is shown.

Figures 7 and 8 are obtained for a magnetic bunch compressor system as shown in Fig. 1. The electron bunch will be further accelerated and transported throughout the rest of the accelerator to reach the final beam energy and peak current in order to drive an x-ray FEL (not studied in this paper). A microbunched electron beam as illustrated in Figs. 7(a) and 8(a), i.e., when the reversible beam heater system is switched off, will accumulate additional energy and density modulations, which would lead to unacceptable longitudinal phase space properties for an x-ray FEL such as a large slice energy spread.

## V. PRACTICAL CONSIDERATIONS

The previous sections covered the principle of reversible electron beam heating and microbunching gain suppression by means of analytical calculations and numerical simulations. In real accelerators, we also have to deal with imperfections, jitter, and drifts of various parameters, and accordingly supplementary studies with respect to sensitivity on jitter sources and tolerances have to be performed. In the following, we discuss the impact of beam and rf jitter on the reversible beam heater system, and also point out the inherent possibility of longitudinal phase space diagnostics and on-line monitoring.

### A. Jitter and tolerances

The impact of beam and rf jitter on the reversible beam heater method can effectively be discussed using Eqs. (2) and (14) with the condition in Eq. (15). Deviations from the conditions in Eq. (15) can appear from jitter of the individual peak deflection voltages $V_1$ and $V_2$ of the TDSs, and lead to growth of the projected vertical emittance as is shown in Fig. 5(a), where the voltage of the second TDS is varied. Even in the case of a large TDS voltage jitter of 1%, the vertical projected emittance growth is less than 2% [see Fig. 5(a)]. In the case of acceleration between the first and second TDS, also energy jitter, which is similar or smaller than TDS voltage jitter, due to this intermediate acceleration leads to deviation of the condition in Eq. (15). The choice of superconducting accelerator technology even provide much better rf stability [38,39]. Pure arrival time jitter upstream of the first TDS has no impact as long as the condition in Eq. (15), which describes the coupling between $y'$ and $t = z/c$, is fulfilled. In the case that Eq. (15) is not exactly fulfilled, e.g., due to TDS voltage jitter which is on the percent level, the impact of typical arrival time jitter well below 100 fs, like at the LCLS [3] or FLASH [39], is negligible. The most critical jitter sources arise from energy jitter upstream of the bunch compressor chicane and from rf phase jitter in the TDSs. The momentum compaction factor translates energy jitter into arrival time jitter, which leads to vertical kicks in the second TDS. The same effect of additional vertical kicks is generated by rf phase jitter in the TDSs. In order to have small impact of vertical kicks on the remaining beam transport, we demand $\Delta\sigma_{y'} \ll \sigma_{y'}$ directly downstream of the second TDS with the induced vertical rms kick $\Delta\sigma_{y'}$ and the intrinsic beam divergence $\sigma_{y'}$. The relevant total vertical rms kick is given by

$$\begin{aligned}\Delta\sigma_{y'} &= \sqrt{\left(K_2 R_{56}\frac{\sigma_E}{E}\right)^2 + \left(K_2\frac{c}{\omega}\sigma_{\varphi_2}\right)^2 + \left(\frac{K_1}{R_{33}}\frac{c}{\omega}\sigma_{\varphi_1}\right)^2} \\ &= \sqrt{\left(K_2 R_{56}\frac{\sigma_E}{E}\right)^2 + \left(K_2\frac{c}{\omega}\right)^2\left(\sigma_{\varphi_2}^2 + \frac{1}{C^2}\sigma_{\varphi_1}^2\right)} \\ &\approx \sqrt{\left(K_2 R_{56}\frac{\sigma_E}{E}\right)^2 + \left(K_2\frac{c}{\omega}\right)^2\sigma_{\varphi_2}^2} \qquad (22)\end{aligned}$$

with the energy jitter $\sigma_E/E$ upstream of the bunch compressor, the rf phase jitter $\sigma_{\varphi_{1,2}}$ of the TDSs, the magnification factor $R_{33}$ from the first to the second TDS [see Eq. (13)], and using Eq. (15) with the compression factor $C = (1 + hR_{56})^{-1}$. We see that the vertical rms kick due to rf phase jitter in the first TDS scales with $C^{-2}$ and can be neglected compared to the vertical rms kick induced by the

second TDS when we assume the same amount of rf phase jitter in both TDSs. The condition for trajectory stability $\Delta\sigma_{y'} \ll \sigma_{y'_2} = \sqrt{\epsilon_{y_2}/\beta_{y_2}}$ with the intrinsic (uncorrelated) rms beam divergence $\sigma_{y'_2}$ downstream of the bunch compressor at TDS2, where $\epsilon_{y_2}$ is the geometrical emittance, can be restated as

$$\sqrt{\left(R_{56}\frac{\sigma_E}{E}\right)^2 + \left(\frac{c}{\omega}\sigma_{\varphi_2}\right)^2} \ll \frac{\epsilon_{y_2}}{K_2\sqrt{\beta_{y_2}\epsilon_{y_2}}} = \frac{\sqrt{\epsilon_{y_2}\epsilon_{y_1}}}{C\Delta\sigma_{\delta_1}}. \quad (23)$$

Here, $\Delta\sigma_{\delta_1}$ is the additional relative energy spread induced by the first TDS for suppression of microbunching instabilities, and $\epsilon_{y_1}$ denotes the geometrical emittance upstream of the bunch compressor at TDS1.

For the example parameters discussed throughout this paper (see also Table I), i.e., $C = 13$, $\gamma\epsilon_{y_1} = 0.6\ \mu$m, $\gamma\epsilon_{y_2} = 0.72\ \mu$m [see Fig. 5(a)], and $\Delta\sigma_{\delta_1}E \approx 10$ keV with $E = 350$ MeV ($\gamma = 685$), the stability condition in Eq. (23) yields pure relative energy jitter (neglecting rf phase jitter) of $\sigma_E/E \ll 1.9 \times 10^{-5}$ or pure rf phase jitter (neglecting energy jitter) of $\sigma_{\varphi_2} \ll 0.012°$. A combination of both will obviously tighten the acceptable jitter. This level of rf stability is difficult to achieve in normal conducting linacs with single bunch operation, but might be achieved with superconducting accelerator technology like at FLASH or as planned for NGLS, where many bunches can be accelerated in a long rf pulse, i.e., in a bunch train. Currently, several rf feedforward and feedback controls are able to stabilize the bunches at FLASH to $\sigma_E/E = 3.0 \times 10^{-5}$ and $\sigma_\varphi = 0.007°$ at 150 MeV [38,40], and further improvements towards $\sigma_E/E \leq 1.0 \times 10^{-5}$ are planned using a fast normal conducting cavity upstream of the bunch compressors [38,39]. With perfect scaling of rf jitter from several independent rf power stations that adds uncorrelated, we would expect an improvement of $\sqrt{150\ \text{MeV}/350\ \text{MeV}} \approx 0.66$ compared to the results at FLASH with 150 MeV and assuming the beam energy of 350 MeV in the bunch compressor of the NGLS design. Continuous-wave rf operation, as planned for the NGLS design [26], and a proper choice of rf working points for FEL operation might improve the stability further.

### B. Integrated longitudinal phase space diagnostics

A practical spin-off of the reversible beam heater system is the availability of longitudinal phase space diagnostics. The vertical betatron motion of electrons passing through a TDS is described by Eq. (4), which enables a mapping from time (longitudinal coordinate) to the vertical [14–16], and finally a possibility to obtain temporal bunch information by means of transverse beam diagnostics. In a similar manner, the relative energy deviation is mapped to the horizontal in the presence of horizontal momentum dispersion, like in a magnetic bunch compressor chicane (see, e.g., Refs. [15,16]). The combined operation makes single-shot measurements of the longitudinal phase space possible, and in the case of the generic layout of a reversible electron beam heater system as depicted in Fig. 1, longitudinal phase space measurements become feasible using the first TDS and observation screens in the dispersive section of the bunch compressor chicane. In order to get information of the bunch length after the bunch compression, the second TDS can be used with downstream observation screens (not shown in Fig. 1).

In addition to invasive longitudinal phase space measurements of a single bunch using observation screens, even fully noninvasive measurements utilizing incoherent synchrotron radiation, emitted in the bunch compressor bending magnets, are possible (see, e.g., Ref. [41]). When using a fast gated camera, the implication will be the possibility of on-line monitoring the longitudinal phase space of individual bunches in multibunch accelerators.

## VI. SUMMARY AND CONCLUSIONS

Our studies show that the reversible beam heater system proposed here can suppress microbunching instabilities and preserve the high beam brightness at the same time. Because of CSR effects, some vertical emittance degradation in the head and tail region of the bunch occurs, but the core emittances are well preserved. In the numerical demonstrations using the code ELEGANT, the first TDS generates about 10 keV (rms) slice energy spread, which is similar to the laser heater but with a more Gaussian energy distribution (cf. laser heater). The bunch compression process increases the slice energy spread to ~130 keV (rms), which is then reversed to ~17 keV (rms) after the second TDS in the presence of CSR effects. Without CSR effects, the slice energy spread is reversed to ~13 keV (rms), which demonstrates perfect cancellation. The simulations also show that initial bunching in energy and density in the beam can be smeared out during the process in the reversible beam heater system, i.e., microbunching instabilities can be suppressed. The resulting smooth beam can then propagate through the remaining accelerator without further generation of much additional energy spread and is advantageous for any kind of laser seeding manipulations and experiments. For example, this scheme significantly loosens the required laser power for seeding using short-wavelength high harmonic generation sources [10] and may strongly impact the design of future seeded FELs. In addition, the reversible beam heater system exhibits integrated options for diagnosis and on-line monitoring of the longitudinal phase space applicable for multibunch machines, which is also the preferred type of accelerator for the reversible heater system due to large sensitivities on energy and rf jitter. Linear accelerators based on superconducting rf technology might be able to match the strict tolerances in order to keep vertical kicks small and to achieve a sufficient trajectory stability in the downstream undulators.

## ACKNOWLEDGMENTS

We would like to thank P. Emma, Ch. Gerth, A. Lumpkin, H. Schlarb, and J. Thangaraj for useful discussions and suggestions. This work was supported by Department of Energy Contract No. DE-AC02-76SF00515.

[1] S. Jamison, Nature Photon. **4**, 589 (2010).
[2] W. Ackermann *et al.*, Nature Photon. **1**, 336 (2007).
[3] P. Emma *et al.*, Nature Photon. **4**, 641 (2010).
[4] D. Pile, Nature Photon. **5**, 456 (2011).
[5] E. L. Saldin, E. A. Schneidmiller, and M. V. Yurkov, Nucl. Instrum. Methods Phys. Res., Sect. A **398**, 373 (1997).
[6] M. Borland *et al.*, Nucl. Instrum. Methods Phys. Res., Sect. A **483**, 268 (2002).
[7] E. L. Saldin, E. A. Schneidmiller, and M. V. Yurkov, Nucl. Instrum. Methods Phys. Res., Sect. A **528**, 355 (2004).
[8] Z. Huang, M. Borland, P. Emma, J. Wu, C. Limborg, G. Stupakov, and J. Welch, Phys. Rev. ST Accel. Beams **7**, 074401 (2004).
[9] Z. Huang *et al.*, Phys. Rev. ST Accel. Beams **13**, 020703 (2010).
[10] D. J. Dunning *et al.*, in *Proceedings of the 1st International Particle Accelerator Conference, Kyoto, Japan, 2010* (ICR, Kyoto, 2010), TUPE049.
[11] M. Cornacchia, S. Di Mitri, G. Penco, and A. Zholents, Phys. Rev. ST Accel. Beams **9**, 120701 (2006).
[12] Y. Ding, P. Emma, Z. Huang, and V. Kumar, Phys. Rev. ST Accel. Beams **9**, 070702 (2006).
[13] O. Altenmueller, R. Larsen, and G. Loew, Rev. Sci. Instrum. **35**, 438 (1964).
[14] P. Emma, J. Frisch, and P. Krejcik, Technical Report No. LCLS-TN-00-12, 2000.
[15] M. Röhrs, Ch. Gerth, H. Schlarb, B. Schmidt, and P. Schmüser, Phys. Rev. ST Accel. Beams **12**, 050704 (2009).
[16] D. Filippetto *et al.*, Phys. Rev. ST Accel. Beams **14**, 092804 (2011).
[17] Y. Ding, C. Behrens, P. Emma, J. Frisch, Z. Huang, H. Loos, P. Krejcik, and M-H. Wang, Phys. Rev. ST Accel. Beams **14**, 120701 (2011).
[18] A. Zholents, P. Heimann, M. Zolotorev, and J. Byrd, Nucl. Instrum. Methods Phys. Res., Sect. A **425**, 385 (1999).
[19] M. Cornacchia and P. Emma, Phys. Rev. ST Accel. Beams **5**, 084001 (2002).
[20] P. Emma, Z. Huang, K.-J. Kim, and P. Piot, Phys. Rev. ST Accel. Beams **9**, 100702 (2006).
[21] D. Xiang and Y. Ding, Phys. Rev. ST Accel. Beams **13**, 094001 (2010).
[22] P. Piot, Y.-E Sun, J. G. Power, and M. Rihaoui, Phys. Rev. ST Accel. Beams **14**, 022801 (2011).
[23] D. Xiang and A. Chao, Phys. Rev. ST Accel. Beams **14**, 114001 (2011).
[24] D. Xiang *et al.*, Phys. Rev. Lett. **105**, 114801 (2010).
[25] D. Xiang *et al.*, Phys. Rev. Lett. **108**, 024802 (2012).
[26] J. Corlett *et al.*, in Proceedings of the 24th Particle Accelerator Conference, New York, 2011, TUOCS5.
[27] M. Venturini and A. Zholents, Nucl. Instrum. Methods Phys. Res., Sect. A **593**, 53 (2008).
[28] H. Edwards, C. Behrens, and E. Harms, Proceedings of the 25th International Linear Accelerator Conference, Tsukuba, Japan, 2010, MO304.
[29] W. Panofsky and W. Wenzel, Rev. Sci. Instrum. **27**, 967 (1956).
[30] M. J. Browman, in *Proceedings of the 15th Particle Accelerator Conference, Washington, DC, 1993* (IEEE, New York, 1993), p. 800.
[31] S. Korepanov, M. Krasilnikov, F. Stephan, D. Alesini, and L. Ficcadenti, in Proceedings of the 8th European Workshop on Beam Diagnostics and Instrumentation for Particle Accelerators, Venice, Italy, 2007, TUPB32.
[32] C. Behrens and Ch. Gerth, in Proceedings of the 9th European Workshop on Beam Diagnostics and Instrumentation for Particle Accelerators, Basel, Switzerland, 2009, TUPB44.
[33] C. Behrens and Ch. Gerth, Proceedings of the 10th European Workshop on Beam Diagnostics and Instrumentation for Particle Accelerators, Hamburg, Germany, 2011, TUPD31.
[34] P. Emma (private communication).
[35] M. Borland, ANL/APS Report No. LS-287, 2000.
[36] M. Venturini *et al.*, in Proceedings of the 24th Particle Accelerator Conference, New York, 2011, THP180.
[37] M. Dohlus and T. Limberg, in *Proceedings of the 26th International Free Electron Laser Conference, Trieste, Italy, 2004* (Comitato Conferenze Elettra, Trieste, Italy, 2004), MOCOS05.
[38] H. Schlarb (private communication).
[39] C. Schmidt *et al.*, Proceedings of the 33rd International Free Electron Laser Conference, Shanghai, China, 2011, THPA26.
[40] S. Pfeiffer *et al.*, LLRF-2011 workshop, Hamburg, Germany, 2011.
[41] Ch. Gerth, in Proceedings of the 8th European Workshop on Beam Diagnostics and Instrumentation for Particle Accelerators, Venice, Italy, 2007, TUPC03.

# 5 Femtosecond X-ray pulse characterization

X-ray free-electron lasers open up new frontiers in photon science, which is a consequence of their outstanding characteristics in terms of the generated FEL radiation (see, e.g., Ref.[23]). The laserlike X-ray radiation with high spectral brightness, wide tunability, and almost full spatial coherence meets many requirements of experimental techniques in photon science. Femtosecond FEL radiation pulses (e.g., Refs. [40, 41, 42]) extend the capabilities of these unique accelerator-based light sources. However, to fully utilize these ultrashort radiation pulses, single-shot characterization of their duration, temporal profile, and arrival time with high accuracy is required. Arrival time information is crucial for carrying out time-resolved pump-probe experiments with an external (pump) quantum laser (e.g., Refs. [105, 106]).

The temporal profile of the power in FEL radiation pulses is generally determined by the time-dependent parameters (so-called slice parameters) of the FEL driving electron beams. Precise knowledge of these slice parameters would enable to calculate the temporal profile of the FEL radiation pulses, and time-resolved electron beam diagnostics can thus be utilized to estimate the expected radiation pulse durations [57]. A similar approach, based on longitudinal phase space diagnostics for electron beams, makes use of the energy transfer during the FEL amplification. The temporal profile of the FEL radiation pulse appears as a "replica" in the longitudinal phase space of the electron bunch downstream of the undulator [74, 107]. A different approach, utilizing streaking techniques with THz fields, allows direct temporal FEL radiation pulse characterization [108, 109] and demonstrated simultaneous arrival time measurements of FEL radiation pulses with respect to an external pump laser [109].

In the following, three articles in the research field of femtosecond X-ray pulse characterization are introduced and presented. The first article deals with the constraints on photon pulse durations from longitudinal electron beam diagnostics at a soft X-ray FEL and has been published in *Phys. Rev. ST Accel. Beams*. The second article describes femtosecond X-ray pulse temporal characterization in FELs using a transverse deflector and has been published in *Phys. Rev. ST Accel. Beams*. The third article reports on ultrafast X-ray pulse characterization at FELs and has been accepted for publication in *Nature Photonics*.

## 5.1 Constraints on photon pulse durations from longitudinal electron beam diagnostics at a soft x-ray free-electron laser

Electron beam diagnostics are of crucial importance for the operation of any particle accelerator (e.g., Ref. [52]), and X-ray free-electron lasers driven by linear accelerators have particular requirements for time-resolved diagnostics with single-shot capability (see chapter 3). The slice parameters of the FEL driving electron beams generally determine the temporal profile of the resulting FEL radiation pulses, hence time-resolved electron beam diagnostics are supposed to provide *a priori* estimates on the expected FEL radiation pulse durations.

For FELs operating in the self-amplified spontaneous emission mode, the statistical properties of SASE have considerable impact on the temporal profile and spectrum of the radiation pulses (see Sec. 2.3). As has been pointed out in Refs. [110, 111], the radiation pulse energy statistics of SASE FELs tuned to the exponential gain regime (see Sec. 2.1.2) can be used to determine the number of wave packets (modes $M$) in the FEL radiation pulse. The same number of modes is also related to the number of peaks in the FEL radiation spectra (see Sec. 2.3), which can be measured with a high-resolution spectrometer (e.g., Refs. [57, 112]). By using the coherence time $\tau_c$ given in Eq. (2.40), the FEL radiation pulse duration $T_p$ can be estimated as $\sim M \times \tau_c$ [cf. Eq. (2.41)]. Theoretical treatments and numerical simulations have shown that these estimates of the radiation pulse durations can be connected to the r.m.s. bunch durations of the FEL driving electron beams [57]. A theoretical model allows to extrapolate the estimated FEL pulse durations to the saturation regime and beyond [57].

As has been discussed in chapter 3, time-resolved electron beam diagnostics with high resolution and single-shot capability can be achieved in the time-domain by using transverse deflecting r.f. structures and in the frequency-domain by spectroscopy of coherent THz radiation. The combination of a TDS with a magnetic energy spectrometer even makes longitudinal phase space measurements (e.g., Refs. [57, 101, 113]) with simultaneous suppression of coherent optical radiation possible [64]. Whereas the r.m.s. electron bunch durations can be calculated directly from the time-domain diagnostics, the spectroscopic measurements from the frequency-domain diagnostics need to be Fourier transformed into the time-domain, which requires phase retrieval techniques (Kramer-Kronig relations) [75].

The following article reports on how time-resolved electron beam diagnostics can be utilized to provide constraints on the expected radiation pulse durations at FELs. Comparative measurements of FEL pulse durations and temporal electron bunch profiles are presented, and their relationship is discussed by theoretical considerations and numerical simulations.

# Constraints on photon pulse duration from longitudinal electron beam diagnostics at a soft x-ray free-electron laser

C. Behrens,[1,*] N. Gerasimova,[1] Ch. Gerth,[1] B. Schmidt,[1] E. A. Schneidmiller,[1] S. Serkez,[1,2] S. Wesch,[1] and M. V. Yurkov[1]

[1]*Deutsches Elektronen-Synchrotron DESY, Notkestraße 85, 22607 Hamburg, Germany*

[2]*Ivan Franko National University of Lviv, 8 Kyryla i Mefodiya Street, 79005 Lviv, Ukraine*

(Received 20 January 2012; published 22 March 2012; publisher error corrected 13 June 2012)

The successful operation of x-ray free-electron lasers (FELs), like the Linac Coherent Light Source or the Free-Electron Laser in Hamburg (FLASH), makes unprecedented research on matter at atomic length and ultrafast time scales possible. However, in order to take advantage of these unique light sources and to meet the strict requirements of many experiments in photon science, FEL photon pulse durations need to be known and tunable. This can be achieved by controlling the FEL driving electron beams, and high-resolution longitudinal electron beam diagnostics can be utilized to provide constraints on the expected FEL photon pulse durations. In this paper, we present comparative measurements of soft x-ray pulse durations and electron bunch lengths at FLASH. The soft x-ray pulse durations were measured by FEL radiation pulse energy statistics and compared to electron bunch lengths determined by frequency-domain spectroscopy of coherent transition radiation in the terahertz range and time-domain longitudinal phase space measurements. The experimental results, theoretical considerations, and simulations show that high-resolution longitudinal electron beam diagnostics provide reasonable constraints on the expected FEL photon pulse durations. In addition, we demonstrated the generation of soft x-ray pulses with durations below 50 fs (FWHM) after the implementation of the new uniform electron bunch compression scheme used at FLASH.

DOI: 10.1103/PhysRevSTAB.15.030707 PACS numbers: 29.27.−a, 41.60.Cr, 41.50.+h

## I. INTRODUCTION

Since the first operation of a laser in 1960 [1], a tremendous number of new experimental techniques became possible with continuously changing and growing requirements on the laser systems, e.g., higher spectral brightness, shorter wavelengths, or photon pulse durations with simultaneous tunability. High-gain free-electron lasers (FELs) meet many of these requirements, and the successful operation of x-ray FELs like the Free-Electron Laser in Hamburg (FLASH) [2], the Linac Coherent Light Source (LCLS) [3], or the SPring-8 Angstrom Compact Free Electron Laser [4] make unprecedented research on matter at atomic length scales possible [5]. The demonstration of FEL photon pulse durations in the femtosecond range (e.g., Refs. [6,7]) has further extended the capabilities to research of dynamical processes at ultrafast time scales (see, e.g., Ref. [8]) with ongoing demands on the generation and control of ultrashort photon pulses.

In recent years, several methods to control FEL photon pulse durations have been proposed by manipulating and controlling the FEL driving electron bunches. The low-charge operation at LCLS [9] demonstrated electron bunch lengths below 10 fs [10], and the same strategy of low-charge operation is planned for the European XFEL and FLASH [11]. Other methods, with additional prospects of generating photon pulses in the attosecond range, make use of electron bunch manipulation with conventional quantum lasers (e.g., Refs. [12–16]) or by selectively spoiling the transverse emittance of the electron beam [17]. However, reliable operation of these methods requires capabilities to diagnose the FEL photon pulse shapes and durations with high accuracy, which is a tremendous challenge and an active field of research.

First single-shot measurements of FEL photon pulse durations with femtosecond accuracy have recently been demonstrated by terahertz-field driven streaking experiments in the time domain [18,19], and the statistical and spectral properties of FEL radiation emitted in the exponential gain regime allow one to measure the mean photon pulse duration (e.g., Refs. [20–23]). Other proposed methods make use of the FEL-induced slice energy loss in order to measure ''replicas'' of the FEL photon pulses (see Refs. [24,25]). As is presented in this paper, high-resolution longitudinal electron beam diagnostics in standard configurations, i.e., as commonly used at present x-ray FELs, can provide reasonable and complementary constraints on the expected FEL photon pulse durations.

In this paper, we compare measurements of electron bunch lengths with corresponding soft x-ray pulse durations at FLASH, and discuss their relationship by theoretical considerations and simulations. The experimental setup

*christopher.behrens@desy.de

and applied methods are described in Sec. II, and in Sec. III we discuss the experimental results for FEL operation with different bunch charges, which corresponds to different electron bunch lengths and soft x-ray pulse durations. The final results are compared in Sec. IV, and the summary and conclusions are presented in Sec. V.

## II. EXPERIMENTAL SETUP AND METHODS

The measurements presented in this paper were carried out at FLASH, which is a self-amplified spontaneous emission (SASE) FEL [26] for extreme-ultraviolet and soft x-ray radiation, driven by a superconducting radio-frequency (rf) linear accelerator [2]. The schematic layout of FLASH is depicted in Fig. 1, showing the injector, which is based on a laser-driven normal conducting rf gun, the superconducting accelerating structures, two magnetic bunch compressor chicanes, and the undulator magnet system. The positions of the diagnostics used for FEL photon pulse duration and electron bunch length measurements are indicated by green dots and arrows.

In 2010, FLASH was upgraded [27] to a maximum beam energy of 1.25 GeV, allowing for the generation of soft x rays below 4.4 nm (water window) with its fundamental. One of the major upgrades was the installation of the third-harmonic rf system, which is dedicated for the linearization of the longitudinal phase space upstream of the first bunch compressor [28,29]. Before this upgrade, FLASH was operated with nonuniformly compressed electron bunches with a short leading spike [30,31]. The corresponding FEL photon pulses had short durations but low pulse energies due to the fact that only a small fraction of the bunch (the short leading spike) contributed to lasing [2,6]. In Sec. III, it is shown that the third-harmonic rf linearizer system permits more uniform bunch compression with higher FEL photon pulse energies and simultaneous tunability of the pulse durations.

In the following, we describe the experimental setup and applied methods to measure the FEL photon pulse durations and electron bunch lengths. The photon pulse durations were estimated by the statistics of FEL radiation pulse energies measured with a microchannel plate based detector. The electron bunch lengths were measured in the time domain by using a transverse deflecting rf structure in combination with a magnetic energy spectrometer and in the frequency domain by spectroscopy of coherent transition radiation in the terahertz range.

### A. Time-domain longitudinal phase space diagnostics for electron beams

The time-domain electron bunch length measurements were done by using a transverse deflecting rf structure (TDS) [32] in combination with a magnetic energy spectrometer. Transverse deflecting rf structures are widely used for electron bunch length and longitudinal profile measurements at present FELs, and provide high-resolution single-shot diagnostics (see, e.g., Ref. [33]). In combination with standard techniques for transverse emittance measurements, the operation of TDSs makes time-resolved emittance, i.e., slice emittance, measurements possible. The complementary use of an energy spectrometer allows direct longitudinal phase space and slice energy spread measurements (e.g., Refs. [31,34–36]). Recently, a TDS in combination with a magnetic energy spectrometer downstream of FEL undulators have been proposed to measure the FEL-induced slice energy spread for temporal x-ray pulse characterization [25].

At FLASH, a LOLA-type [32] TDS was successfully operated upstream of the energy collimator [31] before it was moved close to the undulators during the FLASH upgrade in 2010 [27]. The TDS has been integrated in a dedicated setup for measurements of the longitudinal phase space [35,36]. As depicted in Fig. 1, the TDS can either be operated in combination with the dispersive energy spectrometer or by using off-axis screens in the nondispersive main beam line during FEL operation. In both cases, the screen stations are equipped with different imaging screens and a camera system with motorized optics. A fast kicker magnet (not shown in Fig. 1) can operate the off-axis screens for TDS measurements and frequency-domain electron bunch length diagnostics by terahertz spectroscopy (see Sec. II B) in parallel. Technical details and performance measurements on the new measurement setup can be found in Refs. [35,36], and technical information about the TDS at FLASH and detailed descriptions of time-domain electron bunch diagnostics using a TDS can be found in Refs. [31,37]. Here, we describe only the basic principles of longitudinal phase space diagnostics required throughout this paper.

The vertical betatron motion of an electron passing a TDS around rf phase zero crossing is given by [31,37]

$$y_{\pm}(s) = y_0(s) + C_y(s, s_0)c^{-1}z \pm S_y(s, s_0)c^{-1}z \quad (1)$$

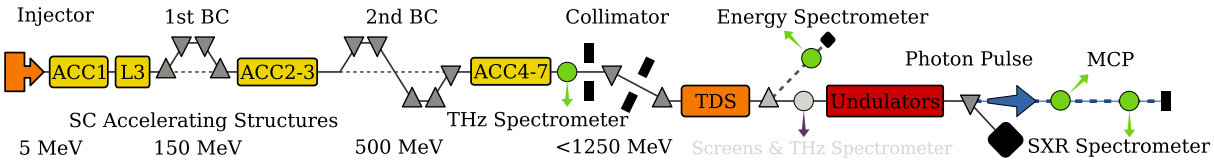


FIG. 1. Layout of the Free-Electron Laser in Hamburg (FLASH) with its superconducting (SC) accelerating structures (ACC), the two magnetic bunch compressor (BC) chicanes, and the new third-harmonic rf linearizer system (L3). The positions of the diagnostics used for photon pulse duration and electron bunch length measurements are indicated by green dots and arrows.

with the linear correlation $C_y(s, s_0)$ and shear function

$$S_y(s, s_0) = R_{34}K_y = \sqrt{\beta_y(s)\beta_y(s_0)}\sin(\Delta\phi_y)\frac{e\omega V_y}{E}, \quad (2)$$

where $R_{34} = \sqrt{\beta_y(s)\beta_y(s_0)}\sin(\Delta\phi_y)$ is the angular-to-spatial element of the vertical beam transfer matrix from the TDS at $s_0$ to any position $s$, $\beta_y$ is the vertical beta function, $\Delta\phi_y$ is the vertical phase advance between $s_0$ and $s$, and $y_0$ describes the intrinsic offset. The expression $K_y = e\omega V_y/E$ is the vertical kick strength with the peak deflection voltage $V_y$ in the TDS, $c$ is the speed of light in vacuum, $e$ is the elementary charge, $E$ is the electron energy, $z$ is the longitudinal position of the electron relative to the zero-crossing rf phase, and $\omega/(2\pi)$ is the operating rf frequency. The longitudinal-to-vertical correlation $C_y$ in Eq. (1) is independent of the TDS operation and can exist intrinsically due to time-dependent kicks generated from collective effects such as coherent synchrotron radiation or wakefields. This linear correlation may lead to systematical errors in electron bunch length measurements, which, however, can be removed by performing measurements at two zero-crossing TDS rf phases shifted by 180 deg, i.e., with $\pm S_y$ [cf. Eq. (1)].

The expression in Eq. (1) shows a linear mapping from the longitudinal to the vertical coordinate and allows longitudinal electron bunch profile measurements by means of transverse beam diagnostics using imaging screens or wire scanners. The vertical shear function $S_y$ determines the slope of this mapping and can be calibrated by measuring the vertical centroid offset of the bunch as a function of the TDS rf phase. The electron bunch current is given by the calibrated and normalized longitudinal bunch profile multiplied by the measured electron bunch charge. In the following, the longitudinal coordinate $z$ is expressed by a time coordinate via $t = -z/c$ and the bunch length by the corresponding bunch duration. The latter is expressed by the root mean square (rms) value $\Sigma_{t,\mathrm{e}} = |C_y \pm S_y|^{-1}(\sigma_{y\pm}^2 - \sigma_{y0}^2)^{1/2}$, where $\sigma_{y\pm}$ is the measured vertical rms beam size during TDS operation corresponding to $\pm S_y$, respectively. The rms bunch duration $\Sigma_{t,\mathrm{e}}$ describes a quadratic equation for $\sigma_{y\pm}^2$, and by performing measurements of the vertical rms beam size at $\pm S_y$ and $S_y = 0$ (TDS switched off), the longitudinal-to-vertical correlation $C_y$ and the intrinsic vertical rms beam size $\sigma_{y0}$ can be determined. These parameters limit the rms time resolution to $\mathcal{R}_{t,\mathrm{e}} = \sigma_{y0}/|C_y \pm S_y|$ (cf. Refs. [31,37]).

By combining the operation of a TDS with an energy spectrometer and using imaging screens to get two-dimensional transverse beam profiles, longitudinal phase space (energy versus time) measurements with single-shot capability can be achieved. The simplest magnetic energy spectrometer consists of a dispersive beam line downstream of a dipole magnet. The corresponding horizontal betatron motion, which is perpendicular to the shearing plane of the TDS, is given by (e.g., Refs. [31,37])

$$x(s) = x_0(s) + D_x(s, s_0)\delta \quad (3)$$

with the horizontal dispersion $D_x$ and the relative momentum deviation $\delta = \Delta p/p$. The magnetic energy spectrometer used at FLASH has a nominal horizontal dispersion of about 750 mm at the position of the screen station [36]. For relativistic electron beam energies with a Lorentz factor of $\gamma \gg 1$, which is the case throughout this paper, the electron beam energy is given by $E \approx pc$, and $\delta$ can be described as the relative energy deviation. Then the expression in Eq. (3) represents a linear mapping between the relative energy deviation and the horizontal coordinate, where $D_x$ determines the slope of the mapping. The dispersion $D_x$ can be calibrated by measuring the horizontal centroid offset of the bunch as a function of the energy deviation. The rms resolution of the relative energy deviation is defined as $\mathcal{R}_{\delta,\mathrm{e}} = \sigma_{x0}/D_x$ (cf. time resolution $\mathcal{R}_{t,\mathrm{e}}$), but here, the intrinsic beam size, and correspondingly the energy resolution cannot simply be measured by switching the dipole magnet off. A possibility to estimate the relative energy resolution is given by the deviations in the measurement of a well-known energy spread (see Refs. [31,36] for more details).

### B. Frequency-domain terahertz spectroscopy of coherent transition radiation

The frequency-domain longitudinal electron bunch profile measurements were carried out by spectroscopy of coherent transition radiation using a multichannel terahertz (THz) spectrometer. The schematic and basic layout of the THz spectrometer is shown in Fig. 2. The design is based on five stages of blazed reflection gratings in combination with focusing ring mirrors. Fast readout of the pyroelectric detector arrays allows single-shot diagnostics. The technical details about the focusing ring mirror design and the spectrometer principle can be found in Ref. [38], and technical details and performance measurements on the particular THz spectrometer used throughout the measurements presented in this paper can be found in Ref. [39]. At FLASH, two identical THz spectrometers exist, one upstream of the energy collimator (see Fig. 1), which was used for the spectroscopic measurements presented in this paper, and one close to the undulators, which is currently being commissioned.

The basic principle of spectroscopy for longitudinal electron bunch profile diagnostics relies on the spectral intensity of transition radiation (diffraction or synchrotron radiation are also suitable) emitted by an electron bunch with $N$ electrons which is given by [39–42]

$$\frac{dI}{d\lambda} = \frac{dI_1}{d\lambda}[N + (N-1)N|F(\lambda)|^2], \quad (4)$$

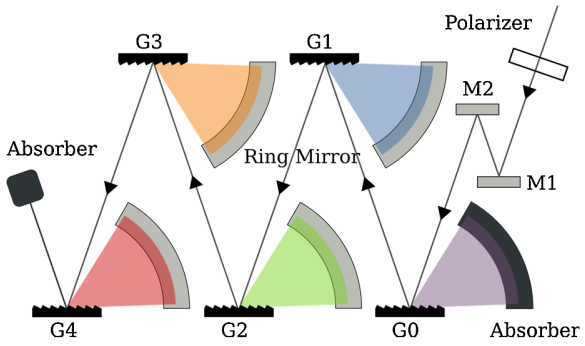


(a) Spectrometer layout with multiple stages (top view).

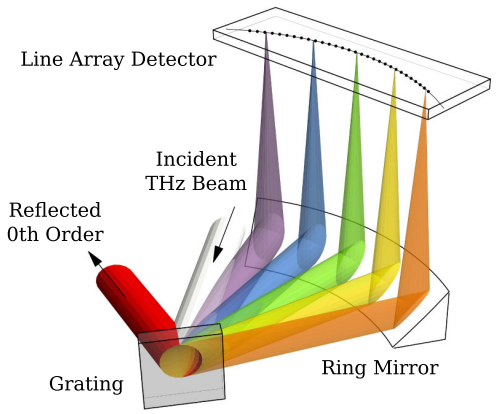


(b) One stage with grating, ring mirror, and detector.

FIG. 2. Principle of the multichannel THz and infrared spectrometer based on five stages of blazed reflection gratings in combination with focusing ring mirrors. The schematic layout is depicted in (a), and (b) shows one stage exemplarily (see Refs. [38,39] for technical details). The fast readout of the pyroelectric detector arrays allows single-shot spectroscopy.

where $d\mathcal{I}_1/d\lambda$ is the spectral intensity of a single electron, and $F(\lambda)$ is the longitudinal form factor of the bunch as a function of the wavelength $\lambda$, which can be expressed by the Fourier transform of the normalized longitudinal charge density $\rho_N(z)$, i.e., the electron bunch current, as

$$F(\lambda) = \int_{-\infty}^{\infty} \rho_N(z) e^{-i2\pi z/\lambda} dz. \tag{5}$$

In Eq. (4) we have made use of the fact that radiation from relativistic electrons is confined to small angles, hence we have neglected transverse beam size effects [39]. Inverse Fourier transform permits the reconstruction of the longitudinal electron bunch profile, i.e., the bunch current $I(z) = Q\rho_N(z)$ with the bunch charge $Q$, when the complex form factor $F(\lambda) = |F(\lambda)|e^{i\Phi(\lambda)}$ is known.

Only the modulus of the longitudinal form factor $|F(\lambda)|$ can be determined experimentally [see Eq. (4)], and the phase information $\Phi(\lambda)$ remains unknown. However, a phase retrieval can be achieved by applying the Kramers-Kronig relations (e.g., Refs. [40–42]), which connect the real and imaginary parts of a complex function. Taking the logarithm of the complex form factor $\ln F = \ln|F| + i\Phi$ and applying a Hilbert transform yields

$$\begin{aligned}\Phi(\omega) &= -\frac{1}{\pi}\mathcal{P}\int_{-\infty}^{\infty} \frac{\ln|F(\omega')|}{\omega' - \omega} d\omega' + \Phi_B(\omega) \\ &= -\frac{2\omega}{\pi}\mathcal{P}\int_{0}^{\infty} \frac{\ln|F(\omega')|}{\omega'^2 - \omega^2} d\omega' + \Phi_B(\omega),\end{aligned} \tag{6}$$

where $\Phi_B$ is the Blaschke phase, $\mathcal{P}$ denotes the Cauchy principal value, and $\omega = 2\pi c/\lambda$. The Blaschke phase cannot be determined from the modulus of the form factor and is omitted [$\Phi_B(\omega) \equiv 0$] in the following. A profile reconstruction with the remaining minimal phase gives the most compact profile compatible with the measured form factor $|F|$. In general, this is a good approximation, as demonstrated in Sec. III B, and uncertainties due to measurement errors may have larger impact (see, e.g., Refs. [40,42]). Changing to wavelengths and removing the singularity at $\omega = \omega'$ in Eq. (6) results in [40,42]

$$\Phi(\lambda) = \frac{2}{\pi\lambda}\int_{0}^{\infty} \frac{\ln[|F(\lambda')|/|F(\lambda)|]}{1 - (\lambda'/\lambda)^2} d\lambda'. \tag{7}$$

The inverse Fourier transform of Eq. (5) can be given by

$$\rho_N(z) = -2\int_{0}^{\infty} |F(\lambda')|\cos[2\pi z/\lambda' - \Phi(\lambda')]\frac{d\lambda'}{\lambda'^2} \tag{8}$$

when considering only positive wavelengths ($\lambda > 0$). Equations (7) and (8) are the fundamental expressions for longitudinal electron bunch profile reconstruction from spectroscopic measurements and are used later in Sec. III B.

### C. Statistical fluctuations of the radiation pulse energy in SASE FELs

The amplification process in a SASE FEL starts from shot noise in the electron beam, passes the stage of exponential amplification ($s/L_{\mathrm{sat}} \approx 0.8$), and finally enters the saturation regime ($s/L_{\mathrm{sat}} \approx 1$), where $s/L_{\mathrm{sat}}$ is the normalized undulator length with $L_{\mathrm{sat}}$ being the saturation length (see Fig. 3). The FEL radiation pulse energy exhibits shot-to-shot fluctuations, which are larger for shorter pulse durations. The maximum fluctuations are present at the end of the high-gain exponential gain regime. Radiation from a SASE FEL operating in the exponential gain regime possesses the properties of completely chaotic polarized light [20,21]. One consequence is that the probability distribution of the energy in the radiation pulse is given by the gamma distribution

$$p(E) = \frac{M^M}{\Gamma(M)}\left(\frac{E}{\langle E\rangle}\right)^{M-1}\frac{1}{\langle E\rangle}\exp\left(-M\frac{E}{\langle E\rangle}\right), \tag{9}$$

where $\Gamma(M)$ is the gamma function, $M = 1/(\sigma_E/\langle E\rangle)^2$, and $\sigma_E = \sqrt{\langle(E - \langle E\rangle)^2\rangle}$ is the FEL radiation pulse energy

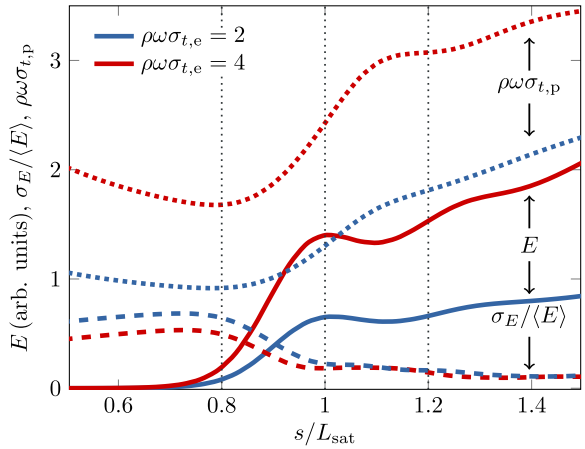


(a) Absolute values.

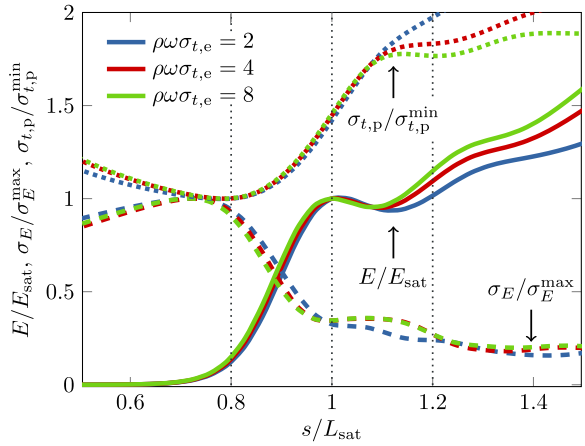


FIG. 3. Simulations on the evolution of FEL related parameters versus normalized undulator length $s/L_{sat}$: (a) Evolution of the energy $E$ in the radiation pulse (solid lines), the fluctuations of the radiation pulse energy $\sigma_E/\langle E\rangle$ (dashed lines), and the normalized rms FEL radiation pulse duration $\rho\omega\sigma_{t,p}$ (dotted lines) for normalized rms electron bunch lengths of $\rho\omega\sigma_{t,e} = 2$ and 4 (blue and red), and (b) the normalized values of $E/E_{sat}$, $\sigma_E/\sigma_E^{max}$, and $\sigma_{t,p}/\sigma_{t,p}^{min}$ for the rms electron bunch lengths of $\rho\omega\sigma_{t,e} = 2$, 4, and 8 (blue, red, and green).

spread. The parameter $M$ can be interpreted as the average number of "degrees of freedom" or "modes" in the radiation pulse (see, e.g., Refs. [20,21]). With knowledge of the coherence time $\tau_c$, the FEL radiation pulse duration can be estimated as $\sim M \times \tau_c$. This estimate assumes a high degree of transverse coherence, which is true for the parameter space of well designed SASE FELs like FLASH. In the framework of a one-dimensional model, the maximum value of the coherence time

$$\tau_c^{max} \simeq \frac{1}{\rho\omega}\sqrt{\frac{\pi \ln N_c}{18}} \tag{10}$$

and the saturation length

$$L_{sat} \simeq \frac{\lambda_u}{4\pi\rho}\left(3 + \frac{\ln N_c}{\sqrt{3}}\right) \tag{11}$$

are expressed in terms of the FEL parameter $\rho$ [43] and the number of the electrons $N_c = I/(e\rho\omega)$ cooperating to the SASE FEL process [20,21,44]. Here, $\omega/(2\pi) = c/\lambda$ is the frequency of the amplified wave, $I$ is the electron bunch current, and $\lambda_u$ is the undulator period. A suitable estimate for the parameter $\rho$ comes from the observation that in the parameter range of SASE FELs operating in the extreme-ultraviolet and x-ray wavelength range, the number of field gain lengths to saturation is about 10 (e.g., Ref. [20]). The FEL parameter $\rho$ and the coherence time $\tau_c$ are related to the saturation length $L_{sat}$ as

$$\rho \simeq \lambda_u/L_{sat}, \qquad \tau_c \simeq \lambda L_{sat}/(2\sqrt{\pi}c\lambda_u). \tag{12}$$

These simple physical considerations are confirmed with numerical simulations using the time-dependent simulation code FAST [45]. Here, we consider the model of a Gaussian longitudinal electron bunch profile, and trace FEL parameters for different values of the rms electron bunch length $\sigma_{t,e}$. Figure 3(a) shows the evolution of the energy $E$ in the radiation pulse, the fluctuations of the radiation pulse energy $\sigma_E/\langle E\rangle$, and the normalized rms FEL radiation pulse duration $\rho\omega\sigma_{t,p}$ along the undulator. Qualitative observations are that the radiation pulse energy and pulse duration grow with increasing electron bunch length, and the maximum fluctuations of the radiation pulse energy and the minimum rms radiation pulse duration are observed at the end of the exponential gain regime ($s/L_{sat} \lesssim 0.8$). The normalized values of these parameters, i.e., $E/E_{sat}$, $\sigma_E/\sigma_E^{max}$, and $\sigma_{t,p}/\sigma_{t,p}^{min}$, exhibit nearly universal dependencies for a normalized electron bunch length $\rho\omega\sigma_{t,e} \gtrsim 1$ as it is shown in Fig. 3(b). This allows one to derive a universal dependency between the rms electron bunch length $\sigma_{t,e}$ and the full width at half maximum (FWHM) radiation pulse duration $T_p^{min} = 2\sqrt{2\ln 2}\sigma_{t,p}^{min}$ at the end of the exponential gain regime as a function of the number of modes $M$ in the FEL radiation pulse (see Fig. 4). For $M \gtrsim 2$ and with reasonable practical accuracy we have

$$\sigma_{t,E} \simeq 2\sqrt{2\ln 2}\sigma_{t,p}^{min} = T_p^{min} \simeq \frac{M\lambda}{5c\rho} \simeq \frac{M\lambda L_{sat}}{5c\lambda_u}. \tag{13}$$

The minimum FWHM FEL radiation pulse duration expressed in terms of the coherence time [cf. Eq. (12)] is $T_p^{min} \simeq 0.7 \times M \times \tau_c$. Lengthening of the FEL radiation pulse occurs when the amplification process enters the saturation regime and happens due to two effects. The first effect is lasing toward saturation in the tails of the electron bunch, and the second effect is radiation pulse lengthening due to slippage effects, which is one radiation wavelength per undulator period. The effect of lasing in the tails gives

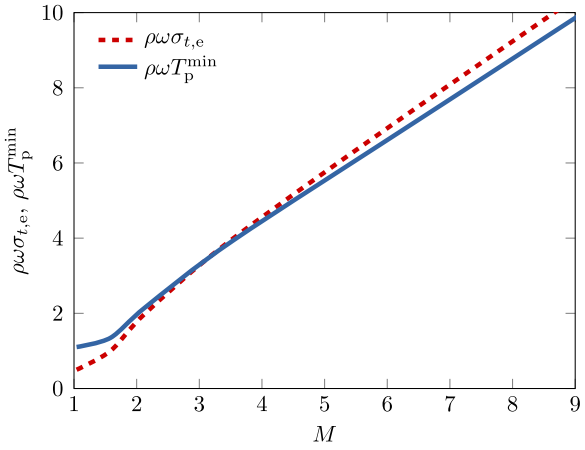


FIG. 4. Normalized rms electron bunch length $\rho\omega\sigma_{t,\mathrm{e}}$ contributing to the FEL process (red dashed line) and the corresponding normalized minimum FWHM radiation pulse duration $\rho\omega T_p^{\mathrm{min}}$ (blue solid line) at the end of the exponential gain regime ($s/L_{\mathrm{sat}} \lesssim 0.8$) versus the number of modes $M$.

the relative radiation pulse lengthening as it is illustrated in Fig. 3(a). At saturation ($s/L_{\mathrm{sat}} \approx 1$), the pulse lengthening is a factor of about 1.4 with respect to the minimum pulse duration in the exponential gain regime ($s/L_{\mathrm{sat}} \lesssim 0.8$) given by Eq. (13), and it is increased up to a factor of 2 in the deep nonlinear regime ($s/L_{\mathrm{sat}} \gtrsim 1.2$). It is also seen that the slippage effect is more pronounced for relative lengthening of short pulses.

Measurements of statistical properties of SASE FELs allow one to estimate mean photon pulse durations and the lasing fraction of the FEL driving electron bunches, and this technique has been effectively used at FLASH and LCLS [2,6,23]. First, the FEL process is tuned to the maximum radiation pulse energy, which occurs in the saturation regime and beyond ($s/L_{\mathrm{sat}} \gtrsim 1$), and then the FEL radiation pulse energy is recorded at different positions along the undulators by applying orbit kicks in order to suppress lasing. The resulting "FEL gain curve" permits the estimation of the saturation length $L_{\mathrm{sat}}$, and the FEL parameter $\rho$ and the coherence time $\tau_c$ can be calculated by using Eq. (12). Then the FEL process is tuned to the end of the exponential regime at $s/L_{\mathrm{sat}} \lesssim 0.8$ where the FEL radiation power is reduced by a factor of $\sim$20 with respect to the saturation regime [see Fig. 3(a)]. The fluctuations of the FEL radiation pulse energy reach their maximum value at this point, and the inverse squared value of radiation pulse energy fluctuations gives the number of the modes in the radiation pulse. The electron bunch length and the minimum photon pulse duration at the end of the exponential gain regime are then derived from Eq. (13). The relative photon pulse lengthening at saturation corresponds to a factor of about 1.4, and in the (deep) nonlinear regime, it depends on the electron bunch length [see Fig. 3(b)].

## III. EXPERIMENTAL RESULTS AT FLASH

Comparative measurements of soft x-ray pulse durations and electron bunch lengths were carried out for two accelerator and beam settings. In the first step, we measured longitudinal electron bunch profiles determined by both time-domain longitudinal phase measurements and frequency-domain THz spectroscopy for electron bunch charges of 100 and 500 pC in order to verify the consistency of both methods. In the second step, we compared longitudinal electron bunch profiles determined by longitudinal phase measurements with the soft x-ray pulse durations estimated by SASE FEL radiation pulse energy statistics for electron bunch charges of 150 and 500 pC. The relevant parameters are given in Table I.

### A. Longitudinal phase space measurements

The longitudinal phase space measurements were performed using a 100 $\mu$m thick scintillator (YAG:Ce) imaging screen, and the camera system was set up with a spatial resolution of better than 16 $\mu$m. The time calibration was achieved by measuring the vertical electron bunch centroid on the imaging screen during a TDS rf phase scan. By measuring the intrinsic vertical rms beam size, i.e., with the TDS rf power switched off, the rms time resolutions was estimated (see Sec. II A) for each measurement individually. For comparisons with soft x-ray pulse durations (see Sec. IV), 50 consecutive single-shot measurements of the longitudinal phase space were taken for each set of electron beam parameters with bunch charges of 150 and 500 pC. The longitudinal phase space and electron bunch current of typical single shots, together with the single-shot rms bunch lengths, are shown in Fig. 5. The presented measurements were performed for one zero-crossing TDS rf phase, and corrections of a potential longitudinal-to-vertical correlation $C_y$ were neglected with $S_y \gg C_y \approx 0$. This is justified by the large shear parameter (see below) and the agreement in the comparative measurements between TDS and THz spectrometer presented in Fig. 6, where the latter is not sensitive to longitudinal-to-vertical correlations.

The single-shot rms time resolution $\mathcal{R}_{t,\mathrm{e}}$ reached unprecedented 8 fs for the 150 pC case, which corresponds to

TABLE I. Parameters for the comparative measurements of FEL photon pulse durations and electron bunch lengths. The numbers in the brackets of the electron bunch charge and the FEL radiation saturation level are related to each other.

| Parameter | Symbol | Value | Unit |
|---|---|---|---|
| Electron beam energy | $E_{\mathrm{e}}$ | 660 | MeV |
| FEL radiation wavelength | $\lambda$ | 14.6 | nm |
| Electron bunch charge | $Q$ | 150 (500) | pC |
| Saturation level of FEL radiation | $E_{\mathrm{sat}}$ | 30 (200) | $\mu$J |
| Undulator period | $\lambda_u$ | 27.3 | mm |

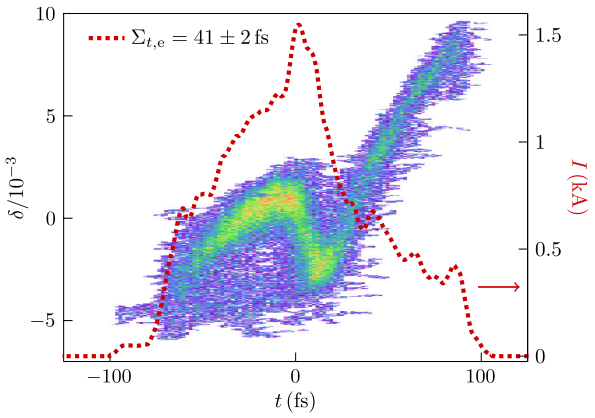


(a) $Q = 150$ pC.

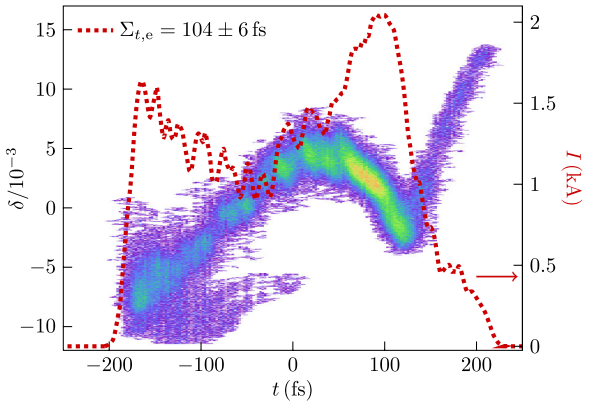


(b) $Q = 500$ pC.

FIG. 5. Single-shot longitudinal phase space and electron bunch current (dotted red lines) measurements using the TDS in combination with the energy spectrometer for bunch charges of (a) 150 pC and (b) 500 pC. The selected single shots represent typical bunches out of 50 measurements, and the rms bunch length values ($\Sigma_{t,e}$) including measurement error in the legends correspond to the shown single shots.

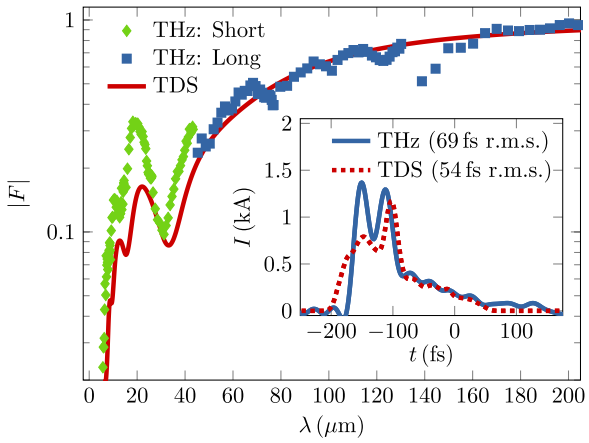


(a) $Q = 100$ pC.

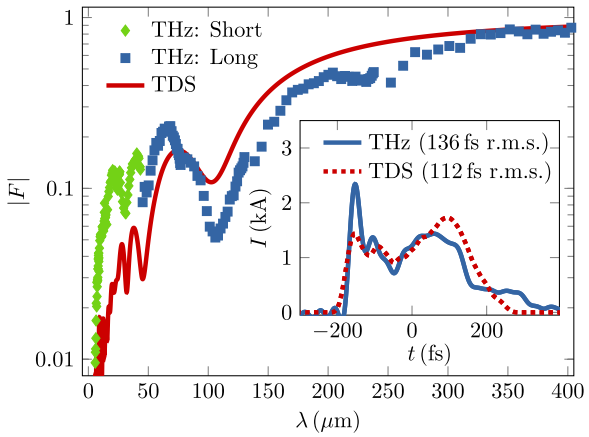


(b) $Q = 500$ pC.

FIG. 6. Mean moduli of the longitudinal form factors measured by THz spectroscopy of coherent transition radiation (green diamonds and blue squares) and derived from TDS measurements (solid red lines), generated by electron bunches with charges of (a) 100 pC and (b) 500 pC, respectively. The insets show single-shot electron bunch currents reconstructed from THz spectra (solid blue lines) in comparison with single-shot TDS measurements (dotted red lines), and the numbers in the brackets represent the calculated rms bunch lengths.

a shear parameter of $S_y c^{-1} = 30$ (significantly larger than any longitudinal-to-vertical correlation $C_y$ observed at FLASH) and an intrinsic vertical rms beam size of $\sigma_{y0} = 70$ $\mu$m. For the 500 pC settings, we achieved an rms time resolution of 13 fs, which is due to a larger intrinsic vertical beam size. The average rms electron bunch lengths, including statistical errors due to fluctuations of electron beam parameters and accelerator settings, of 50 consecutive single shots are $\langle \Sigma_{t,e} \rangle = 41 \pm 3$ fs and $103 \pm 4$ fs for the bunch charges of 150 and 500 pC, respectively. In order to take account of the unknown correlation $C_y$, we admit a systematical uncertainty of $\pm 10\%$ in the rms electron bunch length measurements.

The longitudinal phase space has a similar shape in both cases [Figs. 5(a) and 5(b)] with an overall negative energy chirp $-d\delta/dt$, i.e., electrons in the leading part of the bunch (on the left in Fig. 5) have less energy than those in the trailing part. However, both distributions show a distinct core region with a positive energy chirp, which is most probably generated by space charge forces. In general, the implementation of the new electron bunch compression scheme using the third third-harmonic rf linearizer system [28,29] results in electron bunches with significantly more confined bunch current profiles without trailing tails of picosecond duration [2,6].

### B. Measurement of longitudinal form factors

The principle of longitudinal electron beam diagnostics based on spectroscopy of coherent radiation has been described in Sec. II B. The measurements of the longitudinal form factors were performed by spectroscopy of coherent transition radiation generated from an aluminum

coated silicon screen and using the THz spectrometer upstream of the collimator (see Fig. 1). Technical details about the THz spectrometer and the transport beam line for THz radiation can be found in Refs. [38,39,46]. Several hundred single-shot THz spectra in the wavelength range 5–430 $\mu$m were recorded for electron bunch charges of 100 and 500 pC. At the same time, single-shot longitudinal phase space measurements using the TDS in combination with the energy spectrometer were carried out in order to compare and verify the reconstruction of the longitudinal electron bunch profiles from the spectroscopic measurements. Diagnostics for FEL photon pulse durations were not available during these measurements.

Figure 6 shows the measured mean moduli of the longitudinal form factors, including $|F|$ derived from TDS measurements (red line), together with the reconstructed electron bunch currents in comparison with the corresponding time-domain TDS measurements (insets of Fig. 6). The measurements of the longitudinal form factors $|F|$ were done with two reflection grating sets (''THz: Short'' and ''THz: Long'') and averaged over ~300 single shots. The insets of Fig. 6 show single-shot electron bunch currents reconstructed by means of an inverse Fourier transform using the Kramers-Kronig relations for the phase retrieval in comparison with direct measurements in the time domain using the TDS. The integrals in Eqs. (7) and (8) for the electron bunch profile reconstruction were computed for single shots, representing the typical form factor out of the ~300 measurements, with a short-wavelength cutoff at 5 $\mu$m and by applying an extrapolation with $|F| \rightarrow 1$ for long wavelengths.

The results of both experimental methods are in good agreement and show the same features within the electron bunch currents. The deviations can be explained by uncertainties of both methods, including the unknown and omitted Blaschke phase in Eq. (7), and due to the fact that both diagnostics are not located at the same position along the beam line. In fact, the collimator between the two positions (see Fig. 1) generates longitudinal dispersion, which changes the longitudinal electron bunch profile depending on the actual energy chirp of the electron bunch and the settings of the collimator magnets. Nevertheless, the good overall agreement of the comparative measurement confirms the consistency of both high-resolution longitudinal electron beam diagnostics.

### C. Measurement of FEL pulse energy statistics

The physical background of the FEL photon pulse duration estimations based on statistical properties of SASE FEL radiation has been described in Sec. II C. FLASH is equipped with the following set of detectors for single-shot measurements of the radiation pulse energy: gas monitor detectors, microchannel plate (MCP) based detectors, photodiodes, and thermopiles [47–50]. The detectors are installed at several positions along the photon beam line (see also Fig. 1). The MCP detector is installed in front of all other detectors and is used for precise measurements of the FEL photon pulse energy. The MCP measures the radiation scattered by a metallic mesh (Cu, Fe, and Au targets are being used) placed behind an aperture located downstream of the undulator magnets. The electronics of the MCP detector has an excellent signal-to-noise ratio of about 100 and thus allows high-resolution measurements of the energy fluctuation.

The measurement procedure was organized as follows. First, the SASE FEL process was tuned to the maximum MCP signal at full undulator length of 27 m (six undulator modules). Then an orbit kick was applied by switching on steerer magnets after the fourth undulator module such that the FEL amplification process was suppressed in the last two undulator modules. The level of the FEL radiation pulse energy after four undulator modules was about a factor of ~20 less compared to the level at saturation, and by taking into account the saturation length, which was estimated to be $L_{\mathrm{sat}} = 22.5 \pm 2.5$ m for both electron bunch charges within the presented experimental conditions, the normalized undulator length was $s/L_{\mathrm{sat}} = 0.80 \pm 0.09$ there. It has been shown in Sec. II C that this point corresponds to the end of the exponential gain regime. The aperture of the detector was adjusted such that all photons passed through the scattering target of the detector. Thus, the MCP signal is proportional to the single-shot FEL radiation pulse energy. However, the fluctuations of electron beam and accelerator parameters contribute to the fluctuations of the radiation pulse energies, while only fundamental SASE FEL fluctuations are essential. For this reason, a selection procedure had to be applied to the recorded data. The important electron beam and accelerator parameters, e.g., bunch charge monitor readings, beam position monitor readings, readings of the bunch compression monitors, and read back values of rf parameters were recorded for each shot together with the readings of the MCP detector. If electron beam or accelerator parameters deviated more than the prescribed threshold, the events were excluded from the data set. We note that the number of events in the data set after the selection procedure must be sufficiently large in order to provide an acceptable statistical accuracy.

Figure 7 shows the probability distribution of the FEL radiation pulse energies for the electron bunch charges of 150 and 500 pC. The sets of raw data contained about 1400 (1700) single-shot measurements, and about 800 (550) measurements remained after the data selection procedure for 150 pC (500 pC). The selection was mainly achieved by removing large electron bunch charge fluctuations and rf phase drifts in the first accelerating structure (ACC1) upstream of the first bunch compressor. The data selection thresholds were chosen to remove clear correlations with the MCP readings. The measured number of modes amount to $M = 2.8 \pm 0.5$ and $12 \pm 2$ for the settings

with 150 and 500 pC, respectively, and the quoted errors are based on uncertainties of the data selection procedure. If a Gaussian shape for the lasing fraction of the electron bunch is assumed, we can apply Eq. (13) in order to determine the rms electron bunch length that contributes to lasing and get $\sigma_{t,\mathrm{e}} = 23 \pm 4$ fs and $96 \pm 18$ fs for the electron bunch charge of 150 and 500 pC, respectively. The minimum FWHM photon pulse durations $T_p^{\mathrm{min}}$ at the end of the exponential gain regime are estimated to be these obtained rms electron bunch lengths [see Eq. (13)], i.e., $T_p^{\mathrm{min}} = 23 \pm 4$ fs and $96 \pm 18$ fs, respectively. The quoted errors are purely statistical and assume a Gaussian shape for the lasing fraction of the electron bunch. Significant systematical errors can appear due to large deviations from the assumed longitudinal electron bunch profile and time-dependent electron bunch properties such as the transverse slice emittance.

In parallel with statistical measurements, FEL photon spectra were recorded using the soft x-ray (SXR) spectrometer in the photon beam line. We note that the spectrum is simply a Fourier transform of the temporal structure, and the average number of spikes (modes) in the time domain should be about the same as the number of spikes in the spectral domain. The single-shot soft x-ray spectra were obtained by using a plane grating monochromator, operating in a spectrographic mode with a resolving power $\lambda/\Delta\lambda > 10\,000$ [51]. We observed qualitative agreement between the spectral measurements (number of spikes) and the number of modes measured by FEL pulse energy statistics (see Fig. 8). The detailed analysis of the spectral measurements, taking into account the energy

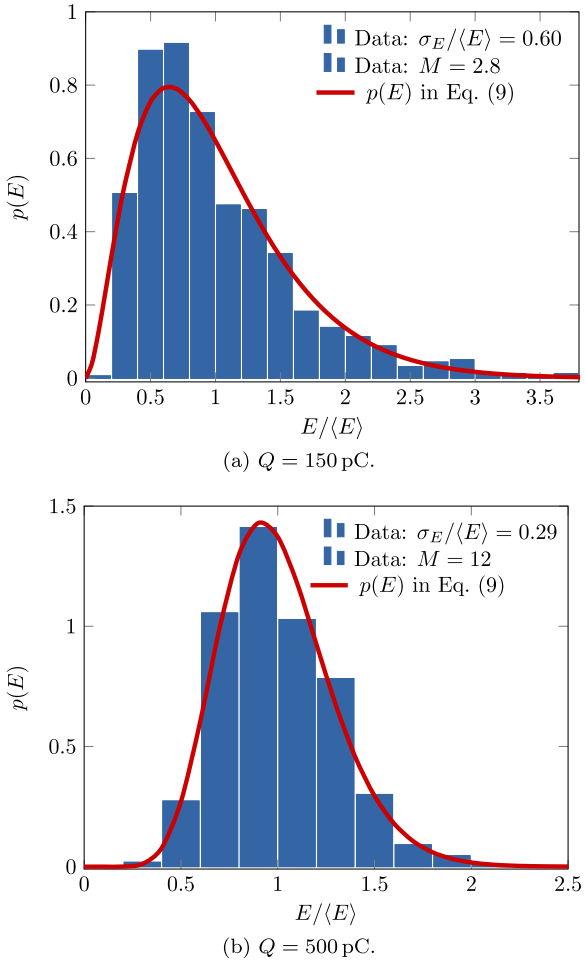


(a) $Q = 150$ pC.

(b) $Q = 500$ pC.

FIG. 7. The probability distributions $p(E)$ of the FEL radiation pulse energy $E$ of soft x-ray pulses at the end of the exponential gain regime for electron bunch charges of (a) 150 pC and (b) 500 pC. The histograms (blue bars) represent the data with the relative radiation pulse energy spread $\sigma_E/\langle E\rangle$, and the solid curve (red lines) show the gamma distribution using $M = 2.8$ and 12 (modes) for 150 and 500 pC, respectively.

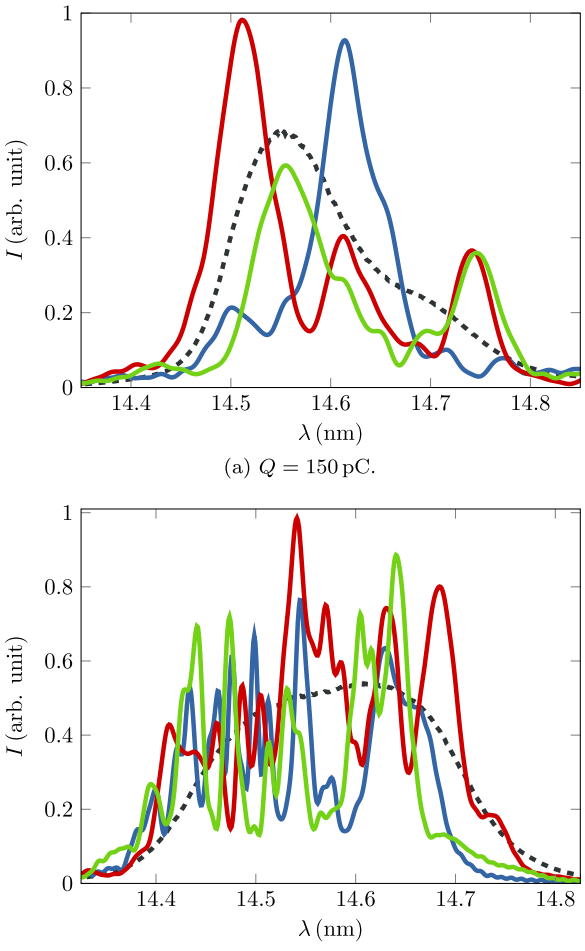


(a) $Q = 150$ pC.

(b) $Q = 500$ pC.

FIG. 8. Single-shot (red, green, and blue solid lines) and mean (dashed black lines) spectra of soft x-ray pulses measured at the end of the exponential gain regime using the SXR spectrometer for the settings with (a) 150 pC and (b) 500 pC. The mean spectra represent an average over ~2500 single shots.

chirp of the electron bunches, is beyond the scope of this paper and will be reported elsewhere.

Based on the theoretical model described in Sec. II C and according to Fig. 3(b), the expected FEL photon pulse durations at saturation and beyond can be extrapolated by the minimum FWHM photon pulse durations measured at the end of the exponential gain regime. In the nonlinear regime at $s/L_{\mathrm{sat}} \approx 1.2$ [see Fig. 3(b)] and by using the measured minimum FWHM photon pulse durations $T_p^{\mathrm{min}}$, we would expect FWHM FEL photon pulse durations of $T_p = 43 \pm 8$ fs (lengthening of ~1.9) and $T_p = 169 \pm 32$ fs (lengthening of ~1.75) for the beam settings with 150 and 500 pC, respectively. For these expected FEL photon pulse durations and by considering the measured average FEL pulse energies (see Table I) of 30 $\mu$J (150 pC) and 200 $\mu$J (500 pC), the peak powers result in $0.7 \pm 0.1$ GW and $1.1 \pm 0.2$ GW, respectively.

## IV. SOFT X-RAY PULSE DURATIONS VERSUS ELECTRON BUNCH LENGTHS

The average rms electron bunch lengths determined by time-domain longitudinal phase space diagnostics are $\langle \Sigma_{t,\mathrm{e}} \rangle = 41 \pm 3$ fs and $103 \pm 4$ fs for the bunch charges of 150 and 500 pC, respectively. The corresponding minimum FWHM soft x-ray pulse durations at the end of the exponential gain regime estimated by SASE FEL pulse energy statistics are $T_p^{\mathrm{min}} = 23 \pm 4$ fs and $96 \pm 18$ fs, respectively, for the same electron bunch charges.

As described in Sec. II C for Gaussian longitudinal profiles, the rms electron bunch length $\sigma_{t,\mathrm{e}}$ that contributes to lasing is related to the minimum FWHM FEL photon pulse duration $T_p^{\mathrm{min}}$ by $\sigma_{t,\mathrm{e}} \simeq T_p^{\mathrm{min}}$ [see Eq. (13)], where $T_p^{\mathrm{min}} = 2\sqrt{2\ln 2}\sigma_{t,p}^{\mathrm{min}}$ with the corresponding minimum rms FEL photon pulse duration $\sigma_{t,p}^{\mathrm{min}}$. The comparison of $\Sigma_{t,\mathrm{e}}$ and $T_p^{\mathrm{min}}$ ($\sigma_{t,\mathrm{e}}$) shows that the rms electron bunch lengths measured by longitudinal phase space diagnostics are larger than estimated by SASE FEL pulse energy statistics, which is more significant for the bunch charge of 150 pC. Figure 9 shows a measured single-shot longitudinal electron bunch profile ($I$ in kA) for 150 pC and two Gaussians ($\mathcal{I}$ in arbitrary units) with standard deviations $\sigma = \sigma_{t,\mathrm{e}} \simeq T_p^{\mathrm{min}}$, which represents a potential lasing part of the electron bunch, and $\sigma = \sigma_{t,p}^{\mathrm{min}} = T_p^{\mathrm{min}}/(2\sqrt{2\ln 2})$, representing the corresponding soft x-ray pulse. The amplitudes and peak positions of the Gaussians were chosen to fit the core region of the measured longitudinal electron bunch profile. The deviations of the estimated minimum FWHM soft x-ray pulse duration $T_p^{\mathrm{min}}$, i.e., the lasing fraction of the electron bunch $\sigma_{t,\mathrm{e}}$, from the measured rms electron bunch length $\Sigma_{t,\mathrm{e}}$ can be explained most likely by the non-Gaussian longitudinal electron beam profile with low currents in the tails that do not contribute to lasing but to the rms electron bunch length value.

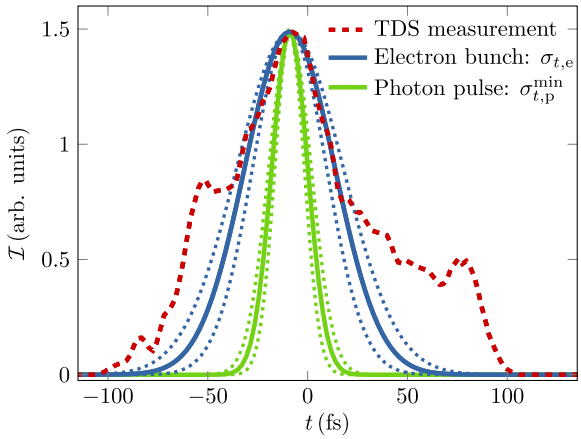


FIG. 9. Single-shot longitudinal electron bunch profile measurement using the TDS for a bunch charge of 150 pC (dashed red line). The selected single shot represents a typical bunch out of 50 measurements [cf. Fig. 5(a)] with an rms bunch length of $\Sigma_{t,\mathrm{e}} = 41 \pm 2$ fs. The blue solid (dotted) line shows a Gaussian with $\sigma = 23 \pm 4$ fs representing the width $\sigma_{t,\mathrm{e}}$ of a potential lasing part of the electron bunch. The green solid (dotted) line shows a Gaussian with $\sigma = (23 \pm 4)/(2\sqrt{2\ln 2})$ fs representing the corresponding soft x-ray (photon) pulse duration $\sigma_{t,p}^{\mathrm{min}}$. The dotted lines describe the error bands ( $\pm$ ).

In cases of non-Gaussian longitudinal electron bunch profiles, e.g., an electron bunch compression mode with a short leading spike (e.g., Refs. [2,6]), a Gaussian-like core region needs to be identified in order to determine the pulse durations. For instance, the FWHM bunch length value, which is not that sensitive to tails in the electron bunch, can be determined and used to calculate an effective rms bunch length for comparison with the minimum FWHM FEL photon pulse duration. For the settings with 150 pC, the FWHM electron bunch length is $70 \pm 17$ fs which corresponds to an effective rms electron bunch length of $30 \pm 7$ fs (cf. with $T_p^{\mathrm{min}} = 23 \pm 4$ fs).

For a more precise identification of the lasing part within the electron bunches, simultaneous information of other parameters, e.g., the slice emittance, or time-domain measurements of the FEL photon pulse profiles (e.g., Refs. [18,19,25]) are required. However, the longitudinal electron beam diagnostics discussed here provide robust estimates on the upper limits of the expected FEL photon pulse durations and allows their monitoring.

## V. SUMMARY AND CONCLUSIONS

Information on the FEL photon pulse durations is important for time-resolved and high intensity experiments in photon science. However, direct measurement of femtosecond FEL photon pulse durations in the extreme-ultraviolet and x-ray wavelength range is a tremendous challenge, and well established methods are not yet available. The theoretical considerations, simulations, and experimental data presented in this paper show that

high-resolution electron beam diagnostics can be utilized to provide reasonable constraints on expected FEL photon pulse durations. We discussed two different longitudinal electron beam diagnostics with single-shot capability and femtosecond accuracy, and presented consistent single-shot measurements of longitudinal electron bunch profiles with good agreement. The electron beam measurements were performed in the frequency domain by THz spectroscopy of coherent transition radiation and in the time domain by longitudinal phase space measurements using a TDS in combination with a magnetic energy spectrometer. In the latter case, an unprecedented single-shot rms time resolution of 8 fs has been achieved. The results from the longitudinal phase space measurements were compared with soft x-ray pulse durations estimated by SASE FEL pulse energy statistics, and the consistent results show that rms electron bunch lengths, determined by longitudinal electron beam diagnostics, provide upper limits on the expected FWHM FEL photon pulse durations. Theoretical considerations and FEL simulations verify this experimental observation and facilitate the extrapolation of the expected FEL photon pulse durations in the saturation regime and beyond based on the measurements in exponential gain regime. In addition, we demonstrated the generation of soft x-ray pulses with a peak radiation power in the GW level and with durations well below 50 fs (FWHM) after implementation of the new uniform electron bunch compression scheme using a third-harmonic rf linearizer system at FLASH.

## ACKNOWLEDGMENTS

We would like to thank the entire FLASH team, and the engineers and technicians of the DESY groups FLA, MCS, and MVS for their support. In particular, we thank T. Limberg, S. Schreiber, and R. Treusch for general support, B. Faatz and K. Honkavaara for providing beam time, and P. Emma and Z. Huang for helpful discussions.

[1] T. H. Maiman, Nature (London) **187**, 493 (1960).
[2] W. Ackermann *et al.*, Nature Photon. **1**, 336 (2007).
[3] P. Emma *et al.*, Nature Photon. **4**, 641 (2010).
[4] D. Pile, Nature Photon. **5**, 456 (2011).
[5] S. Jamison, Nature Photon. **4**, 589 (2010).
[6] V. Ayvazyan *et al.*, Phys. Rev. Lett. **88**, 104802 (2002).
[7] S. Düsterer, P. Radcliffe, C. Bostedt, J. Bozek, A. L. Cavalieri, R. Coffee, J. T. Costello, D. Cubaynes, L. F. DiMauro, Y. Ding, G. Doumy, F. Grüner, W. Helml, W. Schweinberger, R. Kienberger, A. R. Maier, M. Messerschmidt, V. Richardson, C. Roedig, T. Tschentscher, and M. Meyer, New J. Phys. **13**, 093024 (2011).
[8] R. Neutze, R. Wouts, D. van der Spoel, E. Weckert, and J. Hajdu, Nature (London) **406**, 752 (2000).
[9] Y. Ding, A. Brachmann, F.-J. Decker, D. Dowell, P. Emma, J. Frisch, S. Gilevich, G. Hays, Ph. Hering, Z. Huang, R. Iverson, H. Loos, A. Miahnahri, H.-D. Nuhn, D. Ratner, J. Turner, J. Welch, W. White, and J. Wu, Phys. Rev. Lett. **102**, 254801 (2009).
[10] Z. Huang, A. Baker, C. Behrens, M. Boyes, J. Craft, F.-J. Decker, Y. Ding, P. Emma, J. Frisch, R. Iverson, J. Lipari, H. Loos, and D. Walz, in Proceedings of the 24th Particle Accelerator Conference, New York, USA, 2011, THP183.
[11] I. Zagorodnov, in Proceedings of the 32nd International Free Electron Laser Conference, Malmö, Sweden, 2010, WEOBI2.
[12] E. L. Saldin, E. A. Schneidmiller, and M. V. Yurkov, Opt. Commun. **212**, 377 (2002).
[13] A. A. Zholents and W. M. Fawley, Phys. Rev. Lett. **92**, 224801 (2004).
[14] E. L. Saldin, E. A. Schneidmiller, and M. V. Yurkov, Phys. Rev. ST Accel. Beams **9**, 050702 (2006).
[15] D. Xiang, Z. Huang, and G. Stupakov, Phys. Rev. ST Accel. Beams **12**, 060701 (2009).
[16] M. Dohlus, E. A. Schneidmiller, and M. V. Yurkov, Phys. Rev. ST Accel. Beams **14**, 090702 (2011).
[17] P. Emma, K. Bane, M. Cornacchia, Z. Huang, H. Schlarb, G. Stupakov, and D. Walz, Phys. Rev. Lett. **92**, 074801 (2004).
[18] U. Frühling, M. Wieland, M. Gensch, T. Gebert, B. Schütte, M. Krikunova, R. Kalms, F. Budzyn, O. Grimm, J. Rossbach, E. Plönjes, and M. Drescher, Nature Photon. **3**, 523 (2009).
[19] A. L. Cavalieri and H. Schlarb (private communication).
[20] E. L. Saldin, E. A. Schneidmiller, and M. V. Yurkov, Opt. Commun. **148**, 383 (1998).
[21] E. L. Saldin, E. A. Schneidmiller, and M. V. Yurkov, *The Physics of Free Electron Lasers* (Springer-Verlag, Berlin, 1999).
[22] E. L. Saldin, E. A. Schneidmiller, and M. V. Yurkov, New J. Phys. **12**, 035010 (2010).
[23] J. Wu, Y. Ding, P. Emma, Z. Huang, H. Loos, M. Messerschmidt, E. A. Schneidmiller, and M. V. Yurkov, in Proceedings of the 32nd International Free Electron Laser Conference, Malmö, Sweden, 2010, MOPC14.
[24] E. L. Saldin, E. A. Schneidmiller, and M. V. Yurkov, Phys. Rev. ST Accel. Beams **13**, 030701 (2010).
[25] Y. Ding, C. Behrens, P. Emma, J. Frisch, Z. Huang, H. Loos, P. Krejcik, and M-H. Wang, Phys. Rev. ST Accel. Beams **14**, 120701 (2011).
[26] A. M. Kondratenko and E. L. Saldin, Part. Accel. **10**, 207 (1980).
[27] S. Schreiber, B. Faatz, J. Feldhaus, K. Honkavaara, R. Treusch, M. Vogt, and J. Rossbach, in Proceedings of the 32nd International Free Electron Laser Conference, Malmö, Sweden, 2010, TUOBI2.
[28] E. Vogel *et al.*, in *Proceedings of the 1st International Particle Accelerator Conference, Kyoto, Japan, 2010* (ICR, Kyoto, 2010), THPD0003.
[29] H. Edwards, C. Behrens, and E. Harms, in Proceedings of the 25th International Linear Accelerator Conference, Tsukuba, Japan, 2010, MO304.
[30] E. L. Saldin, E. A. Schneidmiller, and M. V. Yurkov, Report No. TESLA-FEL-2004-06, 2004.
[31] M. Röhrs, Ch. Gerth, H. Schlarb, B. Schmidt, and P. Schmüser, Phys. Rev. ST Accel. Beams **12**, 050704 (2009).

[32] O. Altenmueller, R. Larsen, and G. Loew, Rev. Sci. Instrum. **35**, 438 (1964).
[33] P. Emma, J. Frisch, and P. Krejcik, Technical Report No. LCLS-TN-00-12, 2000.
[34] D. Filippetto *et al.*, Phys. Rev. ST Accel. Beams **14**, 092804 (2011).
[35] C. Behrens, Ch. Gerth, and I. Zagorodnov, in *Proceedings of the 31st International Free Electron Laser Conference, Liverpool, United Kingdom, 2009* (STFC Daresbury Laboratory, Warrington, 2009), WEPC45.
[36] C. Behrens and Ch. Gerth, in Proceedings of the 32nd International Free Electron Laser Conference, Malmö, Sweden, 2010, MOPC08.
[37] C. Behrens and Ch. Gerth, in Proceedings of the 9th European Workshop on Beam Diagnostics and Instrumentation for Particle Accelerators, Basel, Switzerland, 2009, TUPB44.
[38] H. Delsim-Hashemi, Report No. DESY-THESIS-2008-024, 2008.
[39] S. Wesch, B. Schmidt, C. Behrens, H. Delsim-Hashemi, and P. Schmüser, Nucl. Instrum. Methods Phys. Res., Sect. A **665**, 40 (2011).
[40] R. Lai and A. J. Sievers, Nucl. Instrum. Methods Phys. Res., Sect. A **397**, 221 (1997).
[41] D. Mihalcea, C. L. Bohn, U. Happek, and P. Piot, Phys. Rev. ST Accel. Beams **9**, 082801 (2006).
[42] O. Grimm and P. Schmüser, Report No. TESLA-FEL-2006-03, 2006.
[43] R. Bonifacio, C. Pellegrini, and L. M. Narducci, Opt. Commun. **50**, 373 (1984).
[44] R. Bonifacio, L. De Salvo, P. Pierini, N. Piovella, and C. Pellegrini, Phys. Rev. Lett. **73**, 70 (1994).
[45] E. L. Saldin, E. A. Schneidmiller, and M. V. Yurkov, Nucl. Instrum. Methods Phys. Res., Sect. A **429**, 233 (1999).
[46] S. Casalbuoni, B. Schmidt, P. Schmüser, V. Arsov, and S. Wesch, Phys. Rev. ST Accel. Beams **12**, 030705 (2009).
[47] M. Richter, A. Gottwald, U. Kroth, A. A. Sorokin, S. V. Bobashev, L. A. Shmaenok, J. Feldhaus, Ch. Gerth, B. Steeg, K. Tiedtke, and R. Treusch, Appl. Phys. Lett. **83**, 2970 (2003).
[48] A. Bytchkov, A. A Fateev, J. Feldhaus, U. Hahn, M. Hesse, U. Jastrow, V. Kocharyan, N. I. Lebedev, E. A. Matyushevskiy, E. L. Saldin, E. A. Schneidmiller, A. V. Shabunov, K. P. Sytchev, K. Tiedtke, R. Treusch, and M. V. Yurkov, Nucl. Instrum. Methods Phys. Res., Sect. A **528**, 254 (2004).
[49] L. Bittner, J. Feldhaus, U. Hahn, M. Hesse, U. Jastrow, V. Kocharyan, P. Radcliffe, E. L. Saldin, E. A. Schneidmiller, K. Tiedtke, B. Timmann, R. Treusch, N. von Bargen, M. V. Yurkov, O. I. Brovko, D. Kharlamov, V. I. Lokhmatov, E. A. Matyushevskiy, A. V. Shabunov, and E. M. Syresin, in Proceedings of the 29th International Free Electron Laser Conference, Novosibirsk, Russia, 2007, WEPPH007.
[50] K. Tiedtke *et al.*, New J. Phys. **11**, 023029 (2009).
[51] N. Gerasimova, S. Dziarzhytski, and J. Feldhaus, J. Mod. Opt. **58**, 1480 (2011).

## 5.2 Femtosecond x-ray pulse temporal characterization in free-electron lasers using a transverse deflector

The realization and interpretation of various experiments on ultrafast dynamics in photon science at X-ray free-electron lasers (see Sec. 1.2) are based on the reliable generation and temporal characterization of femtosecond FEL radiation pulses. Time-resolved electron beam diagnostics at a soft X-ray FEL demonstrated robust estimates on the upper limits of the expected FEL radiation pulse durations [57] and allow their monitoring during the FEL operation. However, for a more precise identification of the lasing part within the electron bunches and for actual temporal profiles of the power in the FEL radiation pulses, direct time-domain measurements of the temporal FEL radiation pulse profiles are required.

As has been discussed in chapter 2, the principle of X-ray FELs is based on the resonant energy transfer between a relativistic electron beam and an EM wave copropagating through a long undulator. When FEL amplification takes place, charge density modulations on the scale of the resonant wavelength develop and lead to a corresponding net energy transfer from the electrons to the EM wave. As a consequence, the FEL amplification process induces a time-dependent energy loss and spread within the electron bunches. The temporal FEL radiation pulse profiles appear then as a replica within the longitudinal phase space of the FEL driving electron bunches downstream of the undulator (e.g., Refs. [74, 107, 114]) and can thus be measured by longitudinal phase space diagnostics for electron beams.

In order to separate the FEL radiation pulses for experiments and to finally dump the electron beams, X-ray FELs have a large dispersive beamline downstream of the undulator, which can be utilized as a magnetic energy spectrometer. The combination of such a dispersive beamline with a transverse deflecting r.f. structures allows single-shot measurements of the longitudinal phase space, which do not disturb the FEL operation. Transverse deflecting r.f. structures in combination with magnetic energy spectrometers (e.g., Refs. [57, 101, 113]) demonstrated temporal resolutions of sub-10 fs r.m.s. [57] and relative energy resolutions of $\sim 10^{-4}$ r.m.s. [88]. By using X-band r.f. technology and magnetic energy spectrometers with optimized dispersion, temporal resolutions of $\sim$ 1 fs r.m.s. and relative energy resolutions well below $\sim 10^{-5}$ r.m.s. can be expected [74]. These unprecedented resolutions will be sufficient to measure the induced time-dependent energy change within the electron bunches, making single-shot characterization of the temporal FEL radiation pulses possible.

The following article reports on a novel concept for temporal X-ray pulse characterization at FELs based on single-shot longitudinal phase space diagnostics for electron beams. The presented calculations and simulations show the capability for simultaneous measurements of temporal X-ray pulse and electron bunch profiles with femtosecond resolution.

# Femtosecond x-ray pulse temporal characterization in free-electron lasers using a transverse deflector

Y. Ding,[1,*] C. Behrens,[2] P. Emma,[1] J. Frisch,[1] Z. Huang,[1] H. Loos,[1] P. Krejcik,[1] and M-H. Wang[1]

[1]*SLAC National Accelerator Laboratory, Menlo Park, California 94025, USA*

[2]*Deutsches Elektronen-Synchrotron (DESY), Hamburg, Germany*

(Received 18 August 2011; published 7 December 2011)

We propose a novel method to characterize the temporal duration and shape of femtosecond x-ray pulses in a free-electron laser (FEL) by measuring the time-resolved electron-beam energy loss and energy spread induced by the FEL process, with a transverse radio-frequency deflector located after the undulator. Its merits are simplicity, high resolution, wide diagnostic range, and noninvasive to user operation. When the system is applied to the Linac Coherent Light Source, the world's most powerful x-ray FEL, it can provide single-shot measurements of the electron-beam and x-ray pulses with a resolution on the order of 1–2 femtoseconds rms.

DOI: 10.1103/PhysRevSTAB.14.120701 PACS numbers: 41.60.Cr, 41.50.+h

## I. INTRODUCTION

The successful operation of the Linac Coherent Light Source (LCLS) [1], with its capability of generating free-electron laser (FEL) x-ray pulses from a few femtoseconds (fs) up to a few hundred fs, opens up vast opportunities for studying atoms and molecules on this unprecedented ultrashort time scale. However, tremendous challenges remain in the measurement and control of these ultrashort pulses with femtosecond precision, for both the electron-beam (e-beam) and the x-ray pulses.

For ultrashort e-beam bunch length measurements, a standard method has been established at LCLS using an S-band radio-frequency (rf) deflector, which works like a streak camera for electrons and is capable of resolving bunch lengths as short as ~10 fs rms [1]. However, the e-beam with low charges of 20 pC at LCLS, which is expected to be less than 10 fs in duration, is too short to be measured using this transverse deflector [2]. Recently, a new method of measurement that maps time to energy has been proposed [3] and demonstrated [4] at LCLS, with a measured e-beam resolution about 1 fs rms.

The measurement of the electron bunch length is helpful in estimating the FEL x-ray pulse duration. However, for a realistic beam, such as that with a Gaussian shape or a spiky profile, the FEL amplification varies along the bunch due to peak current or emittance variation. This will result in differences between the temporal shape or duration of the electron bunch and the x-ray pulse. Initial experiments at LCLS have revealed that characterization of the x-ray pulse duration on a shot-by-shot basis is critical for the interpretation of the data. However, in the femtosecond regime, conventional photodetectors and streak cameras do not have a fast enough response time for characterizing the ultrashort x-ray pulses. In addition, because of the vanishingly small cross sections in nonlinear processes at x-ray wavelengths, it makes the temporal correlation techniques very difficult to realize. To overcome these difficulties, some new methods have been studied recently. One of the time-domain methods is the terahertz-field-driven x-ray streak camera [5], where a terahertz field is used to modulate the photoelectrons generated from x-ray gas ionization. By measuring the energy distribution of the photoelectrons the x-ray pulse length can be determined. Here the terahertz radiation is generated from the same electron bunch in a dedicated undulator to achieve a synchronization between the x-ray and terahertz fields. An external optical laser has also been tested to streak the photoelectrons at the LCLS, but single-shot measurements are not possible due to the synchronization difficulties [6]. In the frequency domain, pulse length measurements based on statistical analysis of the fluctuations in the radiation spectrum have been reported [7], and recently this technique has been experimentally studied at LCLS from multishot analysis of the spectral correlation function [8]. There are also other techniques proposed or tested, such as x-ray autocorrelation or x-ray gas interactions [9,10].

We propose a novel method in this paper to characterize the FEL x-ray pulse duration and temporal shape. A transverse rf deflector is used in conjunction with an e-beam energy spectrometer, located after the FEL undulator. By measuring the difference in the e-beam longitudinal phase space between FEL-on and FEL-off, we can obtain the time-resolved energy loss and energy spread induced from the FEL radiation, allowing the FEL x-ray temporal shape to be reconstructed. This is a simple, single-shot method that is noninvasive to the FEL operation. The X-band transverse deflector that has been designed for the LCLS

*ding@slac.stanford.edu

will cover the diagnostic range from a few fs to a few hundred fs over the full range of the FEL radiation wavelengths.

## II. RF DEFLECTOR AND SYSTEM LAYOUT

The idea of using an rf deflecting structure (operating in the TM11 mode) to kick the electron beam was first proposed in the 1960s [11], and has been recently used for e-beam bunch length and temporal profile measurements in FELs and other accelerator facilities [12]. We assume the bunch is deflected in the horizontal plane by the high-frequency time variation of the deflecting fields, where the resulting horizontal beam width measured on a downstream screen (with a phase advance near $\pi/2$) represents a single-shot measure of the absolute bunch temporal profile. This horizontally ''streaked'' e-beam is then sent to an energy spectrometer, which is composed of dipoles and quadrupoles providing large vertical momentum dispersion. If the optics is designed to have a vertical beta function small enough at the downstream screen, the vertical beam extent across the screen represents a momentum spread in the beam. With this setup, the e-beam longitudinal phase space dimensions (time and energy) are mapped into the real space transverse dimensions (horizontal and vertical).

In the FEL process, the interaction between an e-beam and an electromagnetic wave leads to e-beam energy modulation at the fundamental radiation wavelength. As electrons oscillate in the undulator, a periodic density modulation (the so-called ''microbunching'') at the radiation wavelength builds up. The microbunched e-beam then emits coherent radiation at the expense of the electron kinetic energy. The collective interaction of the beam-radiation system leads to an exponential growth of the radiation intensity along the undulator distance. As a result, it causes electron energy loss and energy spread increase and the FEL power reaches saturation. At LCLS, the typical FEL-induced electron energy loss at saturation is more than 10 MeV [1]. To obtain the x-ray temporal profile, we first suppress the FEL process (e.g., by kicking e-beam to make a local oscillating orbit inside the undulator) and measure the e-beam time-energy phase space, from which we can get the e-beam temporal profile and also achieve a baseline (background) on the energy loss. To overcome the fluctuation of the measured background in the FEL-off case, multishot average and jitter correction should be considered in the practical measurements. Next, the FEL is restored and we measure the time-energy phase space again for each bunch. By subtracting the baseline measured with FEL-off, we can obtain the time-resolved energy loss or energy spread due to FEL radiation, shot by shot. The x-ray temporal power profile is then determined by combining the e-beam current profile and the time-resolved energy loss.

Figure 1 shows the beam line layout of this diagnostic system to be installed at the end of the LCLS main undulator. We use two 1-meter long X-band rf deflecting structures to provide a maximum horizontal kick of 46 MeV/c, with 40 MW input rf power at the deflecting structure [13].

## III. APPLICATION OF THE METHOD

The deflecting force imparts a transverse momentum on the bunch with a small kick angle, $\Delta x'$, given by

$$\Delta x'(t) = \frac{eV_0}{pc}\sin(2\pi ct/\lambda + \varphi) \approx \frac{eV_0}{pc}\left(\frac{2\pi}{\lambda}ct\cos\varphi + \sin\varphi\right), \quad (1)$$

where $V_0$ is the deflector peak voltage, $p$ is the beam's longitudinal momentum in the structure, $\lambda = 2.63$ cm is the rf wavelength, $\varphi$ is the rf phase ($= 0$ at zero crossing), and $t$ is the electron time coordinate relative to the bunch center. The approximation is made that the bunch length is much shorter than the rf wavelength, $|ct| \ll \lambda/2\pi$.

From the deflecting point to the downstream screen, the beam is transported through a transfer matrix with angular-to-spatial element $R_{12} = (\beta_{xd}\beta_{xs})^{1/2}\sin\Delta\Psi$. Here $\beta_{xd}$ and $\beta_{xs}$ are the horizontal beta functions at the deflector and the screen, respectively, and $\Delta\Psi$ is the horizontal betatron phase advance from the deflector to the screen. The transverse position of each ultrarelativistic electron on the screen is then given:

$$\Delta x(t) = \frac{eV_0}{pc}\sqrt{\beta_{xd}\beta_{xs}}|\sin\Delta\Psi|\left(\frac{2\pi}{\lambda}ct\cos\varphi + \sin\varphi\right). \quad (2)$$

From Eq. (2) it is clear that, for bunch length measurement, operating at the zero-crossing phase ($\varphi = 0$) gives

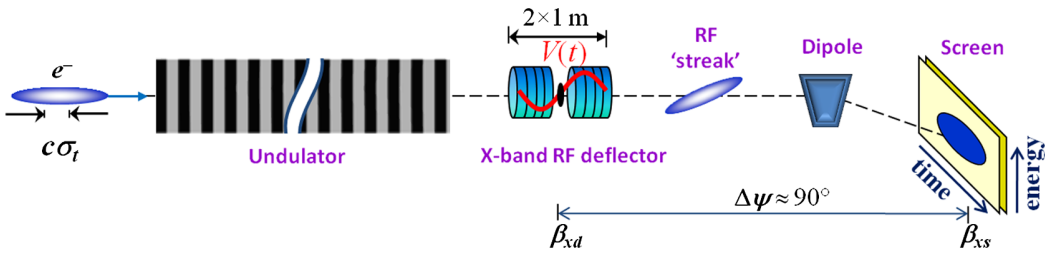


FIG. 1. A layout of the diagnostic system with a transverse rf deflector and an energy spectrometer.

the best streaking effect with the horizontal beam size corresponding to the bunch length ($\sigma_x \propto c\sigma_t$), while $\sin\varphi \neq 0$ gives a centroid offset which can be used for the calibration ($\langle \Delta x \rangle \propto \sin\varphi$). For example, by measuring the horizontal centroid offset with a small rf phase shift around zero crossing, the size of horizontal dimension is calibrated relative to the absolute rf wavelength. From Eq. (2), near zero crossing, the time calibration factor can be written as

$$S = \frac{\sigma_x}{c\sigma_t} = \frac{eV_0}{pc}\sqrt{\beta_{xd}\beta_{xs}}|\sin\Delta\Psi|\frac{2\pi}{\lambda}. \tag{3}$$

For the LCLS e-beam high-energy case of 14 GeV, based on the parameters listed in Table I, $S = 128$. This means if the measured horizontal beam size $\sigma_x = 128$ $\mu$m, the actual bunch length is $c\sigma_t = 1$ $\mu$m.

Note that an X-band rf deflector has been chosen over an S-band one—like the original transverse deflector [11]—in order to impart a stronger sweep to the beam and thus improve the temporal resolution. At X-band the rf wavelength, $\lambda$, is smaller, giving a factor 4 improvement in Eq. (2). Furthermore, higher rf gradients can be achieved at X-band, allowing $V_0$ to be increased and further improving the gain in Eq. (2).

The vertical beam size measured after the vertically bent spectrometer represents the electron energy deviation, which is given by

$$\Delta y = \eta_{ys}\delta, \tag{4}$$

where $\eta_{ys}$ is the vertical momentum dispersion function at the screen, and $\delta$ is the relative energy deviation before the energy spectrometer. Note now we have a two-dimensional image on the screen with $x$ corresponding to time, and $y$ corresponding to energy.

Temporal resolution $\sigma_{t,r}$ and energy resolution $\sigma_{E,r}$ can be defined as

$$\sigma_{t,r} = \frac{\sigma_{x0}}{cS}, \qquad \sigma_{E,r} = \frac{\sigma_{y0}}{\eta_{ys}}E_0, \tag{5}$$

TABLE I. X-band transverse deflector parameters.

| Parameter | Symbol | Value | Unit |
|---|---|---|---|
| rf frequency | $f$ | 11.424 | GHz |
| Deflecting structure length | $L$ | $2 \times 1$ | m |
| rf input power | $P$ | 40 | MW |
| Deflecting voltage (on crest) | $V_0$ | 48 | MV |
| Soft x-ray (e-beam 4.3 GeV) | | | |
| Calibration factor | S | 400 | |
| Temporal resolution (rms) | $\sigma_{t,r}$ | ~1 | fs |
| Energy resolution (rms) | $\sigma_{E,r}$ | 56 | keV |
| Hard x-ray (e-beam 14 GeV) | | | |
| Calibration factor | S | 128 | |
| Temporal resolution (rms) | $\sigma_{t,r}$ | ~2 | fs |
| Energy resolution (rms) | $\sigma_{E,r}$ | 100 | keV |

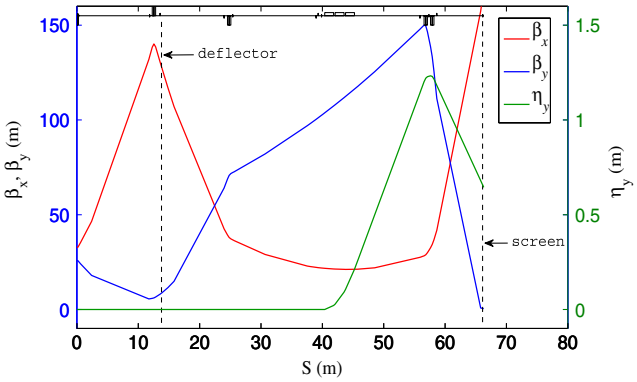


FIG. 2. The optics layout for this diagnostics. The locations of the deflector and screen are marked in the picture.

where $\sigma_{x0}$ or $\sigma_{y0}$ is the nominal transverse beam size at the screen (i.e., in the absence of deflecting voltage for $\sigma_{x0}$, and in the absence of dispersion for $\sigma_{y0}$), and $E_0$ is the average electron energy.

As seen from Eqs. (2), (4), and (5), the beam transportation optics should be optimized to achieve the best resolution. Larger horizontal beta function at the deflector and smaller vertical beta function at the screen are preferred. The optics beta and dispersion functions for the LCLS high-energy case (14 GeV) are shown in Fig. 2, where the existing LCLS beam line magnets are used but their strengths have been adjusted to optimize the beta functions. In this example, the horizontal $\beta_{xd} = 120$ m, $\beta_{xs} = 170$ m, the phase advance $\Delta\Psi = 90°$, the vertical beta function at the screen $\beta_{ys} = 0.54$ m, and the dispersive function $\eta_{ys} = 0.65$ m. A very similar optics setup has also been achieved at low electron energy (4.3 GeV) for soft x-ray generation.

The main parameters are summarized in Table I, based on a normalized projected emittance of 0.6 $\mu$m. The potential temporal resolution is ~1 fs rms for LCLS soft x rays, and ~2 fs rms for hard x rays.

## IV. SIMULATION STUDIES

Start-to-end simulations have been carried out to verify this scheme. IMPACT-T [14] and ELEGANT [15] codes have been used in the injector and main linac, including bunch compressors. In the undulator, a three-dimensional (3D) FEL simulation code GENESIS [16] has been adopted for FEL simulations, where the resistive wakefields from the undulator chamber and the spontaneous undulator radiation are also included. At the end of the undulator, the dumped particles are used again by ELEGANT to track them through the transverse deflector and the energy spectrometer down to the dump screen. From the simulated images with FEL-off and FEL-on on the dump screen, we can analyze the x-ray pulse duration.

We first show an example of the LCLS hard x-ray case (radiation wavelength of 1.5 Å, e-beam energy of

13.6 GeV, total undulator length of 132 m including breaks) with a nominal operating charge of 250 pC. The average e-beam peak current is about 3 kA. Since the resistive wakefields in the linac rf structure lead to a third-order nonlinear curvature in the longitudinal phase space, we typically have a "double-horn" shape in the current profile. It is of great importance and interest to characterize the lasing process from this complicated bunch shape.

Figures 3(a) and 3(b) show the simulated "measurements" of the projected transverse images at the dump screen, with the horizontal axis representing time, and the vertical axis representing energy. Clearly, we can see the difference in the energy dimension between FEL-on and FEL-off. When the FEL is switched off [Fig. 3(a)], we measure a time-resolved e-beam energy [$E_{\mathrm{FEL\,off}}(t)$] and energy spread [$\sigma_{E_{\mathrm{FEL\,off}}}(t)$]. The main collective effects include those from undulator chamber wakes, undulator spontaneous radiation, transverse deflecting, and coherent synchrotron radiation (CSR) in the spectrometer dipoles. When switched on [Fig. 3(b)], the FEL radiation results in an additional energy loss [$\Delta E_{\mathrm{FEL}}(t)$] and energy spread [$\sigma_{E_{\mathrm{FEL}}}(t)$]. Then we measure the e-beam energy ($E_{\mathrm{FEL\,on}}$) and energy spread ($\sigma_{E_{\mathrm{FEL\,on}}}$) for the FEL-on case. From the two measurements we can determine the time-sliced energy loss or energy spread increase purely induced from the FEL radiation:

$$\Delta E_{\mathrm{FEL}}(t) = E_{\mathrm{FEL\,off}}(t) - E_{\mathrm{FEL\,on}}(t),$$
$$\sigma_{E_{\mathrm{FEL}}}(t) = \sqrt{\sigma^2_{E_{\mathrm{FEL\,on}}}(t) - \sigma^2_{E_{\mathrm{FEL\,off}}}(t)}. \quad (6)$$

The horizontal projection of the images in Figs. 3(a) and 3(b) represents the e-beam temporal profile $I(t)$. The transverse deflector method provides an additional technique for eliminating systematic correlation errors. The upstream bunch compressors in the LCLS are in the horizontal plane and the CSR from their bends introduces a transverse kick to the electrons which is correlated to their longitudinal position in the bunch [17]. This correlation between the horizontal and longitudinal planes can affect the phase

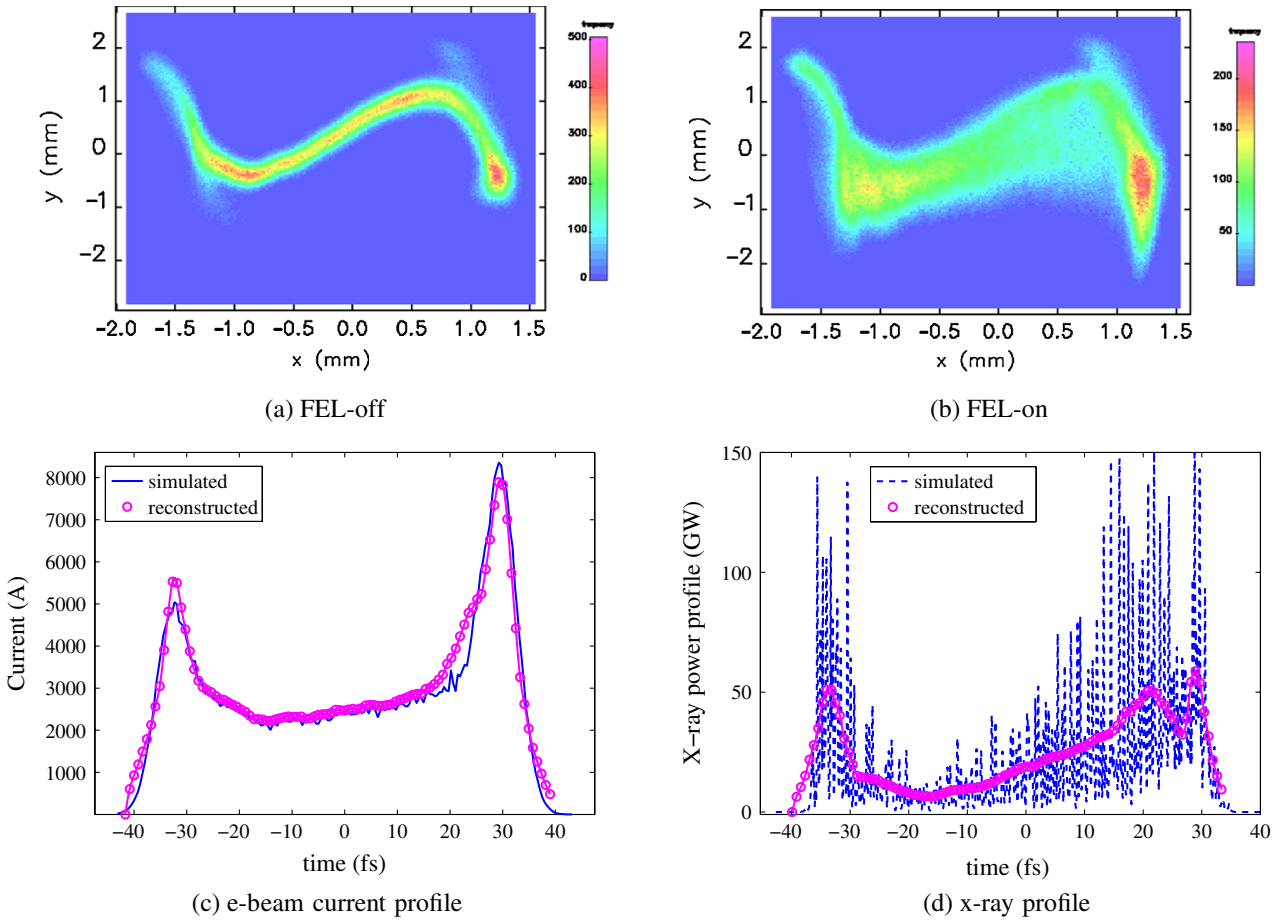


(a) FEL-off (b) FEL-on

(c) e-beam current profile (d) x-ray profile

FIG. 3. The simulated images on the screen representing e-beam longitudinal phase space for FEL-off (a) and FEL-on (b). The bunch charge is 250 pC with an energy of 13.6 GeV. Parts (c) and (d) show the reconstructed e-beam current and FEL x-ray profiles (magenta) comparing with the simulated ones (blue). The bunch head is to the left.

space reconstruction technique because the deflector also streaks the beam horizontally. This effect can be canceled by performing a second measurement at the other rf zero-crossing phase, 180° from the first measurement [18]. An effective calibration factor can be defined after the dual rf zero-crossing measurements. Figure 3(c) shows the reconstructed e-beam current profile from two zero-crossing phases comparing with the original one.

With the obtained time-sliced energy loss and current, the x-ray power profile is directly determined with an absolute power scale [$P(t) = \Delta E_{\mathrm{FEL}}(t) \times I(t)$]. The reconstructed x-ray profile from the energy loss for this hard x-ray example is shown in Fig. 3(d). Since LCLS is operating in the self-amplified spontaneous emission (SASE) mode, there are many longitudinal spikes whose typical width is ~0.2 fs in this hard x-ray wavelength. The reconstructed pulse shape is a smooth approximation to the actual profile, where the finer spikes are smeared out due to the limited temporal resolution. Using the energy spread data we get a similar x-ray profile. To obtain the absolute power scale from the energy spread analysis it requires an additional measurement of the total x-ray pulse energy.

Comparing the e-beam current profile with the x-ray profile shown in Fig. 3, we can see that the shape of the x-ray profile deviates from the e-beam current profile, with less lasing right after the horn at the head of the bunch. This is the result of the wakefields in the undulator chamber suppressing the FEL lasing from the first horn at the head of the bunch.

Low charge operation mode with 20 pC at LCLS has been used in many x-ray user experiments for producing x-ray pulses of a few fs [2]. Since these short x-ray pulses typically only have a few spikes, there is a large variation on the pulse shape. This makes the measurement of the actual x-ray pulse profile even more critical. We show an example of the soft x-ray case right after saturation. The e-beam bunch charge is 20 pC and the energy is 4.3 GeV. In the second bunch compressor, the e-beam is overcompressed so we can have a Gaussian-like current profile to generate a shorter x-ray pulse [2]. The longitudinal phase space simulated at the dump screen is shown in Fig. 4. By

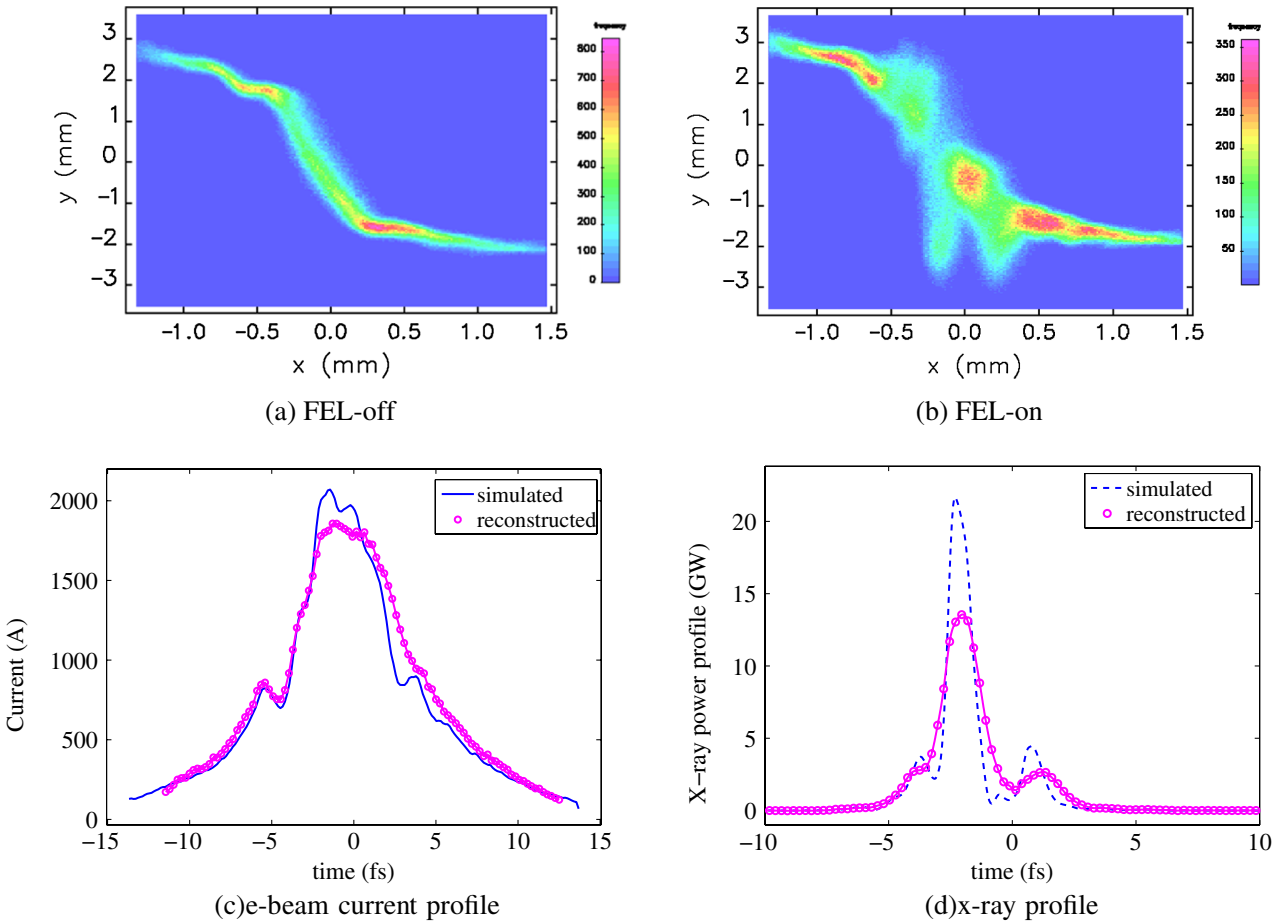


FIG. 4. The simulated images on the screen representing e-beam longitudinal phase space for FEL-off (a) and FEL-on (b). The bunch charge is 20 pC with an energy of 4.3 GeV. Parts (c) and (d) show the reconstructed e-beam current and FEL x-ray profiles (magenta) comparing with the simulated ones (blue). The bunch head is to the left.

subtracting the nonlasing background, the x-ray profile is reconstructed [Fig. 4(d)]. The e-beam is about 4 fs FWHM, and the FEL profile in this snapshot has one main spike, and two small side spikes. Comparing the reconstructed x-ray profile with the simulated one, we see some distortions in the profile peaks but still it is very encouraging. Running into the deep saturation regime, the slippage effect between FEL and e-beam may affect the shape of the reconstructed x-ray power profile, especially for long-wavelength radiations. At the x-ray wavelengths, this slippage effect after saturation is not a big problem.

## V. DISCUSSIONS AND SUMMARY

As described earlier, we suppress the FEL lasing process and record the e-beam longitudinal phase space as a baseline, then compare the FEL-on case with the saved baseline image to analyze the FEL x-ray profile. In the simulation examples, we assume a stable e-beam without timing or energy jitter from shot to shot. The pulse-by-pulse jitter issues have to be considered during the real measurements. By choosing the X-band rf deflector, an increased temporal resolution has been achieved, but the price to be paid is an increased sensitivity to phase jitter between the bunch arrival time and the X-band rf system. This must be minimized by designing tight rf phase tolerances into the system. The present achievable X-band rf phase stability could be $<0.1°$, however, the measured LCLS arrival time jitter is $\sim$50 fs rms [1]. This beam arrival time jitter makes the calibration very difficult. At LCLS, two phase cavities located after the undulator are used to measure the beam arrival time with an accuracy of $\sim$10 fs rms [19]. These arrival time data measured from the phase cavities can be used to correct the timing jitter during the transverse deflector calibration measurements. Using these corrections combined with multishot averaging, we can achieve a reasonably good calibration within a useful rf phase range. We can also consider reducing the rf power during the calibration and then scale the calibration factor based on the measured rf power. During the phase space measurements, since we operate at the zero-crossing phase region where the rf amplitude versus the phase is quite linear, these rf phase jitter and beam arrival jitter do not affect the measurement, though a relatively large size screen should be considered for the system design. The e-beam pulse-by-pulse energy jitter can also be corrected with the beam position monitors in the dogleg before the undulator. The transverse jitter out of the undulator is small and does not cause an additional effect on the measurement. Also note that the transverse deflector introduces additional correlation between the horizontal position and the energy. This effect has been included in the simulation examples in this paper, and it should be small since this energy spread can be subtracted in the analysis using Eq. (6).

In summary, we have shown that the proposed transverse rf deflector located after the FEL undulator has the potential to reconstruct the x-ray temporal profiles with a very high resolution down to a few fs. This single-shot method is widely applicable to any radiation wavelength, SASE or seeded FEL mode, without interruption to user operation. This data can be delivered to the x-ray experiments in real time on a pulse-by-pulse basis. In addition, the e-beam bunch length and temporal profile are also obtained, providing a useful tool for a detailed study on the FEL lasing process.

## ACKNOWLEDGMENTS

We thank G. Bowden, V. Dolgashev, J. Wang, J. Welch, and D. Xiang for helpful discussions. This work was supported by Department of Energy Contract No. DE-AC02-76SF00515.

[1] P. Emma *et al.*, Nat. Photon. **4**, 641 (2010).
[2] Y. Ding *et al.*, Phys. Rev. Lett. **102**, 254801 (2009).
[3] Z. Huang *et al.*, Phys. Rev. ST Accel. Beams **13**, 092801 (2010).
[4] Z. Huang *et al.*, in Proceedings of 2011 Particle Accelerator Conference, New York, USA (2011), p. 2459.
[5] U. Frühling *et al.*, Nat. Photon. **3**, 523 (2009).
[6] A. Maier (private communication).
[7] P. Catravas *et al.*, Phys. Rev. Lett. **82**, 5261 (1999).
[8] A. Lutman *et al.*, in Proceedings of FEL2011, Shanghai, China (2011).
[9] G. Geloni *et al.*, arXiv:1001.3544v1.
[10] S. Düsterer *et al.*, New J. Phys. **13**, 093024 (2011).
[11] G. A. Loew and O. H. Altenmueller, SLAC Report No. SLAC-PUB-135, 1965.
[12] For example, see R. Akre *et al.*, in *Proceedings of the 8th European Particle Accelerator Conference, Paris, 2002* (EPS-IGA and CERN, Geneva, 2002), p. 1882; Z. Huang *et al.*, Phys. Rev. ST Accel. Beams **13**, 020703 (2010); M. Röhrs *et al.*, Phys. Rev. ST Accel. Beams **12**, 050704 (2009); P. Musumeci *et al.*, Phys. Rev. Lett. **106**, 184801 (2011).
[13] J. Wang and S. Tantawi, in Proceedings of LINAC 08, Victoria, BC, Canada.
[14] J. Qiang *et al.*, Phys. Rev. ST Accel. Beams **9**, 044204 (2006).
[15] M. Borland, Advanced Photon Source Report No. LS-287, 2000.
[16] S. Reiche *et al.*, Nucl. Instrum. Methods Phys. Res., Sect. A **429**, 243 (1999).
[17] K. Bane *et al.*, Phys. Rev. ST Accel. Beams **12**, 030704 (2009).
[18] H. Loos *et al.*, Proceedings of FEL2005, Stanford, CA (2005), p. 632.
[19] A. Brachmann *et al.*, in *Proceedings of the IPAC'10 Conference, Kyoto, Japan* (ICR, Kyoto, 2010); see also Report No. SLAC-PUB-14234.

## 5.3 Ultrafast X-ray pulse characterization at free-electron lasers

The study of dynamics on natural time scales in photon science with femtosecond X-ray pulses at free-electron lasers (cf. Sec. 1.2) does not only rely on the measurement of the temporal FEL radiation pulse profiles but also on the precise information of their time of arrival at the actual experiment (see, e.g., Refs. [60, 115, 116]). The arrival time information is of particular importance for carrying out time-resolved pump-probe experiments with an external (pump) quantum laser (e.g., Refs. [105, 106]), where the dynamics of matter is initiated, i.e., excited, by the pump laser pulse and then subsequently probed by the FEL radiation pulse with a variable time delay. Thus, the accuracy of time-resolved pump-probe experiments is obviously limited by the arrival time jitter between the pump and probe radiation pulses.

Characterization of temporal FEL radiation pulse profiles with single-shot capability at X-ray FELs has been proposed in Ref. [74] by an indirect method using longitudinal phase space diagnostics for electron beams, and demonstrated in Refs. [108, 109] by a direct method using streaking techniques with THz fields. The latter is based on the interaction of the FEL radiation pulse with a noble gas, which leads to the ejection of Auger or photoelectrons with a temporal density profile that resembles the temporal profile of the incident FEL radiation pulse. The ejected nonrelativistic electrons can then be accelerated in a time-dependent THz field, leading to a mapping (streaking) from the time coordinate to a kinetic energy shift, which can be measured with a time-of-flight spectrometer and allows single-shot measurements of the temporal FEL radiation pulse profiles. However, to fully take advantage of femtosecond X-ray pulses at FELs, single-shot characterization of both their temporal profile and arrival time with high accuracy is required (see, e.g., Ref. [109]).

Terahertz fields for streaking techniques at X-ray FELs can be generated either by the FEL driving electron bunch itself, e.g., in an undulator for THz and infrared radiation (e.g., Ref. [117]), or externally by optical rectification of a quantum laser pulse in a lithium niobate crystal (e.g., Ref. [118]). In the latter case, the THz generation can be accomplished with the same external quantum laser system that is used for time-resolved pump-probe experiments. As a consequence, the pump laser pulse and the generated THz field for streaking intrinsically have the same arrival time jitter, and the center of mass of the streaked photoelectron spectra is thus a measure of the relative timing between the pump and probe pulses [109].

The following article reports on ultrafast X-ray pulse characterization at FELs by using streaking techniques with THz fields generated by an external quantum laser. The presented results demonstrate simultaneous single-shot measurements of temporal X-ray pulse profiles and their time of arrival with respect to an external quantum laser.

# Ultrafast X-ray pulse characterization at free-electron lasers

I. Grguraš[1*], A. R. Maier[2,3*], C. Behrens[4*], T. Mazza[5], T. J. Kelly[6], P. Radcliffe[5], S. Düsterer[4], A. K. Kazansky[7,8,9], N. M. Kabachnik[5,9,10], Th. Tschentscher[5], J. T. Costello[6], M. Meyer[5], M. C. Hoffmann[1,11], H. Schlarb[4] & A. L. Cavalieri[1§]

[1] *Max-Planck Research Department for Structural Dynamics, University of Hamburg, Center for Free Electron Laser Science, Notkestr. 85, 22607 Hamburg, Germany.*

[2] *Max-Planck Institute of Quantum Optics, Hans-Kopfermann-Str. 1, 85748 Garching, Germany.*

[3] *Ludwig-Maximilians Universität München, Am Coulombwall 1, 85746 Garching, Germany.*

[4] *Deutsches Elektronen-Synchrotron DESY, Notkestr. 85, 22607 Hamburg, Germany.*

[5] *European XFEL GmbH, Albert-Einstein-Ring 19, 22761 Hamburg, Germany.*

[6] *School of Physical Science and National Center for Plasma Science and Technology (NCPST), Dublin City University, Glasnevin, Dublin 9, Ireland.*

[7] *Departamento de Fisica de Materiales, University of the Basque Country UPV/EHU, E-20018 San Sebastian/Donostia, Spain.*

[8] *IKERBASQUE, Basque Foundation for Science, E-48011, Bilbao, Spain.*

[9] *Donostia International Physics Center (DIPC), E-20018 San Sebastian/Donostia, Spain.*

[10] *Skobeltsyn Institute of Nuclear Physics, Lomonosov Moscow State University, Moscow 119991, Russia.*

[11] *SLAC National Accelerator Laboratory, 2575 Sand Hill Rd., Menlo Park, CA 94025, USA.*

[*] *These authors contributed equally to this work.*

[§] *corresponding author (adrian.cavalieri@mpsd.cfel.de)*

**The ability to fully characterize ultrashort, ultra-intense X-ray pulses at free electron-lasers (FELs) will be crucial in experiments ranging from single-molecule imaging to extreme timescale X-ray science. This issue is especially important at current generation FELs, which are primarily based on self-amplified spontaneous emission and radiate with parameters that fluctuate strongly from pulse to pulse. Using single-cycle THz pulses from an optical laser, we have extended the streaking techniques of attosecond metrology to measure the temporal profile of individual FEL pulses with 5 fs FWHM accuracy, as well as their arrival on a time-base synchronized to the external laser to within 6 fs rms. Optical laser-driven THz streaking can be utilized at any X-ray photon energy and is non-invasive, allowing it to be incorporated in any pump-probe experiment, eventually characterizing pulses before and after interaction with most sample environments.**

Theoretical studies and user operations at the extreme ultra-violet (XUV) and soft X-ray Free-Electron Laser in Hamburg (FLASH)[1], at the hard X-ray Linac Coherent Light Source at the SLAC National Accelerator Laboratory[2] and at the SPring-8 Angstrom Compact Free Electron Laser at RIKEN Harima Institute[3,4] indicate that FELs can deliver pulses with duration in the range of tens of femtoseconds to less than a femtosecond with ~$10^{11}$ - $10^{13}$ photons per pulse[5,6]. The unique combination of unprecedented brightness and ultrashort pulse duration ensures new possibilities for high-resolution time-resolved X-ray studies[7,8], for experiments involving high-intensity X-ray matter interaction[9-11], and will allow for a new class of biomolecular imaging experiments[12-14].

However, currently X-ray FELs rely primarily on the stochastic process of self-amplified spontaneous emission (SASE) and emit pulses without a well-defined

temporal profile. SASE FEL pulses are composed of independent, temporally coherent emission spikes. The duration of these spikes can range from hundreds of attoseconds to several femtoseconds depending on the coherence length of the FEL process[15]. The full length of the intensity envelope formed by the stochastically distributed emission spikes is expected to be one hundred femtoseconds or less and it may fluctuate dramatically from shot to shot due to phase space density variations across the driving electron bunch. Therefore, in experiments where dynamic processes are expected to occur during the FEL exposure, such as in biological imaging where the onset of radiation damage is expected within the first few femtoseconds, the FEL pulse profile must be measured with femtosecond accuracy on a single-shot basis.

In two-color, time-resolved experiments using an optical laser and the FEL, significant temporal jitter and drift exists between the two distinct sources of pump and probe. Without additional information, the exact delay between excitation and observation is unknown and the time-resolution is reduced to the level of the timing jitter. The largest contribution to the timing jitter is caused by insufficient synchronization between the optical laser pulse and FEL driving electron bunch. When timing is required with resolution equivalent to or better than the FEL pulse duration, shot-to-shot fluctuation in the regions or portion of the electron bunch that generate SASE amplified radiation become a significant source of additional jitter.

Insufficient synchronization can be mitigated by simple time-of-arrival measurements of the electron bunch with respect to the pump laser pulse[16-18]. However, these measurements cannot be used to address fluctuations in SASE amplification over the length of the electron bunch and they introduce an internal source of unaccounted timing jitter that accumulates in the long optical paths between

the bunch measurement and experiment endstation. More recently, arrival-time measurements based on transient X-ray fluence dependent effects have been made directly on the FEL photon pulse[19-24]. However, because the FEL intensity and pulse shape changes from shot to shot, these effects can be triggered at different points within the FEL emission envelope. This source of error will still be present in seeded FEL operation, where the pulse shape is expected to remain stable, but its intensity can still fluctuate significantly[25]. As a result, a timestamp of the FEL pulse arrival, regardless of the accuracy, may not provide enough information to achieve sub-X-ray pulse duration time-resolution in pump-probe experiments. To ensure that the highest time-resolution can be reached at FELs, full shot-to-shot temporal characterization of the X-ray pulse profile on a time-base synchronized to the pump laser that drives the experiment dynamics is essential.

We have now achieved this full temporal characterization using independent optical laser-driven single-cycle THz pulses for femtosecond time-resolved photoelectron spectroscopy. This unique method is implemented in a transparent inline geometry, can accommodate fluctuating X-ray pulse intensity, is applicable over the full range of photon energies produced by FELs from the XUV to hard X-ray regime, and can be applied to pulses ranging from less than 10 femtoseconds to ~100 femtoseconds.

**Ultrashort XUV pulse characterization**

The measurement is adapted from attosecond metrology, where fully coherent XUV pulses generated through high-harmonic generation[26] have been characterized with attosecond precision[27,28]. In these measurements, a few-cycle laser pulse at 750 nm central wavelength is used to broaden and shift the initial kinetic energy

distribution of photoelectrons ejected from a noble gas target by the XUV pulse. When the photoemission process that replicates the temporal structure of the ionizing XUV pulse[29] is confined to within one half-cycle of the laser field (1.25 fs for 750nm carrier wavelength), the detected photoelectron spectrum is said to be streaked. In the classical model[30] the shift in kinetic energy of the streaked photoemission peak is governed by the amplitude of the vector potential of the streaking pulse at the instant of ionization. The degree of spectral broadening depends on both the temporal extent of the ionizing pulse and the variation of the streaking field over its duration.

Retrieval of the ionizing XUV pulse profile from the streaked spectrum requires characterization of the streaking field. For perfectly synchronized identical pulses from the same source, the streaking field is accessed through a set of sequential measurements over the full range of delays between optical and XUV pulse. As all parameters remain constant throughout the multi-shot acquisition[31], a spectrogram constructed from the series of measurements reveals the precise streaking field parameters and the XUV pulse characteristics can subsequently be obtained for streaked spectra averaged at fixed delays with demonstrated sub-100 attosecond resolution[28,32].

While attosecond XUV pulses produced by high-harmonic generation are confined to the half-cycle of an optical laser field, SASE FEL pulses are expected to be as long as ~100 femtoseconds. Therefore, longer streaking fields in the terahertz regime must be used for the application of streaking techniques. Direct extension of attosecond streaking to the femtosecond regime has been achieved at FLASH by using the FEL driving electron bunch in an additional dedicated undulator structure to generate multi-cycle, phase-stable THz fields for streaking [33]. The THz pulse is intrinsically synchronized to the electron bunch, which allows the streaking field

parameters to be accessed by traditional attosecond methods. However, this synchronization does not permit for access to any timing information relative to an external pump-laser system. Furthermore, as the electron bunch generates the streaking field, the THz characteristics change as the electron beam is tuned, limiting the utility of this technique for FEL studies where beam parameters are varied systematically. In the worst case, when the accelerator is tuned for the shortest FEL pulses using very low charge and highly compressed bunches, the beam-based THz generation will not be strong enough for streaking. Application of this technique is additionally complicated, as the FEL pulse and subsequently the THz streaking pulse are generated sequentially and the FEL pulse must be delayed with respect to the THz pulse to allow for temporal overlap. While this is accomplished at FLASH using normal incidence multi-layer optics, these optics cannot be produced at arbitrary wavelengths or with arbitrary bandwidths and currently cannot be produced for photon energies above ~ 400 eV[34,35].

**Optical laser-driven THz streaking spectroscopy**

FEL pulse characterization by an independent laser-driven THz source overcomes the limitations of streaking with accelerator-based THz sources while maintaining the capability to sample hundred-femtosecond pulses. Furthermore, as laser-driven THz fields are locked to the external laser, the resulting FEL pulse profile measurements are given on a time-base that is synchronized to the pump-probe experiment environment. To accommodate the full range of photon energies, appropriate target atoms can be chosen according to the kinetic energy spectrum of their emitted Auger electrons or photoelectrons, allowing extension of THz streaking into the hard X-ray regime.

In contrast to standard attosecond streaking spectroscopy, in the measurements presented here, retrieval of the calibrated FEL temporal profile is achieved without intrinsic synchronization between the ionizing pulse and the streaking field. This is enabled by using single-cycle THz pulses that are characterized independently by electro-optic sampling (EOS). Single-cycle THz pulses generated by optical rectification of femtosecond Ti:Sapphire laser pulses have a streaking field half-cycle or ramp of ~600 fs (ref. 36 and supplementary information), significantly longer than the maximum expected FEL pulse duration and timing jitter. As a result, once the streaking pulse and FEL pulse have been temporally overlapped, all single-shot acquisitions occur on a uniquely defined, nearly linear portion of the streaking ramp.

As illustrated in Fig. 1, overlap with the THz streaking ramp leads to spectral broadening, as photoelectrons ejected by the FEL pulse are subject to different streaking strengths depending on their instant of emission. Broader streaked spectra are observed by increasing the variation in streaking field strength over the FEL pulse envelope, either by increasing the temporal extent of the photoelectron emission, i.e. introducing longer X-ray pulses, or by using stronger THz fields with steeper gradients. To take advantage of this mutual dependence and retrieve a calibrated FEL temporal profile, a streaking map is created from the THz electric field, measured independently by EOS, and the classical equation that governs streaking[30]:

$$E_{kin}^{shift}(t_0) = -p_i A(t_0) - \frac{A^2(t_0)}{2} \quad \text{where} \quad A(t_0) = -\int_{t_0}^{\infty} E(t)dt. \qquad (1)$$

Here $E_{kin}^{shift}$ refers to the kinetic energy shift of the photoelectron, $p_i$ is the initial undressed momentum, $A(t_0)$ is the THz vector potential and $E$ the THz electric field. Using this relationship, a unique transformation between the streaked kinetic

energy spectrum and pump-probe experiment time-base is established. When the streaked photoelectron spectra are significantly broader than the initial spectral bandwidth of the FEL photon pulse, the temporal profile of the FEL pulse can be directly recovered.

The layout of the THz streaking experiment at FLASH is shown in Fig. 2. An approximately 3 mJ, ~100 fs Ti:sapphire NIR laser pulse is split into two parts, with 99% of the pulse used for THz generation, while the remainder is used for in-situ EOS characterization of the THz pulse. To phase-match the optical rectification process, the pulse front of the driving NIR pulse is tilted with a diffraction grating and then imaged onto the $LiNbO_3$ crystal[37]. The resultant single-cycle THz pulse is ~2 ps in duration with a frequency spectrum centred at ~0.6 THz and energy of ~ 4 μJ (see supplementary information for details).

Undressed 2*p* and 2*s* photoemission peaks from neon were used to calibrate the time-of-flight (TOF) photoelectron spectrometer, as they lie in the spectral region of interest. However, helium was used for the streaking measurement because it has an isolated photoemission line, which avoids the possibility of photoelectrons from different binding energies overlapping with each other when they are broadened during streaking. Approximately 10 μJ soft X-ray FEL pulses[38] at 4.8 nm (258 eV) with an independently measured average bandwidth of ~2.5 eV FWHM (ref. 39) were used to eject the He 1s electrons with an initial kinetic energy of ~233 eV. The THz and FEL pulses were polarized along the direction of detection such that the streaking effect couples directly to the observed photoelectron kinetic energy.

For short periods of time, during which thermal and other environmental drifts are negligible, the optical laser and THz streaking pulse that it produces, as well as the FEL pulse, are electronically synchronized to a common rf-distribution network[40,41] at

the accelerator facility to within ~100 fs rms. By taking advantage of this coarse electronic synchronization, spectra were recorded as the desired delay between THz and soft X-ray pulses was varied in 100-fs steps. Approximately 400 single-shot spectra were collected at each delay step and combined to generate the averaged spectrogram shown in Fig. 3. For large delays, where the THz field is weak, the He 1*s* photoemission peak is nearly unaffected and located near its undressed, field-free kinetic energy. Around the zero-crossing of the vector potential, the kinetic energy of the photoelectrons is shifted and broadened depending on the THz streaking field parameters.

The streaking map is constructed using equation (1) and the THz electric field measured by EOS. While the shape of the measured electric field is exact, measurement of the absolute peak electric field strength is less precise due to imperfect orientation and impurities in the EO crystal that result in a reduced effective electro-optic coefficient. Therefore, the single-shot photoelectron spectra from the full time scan that experience the greatest positive or negative kinetic energy shift are used to scale the amplitude of the streaking map. This additional measurement allows us to determine the absolute electric field strength with much greater accuracy than by EOS alone. The streaking map used in our measurements spans the maximum observed single-shot shift of the photoemission peak of +23/-37 eV, corresponding to a peak THz electric field strength of 165 kV/cm.

The resolution of the timing measurements is limited by both the strength of the THz streaking field, or degree of spectral broadening, and the energy resolution of the photoelectron spectrometer. In these experiments, the energy resolution of the photoelectron spectrometer can be determined by comparing the bandwidth of the average field-free photoelectron spectrum of the He 1s line to an independent

measurement of the average FEL photon bandwidth. The unstreaked, field-free photoelectron spectrum is nearly Gaussian with an observed bandwidth of 7.2 eV FWHM, which is a convolution of the energy resolution with the FEL bandwidth. Because the independently measured FEL bandwidth is 2.5 eV FWHM, the photoelectron spectrometer resolution is 6.8 eV FWHM. The energy resolution of the photoelectron spectrometer in conjunction with the THz streaking map is used to determine the minimum separation between two distinguishable features in the FEL pulse temporal profile. In these measurements, the minimum separation is ~40 fs. It is expected that this resolution limit can be improved to better than 10 fs.

**Complete single-shot FEL temporal pulse characterization**

Characteristic streaking measurements made at FLASH are shown in Fig. 4. Figures 4a and 4c show the streaked single-shot spectra of two different FEL pulses. Statistical error in the single-shot spectrum is calculated according to the number of electrons collected within the energy resolution window of the detector. Because the photoelectron spectrum is heavily oversampled, boxcar integration is performed across the spectrum, resulting in a smooth error envelope that bounds the measured spectrum.

To recover the FEL pulse profile, the energy resolution of the TOF spectrometer is first deconvolved from the measured streaked photoelectron spectra as shown in Fig. 4. Figures 4b and 4d show the corresponding transformation of the measured and deconvolved spectra to time. In the temporal profile plots, positive time corresponds to the leading edge of the soft X-ray pulse. The FEL pulse in Fig. 4b exhibits a dominant central feature that is (53 ± 5) fs FWHM, with weaker satellite features at approximately 100 fs from the main peak. In contrast, the other displayed

FEL pulse exhibits nearly equal peaks with individual duration of (~ 40 ± 5) fs FWHM separated by ~85 fs in time. The accuracy of these measurements is determined from the upper and lower statistical error bounds on the streaked photoelectron spectrum (details are given in the methods section).

Structure observed in these FEL pulses is not caused by individual longitudinal FEL emission modes, which would typically have a duration of ~ 5 femtoseconds for the operating parameters at FLASH. Rather, the structure is due to uneven soft X-ray amplification over the length of the electron bunch caused by small variations in its composition and inherent instability in the highly nonlinear SASE process. During these particular measurements, the FEL was operating in the exponential gain regime, where it is especially sensitive to electron beam parameters[42,43]. This mode of operation serves as an ideal test of the utility of these streaking measurements, as the pulse-to-pulse FEL fluctuations are more severe and the FEL flux is relatively low. Under normal saturated user operation with higher flux, the measurement is expected to be even more reliable, as the number of detected photoelectrons will increase.

The accuracy of the pulse arrival information is governed by the stability of the THz streaking field and fluctuation in the mean FEL photon energy, which results in a photoelectron kinetic energy offset and corresponding temporal offset. The stability of the THz pulse is a function of the driving optical laser. In these experiments, the optical laser pulse energy was measured to be stable to within 1% rms. For saturated THz generation, as was the case in these measurements, the THz field scales with the square root of the driving laser pulse energy. As a result, the THz field is stable to within 0.5% rms and its fluctuation can be neglected when considering the stability of the transformed time-base. However, the FEL photon

energy during these measurements fluctuated from shot-to-shot at a level of 1 eV rms (ref. 39), which constitutes the main source of uncertainty in the time-base of the retrieved FEL pulse profile of ~6 fs rms. Using existing technology, this uncertainty can be significantly reduced with online measurement of the single-shot FEL photon spectrum. It should also be noted that fluctuation in the FEL photon energy has a minimal effect on the retrieved pulse profile, as the streaking map transformation is nearly linear at the zero-crossing and a small offset in the kinetic energy does not affect the spectral broadening due to streaking.

These streaking measurements can be used to assess the timing jitter at FLASH between the external pump-probe laser and FEL pulse. For this particular purpose, we ignore fluctuations in the pulse shape and the arrival of the FEL pulse is clocked by calculating the centre-of-mass of the retrieved FEL pulse temporal profile. The arrival times of ~ 450 consecutive FEL pulses measured near time-zero in the delay scan shown in Fig. 3, are calculated and displayed in Fig. 5. The distribution of arrival times has a width of 87 fs rms, which is consistent with the expected performance of the electronic laser synchronization[17].

**Discussion and outlook**

In the future, laser-based THz streaking measurements may be improved to allow characterization of fundamental FEL pulse substructure, separated by only several femtoseconds, by increasing the energy resolution of the photoelectron spectrometer, as well as by increasing the THz streaking strength. A number of current advances in THz generation[44] and photoelectron spectroscopy indicate that significant improvements in our measurement technique could be realised in the near future. Single-shot photoelectron detection at FELs has recently been demonstrated at

an energy resolution of $\Delta E/E = 0.4\%$ (ref. 45), an improvement of nearly an order of magnitude in comparison to the energy resolution achieved in these experiments. Stronger, steeper streaking fields can be achieved by decreasing the rise-time of the streaking ramp[46] or by scaling up the THz field strength with stronger driving optical laser pulses. Using the tilted pulse-front method and advanced focusing, fields exceeding 1 MV/cm have been achieved[47].

Optical laser-driven THz streaking is currently the only method that can provide full temporal characterization of FEL photon pulses, which is crucial for their most effective and complete utilization. This technique is implemented with standard laser technology and the apparatus does not require dedicated accelerator infrastructure. Furthermore, this method is ideally suited for use as a diagnostic for machine studies and FEL optimization for specific lasing parameters and pulse shapes, as it is completely decoupled from all other FEL parameters. Because the measurement is made in transmission geometry and does not affect the FEL pulse, it can be used as a standard diagnostic between the FEL source and user experiments. As a result, it will be possible to perform experiments with sub-pulse duration time-resolution and the ability to post-process arbitrary experimental data based on the true single-shot FEL intensity profile will exist.

## Methods:

### Error Analysis

Statistical error in the single-shot photoelectron spectra is evaluated by counting the number of detected photoelectrons within the 6.8 eV energy resolution window of the detector by boxcar integration centered at each collected data point. As the spectra are heavily oversampled (275 data points were collected within the ~60 eV streaked kinetic energy range), an error-envelope is generated rather than discrete points with individual error bars.

The 6.8 eV photoelectron spectrometer energy resolution is deconvolved from the upper and lower bound of the error-envelope in addition to the measured spectrum and mapped to time. Mapping the error-envelope provides an upper and lower bound on the pulse temporal profile. Following this procedure, the width of the central peak in the measurement shown in the main text (see Fig. 4b), which is 53 fs FWHM, is found to have an upper and lower bound of 58 and 48 fs FWHM, respectively. Based on this analysis, we conclude that the temporal profile is measured with an accuracy of ± 5 fs FWHM. This procedure is illustrated in the Supplementary Information Fig. S2.

## References:


1. Ackermann, W. *et al.* Operation of a free-electron laser from the extreme ultraviolet to the water window. *Nature Photonics* **1**, 336-342 (2007).
2. Emma, P. *et al.* First lasing and operation of an angstrom-wavelength free-electron laser. *Nature Photonics* **4**, 641-647 (2010).
3. Pile, D. X-rays first light from SACLA. *Nature Photonics* **5**, 456-457 (2011).
4. Ishikawa, T. et al. A compact X-ray free-electron laser emitting in the sub-ångström region. *Nature Photonics*. (2012).
5. Ding, Y. *et al.* Measurements and simulations of ultralow emittance and ultrashort electron beams in the Linac Coherent Light Source. *Phys. Rev. Lett.* **102**, 254801 (2009).
6. Helml, W. *et al.* Direct time domain measurement of the world's shortest X-ray pulses. *Manuscript in submission*.
7. Meyer, M. *et al.* Angle-resolved electron spectroscopy of laser-assisted Auger decay induced by a few-femtosecond X-ray pulse. *Phys. Rev. Lett.* **108**, 063007 (2012).
8. Först, M. *et al.* Driving magnetic order in a manganite by ultrafast lattice excitation. *Physical Review B* **84**, 241104 (2011).
9. Rohringer, N. *et al.* Atomic inner-shell X-ray laser at 1.46 nanometres pumped by an X-ray free-electron laser. *Nature* **481**, 488-491 (2012).
10. Vinko, S. M. *et al.* Creation and diagnosis of a solid-density plasma with an X-ray free-electron laser. *Nature* **482**, 59-U75 (2012).
11. Young, L. *et al.* Femtosecond electronic response of atoms to ultra-intense X-rays. *Nature* **466**, 56-U66 (2010).
12. Neutze, R., Wouts, R., van der Spoel, D., Weckert, E. & Hajdu, J. Potential for biomolecular imaging with femtosecond X-ray pulses. *Nature* **406**, 752-757 (2000).
13. Siebert, M. M. *et al.* Single mimivirus particles intercepted and imaged with an X-ray laser. *Nature* **470**, 78-U86 (2011).
14. Barty, A. *et al.* Self-terminating diffraction gates femtosecond X-ray nanocrystallography measurements. *Nature Photonics* **6**, 35-40 (2012).
15. Saldin, E. L., Schneidmiller, E. A. & Yurkov, M. V. Statistical and coherence properties of radiation from x-ray free-electron laser. *New Journal of Physics* **12**, 035010 (2010).
16. Cavalieri, A. L. *et al.* Clocking femtosecond X-rays. *Phys. Rev. Lett.* **94**, 114801 (2005).
17. Azima, A. *et al.* Time resolved pump-probe experiments beyond the jitter limitations at FLASH. *Applied Physics Letters* **94** 144102 (2009).
18. Tavella, F., Stojanovic, N., Geloni, G. & Gensch, M. Few femtosecond timing at fourth- generation X-ray light sources. *Nature Photonics* **5**, 162-165 (2011).
19. Radcliffe, P. *et al.* Single-shot characterization of independent femtosecond extreme ultraviolet free electron and infrared laser pulses. *Applied Physics Letters* **90**, 131108 (2007).
20. Gahl, C. *et al.* A femtosecond X-ray/optical cross-correlator. *Nature Photonics* **2**, 165-169 (2008).
21. Maltezopoulos, T. *et al.* Single-shot timing measurement of extreme-ultraviolet free-electron laser pulses. *New J. Phys.* **10**, 033026 (2008).
22. Bionta, M. R. *et al.* Spectral encoding of X-ray/optical relative delay. *Optics Express* **19**, 21855-21865 (2011).
23. Schorb, S. *et al.* X-ray-optical cross-correlator for gas-phase experiments at the Linac Coherent Light Source free-electron laser. *Applied Physics Letters* **100**, 121107 (2012).
24. Beye, M. *et al.* X-ray pulse preserving single-shot optical cross-correlation method for improved experimental temporal resolution. *Applied Physics Letters* **100**, 121108 (2012).
25. Amann, J. *et al.* Demonstration of self-seeding in a hard-X-ray free-electron laser. *Nature Photonics* (2012).
26. Christov, I., Murnane, M. M., & Kapteyn, H. C. High-harmonic generation of attosecond pulses in the "single-cycle" regime. *Phys. Rev. Lett.* **78** 1251-1254 (1997).
27. Kienberger, R. *et al.* Atomic transient recorder. *Nature* **427**, 817-821 (2004).
28. Goulielmakis, E. *et al.* Single-cycle nonlinear optics. *Science* **320**, 1614 (2008).
29. Schultze, M. *et al.* Delay in photoemission. *Science* **328**, 1658-1662 (2010).
30. Itatani, J. *et al.* Attosecond streak camera. *Phys. Rev. Lett.* **88**, 173903 (2002).
31. Baltuska, A. *et al.* Attosecond control of electronic processes by intense light fields. *Nature* **421**, 611-615 (2003).

32. Gagnon, J. Goulielmakis, E. & Yakovlev, V. S. The accurate FROG characterization of attosecond pulses from streaking measurements. *Applied Physics B – Lasers and Optics* **92**, 25-32 (2008).
33. Frühling, U. *et al.* Single-shot terahertz-field-driven X-ray streak camera. *Nature Photonics* **3**, 523-528 (2009).
34. Eriksson, F. *et al.* Atomic scale interface engineering by modulated ion-assisted deposition applied to soft x-ray multilayer optics. *Applied Optics* **47**, 4197-4204 (2008).
35. Bajt, S. *et al.* Multi-layer mirrors by magnetron sputtering and ion beam polishing. *Manuscript in preparation*.
36. Planken, P., Nienhuys, H., Bakker, H. & Wenckebach, T. Measurement and calculation of the orientation dependence of terahertz pulse detection in ZnTe. *Journal of the Optical Society of America B – Optical Physics* **18**, 313-317 (2001).
37. Yeh, K. L., Hoffmann, M. C., Hebling, J. & Nelson, K. A. Generation of 10μJ ultrashort terahertz pulses by optical rectification. *Appl. Phys. Lett.* **90**, 171121 (2007).
38. Tiedtke, K. *et al.* Gas-detectors for X-ray lasers. *J. Appl. Phys.* **103**, 094511 (2008).
39. Nicolosi, P. *et al.* Grazing-incidence spectrometer for the monitoring of the VUV FEL beam at DESY. *Journal of Electron Spectroscopy and Related Phenomena* **144**, 1055-1058.
40. Spence, D. E., Sleat, W. E., Evans, J. M., Sibbett, W. & Kafka J. D. Time synchronization measurements btween 2 self-modlocked Ti:Sapphire Lasers. *Optics Communications* **101,** 286-296 (1993).
41. Ma, L.-S. *et al.* Sub-10 femtosecond active synchronization of two passively mode-locked Ti:sapphire oscillators. *Phys. Rev. A.* **64**, 021802(R) (2001).
42. Bonifacio, R., Pellegrini & C., Narducci, L. Collective instabilities and high-gain regime in a free electron laser. *Opt. Commun.* **50**, 373-378 (1984),
43. Kim, K.-J. An analysis of self-amplified spontaneous emission, *Nucl. Instrum. Methods A* **250**, 396-403 (1986).
44. Hoffmann, M. C. & Fulop, J. A. Intense ultrashort terahertz pulses: generation and applications. *Journal of Physics D- Applied Physics* **44**, 083001 (2011).
45. Duesterer, S. *et al.* Femtosecond X-ray pulse length characterization at the Linac Coherent Light Source free-electron laser. *New Journal of Physics* **13**, 093024 (2011).
46. Hauri, C. P., Ruchert, C., Vicario, C. & Ardana, F. Strong-field single-cycle THz pulses generated in an organic crystal. *Appl. Phys. Lett.* **99**, 161116 (2011).
47. Hirori, H., Doi, A., Blanchard, F. & Tanaka, K. Single-cycle terahertz pulses with amplitudes exceeding 1MV/cm generated by optical rectification in LiNbO(3). *App. Phys. Lett.* **99**, 091106 (2011).

**Acknowledgements**

We owe special thanks to the scientific and technical staff at FLASH at the Deutsches Elektronen-Synchrotron (DESY), Hamburg for operation and delivery of the SASE-FEL beam. Portions of this work were funded by the Max Planck Society through institutional support for the Max Planck Research Department for Structural Dynamics at the University of Hamburg, and by the Munich Centre for Advanced Photonics, and by the Science Foundation Ireland PI Grant No. 07/IN.1/I1771, IRCSET and the EXTATIC EMJD. N.M.K. is grateful to European XFEL GmbH and to Donostia International Physics Center (DIPC) for hospitality and financial support. He also acknowledges the financial support by the program "Physics with Accelerators and Reactors in West Europe" of Russian Ministry of Education and Science.

**Author Contributions:**

A.L.C, M.C.H. and H.S. conceived the project. I. G., and M.C.H. designed and executed the experiments. C.B., A.L.C., J.T.C, S.D., T.J.K., A.R.M, M.M., T.M., P.R., H.S. and Th.T. assisted in the experimental realization. C.B., A.L.C., I.G., M.C.H, A.K.K., N.M.K., A.R.M., T.M., M.M., H.S. and Th.T. analysed and/or interpreted the data. A.L.C., S.D. and M.M. contributed materials to the experiments. A.L.C., J.T.C., I.G., M.C.H., M.M., H.S., and Th.T. wrote the paper.

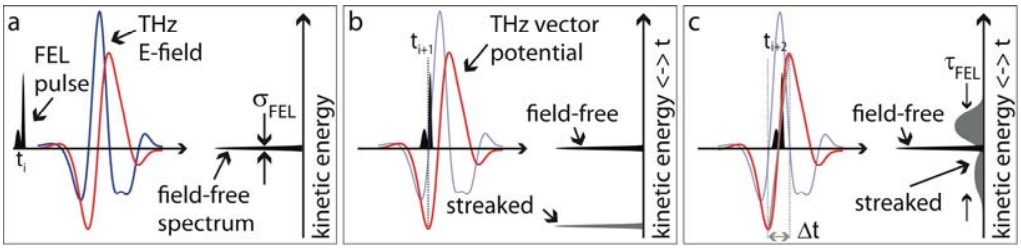


**Figure 1| Schematic of single-shot, single-cycle THz streaking measurement.** The blue and red curves represent the electric-field and corresponding vector potential of a single-cycle THz pulse. In the single-shot measurement depicted in **a**, the FEL pulse does not overlap in time with the THz pulse and the kinetic energy distribution of photoelectrons ejected by the FEL pulse is unaffected. In this case the measured photoelectron spectrum reveals the intrinsic bandwidth $\sigma_{FEL}$ of the FEL pulse. In the single-shot measurements depicted in **b** and **c** the FEL induced photoemission overlaps with the streaking THz field and the photoelectron spectra are broadened and shifted – "streaked" – depending on their instant of release. In **b**, the FEL pulse overlaps with an extreme of the THz vector potential leading to a maximally downshifted photoelectron spectrum with minimized spectral broadening. As a result, temporal structure in the pulse is not observed in the measured spectrum. In **c**, the temporal overlap occurs near the zero-crossing of the THz vector potential where the time of arrival as well as the temporal profile and duration, $\tau_{FEL}$, can be accessed with the highest resolution. The temporal dynamic range of the measurement is given by the length of the THz vector potential half-cycle $(\Delta t)$.

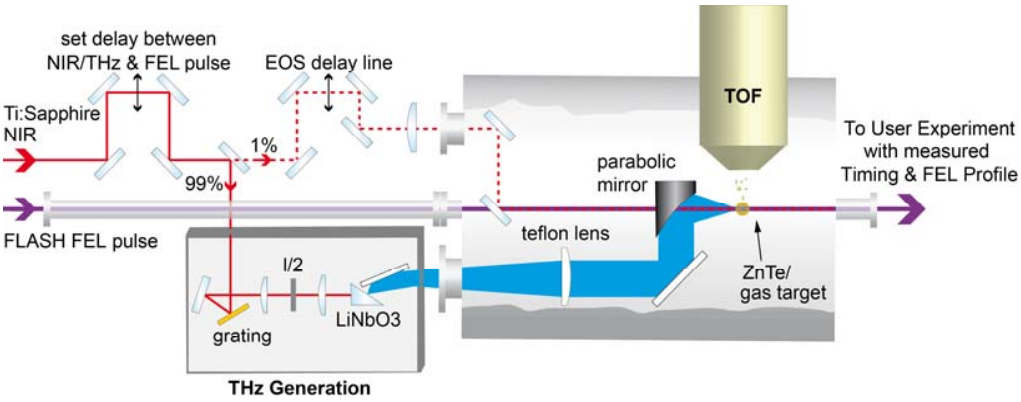


**Figure 2| THz streaking experiment setup.** A Ti:sapphire NIR laser pulse appropriately delayed with respect to the FEL pulse is split into two parts. Most of the pulse energy is used for tilted-wavefront THz generation in $LiNbO_3$, the remaining part can be used for electro-optic sampling (EOS) of the THz pulse in zinc-telluride (ZnTe) for in-situ characterization. In the streaking measurement, the collinear FEL photon pulse ejects a burst of photoelectrons from the gas with a temporal profile identical to the incident soft X-ray FEL pulse. The THz pulse is used to streak the photoelectron burst and consequently characterize the FEL pulse.

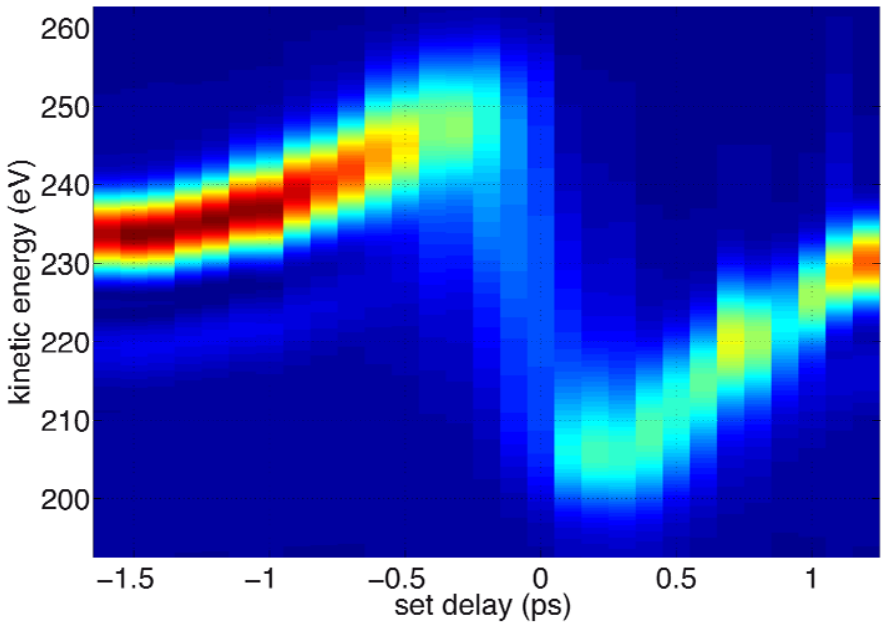


**Figure 3| Averaged spectrogram.** Streaked photoelectron spectra of He as a function of set delay between the THz streaking pulse and ionizing FEL pulse at FLASH. Coarse synchronization between the FEL pulse and streaking pulse was maintained electronically during the scan to ~100 fs rms. Each time slice is an average of ~400 single-shot measurements.

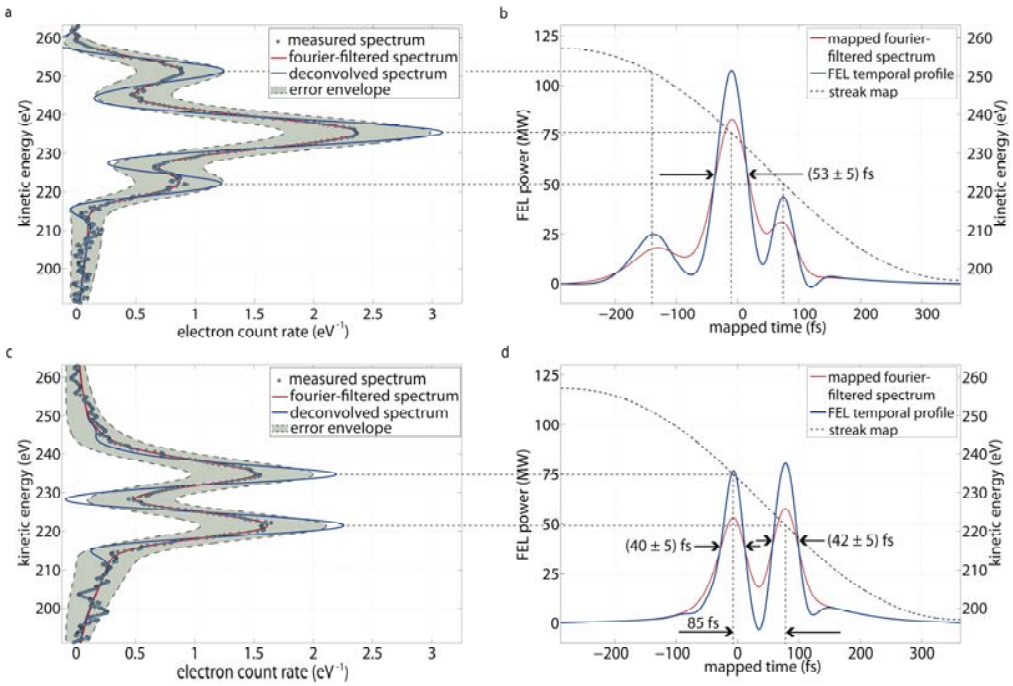


**Figure 4| Single-shot FEL pulse power profile on the pump-probe laser time base.** Panels **a** and **c** show two distinct single-shot streaked photoelectron spectra. Shaded error envelopes are calculated by boxcar integration based on the number of electrons collected within the 6.8 eV FWHM resolution window of the time-of-flight spectrometer. The blue dots are the raw data points in the measured streaked spectra. The red curves show the spectra after Fourier filtering to remove high frequency noise. The blue curves are the filtered streaked spectra following deconvolution of the photoelectron spectrometer resolution. Panels **b** and **d** show the retrieved FEL pulse profiles on the pump-probe laser time base using the single-valued streaking map (black dashed curve). In **b** and **d**, the scales on the right correspond to the streaking map, the scales on the left correspond to the FEL power that is obtained by assuming 10 μJ of pulse energy for the single-shot measurement shown in **a**. 53 ± 5 fs FWHM substructure is observed in the first single-shot measurement while ~ 40 ± 5 fs FWHM substructure is observed in the second.

## Supplementary Information:

## Single-shot signal processing

To access the undistorted streaked photoelectron spectra, steps were taken to reduce high frequency noise in the raw TOF signal and to deconvolve the energy resolution of the spectrometer from the measured photoelectron spectra.

Raw TOF spectra were Fourier filtered to remove frequency components above 2GHz. If the measured photoelectron spectrum is assumed to be a convolution of the undistorted photoelectron spectrum with the spectrometer resolution, the undistorted spectrum $h(E)$ is recovered by inverse Fourier transform of the filtered single-shot spectra $f(E)$.

$$h(E) = \frac{1}{\sqrt{2\pi}} \mathcal{F}^{-1} \left\{ \mathcal{F}[f(E)] \Big/ \mathcal{F}[g(E)] \right\}$$

Here, the spectrometer resolution $g(E)$ is taken as a Gaussian with width of 6.8eV FWHM, as was determined by measurement of the field-free photoelectron spectrum and independent measurement of the initial FEL bandwidth.

High frequency filtering and deconvolution of a measured single-shot spectrum is shown in Fig. S1. Even after filtering of high frequency noise in the raw TOF spectra, the Fourier components in the inverse FFT diverge at high frequencies and must be additionally filtered, resulting in the undershoot evident at ~215 and ~259 eV. As a measure of the fidelity of this technique, considering the additional filtering in the inverse Fourier transform, the deconvolved spectrum has been reconvolved with the instrument resolution. The result in Fig. S1 shows excellent agreement with the original filtered single-shot spectrum.

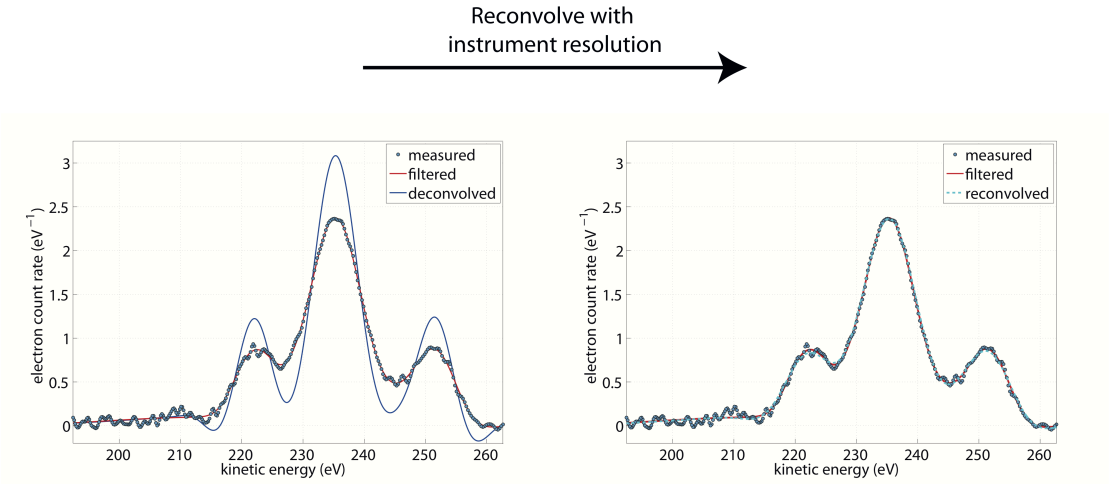


**S1: Spectral deconvolution|** The deconvolution procedure of the photoelectron spectrometer resolution is tested by reconvolving the energy resolution and comparing with the original spectrum.

Statistical error in the measured single-shot streaked spectrum can be evaluated, as discussed in the Methods section. Because the data is heavily oversampled, an error envelope is generated rather than distinct points with error bars. Mapping the error envelope to time allows for upper and lower limits to be placed on the duration of the features observed in the FEL temporal profile.

This procedure has been performed for the single-shot measurement displayed in the main text in Fig 4a and 4b. The recovered accuracy for the central feature is +/-5 fs FWHM as shown in Fig. S2.

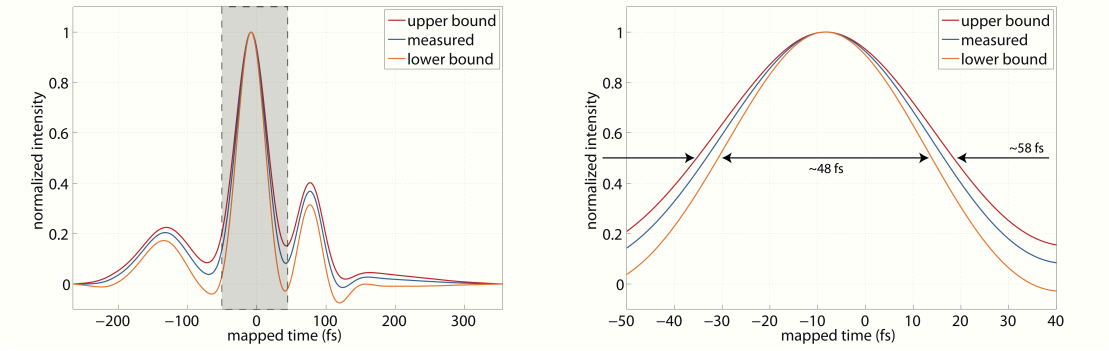


**S2: Measurement accuracy|** Spectrometer energy resolution is deconvolved from the upper and lower bounds of the statistical error-envelope as well as the measured spectrum. In the panel on the left all curves are mapped to time, providing upper and lower bounds on the width of pulse profile. The panel on the right is a blow-up of the central peak, which has a width of 53 fs. Here, the lower bound is 48 fs and the upper bound is 58 fs and the measurement accuracy is found to be ± 5 fs FWHM.

## THz Generation

Single-cycle THz pulses were generated using tilted pulse front excitation of lithium niobate. The pump pulse energy from an amplified Ti-Sapphire system was 3 mJ, with a duration of ~50 fs. The THz pulse energy directly after the generation crystal was ~4 µJ, measured with a calibrated pyroelectric detector from Microtech Instruments. The THz polarization was rotated 90 degrees by a periscope to be horizontal and in-line with the axis of the time-of-flight detector. The THz radiation was collimated using a 275 mm focal length Teflon lens and then focused onto the interaction region by a 3-inch effective focal length, 90 degree off-axis parabolic mirror.

## Electro-Optic characterization

The shape of the THz waveform was measured in the time domain using electro-optic sampling at the position of the streaking interaction region. A 500 µm thick ZnTe crystal was mounted on a manipulator arm that can be moved into the interaction region. A portion of the 800 nm laser pulse was split off before the THz generation and was variably delayed using a motorized linear stage (see Figure 2 in main text). The THz induced birefringence in the ZnTe crystal was analyzed using a Wollaston prism and a quarter wave plate outside the chamber (not shown). The resulting EOS delay scan and corresponding frequency amplitude spectrum are shown in Fig S3.

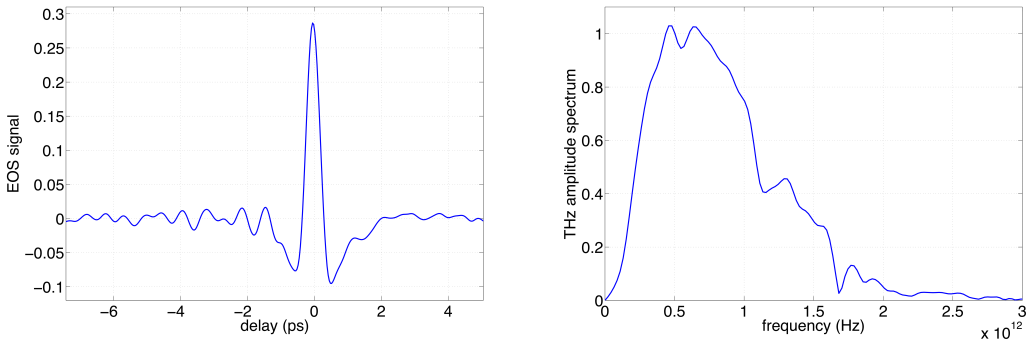


**S3: THz electro-optical sampling.** The electro-optic signal was collected using balanced detection. The single-cycle THz pulse is ~2ps in duration with a carrier frequency of ~0.6THz.

The absolute THz electric field strength is determined independently by observation of the maximum shifted single-shot streaked photoelectron spectra. This is more accurate than calculating the absolute field strength based on the ZnTe electro-optic coefficients due to crystal defects and imperfect crystal orientation, which result in an underestimate of the THz field strength.

In the measurements shown in the main text, the furthest up-shifted photoelectron spectra were found at 257 eV (+23 eV), and the furthest downshifted photoelectron spectra were found at 197 eV (-37 eV). The field-free He 1s photoemission peak is at 234 eV. The furthest upshifted spectra at +23 eV are used to calibrate the measured field shape.

The peak strength of the THz electric field and the corresponding linear scaling of the measured field shape is used as the free parameter in equation (1) to reach a maximum positive kinetic energy shift of +23 eV.

$$E_{kin}^{shift}(t_0) = -p_i A(t_0) - \frac{A^2(t_0)}{2} \quad \text{where} \quad A(t_0) = -\int_{t_0}^{\infty} E(t)dt. \qquad (1)$$

This shift is achieved for a peak THz electric field strength of 165kV/cm, which is in agreement with the measured THz pulse energy and expected focused THz beam diameter. The calibrated THz electric field and corresponding THz vector potential, which is calculated numerically by cumulative integration, are shown in Fig S3.

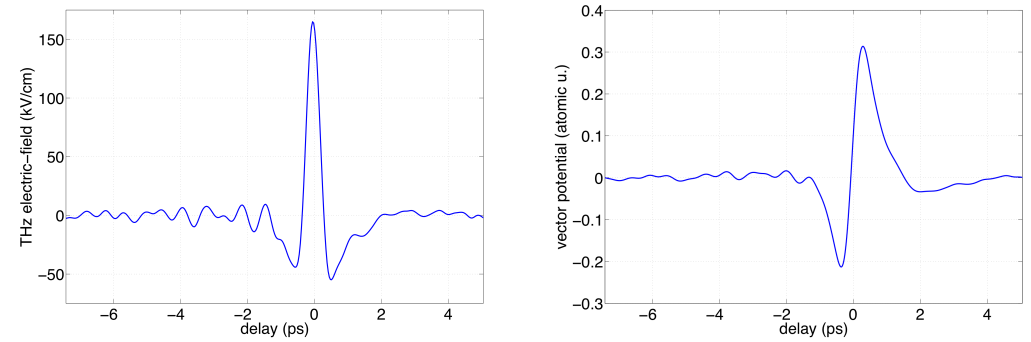


**S4: Characterized THz pulse.** The absolute THz electric field strength is determined using the experimentally observed maximum shifted single-shot spectra. The peak field strength is 165kV/cm. The corresponding THz vector potential is shown in atomic units.

In Fig. S5, using the calibrated THz field, the kinetic energy shift due to streaking is calculated over the range of delays in the spectrogram shown in the main text (Fig. 3). The maximum upshifted kinetic energy of +23 eV is fixed by the calibration of the THz electric field strength. Without any additional adjustment, the calculated maximum downshifted kinetic energy is -37 eV, which is the same as that observed in the streaking measurement. Asymmetry in the kinetic energy shift due to streaking is primarily a consequence of the inherent asymmetry in the THz pulse.

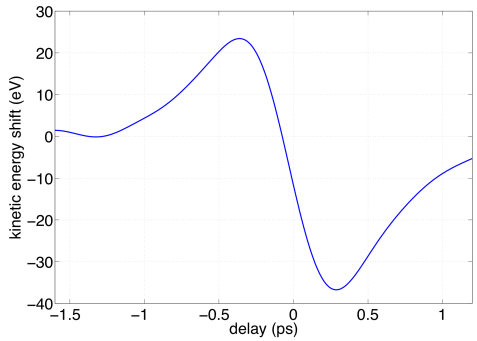


**S5: THz streaking.** After numerically calculating the THz vector potential, it is used to calculate the kinetic energy shift of the photoelectron peak due to streaking. The maximum shift is +23eV/-37eV. Observed asymmetry is primarily due to inherent asymmetry in the THz pulse shape.

# 6 Summary and conclusions

Temporal characterization of the FEL radiation pulses and precise control of the FEL driving electron beams are essential for the operation and utilization of X-ray free-electron lasers. Within this cumulative thesis, recent results achieved within the active research field of femtosecond electron and X-ray beams at FELs have been reported and discussed.

Transverse electron beam profile imaging, crucial for time-resolved diagnostics with single-shot capability, is affected by coherent optical radiation effects, which render imaging with standard screen techniques impossible. Theoretical considerations and experimental data have been presented, showing that coherent optical emission can be strongly suppressed in dispersive beamlines. For transverse beam profile imaging in non-dispersive beamlines, methods to separate the incoherent radiation from scintillation screens and to simultaneously exclude coherent optical radiation from detection have been discussed. The presented experimental results prove the temporal separation technique as a promising method for future applications in transverse beam profile imaging of high-brightness electron beams.

The suppression of coherent optical radiation in transverse electron beam profile imaging is essential for time-resolved single-shot beam diagnostics in the time-domain based on transverse deflecting r.f. structures. The presented electron beam diagnostics utilizing a TDS achieved temporal resolutions of sub-10 fs r.m.s. and show prospects for unprecedented ~ 1 fs r.m.s. resolution. A complementary electron beam diagnostics in the frequency-domain is based on the spectroscopy of coherent THz and infrared radiation, and a corresponding unique multi-channel single-shot spectrometer using reflective blazed gratings has been presented. Temporal bunch profile reconstructions utilizing phase-retrieval techniques have been performed, showing good agreement with the comparative measurements using a TDS. Both the time- and frequency-domain electron beam diagnostics demonstrated to provide reasonable constraints on the expected FEL radiation pulse durations.

Longitudinal phase space measurements with single-shot capability and simultaneous suppression of coherent optical radiation effects have been carried out with combination of a TDS and a magnetic energy spectrometer. That way the FEL driving electron bunches could be analyzed in terms of their durations and energy chirps. Uniform bunch compression has been achieved by longitudinal phase space control using accelerating fields with

multiple, higher harmonic r.f. frequencies. The generation of electron bunches with ramped current profiles has been accomplished by tailoring of the longitudinal phase space in a dual-frequency linear accelerator, demonstrating the potential of high accelerating fields and unprecedentedly large transformer ratios for future wakefield acceleration experiments.

Microbunching instabilities associated with the electron bunch compression in magnetic chicanes can significantly degrade the high beam brightness required to drive a high-gain FEL and may lead to coherent optical radiation effects. Longitudinal phase space control in terms of introducing additional energy spread, i.e., heating the electron beam, can effectively suppress microbunching instabilities. A scheme of two TDSs upstream and downstream of a magnetic chicane has been presented for reversible electron beam heating, capable to suppress microbunching instabilities and to simultaneously preserve the beam brightness.

The realization and interpretation of various experiments on ultrafast dynamics in photon science at X-ray FELs are based on the reliable generation and temporal characterization of femtosecond FEL radiation pulses. A concept for an indirect temporal X-ray pulse characterization has been presented, making use of the energy transfer during the FEL amplification. The temporal FEL radiation pulse profile appears as a replica in the longitudinal phase space of the electron bunch downstream of the undulator and can thus be measured by an appropriate longitudinal phase space diagnostics. The presented streaking technique using THz fields generated by an external quantum laser even demonstrated both direct temporal FEL radiation pulse characterization and simultaneous arrival time measurements of the FEL radiation pulses with respect to the external laser. The external laser can be realized by the pump laser used for pump-probe experiments at FELs, proving the presented streaking technique to provide a measure of the relative timing between pump and probe pulses.

All the transverse and temporal electron bunch profile measurements presented in this cumulative thesis are based on a new, dedicated setup for longitudinal phase space diagnostics at FLASH that has been designed, developed, and commissioned as part of this thesis.

# Bibliography


[1] W.C. Röntgen (translated by A. Stanton from the Sitzungsberichte der Würzburger Physik-medic. Gesellschaft, 1895), *On a New Kind of Rays*, Nature **53**, 274 - 276 (1896).

[2] T.H. Maiman, *Stimulated Optical Emission in Ruby*, Nature **187**, 493 - 494 (1960).

[3] W. Friedrich, P. Knipping, and M. von Laue, *Interferenz-Erscheinungen bei Röntgenstrahlen*, Sitzungsberichte der Königlich Bayerischen Akademie der Wissenschaften, 303 - 322 (1912).

[4] W.H. Bragg, *X-rays and Crystals*, Nature **90**, 219 (1912).

[5] W.L. Bragg, *The Diffraction of Short Electromagnetic Waves by a Crystal*, Proceedings of the Cambridge Philosophical Society **17**, 43 - 57 (1913).

[6] A. Einstein, *Strahlungs-Emission und -Absorption nach der Quantentheorie*, Verhandlungen der Deutschen Physikalischen Gesellschaft **18**, 318 - 323 (1916).

[7] J.P. Gordon, H.J. Zeiger, and C.H. Townes, *The Maser—New Type of Microwave Amplifier, Frequency Standard, and Spectrometer*, Phys. Rev. **99**, 1264 - 1274 (1955).

[8] A.L. Schawlow and C.H. Townes, *Infrared and Optical Masers*, Phys. Rev. **112**, 1940 - 1949 (1958).

[9] D.L. Matthews, P.L. Hagelstein, M.D. Rosen, M.J. Eckart, N.M. Ceglio, A.U. Hazi, H. Medecki, B.J. MacGowan, J.E. Trebes, B.L. Whitten, E.M. Campbell, C.W. Hatcher, A.M. Hawryluk, R.L. Kauffman, L.D. Pleasance, G. Rambach, J.H. Scofield, G. Stone, and T.A. Weaver, *Demonstration of a Soft X-Ray Amplifier*, Phys. Rev. Lett. **54**, 110–113 (1985).

[10] J.M.J. Madey, *Stimulated Emission of Bremsstrahlung in a Periodic Magnetic Field*, J. Appl. Phys. **42**, 1906 - 1913 (1971).

[11] D.A.G. Deacon, L.R. Elias, J.M.J. Madey, G.J. Ramian, H.A. Schwettman, and T.I. Smith, *First Operation of a Free-Electron Laser*, Phys. Rev. Lett. **38**, 892 - 894 (1977).

[12] R. Colella and A. Luccio, *Proposal for a free electron laser in the X-ray region*, Opt. Commun. **50**, 41 - 44 (1984).

[13] A.M. Kondratenko and E.L. Saldin, *Generation of Coherent Radiation by a Relativistic Electron Beam in an Ondulator*, Part. Accel. **10**, 207 (1980).

[14] R. Bonifacio, C. Pellegrini, and L. Narducci, *Collective Instabilities and High-Gain Regime in a Free Electron Laser*, Opt. Commun. **50**, 373 - 378 (1984).

[15] W. Ackermann *et al.*, *Operation of a free-electron laser from the extreme ultraviolet to the water window*, Nature Photonics **1**, 336 - 342 (2007).

[16] P. Emma *et al.*, *First lasing and operation of an ångstrom-wavelength free-electron laser*, Nature Photonics **4**, 641 - 647 (2010).

[17] R. Wideröe, Archiv f. Elektrotechnik **21**, 400 (1938).

[18] D.W. Kerst, *Acceleration of Electrons by Magnetic Induction*, Phys. Rev. **58**, 841 - 841 (1940).

[19] D. Iwanenko and I. Pomeranchuk, *On the Maximal Energy Attainable in a Betatron*, Phys. Rev. **65**, 343 (1944).

[20] V. Veksler, *Concerning Some New Methods of Acceleration of Relativistic Particles*, Phys. Rev. **69**, 244 - 244 (1946).

[21] E.M. McMillan, *The Synchrotron—A Proposed High Energy Particle Accelerator*, Phys. Rev. **68**, 143–144 (1945).

[22] F.R. Elder, A.M. Gurewitsch, R.V. Langmuir, and H.C. Pollock, *Radiation from Electrons in a Synchrotron*, Phys. Rev. **71**, 829 - 830 (1947).

[23] U. Bergmann *et al.*, *Science and Technology of Future Light Sources: A White Paper*, Reports ANL-08/39, BNL-81895-2008, LBNL-1090E-2009, and SLAC-R-917 (2008).

[24] A. Thompson, D. Attwood, E. Gulikson, M. Howells, K.-J. Kim, J. Kirz, J. Kortright, I. Lindau, P. Pianetta, A. Robinson, J. Scofield, J. Underwood, D. Vaughan, and G. Williams, *X-Ray Data Booklet*, LBL PUB-490 Rev.3 (2009).

[25] J. Schwinger, *On the Classical Radiation of Accelerated Electrons*, Phys. Rev. **75**, 1912 - 1925 (1949).

[26] G.K. O'Neill, *Storage-Ring Synchrotron: Device for High-Energy Physics Research*, Phys. Rev. **102**, 1418 - 1419 (1956).

[27] H. Motz, *Applications of the Radiation from Fast Electron Beams*, J. Appl. Phys. **22**, 527 (1951).

[28] Z. Huang and K.-J. Kim, *Review of x-ray free-electron laser theory*, Phys. Rev. ST Accel. Beams **10**, 034801 (2007).

[29] P. Schmüser, M. Dohlus, and J. Rossbach, *Ultraviolet and Soft X-Ray Free-Electron Lasers: Introduction to Physical Principles, Experimental Results, Technological Challenges*, Springer-Verlag, Berlin (2008).

[30] J.A. Clarke, *The Science and Technology of Undulators and Wigglers*, Oxford University Press, Oxford (2004).

[31] W.A. Barletta, J. Bisognano, J.N. Corlett, P. Emma, Z. Huang, K.-J. Kim, R. Lindberg, J.B. Murphy, G.R. Neil, D.C. Nguyen, C. Pellegrini, R.A. Rimmer, F. Sannibale, G. Stupakov, R.P. Walker, and A.A. Zholents, *Free electron lasers: Present status and future challenges*, Nucl. Instrum. Methods Phys. Res., Sect. A **618**, 69 - 96 (2010).

[32] E.L. Saldin, E.A. Schneidmiller, and M.V. Yurkov, *The physics of free electron lasers*, Springer-Verlag, Berlin (1999).

[33] H. Wabnitz *et al.*, *Multiple ionization of atom clusters by intense soft X-rays from a free-electron laser*, Nature **420**, 482 - 485 (2002).

[34] L. Young *et al.*, *Femtosecond electronic response of atoms to ultra-intense X-rays*, Nature **466**, 56 - 61 (2011).

[35] H.N. Chapman *et al.*, *Femtosecond X-ray protein nanocrystallography*, Nature **470**, 73 - 77 (2011).

[36] M.M. Seibert *et al.*, *Single mimivirus particles intercepted and imaged with an X-ray laser*, Nature **470**, 78 - 81 (2011).

[37] R. Neutze, R. Wouts, D. van der Spoel, E. Weckert, and J. Hajdu, *Potential for biomolecular imaging with femtosecond X-ray pulses*, Nature **406**, 752 - 757 (2000).

[38] H.N. Chapman *et al.*, *Femtosecond diffractive imaging with a soft-X-ray free-electron laser*, Nature Physics **2**, 839 - 843 (2006).

[39] A. Barty, S. Boutet, M.J. Bogan, S. Hau-Riege, S. Marchesini, K. Sokolowski-Tinten, N. Stojanovic, R. Tobey, H. Ehrke, A. Cavalleri, S. Düsterer, M. Frank, S. Bajt, B.W. Woods, M.M. Seibert, J. Hajdu, R. Treusch, and H.N. Chapman, *Ultrafast single-shot diffraction imaging of nanoscale dynamics*, Nature Photonics **2**, 415 - 419 (2008).

[40] Y. Ding, A. Brachmann, F.-J. Decker, D. Dowell, P. Emma, J. Frisch, S. Gilevich, G. Hays, Ph. Hering, Z. Huang, R. Iverson, H. Loos, A. Miahnahri, H.-D. Nuhn, D. Ratner, J. Turner, J. Welch, W. White, and J. Wu, *Measurements and Simulations of Ultralow Emittance and Ultrashort Electron Beams in the Linac Coherent Light Source*, Phys. Rev. Lett. **102**, 254801 (2009).

[41] Z. Huang, A. Baker, C. Behrens, M. Boyes, J. Craft, F.-J. Decker, Y. Ding, P. Emma, J. Frisch, R. Iverson, J. Lipari, H. Loos, and D. Walz, *Measurement of Femtosecond LCLS Bunches using the SLAC A-Line Spectrometer*, Proceedings of the 24th Particle Accelerator Conference, New York, USA, THP183 (2011).

[42] P. Emma, K. Bane, M. Cornacchia, Z. Huang, H. Schlarb, G. Stupakov, and D. Walz, *Femtosecond and Subfemtosecond X-Ray Pulses from a Self-Amplified Spontaneous-Emission–Based Free-Electron Laser*, Phys. Rev. Lett. **92**, 074801 (2004).

[43] E.L. Saldin, E.A. Schneidmiller, and M.V. Yurkov, *Terawatt-scale sub-10-fs laser technology – key to generation of GW-level attosecond pulses in X-ray free electron laser*, Opt. Commun. **237**, 153 - 164 (2004).

[44] A.A. Zholents and W.M. Fawley, *Proposal for Intense Attosecond Radiation from an X-Ray Free-Electron Laser*, Phys. Rev. Lett. **92**, 224801 (2004).

[45] D. Xiang, Z. Huang, and G. Stupakov, *Generation of intense attosecond x-ray pulses using ultraviolet laser induced microbunching in electron beams*, Phys. Rev. ST Accel. Beams **12**, 060701 (2009).

[46] K. Wille, *The Physics of Particle Accelerators: An Introduction*, Oxford University Press, Oxford (2001).

[47] J.M.J. Madey, *Relationship between mean radiated energy, mean squared radiated energy and spontaneous power spectrum in a power series expansion of the equations of motion in a free-electron laser*, Nuovo Cimento **50B**, 64 (1979).

[48] E.L. Saldin, E.A. Schneidmiller, and M.V. Yurkov, *FAST: a three-dimensional time-dependent FEL simulation code*, Nucl. Instrum. Methods Phys. Res., Sect. A **429**, 233 - 237 (1999).

[49] S. Reiche, *GENESIS 1.3: a fully 3D time-dependent FEL simulation code*, Nucl. Instrum. Methods Phys. Res., Sect. A **429**, 243 - 248 (1999).

[50] A.W. Chao and M. Tigner, *Handbook of Accelerator Physics and Engineering*, World Scientific, Singapore (1999).

[51] M. Xie, *Exact and variational solutions of 3D eigenmodes in high gain FELs*, Nucl. Instrum. Methods Phys. Res., Sect. A **445**, 59 - 66 (2000).

[52] M.G. Minty and F. Zimmermann, *Measurement and control of charged particle beams*, Springer-Verlag, Berlin (2003).

[53] M. Röhrs, *Investigation of the Phase Space Distribution of Electron Bunches at the FLASH-Linac Using a Transverse Deflecting Structure*, DESY-THESIS-2008-012, Hamburg (2008).

[54] O. Grimm and P. Schmüser, *Principles of Longitudinal Beam Diagnostics with Coherent Radiation*, Report TESLA-FEL-2006-03, Hamburg (2006).

[55] P. Emma, J. Frisch, and P. Krejcik, *A Transverse RF Deflecting Structure for Bunch Length and Phase Space Diagnostics*, Technical Report LCLS-TN-00-12, Menlo Park (2000).

[56] M. Röhrs, Ch. Gerth, H. Schlarb, B. Schmidt, and P. Schmüser, *Time-resolved electron beam phase space tomography at a soft x-ray free-electron laser*, Phys. Rev. ST Accel. Beams **12**, 050704 (2009).

[57] C. Behrens, N. Gerasimova, Ch. Gerth, B. Schmidt, E.A. Schneidmiller, S. Serkez, S. Wesch, and M.V. Yurkov, *Constraints on photon pulse duration from longitudinal electron beam diagnostics at a soft x-ray free-electron laser*, Phys. Rev. ST Accel. Beams **15**, 030707 (2012).

[58] S. Wesch, B. Schmidt, C. Behrens, H. Delsim-Hashemi, and P. Schmüser, *A multichannel THz and infrared spectrometer for femtosecond electron bunch diagnostics by single-shot spectroscopy of coherent radiation*, Nucl. Instrum. Methods Phys. Res., Sect. A **665**, 40 - 47 (2011).

[59] G. Berden, S.P. Jamison, A.M. MacLeod, W.A. Gillespie, B. Redlich, and A.F.G. van der Meer, *Electro-Optic Technique with Improved Time Resolution for Real-Time, Nondestructive, Single-Shot Measurements of Femtosecond Electron Bunch Profiles*, Phys. Rev. Lett. **93**, 114802 (2004).

[60] A.L. Cavalieri *et al.*, *Clocking Femtosecond X Rays*, Phys. Rev. Lett. **94**, 114801 (2005).

[61] B. Steffen, V. Arsov, G. Berden, W.A. Gillespie, S.P. Jamison, A.M. MacLeod, A.F.G. van der Meer, P.J. Phillips, H. Schlarb, B. Schmidt, and P. Schmüser, *Electro-optic Time Profile Monitors for Femtosecond Electron Bunches at the Soft X-Ray Free-Electron Laser FLASH*, Phys. Rev. ST Accel. Beams **12**, 032802 (2009).

[62] R. Akre, D. Dowell, P. Emma, J. Frisch, S. Gilevich, G. Hays, Ph. Hering, R. Iverson, C. Limborg-Deprey, H. Loos, A. Miahnahri, J. Schmerge, J. Turner, J. Welch, W. White, and J. Wu, *Commissioning the Linac Coherent Light Source injector*, Phys. Rev. ST Accel. Beams **11**, 030703 (2008).

[63] H. Loos *et al.*, *Observation of Coherent Optical Transition Radiation in the LCLS Linac*, Proceedings of the 30th International Free Electron Laser Conference, Gyeongju, Korea, 2008, THBAU01.

[64] C. Behrens, Ch. Gerth, G. Kube, B. Schmidt, S. Wesch, and M. Yan, *Electron beam profile imaging in the presence of coherent optical radiation effects*, Phys. Rev. ST Accel. Beams **15**, 062801 (2012).

[65] O. Altenmueller, R. Larsen, and G. Loew, *Investigations of Traveling-Wave Separators for the Stanford Two-Mile Linear Accelerator*, Rev. Sci. Instrum. **35**, 438 (1964).

[66] O. Lundh, J. Lim, C. Rechatin, L. Ammoura, A. Ben-Ismaïl, X. Davoine, G. Gallot, J-P. Goddet, E. Lefebvre, V. Malka, and J. Faure, *Few femtosecond, few kiloampere electron bunch produced by a laser–plasma accelerator*, Nature Physics **7**, 219 - 222 (2011).

[67] M. Borland, Y.C. Chae, P. Emma, J.W. Lewellen, V. Bharadwaj, W.M. Fawley, P. Krejcik, C. Limborg, S.V. Milton, H.-D. Nuhn, R. Soliday, and M. Woodley, *Start-to-end simulation of self-amplified spontaneous emission free electron lasers from the gun through the undulator*, Nucl. Instrum. Methods Phys. Res., Sect. A **483**, 268 (2002).

[68] E.L. Saldin, E.A. Schneidmiller, and M.V. Yurkov, *Longitudinal space charge-driven microbunching instability in the TESLA Test Facility linac*, Nucl. Instrum. Methods Phys. Res., Sect. A **528**, 355 (2004).

[69] S. Wesch, C. Behrens, B. Schmidt, and P. Schmüser, *Observation of Coherent Optical Transition Radiation and Evidence for Microbunching in Magnetic Chicanes*, Proceedings of the 31st International Free Electron Laser Conference, Liverpool, United Kingdom, 2009, WEPC50.

[70] H. Tanaka, *Status Report on the Commissioning of the Japanese XFEL at SPring-8*, Proceedings of the 2nd International Particle Accelerator Conference, San Sebastian, Spain, 2011, MOYCA01.

[71] Z. Huang, M. Borland, P. Emma, J. Wu, C. Limborg, G. Stupakov, and J. Welch, *Suppression of microbunching instability in the linac coherent light source*, Phys. Rev. ST Accel. Beams **7**, 074401 (2004).

[72] C. Behrens, Z. Huang, and D. Xiang, *Reversible electron beam heating for suppression of microbunching instabilities at free-electron lasers*, Phys. Rev. ST Accel. Beams **15**, 022802 (2012).

[73] Z. Huang *et al.*, *Measurements of the linac coherent light source laser heater and its impact on the x-ray free-electron laser performance*, Phys. Rev. ST Accel. Beams **13**, 020703 (2010).

[74] Y. Ding, C. Behrens, P. Emma, J. Frisch, Z. Huang, H. Loos, P. Krejcik, and M-H. Wang, *Femtosecond x-ray pulse temporal characterization in free-electron lasers using a transverse deflector*, Phys. Rev. ST Accel. Beams **14**, 120701 (2011).

[75] R. Lai and A.J. Sievers, *On using the coherent far IR radiation produced by a charged-particle bunch to determine its shape: I Analysis*, Nucl. Instrum. Methods Phys. Res., Sect. A **397**, 221 - 231 (1997).

[76] D. Mihalcea, C.L. Bohn, U. Happek, and P. Piot, *Longitudinal electron bunch diagnostics using coherent transition radiation*, Phys. Rev. ST Accel. Beams **9**, 082801 (2006).

[77] H. Delsim-Hashemi, *Infrared Single-Shot Diagnostics for the Longitudinal Profile of the Electron Bunches at FLASH*, Ph.D. thesis, Universität Hamburg, Report DESY-THESIS-2008-024, 2008.

[78] S. Wesch, *Echtzeitbestimmung longitudinaler Elektronenstrahlparameter mittels absoluter Intensitäts- und Spektralmessung einzelner kohärenter THz Strahlungspulse*, Ph.D. thesis, Universität Hamburg, 2012.

[79] I. Zagorodnov, *Ultra-Short Low Charge Operation at FLASH and the European XFEL*, Proceedings of the 32nd International Free Electron Laser Conference, Malmö, Sweden, 2010, WEOBI2.

[80] C. Behrens, A.S. Fisher, J.C. Frisch, A. Gilevich, H. Loos, and J. Loos, *Design of a Single-Shot Prism Spectrometer in the Near- and Mid-Infrared Wavelength Range for Ultra-Short Bunch Length Diagnostics*, Proceedings of the 10th European Workshop on Beam Diagnostics and Instrumentation for Particle Accelerators, Hamburg, Germany, 2011, TUPD38.

[81] E.L. Saldin, E.A. Schneidmiller, and M.V. Yurkov, *On the coherent radiation of an electron bunch moving in an arc of a circle*, Nucl. Instrum. Methods Phys. Res., Sect. A **398**, 373 (1997).

[82] M. Venturini and A. Zholents, *Modeling microbunching from shot noise using Vlasov solvers*, Nucl. Instrum. Methods Phys. Res., Sect. A **593**, 53 (2008).

[83] I. Zagorodnov and M. Dohlus, *Semianalytical modeling of multistage bunch compression with collective effects*, Phys. Rev. ST Accel. Beams **14**, 014403 (2011).

[84] D.H. Dowell, J.L. Adamski, T.D. Hayward, C.G. Parazzoli, and A. M. Vetter, *The Boeing photocathode accelerator magnetic pulse compression and energy recovery experiment*, Nucl. Instrum. Methods Phys. Res., Sect. A **375**, 108 - 111 (1996).

[85] E. Vogel *et al.*, *Test and Commissioning of the Third Harmonic RF System for FLASH*, Proceedings of the 1st International Particle Accelerator Conference, Kyoto, Japan, 2010, THPD0003.

[86] H. Edwards, C. Behrens, and E. Harms, *3.9 GHz Cavity Module for Linear Bunch Compression at FLASH*, Proceedings of the 25th International Linear Accelerator Conference, Tsukuba, Japan, 2010, MO304 (invited talk).

[87] C. Behrens, C. Gerth, and I. Zagorodnov, *Numerical Performance Studies on the new Sliced-Beam-Parameter Measurement Setup for FLASH*, Proceedings of the 31st International Free Electron Laser Conference, Liverpool, United Kingdom, 2009, WEPC45.

[88] C. Behrens and Ch. Gerth, *Measurements of Sliced-Bunch Parameters at FLASH*, Proceedings of the 32nd International Free Electron Laser Conference, Malmö, Sweden, 2010, MOPC08.

[89] P. Chen, J. M. Dawson, Robert W. Huff, and T. Katsouleas, *Acceleration of Electrons by the Interaction of a Bunched Electron Beam with a Plasma*, Phys. Rev. Lett. **54**, 693 (1985).

[90] G.A. Voss and T. Weiland, *Particle Acceleration by Wake Fields*, Report DESY-M-82-10, Hamburg (1982).

[91] W. Gai, P. Schoessow, B. Cole, R. Konecny, J. Norem, J. Rosenzweig, and J. Simpson, *Experimental Demonstration of Wake-Field Effects in Dielectric Structures*, Phys. Rev. Lett. **61**, 2756 (1988).

[92] K.L.F. Bane, P. Chen, and P.B. Wilson, *Collinear wake field acceleration*, Report SLAC-PUB-3662, Menlo Park (1985).

[93] P. Piot, C. Behrens, C. Gerth, M. Dohlus, F. Lemery, D. Mihalcea, P. Stoltz, and M. Vogt, *Generation and Characterization of Electron Bunches with Ramped Current Profiles in a Dual-Frequency Superconducting Linear Accelerator*, Phys. Rev. Lett. **108**, 034801 (2012).

[94] F. Lemery, C. Behrens, E. Elsen, K. Flöttmann, C. Gerth, G. Kube, D. Mihalcea, J. Osterhoff, P. Piot, B. Schmidt, and P. Stoltz, *Experimental Plans to Explore Dielectric Wakefield Acceleration in the THz Regime*, Proceedings of the 2nd International Particle Accelerator Conference, San Sebastian, Spain, 2011, WEPZ008.

[95] P. Piot, C. Behrens, C. Gerth, F. Lemery, D. Mihalcea, and M. Vogt, *Generation and Characterization of Electron Bunches with Ramped Current Profile at the FLASH Facility*, Proceedings of the 2nd International Particle Accelerator Conference, San Sebastian, Spain, 2011, WEPZ016.

[96] F. Stephan *et al.*, *Detailed characterization of electron sources yielding first demonstration of European X-ray Free-Electron Laser beam quality*, Phys. Rev. ST Accel. Beams **13**, 020704 (2010).

[97] R. Ganter, B. Beutner, S. Binder, H.H. Braun, T. Garvey, C. Gough, C. Hauri, R. Ischebeck, S. Ivkovic, F. Le Pimpec, K. Li, M.L. Paraliev, M. Pedrozzi, T. Schietinger, B. Steffen, A. Trisorio, and A. Wrulich, *Electron beam characterization of a combined diode rf electron gun*, Phys. Rev. ST Accel. Beams **13**, 093502 (2010).

[98] D.J. Dunning, N.R. Thompson, B.W.J. McNeil, R. Bartolini, Z. Huang, and H. Geng, *Optimisation of an HHHG-Seeded Harmonic Cascade FEL Design for the NLS Project*, Proceedings of the 1st International Particle Accelerator Conference, Kyoto, Japan, 2010, TUPE049.

[99] W.K.H. Panofsky and W.A. Wenzel, *Some Considerations Concerning the Transverse Deflection of Charged Particles in Radio [U+2010]Frequency Fields*, Rev. Sci. Instrum. **27**, 967 (1956).

[100] S. Korepanov, M. Krasilnikov, F. Stephan, D. Alesini, and L. Ficcadenti, *An RF Deflector for the Longitudinal and Transverse Beam Phase Space Analysis at PITZ*, Proceedings of the 8th European Workshop on Beam Diagnostics and Instrumentation for Particle Accelerators, Venice, Italy, 2007, TUPB32.

[101] C. Behrens and Ch. Gerth, *On the Limitations of Longitudinal Phase Space Measurements using a Transverse Deflecting Structure*, Proceedings of the 9th European Workshop on Beam Diagnostics and Instrumentation for Particle Accelerators, Basel, Switzerland, 2009, TUPB44.

[102] C. Behrens and Ch. Gerth, *Measurement of the Slice Energy Spread Induced by a Transverse Deflecting RF Structure at FLASH*, Proceedings of the 10th European Workshop on Beam Diagnostics and Instrumentation for Particle Accelerators, Hamburg, Germany, 2011, TUPD31.

[103] C. Behrens, Z. Huang, and D. Xiang, *Reversible Electron Beam Heater for Suppression of Microbunching Instabilities Based on Transverse Deflecting Cavities*, Proceedings of the 33rd International Free Electron Laser Conference, Shanghai, China, 2011, WEPB15.

[104] C. Behrens, Z. Huang, and D. Xiang, *Reversible electron beam heating for suppression of microbunching instabilities at free-electron lasers*, Phys. Rev. ST Accel. Beams **15**, 022802 (2012).

[105] P. Radcliffe, S. Düsterer, A. Azima, H. Redlin, J. Feldhaus, J. Dardis, K. Kavanagh, H. Luna, J. Pedregosa Gutierrez, P. Yeates, E. T. Kennedy, J.T. Costello, A. Delserieys, C.L.S. Lewis, R. Taïeb, A. Maquet, D. Cubaynes, and M. Meyer, *Single-shot characterization of independent femtosecond extreme ultraviolet free electron and infrared laser pulses*, Appl. Phys. Lett. **90**, 131108 (2007).

[106] A. Azima, S. Düsterer, P. Radcliffe, H. Redlin, N. Stojanovic, W. Li, H. Schlarb, J. Feldhaus, D. Cubaynes, M. Meyer, J. Dardis, P. Hayden, P. Hough, V. Richardson, E.T. Kennedy, and J.T. Costello, *Time resolved pump-probe experiments beyond the jitter limitations at FLASH*, Appl. Phys. Lett. **94**, 144102 (2009).

[107] Y. Ding, C. Behrens, P. Emma, J. Frisch, Z. Huang, H. Loos, P. Krejcik, and M-H. Wang, *Ultra-Short Electron Bunch and X-Ray Temporal Diagnostics with an X-Band Transverse Deflector*, Proceedings of the 33rd International Free Electron Laser Conference, Shanghai, China, 2011, WEPB14.

[108] U. Frühling, M. Wieland, M. Gensch, T. Gebert, B. Schütte, M. Krikunova, R. Kalms, F. Budzyn, O. Grimm, J. Rossbach, E. Plönjes, and M. Drescher, *Single-shot terahertz-field-driven X-ray streak camera*, Nature Photonics **3**, 523 - 528 (2009).

[109] I. Grguraš, A.R. Maier, C. Behrens, T. Mazza, T.J. Kelly, P. Radcliffe, S. Düsterer, A. K. Kazansky, N.M. Kabachnik, Th. Tschentscher, J.T. Costello, M. Meyer, M.C. Hoffmann, H. Schlarb, and A.L. Cavalieri, *Ultrafast X-ray pulse characterization at free-electron lasers*, accepted for publication in Nature Photonics (2012).

[110] E.L. Saldin, E.A. Schneidmiller, and M.V. Yurkov, *Statistical properties of radiation from VUV and X-ray free electron laser*, Opt. Commun. **148**, 383 (1998).

[111] E.L. Saldin, E.A. Schneidmiller, and M.V. Yurkov, *Statistical and coherence properties of radiation from x-ray free-electron lasers* , New J. Phys. **12**, 035010 (2010).

[112] N. Gerasimova, S. Dziarzhytski, and J. Feldhaus, *The monochromator beamline at FLASH: performance, capabilities and upgrade plans*, J. Mod. Opt. **58**, 1480 - 1485 (2011).

[113] D. Filippetto *et al.*, *Phase space analysis of velocity bunched beams*, Phys. Rev. ST Accel. Beams **14**, 092804 (2011).

[114] E.L. Saldin, E.A. Schneidmiller, M.V. Yurkov, *Optical afterburner for an x-ray free electron laser as a tool for pump-probe experiments*, Phys. Rev. ST Accel. Beams **13**, 030701 (2010).

[115] F. Löhl, V. Arsov, M. Felber, K. Hacker, W. Jalmuzna, B. Lorbeer, F. Ludwig, K.-H. Matthiesen, H. Schlarb, B. Schmidt, P. Schmüser, S. Schulz, J. Szewinski, A. Winter, and J. Zemella, *Electron Bunch Timing with Femtosecond Precision in a Superconducting Free-Electron Laser*, Phys. Rev. Lett. **104**, 144801 (2010).

[116] F. Tavella, N. Stojanovic, G. Geloni, and M. Gensch, *Few-femtosecond timing at fourth-generation X-ray light sources*, Nature Photonics **5**, 162 - 165 (2011).

[117] M. Gensch *et al.*, *New infrared undulator beamline at FLASH*, Nucl. Instrum. Methods Phys. Res., Sect. A **51**, 423 - 425 (2008).

[118] K.-L. Yeh, M.C. Hoffmann, J. Hebling, and K.A. Nelson, *Generation of* 10 $\mu$J *ultrashort terahertz pulses by optical rectification*, Appl. Phys. Lett. **90**, 171121 (2007).

The references in the journal articles of chapters 3, 4, and 5 are not necessarily listed here.

# Acknowledgments

According to the principle of causality, describing the fundamental relationship between causes and effects, the work presented within this thesis is the result of many people's contributions, efforts, support and hard work, and would not have been possible without:

My advisors Christopher Gerth, Bernhard Schmidt, and Jörg Roßbach

My FLASH colleagues Evgeny Schneidmiller, Mikhail Yurkov, Holger Schlarb, Peter Schmüser, Igor Zagorodnov, Gero Kube, Natalia Gerasimova, and Torsten Limberg

My SLAC colleagues Henrik Loos, Zhirong Huang, Yuantao Ding, Paul Emma, Dao Xiang, Alan Fisher, Joe Frisch, Tonee Smith, Rick Iverson, Sasha Gilevich, and Mark Petree

My "happy banana" THz streaking colleagues Adrian Cavalieri, Ivanka Grguraš, Andreas Maier, Sebastian Huber, Tommaso Mazza, and Hubertus Bromberger

My FNAL colleagues Helen Edwards and Philippe Piot

The support of Reinhard Brinkmann and Alexander Gamp

The camera and control system experts Gerhard Schlesselmann, Vladimir Rybnikov, Tim Wilksen, Thomas Bruns, and Raimund Kammering

The FLASH coordinators Katja Honkaavara, Siegfried Schreiber, Bart Faatz, Mathias Vogt, Karsten Klose, and Max Görler

My PhD mates Stephan Wesch, Minjie Yan, Lasse Schroedter, Sebastian Schulz, Benjamin Dicke, Marie Bock, Eugen Hass, Laurens Wissmann, Jörn Bödewadt, and Johann Zemella

The engineers and technicians Kai Ludwig, Bernd Beyer, Antonio de Zubiaurre Wagner, Nils Mildner, Albert Schleiermacher, Matthias Hoffmann, Martin Staack, and Rolf Jonas

My DESY-FLA colleagues Ursula Djuanda, Ingrid Nikodem, Herbert Kapitza, Iris Kerkhoff, Axel Knabbe, Florian Löhl, Andy Langner, Jonas Breunlin, and Steffen Wunderlich

My teacher in school Lars Eskildsen

My friends Timo Schäpe and Torben Gamroth

My family and, last but not least, my sweetie Elgin Oyrak

*I am deeply indebted to you! Thank you and cheers ...*